DEVELOPMENT AND OPTIMISATION OF TWO-LINE PLANAR LASER INDUCED FLUORESCENCE TECHNIQUE FOR COMBUSTION MEASUREMENTS

A thesis submitted for the degree of Doctor of Philosophy

By

Mohammadreza Anbari Attar

Centre for Advanced Powertrain and Fuels Research (CAPF)

School of Engineering and Design

Brunel University, United Kingdom

October 2012

Brunel UNIVERSITY LONDON

Abstract

This study has focused on development, optimisation and implementation of the 2-line Planar Laser Induced Fluorescence (2-line PLIF) technique for combustion measurements on a single cylinder optical Gasoline Direct Injection (GDI) engine with both Spark Ignition (SI) and Controlled Auto Ignition (CAI) combustion operations. The CAI combustion was achieved by employing Negative Valve Overlap (NVO). Two excitation wavelengths at 308 nm (directly from a XeCl laser) and 277 nm (via Raman shifting a KrF laser output at 248 nm) were exploited for the measurements. A calibration curve of fluorescence signal intensity ratio of the two laser beams as a function of temperature was obtained by conducting a series of static tests on a specially designed Constant Volume Chamber (CVC). The developed technique was validated by measurements of in-cylinder charge temperature during the compression stroke for both motoring and firing cycles and comparing the PLIF values with the temperature values calculated from in-cylinder pressure data assuming a polytropic compression. Following the validation measurements, the technique was applied to study of fuel spray characteristics and simultaneous measurements of in-cylinder charge temperature and mole fraction of Exhaust Gas Residuals (EGR). Further optimisation of the thermometry technique by enhancing the fluorescence Signal to Noise Ratio (SNR) and improving both the temporal and spatial resolutions as well as measurements precision provided the opportunity to apply the technique to other combustion measurements. The thesis presents the first application of the 2-line PLIF diagnostic in study of direct injection charge cooling effects and study of flame thermal stratification in IC engines.

Acknowledgments

I would like to thank my dearest parents, for their help and support over the years.

I would like to express sincere gratitude to my supervisor, Prof. Hua Zhao for his help and guidance through this project.

I must also thank various members of staff who have contributed to this work. I wish them all the best.

To My Dear Mom and Dad

Nomenclature

Abbreviations

ABF	Absolute Fluorescence Method
AFR	Air/Fuel Ratio
AI	Auto-Ignition
AOI	Angle of Incident
AR	Anti-Reflection
ASP	Anti-Scuffing Paste
aTDC	After Top Dead Centre
BBAR	Broad Band Anti Reflection
BDC	Bottom Dead Centre
bTDC	Before Top Dead Centre
CA	Crank Angle
CAI	Controlled Auto-Ignition
CARB	Californian Air Resource Board
CARS	Coherent Anti-Stokes Raman Scattering
CCD	Charged-Coupled Device
CCS	Combined Combustion System
CO	Carbon Monoxide
COT	Coil On Time
COV	Coefficient Of Variation
CR	Compression Ratio
CVC	Constant Volume Chamber
CVCC	Compound Vortex Controlled Combustion
deg	degree
DAQ	Data Acquisition System

DFWM	Degenerate Four-Wave Mixing
DI	Direct Injection
DIF	Double Image Frame
DM	Dichroic Mirror
DOF	Depth Of Field
DRP	Digital Recording Processor
ECU	Electronic Control Unit
EGR	Exhaust Gas Recirculation
EIA	Energy Information Administration
EPA	Environmental Protection Agency
EV	Electric Vehicle
EVC	Exhaust Valve Closing
EVO	Exhaust Valve Opening
FOV	Field Of View
fps	Frame Per Second
FQY	Frequency Quantum Yield
FWHM	Full Width Half Maximum
GCI	Gasoline Compression Ignition
GDI	Gasoline Direct Injection
HC	Hydrocarbons
HCCI	Homogeneous Charge Compression Ignition
HCHO	Formaldehyde
HORSES	Hyper-order Raman spectral excitation spectroscopy
HR	High Reflective
HTR	High Temperature Resistance
HV	High Voltage
IC	Internal Combustion
ICCD	Intensified Charged-Coupled Device
iEGR	Internal Exhaust Gas Recirculation
IMEP	Indicated Mean Effective Pressure
ISFC	Indicated Specific Fuel Consumption
IVC	Intake Valve Closing
IVO	Intake Valve Opening

KrF	Krypton Fluoride
LDT	Laser Damage Threshold
LEV	Low Emission Vehicle
LII	Laser induced incandescence
LIF	Laser induced fluorescence
LIL	Lower Intensity Level
LP	Long Pass
MBT	Minimum Spark Advance for Best Torque
MCP	Micro Channel Plate
MFB	Mass Fraction Burn
MNPT	Male National Pipe Thread
MPFI	Multi-Point Fuel Injector
MPI	Multi-Point Injector
NBR	Nitrile Rubber
NIRAT	Near Infrared Absorption Tomography
NMHC	Non-Methane Hydrocarbons
NMOG	Non-Methane Organic Gas
NOx	Nitrogen Oxides
NVO	Negative Valve Overlap
OH	Hydroxyl radicals
OPEC	Organization of the Petroleum Exporting Countries
PDF	Probability Density Function
PFI	Port Fuel Injection
PLIF	Planar laser induced fluorescence
PM	Particulate Matter
PMEP	Pumping Mean Effective Pressure
ppm	Parts per Million
PS	Polarization Spectroscopy
PTG	Programmable Timing Generator
RIKES	Raman induced Kerr effect
RON	Research Octane Number
PVO	Positive Valve Overlap
RC	Raman Convertor

ROI	Region of Interest
rms	Root Mean Square
rpm	Revolutions Per Minute
rps	Revolutions Per Second
SA-CAI	Spark Assisted Controlled Auto-Ignition
SD	Super Diesel
SIF	Single Image Frame
SI	Spark Ignition
SNR	Signal-to-Noise Ratio
SOI	Start of Injection
SRGS	Stimulated Raman gain/loss spectroscopy
SULEV	Super Low Emissions Vehicle
SVC	Saab Variable Compression
TDC	Top Dead Centre
TEA	Triethylamime
THAF	Thermally Assisted Fluorescence
TLAF	Two-line Atomic Fluorescence
TLMF	Two-line Molecular Fluorescence
TS	Thermal Stratification
uHC	Unburned Hydrocarbons
UV	Ultra Violet
VAT	Value Added Tax
VCR	Variable Compression Ratio
VVA	Variable Valve Actuation
WOT	Wide Open Throttle
XeCl	Xenon Chloride
ZEV	Zero Emission Vehicle

Symbols in Roman

A	apex angle, °
c	speed of light, cm/s
c_p	specific heat at constant pressure, J/kg.K
c_v	specific heat at constant volume, J/kg.K
d	object distance, cm
E	laser fluence, J/cm^2
f	focal point, mm
h	Planck's constant, Js
I	irradiance, W/cm^2
k	Boltzmann constant, J/K
m	mass, kg
M	molecular weight
M^2	beam quality
n	refractive index
	polytropic constant
N	number density, cm^{-3}
P	pressure, bar (or Pa)
R	curvature radii, cm
	signal ratio
$\tilde{R}$	specific gas constant, J/kg.K
S	signal power, W
t_{exp}	exposure time, s
t_R	readout time, s
T	temperature, K (or °C)
V	volume, cm^3
V_c	collection/clearance volume, cm^3
V_d	displacement volume, cm^3
x	non-dimensional size parameter

Symbols in Greek

α	angle of incidence, °
β	angle of refraction at first prism surface, °
γ	angle of incident at second prism surface, °
	ratio of specific heats
δ	angle of refraction exiting the prism, °
ϵ	beam deviation, °
η_c	detection efficiency
η_v	volumetric efficiency
θ	angle, °
$\bar{\nu}$	wavenumber, cm^{-1}
λ	wavelength, nm
	relative air/fuel ratio
ρ	density, kg/m^3
υ	frequency, cm^{-1}
σ	cross section, cm^2
ϕ	fluorescence quantum yield
χ_i	mole fraction of species *i*
Ω_c	solid angle of the collection optics, sr

Contents

CHAPTER 1. Introduction 1
1.1 Introduction 1
1.2 Objectives 2
1.3 Outline of Thesis 3

CHAPTER 2. Literature Review 5
2.1 Introduction 5
2.2 Emission Legislations 5
2.3 Gasoline Direct Injection Engine Technologies and R&D Trends 7
2.3.1 Increased Compression Ratio 8
2.3.1.1 High Octane Fuels 9
2.3.1.2 Atkinson and Miller Cycle Operations 9
2.3.1.3 Engines with Variable Compression Ratio (VCR) 10
2.3.2 Engine Downsizing 11
2.3.3 Stratified Charge Combustion 12
2.3.4 CAI/HCCI Combustion 13
2.3.5 Engine Stop and Start Systems 13
2.4 Combustion Diagnostic Techniques for In-cylinder Charge Temperature Measurements 14
2.4.1 Physical Probes vs. Laser Diagnostic Techniques 15
2.4.2 Laser Diagnostic Techniques: Coherent and Incoherent Approaches 16
2.4.3 Review of Incoherent Approaches: Similarities and Differences 18
2.4.4 Signal Power in Incoherent Techniques 20
2.4.5 Thermometry by Vibrational and Rotational Raman

Scattering 21
2.4.6 Thermometry by Rayleigh Scattering 22
2.4.7 Laser Induced Fluorescence 23
2.4.7.1 Thermometry by Excitation or Fluorescence Scans 23
2.4.7.2 Thermometry by Single-line Fluorescence 24
2.4.7.3 Thermometry by Two-line Fluorescence 24
2.4.7.4 Planar Techniques 25
2. 5 Two-line PLIF Literature Review 25
2. 5.1 Choice of Tracer 25
2.5.2 Two-line PLIF Measurements 28
2.6 Summary 30

CHAPTER 3. Experimental Test Facilities 31
3.1 Introduction 31
3.2 Engine Test Bed 31
3.2.1 Dynamometer 31
3.2.2 Coolant and Oil Systems 32
3.3 Single Cylinder Research Engine 33
3.3.1 General Description 33
3.3.2 Cylinder Head 34
3.3.3 Camshafts 35
3.3.4 Extended Cylinder Block and Extended Piston 36
3.3.5 Compression Ratio 36
3.4 Air Inlet and Exhaust Systems 37
3.5 Spark Ignition System 38
3.6 Fuel and Tracer Injection Systems 39
3.6.1 Air-Assisted Direct Fuel/Tracer Injection System 39
3.6.2 Tracer Manifold Port Injection System 41
3.7 Fuel and Tracer Supply Systems 41
3.8 In-Cylinder Pressure Measurement 42
3.9 Data Acquisition System 43
3.10 Engine Reference Signal 43
3.11 Engine Maintenance and Operation 44

3.12 Engine Modifications 46
3.12.1 New Sandwich Plates Design 46
3.12.2 Extended Cylinder Block and Piston Lubrication 49
3.12.3 Engine Coolant Channels 50
3.13 Fuel/Tracer Injection Quantity and Intake Air Flow Ratio Measurements 51
3.13.1 Manifold Port Injector Calibration 51
3.13.2 Air-Assisted Direct Injector Calibration 52
3.13.3 Intake Air Flow Rate Measurements 53
3.14 Summary 54

CHAPTER 4. Development of the Two-line PLIF Diagnostic Technique 55
4.1 Introduction 55
4.2 Principle of Two-line PLIF Thermometry 55
4.3 Implementation of Two-line PLIF Diagnostic Technique 60
4.4 Laser Diagnostic Experimental Setup 61
4.4.1 Light Sources 61
4.4.1.1 Excimer Lasers 61
4.4.1.2 Raman Convertor 62
4.4.1.2.1 Raman Convertor Filling and Purging Facilities 64
4.4.2 Beam Delivery and Shaping System 65
4.4.2.1 Equilateral Dispersing Prism 67
4.4.2.2 Beam Splitter 68
4.4.2.3 High Reflective and Dichroic Mirrors 68
4.4.2.4 Cylindrical Lenses 69
4.4.3 Imaging System 70
4.4.3.1 PI-MAX III Intensified CCD Camera 71
4.4.3.2 Camera Lenses 73
4.5 Study of Excimer Lasers' beam Characteristics 74
4.5.1 Divergence 75
4.5.2 Shot-to-Shot Pulse Energy Variation 76

4.5.3 Beam Profile 77
4.6 Two-line PLIF System Trigger-in Signal 78
4.7 Time Budgeting and Synchronization 80
4.8 Engine Vibration Measurements 82
4.9 Improving Two-line PLIF Imaging Quality 83
4.9.1 Eliminating DIF Mode Noise 83
4.9.2 Eliminating Unwanted Wavelengths 84
4.9.3 Eliminating In-cylinder Reflections 86
4.9.4 Eliminating CCD Accumulated Dark Charge 87
4.10 Raman Convertor Conversion Efficiency Measurements 89
4.10.1 Results and Discussion 90
4.11 Summary 93

CHAPTER 5. Calibration and Validation Measurements 94
5.1 Introduction 94
5.2 Constant Volume Chamber 94
5.2.1 Heating System 97
5.2.2 Thermal Insulations 97
5.2.3 Tracer Supply System 98
5.3 Constant Volume Chamber Temperature Calibration Measurements 99
5.3.1 Experimental Setup and Test Procedure 99
5.3.2 Results and Discussion 102
5.4 Two-line PLIF Average In-Cylinder Charge Temperature Measurements 105
5.4.1 Average In-Cylinder Charge Temperature Calculation from Pressure Data 105
5.4.2 Engine Setup for Combustion Measurements 106
5.4.3 Experimental Setup 108
5.4.4 Test Procedure 108
5.5.5 Results and Discussion 110
5.5 Summary 112

CHAPTER 6. In-cylinder Fuel Injection, Mixing and Combustion Measurements 113
6.1 Introduction 113
6.2 Motoring Tests 113
6.2.1 Single-line PLIF Fuel Spray Visualization 113
6.2.1.1 Experimental Setup 114
6.2.1.2 Test Procedure 115
6.2.1.3 Results and Discussion 117
6.2.2 Two-Line PLIF Study of Direct Injection Charge Cooling Effects 123
6.2.2.1 Experimental Setup and Test Procedure 123
6.2.2.2 Results and Discussion 123
6.3 Firing Tests 129
6.3.1 High Speed Imaging of Flame Propagation and Combustion 129
6.3.1.1 Experimental Setup 129
6.3.1.2 Test Procedure 131
6.3.2 Study of Flame Formation and Propagation of SI and Spark-assisted CAI Combustion 132
6.3.2.1 Experimental Setup 132
6.3.2.2 Test Procedure 132
6.3.2.3 Results and Discussion 133
6.3.2.3.1 Spark Ignition Combustion 133
6.3.2.3.2 Spark-assisted CAI Combustion 136
6.3.4 Two-line PLIF Study of Flame Thermal Stratification 139
6.3.4.1 Experimental Setup and Test Procedure 139
6.3.4.2 Results and Discussion 141
6.3.5 Two-Line PLIF Simultaneous Exhaust Gas Residual and Temperature Measurements 144
6.3.5.1 Experimental Setup 144
6.3.5.2 Test Procedure 145
6.3.5.3 Results and Discussion 145
6.3.5.3.1 Simultaneous T/EGR Measurements Sample Calculation 151

6.3.5.3.2 Two Dimensional T/EGR Maps 154
6.3.5.3.3 Temperature and EGR Probability Density Functions 166
6.4 Summary 169

CHAPTER 7. Conclusions and Recommendations for Future Work 171
7.1 Conclusions 171
7.1.1 Improving Fluorescence SNR and Imaging Quality 172
7.1.2 Calibration Measurements 173
7.1.3 Validation Measurements 173
7.1.4 Application of the Technique 174
7.1.4.1 Single-line PLIF Fuel Spray Visualization 174
7.1.4.2 Two-line PLIF Study of Direct Injection Charge Cooling Effects 174
7.1.4.3 Two-line PLIF Study of Flame Thermal Stratification 175
7.1.4.4 Two-line PLIF Simultaneous Exhaust Gas Residual and Temperature Measurements 176
7.2 Recommendations for Future Work 176
7.2.1 Sandwich Plate with Side Windows 176
7.2.2 Cylinder Block 177
7.2.3 Calibration Measurements 178
7.2.4 Flame Thermal Stratification 178

Appendices 179
A. Engine Control Units and NIDAQ System Connection Diagram 179
B. Gasketing 180
C. Technical Drawings of the Designed Engine Components 181
D. MPI and DI Injection Calibration Curves 192
E. Raman Convertor Filling Instruction 193
F. Specifications of Optical Components 194
G. Imaging Parameters 200

H. Visual Basic Image Post Processing Codes 201
I. Sample Calculation of the In-cylinder Charge Temperature 204
J. 3-Petanonen FQY Calculation Code 208

References 212

List of Figures

Figure 2.1 MCE-5 VCRi's mechanical arrangement 11
Figure 2.2 The basic Honda CVCC operating mechanism 12
Figure 2.3 Energy level representation of Rayleigh (R), Rotational Raman (RR), Vibrational Raman (VR), and Fluorescence (F) scattering methods. 19
Figure 3.1 Engine test bed 32
Figure 3.2 Single cylinder research engine 33
Figure 3.3 Combustion chamber of the prototype Orbital cylinder head 34
Figure 3.4 Left: high/low valve lift camshafts; Right: adjusting the valve timing 35
Figure 3.5 Piston window assembly arrangement 37
Figure 3.6 Air inlet and exhaust systems 38
Figure 3.7 Schematic diagram of spark ignition system 39
Figure 3.8 Top: Schematic diagram of Orbital air-assisted injector with typical injection sequence; Bottom: Orbital air-assisted injector 40
Figure 3.9 Schematic diagram of air-assisted injector control system. 40
Figure 3.10 Fuel/tracer supply system 42
Figure 3.11 Left: KTK thyristor convertor unit; Right: Hydra control console 45
Figure 3.12 Engine control unites 46
Figure 3.13 Three different manufactured sandwich plates 47
Figure 3.14 NIRAT array mounted on the engine 48
Figure 3.15 Mounting and sealing details of the optical ring 49
Figure 3.16 (a) A metal ring was placed inside the coolant channel (b) The remaining space was filed with an adhesive. (c) and (d) copper gasket and 4130 alloy sheet were attached to the cylinder head. 50

Figure 3.17 Experimental setup for manifold port injector calibration 52
Figure 3.18 Measurements of the clearance volume 54
Figure 4.1 Energy diagram of molecular system 56
Figure 4.2 Relative fluorescence quantum yield for 3-pentanone at 1 bar excited with 248, 266, and 308 nm 58
Figure 4.3 Absorption spectra of 3-pentanone at elevated temperatures 59
Figure 4.4 The timing event of 2-line PLIF technique 60
Figure 4.5 Top: A reverse Keplerian beam expander; Bottom: A reverse Galilean beam expander 63
Figure 4.6 Raman convertor lens assembly 63
Figure 4.7 Raman convertor filling/purging facilities 64
Figure 4.8 Beam delivery and shaping system 66
Figure 4.9 Diagram of dispersing prism 67
Figure 4.10 Illustration of the beam lifting and flipping steps 69
Figure 4.11 Exposure and readout in overlapped mode 72
Figure 4.12 UV-Nikkor 105 mm *f*/4.5 and its lens construction 73
Figure 4.13 Micro-Nikkor 60 mm *f*/2.8 and its lens construction 73
Figure 4.14 Pulse energy variation of Excimer lasers, Top: KrF; Bottom: XeCl 77
Figure 4.15 Typical beam profile of a 248 nm Excimer laser on X and Y axes 77
Figure 4.16 Counter/Divider Board Installed in the Dual Output Angle Delay Unit 80
Figure 4.17 Oscilloscope screen shots, Left: override mode; continues injections; Right: 4 cycles OFF, 1 injection 80
Figure 4.18 Timing diagram of various camera and laser events and adjusted delays for capturing a double image frame (DIF) 82
Figure 4.19 Noise level on the first (left) and second image (right) of a single DIF 83
Figure 4.20 DIF noise level dependency on PTG trigger-in signal frequency 84
Figure 4.21 Scattering regimes 85
Figure 4.22 Comparison of the candle soot and HTR paint reflection for

incident beam at 308 nm with pulse energy of (b) 50 mJ, (c) 25mJ 87
Figure 4.23 Comparison of up to two internal reflections of the laser sheet inside the engine for the sheet focused, Top: Inside the cylinder; Bottom: Behind the cylinder 87
Figure 4.24 Raman convertor conversion efficiency measurements test setup 90
Figure 4.25 Raman convertor output pulse energy at 277 nm as a function of pump pulse energy and RC fill pressure 91
Figure 4.26 Output pulse energy reduction at RC and prism 92
Figure 4.27 RC output pulse energy variation as a function of pump pulse energy and fill pressure 93
Figure 5.1 Constant volume chamber components 96
Figure 5.2 Insulation layers of the CVC assembled on the cylinder block 98
Figure 5.3 Tracer supply system 99
Figure 5.4 Left: Excimer laser pulse rectangular shape (right after the beam shutter) burned on a thermal fax paper; Right: Laser marks at the end of the beam delivery system for; Top: Poorly aligned beam; Bottom: Accurately aligned beam 100
Figure 5.5 UV Nikkor lens focused on the measurement plane inside the CVC 101
Figure 5.6 Left: single-shot background image, Right: single-shot data image 102
Figure 5.7 Image processing algorithm for the CVC temperature calibration curve 103
Figure 5.8 Two-line PLIF sample CVC temperature measurement result 104
Figure 5.9 Intake port arrangements 108
Figure 5.10 Experimental setup for average in-cylinder charge temperature measurements 109
Figure 5.11 Average in-cylinder motoring and firing charge temperature calculated from both pressure data and 2-line PLIF images for the NVO operation 111
Figure 6.1 Single-line PLIF fuel spray visualization experimental setup 114
Figure 6.2 Comparison of focused and expanded laser sheets 115

Figure 6.3 Intake and exhaust valves timing, fuel injection events for both normal and negative valve overlaps 117
Figure 6.4 Fuel injection event at 120 °CA aTDC (Int.) without background subtraction (average of 40 single frames at each crank angle) 118
Figure 6.5 Fuel injection event at 120 °CA aTDC (Int.) after background subtraction (average of 40 single frames at each crank angle) 119
Figure 6.6 Fuel injection event at 140 °CA bTDC (Com.) after background subtraction (average of 40 single frames at each crank angle) 120
Figure 6.7 Fuel injection event at 90 °CA bTDC (Com.) after background subtraction (average of 40 single frames at each crank angle) 121
Figure 6.8 Fuel injection event at 90 °CA bTDC (Com.) after correction for inhomogeneous laser illumination 122
Figure 6.9 Fuel injection event at 90 °CA bTDC (Com.) after correction for inhomogeneous laser illumination using a lower intensity level-adjusted reference image 122
Figure 6.10 Fluorescence intensity ratio and temperature, 10 mg/cycle direct fuel injection at 90 °CA aTDC (Int.) 125
Figure 6.11 Fluorescence intensity ratio and temperature, 10 mg/cycle direct fuel injection at 110 °CA bTDC (Com.) 126
Figure 6.12 Fluorescence intensity ratio and temperature, 30 mg/cycle direct injection at 90 °CA aTDC (Int.) 127
Figure 6.13 Fluorescence intensity ratio and temperature, 30 mg/cycle direct injection 110 °CA bTDC (Com.) 128
Figure 6.14 Effect of focal length and aperture size on field of view and depth of field. Top: same aperture size, different focal length; Bottom: Same focal length, different aperture size 131
Figure 6.15 Single frame images of flame formation and propagation at the selected crank angles 134
Figure 6.16 Single frame images of flame formation and propagation at the selected crank angles 135
Figure 6.17 Averaged images of flame formation and propagation at the

selected crank angles 136
Figure 6.18 Flame formation and propagation in SI and spark-assisted CAI operations 138
Figure 6.19 Autoignition outside the flame region 139
Figure 6.20 Average residual intensity of the first image on the second image in DIF mode as a function of the burst period and shutter compensation time 141
Figure 6.21 Before (left image) and after (right image) removing the effect of laser profile variation and beam attenuation 142
Figure 6.22 Processed single frame images, (a) illumination at 308 nm, (b) illumination at 277 nm, (c) fluorescence intensity ratio of 308 to 277 nm 142
Figure 6.23 Two-line PLIF image of flame thermal stratification 143
Figure 6.24 3-pentanone absorption cross-section as a function of temperature 147
Figure 6.25 Absolute frequency quantum yield as a function of temperature for two excitation wavelengths at 308 and 277 nm. 149
Figure 6.26 Absolute frequency quantum yield of the excitation wavelength at 277 nm as a function of pressure at different mixture temperature 150
Figure 6.27 Absolute frequency quantum yield of the excitation wavelength at 308 nm as a function of pressure at different mixture temperature 150
Figure 6.28 Calculated EGR values from the 2-line PLIF measurements 153
Figure 6.29 Top: Two-line PLIF T/EGR image timing, Bottom: Sample images at 90 °CA aTDC (Com.) (a) background, (b) PI (c) DI 154
Figure 6.30 Top: Single-shot images at 90 °CA aTDC (Com.); Left: Average of 20 frames 155
Figure 6.31 Top: Single-shot images at 110 °CA aTDC (Com.).; Left: Average of 20 frames 156
Figure 6.32 Top: Single-shot images at 180 °CA aTDC (Com.) at the exhaust vale opening (EVO); Left: Average of 20 frames 157
Figure 6.33 Top: Single-shot images at 80 °CA bTDC (R.Com.) at the

exhaust vale closing (EVO); Left: Average of 20 frames 158
Figure 6.34 Top: Single-shot images at 50 °CA bTDC (R.Com); Left: Average of 20 frames 159
Figure 6.35 Top: Single-shot images at 120 °CA aTDC (R.Com.) at the intake valve opening (IVO); Left: Average of 20 frames 160
Figure 6.36 Top: Single-shot images at 140 °CA aTDC (R.Com.); Left: Average of 20 frames 161
Figure 6.37 Top: Single-shot images of the EGR mixture with the fresh charge taken at 90 °CA bTDC (Com.); Bottom: Single-shot simultaneous temperature images at 90 °CA bTDC (Com.) 162
Figure 6.38 Top: Single-shot images of the EGR mixture with the fresh charge taken at 70 °CA bTDC (Com.); Bottom: Single-shot simultaneous temperature images at 70 °CA bTDC (Com.) 163
Figure 6.39 Top: Single-shot images of the EGR mixture with the fresh charge taken at 50 °CA bTDC (Com.); Bottom: Single-shot simultaneous temperature images at 50 °CA bTDC (Com.) 164
Figure 6.40 Top: Single-shot images of the EGR mixture with the fresh charge taken at 35 °CA bTDC (Com.); Bottom: Single-shot simultaneous temperature images at 35 °CA bTDC (Com.) 165
Figure 6.41 EGR and temperature maps 166
Figure 6.42 Calculated temperature PDFs 167
Figure 6.43 Comparison of the temperature PDFs at 90, 70, 50 and 35 °CA bTDC (Com.). 167
Figure 6.44 Calculated EGR PDFs 169
Figure 6.45 Comparison of the EGR PDFs at 90, 70, 50 and 35 °CA bTDC (Com.). 170
Figure C.1 Metal plate with no optical access 181
Figure C.2 Sandwich plate with side windows 182
Figure C.3 Side window 183
Figure C.4 Window clamp 184
Figure C.5 Original ring plate 185
Figure C.6 Modified ring plate 186
Figure C.7 4130 alloy slip ring 187

Figure C.8 4130 alloy gasket plate 188
Figure C.9 Pillar 189
Figure C.10 Optical ring 190
Figure C.11 Piston top window 191
Figure D.1 MPI injection calibration curve 192
Figure D.2 DI injection calibration curve 192
Figure F.1 Reflectivity vs. wavelength of 277/633 nm HR coated mirror 198
Figure F.2 Reflectivity vs. wavelength of 308/633 nm HR coated mirror 198
Figure F.3 BBAR 248-355 coating for UV region for 0° incidence 199
Figure F.4 Structure of the image intensifier 199
Figure F.4 Emission spectra of intensifier phosphor screen coatings 199
Figure I. 1 Average in-cylinder charge pressure for 100 motored cycles 206
Figure I. 2 Calculated average charge temperature of 100 motored cycles during the compression stroke 206
Figure I. 3 Average in-cylinder charge pressure for 100 firing cycles 207
Figure I. 4 Log P- log V diagram 207
Figure I. 5 Calculated average charge temperature of 100 firing cycles during the compression stroke 207

List of Tables

Table 1.1 Fuel duty and Value Added Tax (VAT) in the UK as August 2012 2
Table 2.1 LEV II standard 6
Table 2.2 Progression of the European emission standards for passenger cars 9
Table 2.3 Comparisons of incoherent and coherent diagnostic approaches 17
Table 2.4 Potential combustion diagnostic techniques 18
Table 2.5 Approximate values of the differential cross section for scattering methods 20
Table 2.6 The physical and thermodynamic properties of iso-octane, toluene, acetone and 3-Pentanone 27
Table 3.1 Engine specifications 33
Table 4.1 Excimer lasers specifications 62
Table 4.2 Technical specifications of Micro-Nikkor and UV-Nikkor 74
Table 4.3 Delays in the 2-line PLIF System 81
Table 4.4 Most dominate scattering type of different particle size parameter regimes 85
Table 4.5 Summary of techniques used in this work for improving the 2-line PLIF imaging quality 88
Table 5.1 Average in-cylinder motoring and firing charge temperature calculated from both pressure data and 2-line PLIF images for the NVO operation 112
Table 6.1 In-cylinder averaged peak pressure and peak temperature variation by direct injection timing/quantity 124

Table 6.2 Calculated temperature at 30 °CA bTDC (Com.) from both the PLIF and pressure data 128
Table 6.3 Engine performance of different ignition timings for SI strategy 140
Table 6.4 Coefficient values for the rate of intramolecular non-radiative decay 148
Table 6.5 Two-line PLIF simultaneous T/EGR sample calculatoin 152
Table G.1 DIF imaging parameters 200

Chapter 1
Introduction

1.1 Introduction

Since the advent of internal combustion (IC) engines more than 150 years ago, they have experienced tremendous progress through continuous Research and Development (R&D) and application of new technologies. While for more than a century the main focus was on the performance and reliability of engines, in the last few decades, combustion efficiency and emissions have received more attention. Today, consumers are more concerned about petroleum price while the real issue is the fact that cheap or expensive, all the oil reserves will be exhausted eventually[1] and therefore it is of paramount importance to effectively use them. On the other hand IC engines are the dominant power plant for transport and consume more than half of the petroleum available in industrialised countries. IC engines are considered as one of the main sources of air pollution and contribute 20% of total man made CO_2 emissions. Undesirable IC engine emissions mainly include unburned hydrocarbons (uHC), carbon monoxide (CO), nitrogen oxides (NOx), and particulate matter (PM) which their negative impact on air quality, human health, and global warming are becoming a major concern. Consequently emission legislations have been introduced by governments in collaboration with environmental agencies to set specific limits to the amount of pollutants released by the IC engines. These ever tightening legislation and in some countries, heavy taxation of road transport and fuel duty, have put

[1] The total world proved oil reserves (estimated in 2012) is 1410 BB (billion barrels) and the annual consumption in 2011 was 31 BB [1, 2].

massive pressure on automotive manufacturers to produce cleaner and more fuel-efficient vehicles.

Type of Fuel	Total Cost at Pump	Fuel Duty	VAT	% of Fuel Cost that is Tax
Unleaded	118.7p	58.19p	17.68p	64%
Diesel	122.3p	58.19p	18.21p	62%
LPG	67.5p	31.95p	10.05p	63%

Table 1.1 Fuel duty and Value Added Tax (VAT) in the UK as August 2012 [4]

Despite significant R&D work been carried out to present alternatives to the IC engines, no single technology has yet been introduced that can address all the issues including practicality, price, running costs and even efficiency[2]. As a result the transportation industry still heavily relies on further improvements of the IC engines which require increased knowledge and understanding of the combustion and pollutant formation process. This work is focused on a laser diagnostic technique for in-cylinder measurements that facilitates improved understanding of a variety of combustion phenomena.

1.2 Objectives

The main objective of this project was to develop and optimise a tracer based 2-line Planar Laser Induced Fluorescence (2-line PLIF) technique to:

- Investigate Direct Injection (DI) fuel spray characterizations of different injection timings for both normal and negative value overlap strategies
- Investigate the photo-physical models developed for 3-pentanone absorption cross sections and frequency quantum yield (FQY) through experimental tests on a Constant Volume Chamber (CVC)
- Investigate the direct injection charge cooling effects of different injection timings and quantities
- Study the flame formation and propagation of the Spark-Ignition (SI) combustion strategy

[2] For a realistic energy consumption evaluation of the electric and hydrogen vehicles, concepts such as ‘well to wheel efficiency’ are typically employed [3].

- Study the flame formation and propagation of the spark-assisted CAI combustion strategy
- Investigate the flame thermal stratification
- Perform simultaneous Exhaust Gas Residuals (EGR) and in-cylinder charge temperature measurements

1.3 Outline of Thesis

Following the introduction of the thesis and summary of objectives presented in Chapter 1, Chapter 2 presents a review of relevant literature relating to this work. It begins with an overview of the emission legislations and provides the current and future standards. Current gasoline direct injection engine technologies and R&D trends are presented. Combustion diagnostic techniques are reviewed and the advantages of optical diagnostics over physical probes are presented. The coherent and incoherent laser techniques are compared and the signal power of incoherent approaches is analysed. Thermometry by vibrational and rotational Raman scattering, Rayleigh scattering and laser induced fluorescence (LIF) are briefly compared and discussed. The tracer-based planar laser induced fluorescence (PLIF) is introduced as the diagnostic technique for this work. The final section of this chapter is devoted to a review of papers published on 3-pentoanone 2-line PLIF measurements in a chronological order.

Chapter 3 details the experimental test facilities utilised in this work. The engine test bed and single cylinder research engine, air inlet and exhaust systems, ignition and injection systems, fuel and tracer supply systems as well as engine data acquisition system are described. Engine operation and maintenance are also briefly described. Engine modifications as well as design of the new components including sandwich plates to adapt optics are discussed. Furthermore, the chapter provides description of the experimental setup and test procedures for measurement of fuel/tracer injection quantity and intake air flow rate.

Chapter 4 describes the principle of the 2-line PLIF technique for simultaneous measurements of in-cylinder charge temperature and exhaust gas residuals (EGR). The first section focuses on development of the diagnostic technique for measurements in a single cylinder optical GDI engine utilised in this study. Details

of the light sources, beam delivery and shaping systems, and light capturing devices are presented. In addition, the Excimer lasers' beam characteristics are studied and optimised. The second section focuses on implementation of the technique. Detailed description of time budgeting and synchronization of the diagnostic system with the engine is presented. The third section introduces several optimisation techniques utilized in this work for improving the 2-line PLIF imaging quality. Finally the last section details the experimental tests for engine vibration and Raman conversion efficiency measurements and presents the results.

Chapter 5 outlines the experimental tests carried out in this work to calibrate and validate the 2-line PLIF technique. It starts with a detailed description of the constant volume chamber (CVC) design and explains the CVC heating system, thermal insulations, and tracer supply system. The static measurements on the CVC for calculating the temperature calibration curve are described and the results are presented. The average in-cylinder charge temperature is calculated using in-cylinder pressure data and adiabatic equations. The results are then compared with the 2-line PLIF measurements and the discrepancies of the two methods are investigated.

Chapter 6 covers the applications of the 2-line PLIF technique in this study. Experimental setup and test procedure of both motoring and firing tests are explained in two sections, results are presented and discussed. The motoring tests section describes the single-line PLIF fuel spray visualization and 2-line PLIF measurements of the direct injection charge cooling effects. The firing tests section starts with feasibility studies and high-speed video imaging of combustion. This follows by a study of the flame formation and propagation at a very high temporal and spatial resolution. The 2-line PLIF technique is further optimised to study the flame thermal stratification. Finally the 2-line PLIF is utilized for simultaneous measurements of in-cylinder charge temperature and exhaust gas residuals and the findings are outlined.

Chapter 7 summarises the conclusions that have been drawn from this work. Some further modifications on the single cylinder optical engine and its components are suggested. Recommendations for future work are also given.

Chapter 2
Literature Review

2.1 Introduction

This chapter presents a relevant literature review in four sections. The first section describes the emission legislations for the automotive industry and provides the current and future regulations. The second section is focused on the gasoline direct injection engine technologies and current research and development trends in the field. The third section reviews combustion diagnostic techniques and compares the most common laser based techniques for in-cylinder temperature measurements. Finally the last section discusses publications on the 3-pentanone 2-line PLIF technique.

2.2 Emission Legislations

Emission legislations define the acceptable limits for exhaust emissions of new vehicles. They were first introduced in the United States by the California Air Resource Board (CARB) and Environmental Protection Agency (EPA) in the 1960's, in Japan by the Japanese Government in the 1970's and in Europe by the European Union in the 1990's [5-8]. While EU emission legislations demand that all vehicles comply with the particular standard that is in force at the time they are sold, the US legislations require the average emissions of a total product range of a manufacturer be within the prescribed limits. In addition there are some differences in the test drive cycles and the measurement methods which make direct comparison of these standards difficult. Currently, emissions of nitrogen oxides (NOx), total

hydrocarbons (THC), non-methane hydrocarbons (NMHC), carbon monoxide (CO) and particulate matter (PM) are regulated for most vehicle types[1]. Table 2.1 presents the Low Emission Vehicle II (LEV II) standard, adopted by the CARB in 1998, which is used by US manufacturers to certify vehicles until model year 2019. Table 2.2 shows the progression of the European emission standards for both compression and spark ignition passenger cars [9]. Furthermore in recognition of the need to reduce emissions of carbon dioxide (CO_2), the main greenhouse gas, the European legislation of CO_2 emissions of 130g/km by 2015 (and the proposal to reduce it to 95g/km by 2020) has been introduced. It should be noted that the road transport contributes about one-fifth of the EU's total CO_2 emissions which has increased by almost 23% between 1990 and 2010 [10].

Category	50,000 miles/5 years					120,000 miles/11 years				
	NMOG	CO	NOx	PM	HCHO	NMOG	CO	NOx	PM	HCHO
LEV	0.075	3.4	0.05	-	0.015	0.09	4.2	0.07	0.01	0.018
ULEV	0.04	1.7	0.05	-	0.008	0.055	2.1	0.07	0.01	0.011
SULEV	-	-	-	-	-	0.01	1	0.02	0.01	0.004

Table 2.1 LEV II standard for passenger cars and LDVs [9]

[1] Seagoing ships and airplanes are excluded.

Stage	Date	CO	HC	HC+NOx	NOx	PM	PN
		g/km					#/km
Compression Ignition							
Euro 1	1992.07	2.72	-	0.97	-	0.14	-
Euro 2, IDI	1996.01	1	-	0.7	-	0.08	-
Euro 2, DI	1996.01[a]	1	-	0.9	-	0.1	-
Euro 3	2000.01	0.64	-	0.56	0.5	0.05	-
Euro 4	2005.01	0.5	-	0.3	0.25	0.025	-
Euro 5a	2009.09[b]	0.5	-	0.23	0.18	0.005[f]	-
Euro 5b	2011.09[c]	0.5	-	0.23	0.18	0.005[f]	6.0×10^{11}
Euro 6	2014.09	0.5	-	0.17	0.08	0.005[f]	6.0×10^{11}
Spark Ignition							
Euro 1†	1992.07	2.72	-	0.97	-	-	-
Euro 2	1996.01	2.2	-	0.5	-	-	-
Euro 3	2000.01	2.3	0.2	-	0.15	-	-
Euro 4	2005.01	1	0.1	-	0.08	-	-
Euro 5	2009.09[b]	1	0.10[d]	-	0.06	0.005[e,f]	-
Euro 6	2014.09	1	0.10[d]	-	0.06	0.005[e,f]	6.0×10^{11} [e,g]

a. until 1999.09.30 (after that date DI engines must meet the IDI limits)
b. 2011.01 for all models
c. 2013.01 for all models
d. and NMHC = 0.068 g/km
e. applicable only to vehicles using DI engines
f. 0.0045 g/km using the PMP measurement procedure
g. 6.0×10^{12} 1/km within first three years from Euro 6 effective dates

Table 2.2 Progression of the European emission standards for passenger cars [9]

2.3 Gasoline Direct Injection Engine Technologies and R&D Trends

Today, gasoline engines are still the most dominant power plant for passenger cars throughout the world. This is mainly due to their high specific power and relatively low manufacturing costs compared to diesel engines. Although they have seen a tremendous progress in terms of performance, reliability, fuel-efficiency and exhaust emissions since their invention, still huge R&D work is being carried out by automotive manufacturers and research institutes as a result of ever tightening legislation and public demands.

One of the technologies that has shown a great potential in synergy with other technologies to achieve increased fuel efficiency and high power output while enables more accurate control of the emissions level is Gasoline Direct Injection (GDI). In IC engines, GDI is a variant of fuel injection technique employed in both two- and four-stroke engines. The gasoline is highly pressurized, and injected via a common rail directly into the combustion chamber of each cylinder, as opposed to conventional port fuel injection that takes place in the intake port. The first GDI system for automotive industry was introduced by Goliath and Gutbrod in 1952 on a two-cylinder two-stroke engine for the Goliath GP700, a two-door saloon. In 1955 Mercedes-Benz introduced the 300SL sports car with the first four-stroke GDI engine. Further R&D conducted by several companies in the next three decades were not very successful, mainly due to inflexibility of the injection systems, high costs of fuel pumps and injectors and problems with NO_x emissions. In 1996, Mitsubishi introduced the first modern four-cylinder automotive GDI engine [11] which followed by their first six-cylinder GDI engine. The four-cylinder engine was manufactured in straight-four shape while the six-cylinder had a V configuration. Nissan and Toyota were the next companies released their own GDI engines in 1997 and 1998 [12]. These engines were designed to operate in stratified charge SI combustion mode at part load and low to medium speed operations and in homogeneous charge SI combustion mode at high load and high speed operations. In recent years, introduction of the advanced technologies such as new generation of solenoid-actuated and piezo-actuated injectors and turbochargers have brought new possibilities for further improvements of the gasoline engines that can be summarized as follows:

2.3.1 Increased Compression Ratio

Currently the compression ratio of a typical gasoline engine is limited to ~11:1 by knocking combustion. It is shown that an increase in the compression ratio of 10 to 14 can reduce the specific fuel consumption by 10% [13]. Operation at higher compression ratio can be achieved by:

2.3.1.1 High Octane Fuels

As knocking combustion is most sensitive to the compression temperature, it can be minimized by exploiting the charge cooling effect of direct fuel injection. The effect is particularly noticeable if alcohol fuels are used in GDI engines [14-21]. The Ethanol Turbo Boost™ concept is developed based on this principle [22]. It utilises direct injection of ethanol or methanol as a second fuel under conditions of high torque to avoid knock, while using only conventional port fuel injection gasoline throughout the rest of the engine operating range. As the required engines, with two injectors per cylinder, have already been developed[2] [23], the dual-fuel approach has been introduced an attractive alternative for heavy duty vehicles that could be easily executed. In 2008 the Ford Motor Company co-developed a 5.0 litre V8 engine, demonstrated an improvement of energy consumption of 15-20% on typical drive cycles compared to a production gasoline engine while meeting ULEV II / Tier II Bin 5 emissions. The direct injection of ethanol increases the octane of regular gasoline from 88-91 octane to more than 150 octane [24].

2.3.1.2 Atkinson and Miller Cycle Operations

In the Atkinson cycle, the expansion ratio is made longer than the compression ratio so that extra work can be produced from the extended expansion process whilst avoiding knocking combustion with relatively low compression ratio [25]. The original Atkinson cycle was achieved through a different crank design. In modern engines, this is often implemented by adjusting the effective compression ratio through varied intake valve closure timings in a 4-stroke reciprocating IC engine. This can be realised by advanced IVC before Bottom Dead Centre (bBDC) in the intake stroke [26]. As a result, the engine can operated at a higher geometric compression ratio and hence a greater expansion ratio.

It should be noted that the Atkinson cycle provides good fuel economy, at the expense of a lower power per displacement as compared to a traditional four-stroke engine [27]. However the engine power can be supplemented by an electric motor when more power is needed. In 1997, the Toyota Prius was introduced in Japan with

[2] such as Toyota 2GR-FSE V-6 3.5-litre, exploiting a PFI and a DI injector per cylinder

its Atkinson cycle-based hybrid electric drivetrain which is still the most common drivetrain used in full hybrid-electric vehicles [28]. Alternatively, a supercharger or/and turbocharger can be used to compensate the engine output with retarded IVC, which is commonly known as the Miller cycle [13].

2.3.1.3 Engines with Variable Compression Ratio (VCR)

These engines can operate at higher compression ratios at part load conditions and reduced compression ratios at full load to avoid knocking. Although the VCR technology has existed for several decades but it has been unobtainable for production vehicles due to the mechanical complexity, difficulty of controlling all of the parameters, costs and performance issues. In 1999, Yamaha introduced the Super Diesel (SD) two-stroke[3] engine which could dynamically vary the compression ratio over a 13-18:1 range, achieving 50% increase in torque in the low to middle speed range compared to a conventional diesel of the same displacement [29].The Saab Variable Compression (SVC) engine[4] [30], Lotus Omnivore[5] [31] and MCE-5 VCRi[6] [32] are among other engines equipped with VCR technology.

[3] The comparative simplicity of cylinder head design in the two-stroke engines makes the implementation of VCR technology easier.

[4] four-stroke DI with possible VCR range of 8-14:1

[5] two-stroke DI with possible VCR range of 10-40:1, wide-range HCCI operation on a variety of liquid fuels

[6] four-stroke PFI with possible VCR range of 7-20:1

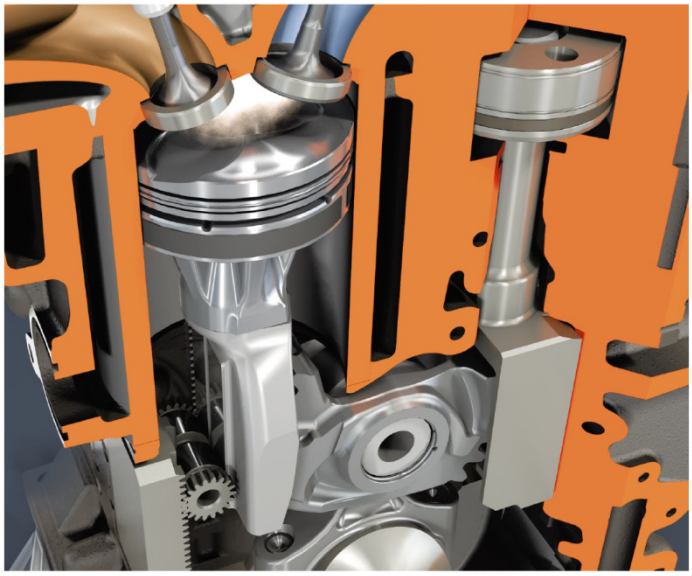

Figure 2.1 MCE-5 VCRi's mechanical arrangement [33]

2.3.2 Engine Downsizing

In engine downsizing a larger displacement naturally aspirated engine is replaced by a smaller displacement boosted engine. The smaller engine reduces the weight and installation requirements for a lighter and safer vehicle. Also as the rubbing loss is proportional to the surface area, a smaller displacement engine with less number of cylinders will suffer less frictional loss. However, the most significant attribute of downsizing is that the smaller engine is forced to operate at higher load and wide open throttle conditions, reducing pumping loses which is the largest contributor to the part load inefficiencies of SI engines. The Volkswagen 1.4 TSI and Ford EcoBoost™ I-3 are successful examples of downsized engines. The first version of 1.4 TSI was a four-cylinder twin-charger[7] GDI engine, introduced in 2005 to replace the FSI 2.0 litre gasoline engine with 14% more power and improved fuel economy of 5% [34]. The EcoBoost™ I-3 is a 1 litre turbocharged GDI engine replacing a non-turbo 1.6 litre from 2012, producing the same power (123 bhp) with reduced fuel consumption of by up to 20% while weights 30 Kg less [35].

[7] Twincharger is a combination of an exhaust-driven turbocharger and an engine-driven supercharger.

2.3.3 Stratified Charge Combustion

The principle of stratified charge combustion is to deliver a mixture that is sufficiently rich for combustion in the immediate vicinity of the spark plug and in the remainder of the cylinder, a very lean mixture. Honda's CVCC [8] engine, introduced in 1971 by Honda Motor Company, was a form of stratified charge engine. The CVCC system (shown in Figure 2.2) had a small auxiliary inlet valve that charged an area around the spark plug, while the conventional inlet valve (main inlet valve) provided a lean air/fuel mixture into the cylinder. The spark plug and CVCC valve were isolated from the main cylinder by a perforated metal plate. The combination of a rich mixture near the spark plug, and a very lean mixture in the cylinder allowed stable running with complete combustion of injected fuel [36].

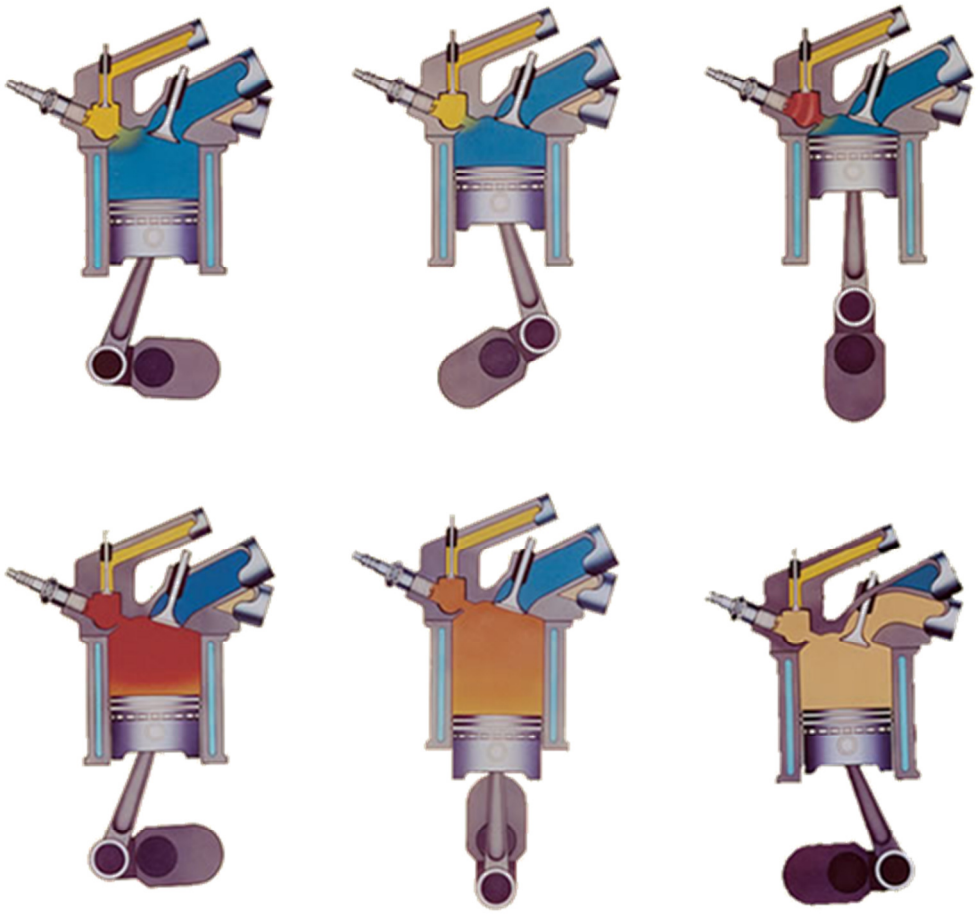

Figure 2.2 The basic Honda CVCC operating mechanism [36]

[8] Compound Vortex Controlled Combustion

However the implementation of stratified charge combustion in mass produced GDI engines was realised by the development of advanced direct fuel injection technologies in the late 1990s by Mitsubishi [11] and Toyota [12] using wall guided technologies. The most recent stratified charge capable GDI engines equipped with the second generation of DI systems (spray-guided systems) were introduced by BMW and Mercedes-Benz in 2006. These engines can achieve fuel savings of 10% to 20% (compared to conventional PFI engines) by operating with globally lean equivalence ratios throughout a wide operating range [37].

2.3.4 CAI/HCCI Combustion

Control Auto Ignition (CAI) or Homogenous Charge Compression Ignition (HCCI) is an alternative combustion. It was initially identified as an abnormal combustion phenomenon that occurs when a SI engine continues to run after the ignition is switched off [38, 39]. In CAI/HCCI combustion, ignition occurs at several places at a time which makes the fuel/air mixture burn nearly simultaneously. Unlike the spark ignition combustion, the density and temperature of the fuel air mixture are raised until the entire mixture reacts spontaneously in CAI/HCCI. This allows a more uniform and repeatable burning of very lean and/or highly diluted mixture in a gasoline engine [40-44]. Direct injection technologies provide flexible injection timing and allow single and multiple injection strategies to be adopted to obtain a degree of closed-loop control over such a combustion process as well as extend the operational range of CAI/HCCI combustion [45-49]. Although there is no CAI/HCCI engine available in the market to date, several car manufacturers have revealed fully-functional prototypes. General Motors' HCCI and Mercedes-Benz's DiesOtto engines, both introduced in 2007, as well as Volkswagen's CCS[9] and GCI[10] engines with production plan for 2015, are among these prototypes [50-52].

[9] Combined Combustion System

[10] Gasoline Compression Ignition

2.3.5 Engine Stop and Start Systems

In a typical urban driving cycle amount of fuel consumed during idling is about 10% of total fuel consumption [53] which can be significantly reduced by a stop and start system that switches off the engine when the vehicle is stopped and restart it immediately when the driver wishes to pull away. Despite such systems have been tested since mid-1970s[11] [54], the direct injection technologies have brought the potential to realize a fast and efficient engine stop and start system that unlike conventional systems does not rely on a starter motor. Mazda i-stop (idling stop system) is an example of such a system that exploits the direct injection technology to restart the engine by combustion, in a mere 0.35 seconds. The system improves the fuel economy by up to 8% under Japan's JC08 mode test cycle [53].

2.4 Combustion Diagnostic Techniques for In-cylinder Charge Temperature Measurements

In internal combustion engines, the thermodynamic state of the cylinder gas is defined by the three properties of pressure, density, and temperature. Measurements of the first two properties are relatively straight forward. Cylinder pressure is normally uniform and can be readily measured with a piezoelectric pressure transducer. Charge density can be easily calculated from the cylinder volume and the amount of gases trapped in the cylinder. But accurate charge temperature measurements, on the other hand, require more sophisticated techniques. These measurements can be used to study various phenomena in IC engines, such as problems with NO_x emission and controlling the auto-ignition. Researchers have exploited numerous techniques to get the most accurate temperature measurements. A detailed description of these techniques can be found in [55-59]. In this work a review of most widely used temperature measurement techniques was carried out to study the suitability of the Planar Laser Induced Fluorescence (PLIF) technique for this research project.

[11] Toyota Crown sedan was fitted with an electronic device that could automatically switch off the engine after sitting stationary for 1.5 seconds.

2.4.1 Physical Probes vs. Laser Diagnostic Techniques

Combustion environments are considered to be hostile because of high temperatures, high gas flow, and high concentration of particles. Physical probes, due to their intrusion, can markedly alter the combustion behaviour they seek to investigate. In the presence of the probe, the combustion process may be affected, either through flow disturbance, thermally or catalytically, and behave quite differently than had the probe not been present. In addition, physical probes are generally limited in both their spatial resolution and temporal response. Although thermocouples, when bare, can be extremely fine, their applicability is generally restricted to relatively benign flames. Under high aerodynamic loads and in the presence of particles e.g., fuel droplets and soot, they must be protected and, as a result, their spatial resolution is reduced, their temporal response diminished and their accuracy degraded. Closely related is the matter of probe survival at high pressures and temperatures. As the environment of interest becomes more severe from a heat transfer standpoint, the probes must be made more physically robust. This increases the chance for perturbation and degrades special and temporal precision. Furthermore, physical probes do not perform measurements in situ and need to be corrected, a process which can introduce ambiguity into a measurement. A thermocouple, for example, measures its own temperature, not the charge temperature. Radiation, convection and conduction corrections have to be made to obtain accurate charge temperature measurement and these vary depending on the environment of the measurement.

Laser techniques offer a number of advantages over the conventional methods which have been traditionally employed to investigate and characterize combustion phenomena. The techniques are remote and, almost always, non-perturbing. Thus, they are ideally suited for application to recirculation zones, boundary layers, and confined locations such as the combustion zone of internal combustion engines. The measurements are performed in situ, i.e., at the measurement location, and thus they are usually unambiguous. Temperatures and species concentrations are measured directly without the requirement for elaborate and often uncertain corrections. Today precise temperatures are measured in laminar flows by averaging over many laser shots, and accurate probability density functions (PDF) can be obtained in turbulent flows by compiling single-shot data at one spatial location [60-62]. Despite all the advantages, laser diagnostic techniques suffer a major limitation which is the

requirement for optical access to the test volume. This often necessitates the addition of windows to an enclosure which can alter the thermodynamic conditions of the engine. In some cases, these can be eliminated by the use of fibre optics or small uncovered apertures if one can tolerate the attendant pressure loss incurred.

2.4.2 Laser Diagnostic Techniques: Coherent and Incoherent Approaches

Many of the physical phenomena presently being exploited for laser diagnostic utilization are not new. For example emission spectroscopy is dating back to Swan's observations of C_2 emissions from flames in 1857 [63]. The elastic scattering of light was studied in 1871 in Rayleigh's research to explain the blue colour of the sky. And the Raman scattering effect was discovered by Raman in 1928. However the discovery of the lasers and their unique properties as a light source, namely, power, coherency and spectral purity, triggered the wider application of previous discoveries and has permitted new techniques to be developed and applied. Laser beams that penetrate through flames without interference have made it possible to measure velocities, particle size, temperature, and concentration of many species.

Laser diagnostic techniques can be divided into two categories of coherent and incoherent approaches. Coherent techniques produce laser-like signal beams while incoherent techniques (light scattering techniques) result in signal being scattered into 4π steradians. The advantages and disadvantages of both approaches are summarized in Table 2.3.

Approach	Incoherent	Coherent
Advantages	Linear Intensity independent Single ported Spectral simplicity Simple calibration	Strong signals Laser-like signal beams Interference tolerant
Disadvantages	Large solid angle Prone to interferences	Nonlinear Intensity dependent Multi ported Complicated spectra Difficult to normalize Refraction sensitive

Table 2.3 Comparisons of incoherent and coherent diagnostic approaches [56]

Table 2.4 lists potential laser diagnostic techniques suitable for in situ point measurements. The elastic and inelastic scattering processes are incoherent techniques. Absorption can either be incoherent or coherent depending on the light source used. With the exception of hyper Raman scattering, the nonlinear optical processes are all coherent. In most cases, suitability or applicability of a technique will depend heavily on the nature of the experiment. Although some coherent techniques such as Coherent Anti-Stokes Raman Scattering (CARS) or Degenerate Four-Wave Mixing (DFWM) have shown potential in sensitive detection of major and minor species respectively, and that both techniques are capable of highly accurate thermometry, incoherent approaches are more attractive as they are linear, experimentally less complex and that they are capable of two-dimensional measurements.

Elastic scattering processes	Rayleigh scattering Mie scattering
Inelastic scattering processes	Spontaneous Raman scattering Near-resonant Raman Laser-induced fluorescence (LIF)
Absorption processes	Resonant line of sight Differential absorption
Nonlinear optical processes	Stimulated Raman gain/loss spectroscopy (SRGS) Raman induced Kerr effect (RIKES) Stimulated Raman scattering Hyper-Raman scattering Coherent anti-Stokes Raman scattering (CARS) Degenerate four-wave mixing (DFWM) Polarization Spectroscopy (PS) Hyper-order Raman spectral excitation spectroscopy (HORSES)

Table 2.4 Potential combustion diagnostic techniques [56]

2.4.3 Review of Incoherent Approaches: Similarities and Differences

Rayleigh scattering, vibration and rotational Raman scattering and laser-induced fluorescence are the most widely used incoherent methods. Raman and Rayleigh scattering measurements require high species concentration and clean laboratory conditions, whereas fluorescence provides intensity and spectral selectivity in flows moderately laden with particles where there is interference due to blackbody radiation, flame emission, or laser-induced incandescence. These four light-scattering methods are compared on an energy level diagram in Figure 2.3 [64].

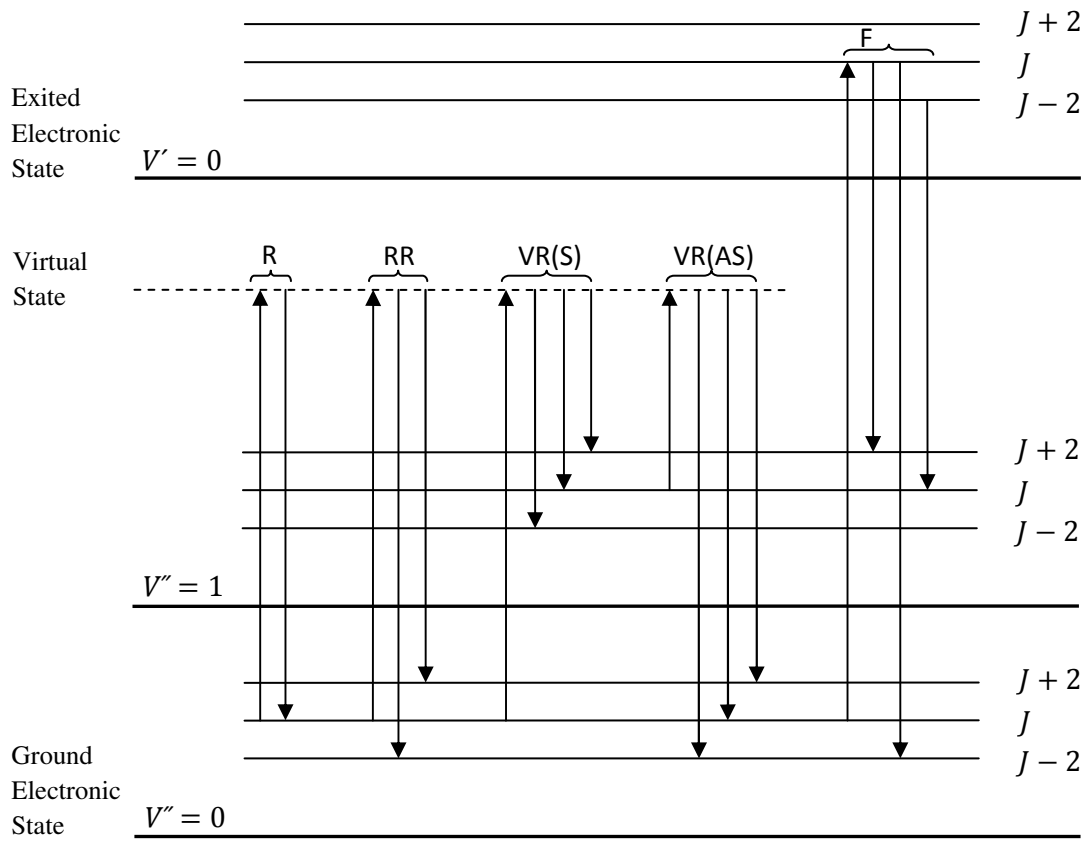

Figure 2.3 Energy level representation of Rayleigh (R), Rotational Raman (RR), Vibrational Raman (VR), and Fluorescence (F) scattering methods.

Rayleigh scattering is an elastic process, so that the scattered signal occurs at the same wavelength as the excitation source. For this reason, the Rayleigh signal is subject to interference from the intense scattered light produced by particles and nearby surfaces. Also being an elastic process, Rayleigh scattering is not species specific.

Raman scattering is an inelastic process in which the oscillating polarizability of the molecule modulates the scattered radiation, thereby leading to the appearance of two sideband frequencies. If a molecule gains energy from the radiative field, the resulting lower frequency scattered radiation is termed the Stokes component; if the molecule loses energy to the radiative field, the scattered radiation is referred to as the anti -Stokes component.

Rayleigh or Raman scattering can occur upon excitation at any visible or ultraviolet wavelength. Fluorescence, however, requires a precise excitation frequency, since

molecules in a particular rovibronic level of the ground electronic state must be excited to a specific rovibronic level in another electronic state. Spontaneous emission can then be monitored from the upper rovibronic level to a variety of such levels in the ground electronic state. Fluorescence can also occur from indirectly excited levels in the upper electronic state owing to collisional dynamics, i.e., rotational and vibrational relaxation.

2.4.4 Signal Power in Incoherent Techniques

The signal power for the four scattering processes depicted in Figure 2.3 can be obtained from [64]

$$S = \eta_c \Omega_c V_c (\frac{d\sigma}{d\Omega}) N_{vJ} I_L \qquad (2.1)$$

where S is the power of the measured signal (W), η_c the detection efficiency, Ω_c the solid angle of the collection optics (sr), V_c the collection volume (cm^3), $\frac{d\sigma}{d\Omega}$ the differential cross section (cm^2/sr), N_{vJ} the number density in the initial rovibronic level ($v", J"$) of the ground electronic state (cm^{-3}), and I_L the irradiance of the laser beam (W/cm^2). For the same experimental conditions, the relative signal for each scattering method depends primarily on the differential cross section. Approximate values (cm^2/sr) for each scattering method are as follows [55]:

Scattering method	**Differential cross section** (cm^2/sr)
Vibrational Raman	10^{-30} _ 10^{-28}
Rotational Raman	10^{-28} _ 10^{-27}
Rayleigh	10^{-27} _ 10^{-25}
Mie	10^{-27} _ 10^{-8}
Fluorescence	10^{-25} _ 10^{-20}

Table 2.5 Approximate values of the differential cross section for scattering methods

The differential cross section for Mie scattering varies depending on the particle size. Because of their low differential cross sections, Raman and Rayleigh scattering measurements normally require high species concentrations. Compared with the

Raman methods, only fluorescence offers the intensity and spectral selectivity for thermometry in moderately dirty flows, where interferences can also arise owing to blackbody radiation, flame emission, or laser-induced incandescence.

2.4.5 Thermometry by Vibrational and Rotational Raman Scattering

For the Raman scattering, visible or ultraviolet wavelength lasers are typically employed since the strength of the scattering scales as the fourth power of the Raman frequency, but no specific wavelength is required. Depending on the nature of the energy exchange which occurs between the incident light quanta and the molecules, Raman scattering is termed rotational, vibrational or electronic [65]. Because of the weakness of the Raman effect, the most useful Raman scatterers are major stable species such as N_2, O_2, and H_2 [66-68].

Temperature measurement by Raman scattering can be achieved via two main approaches. The first involves least-squares fitting a library of theoretical spectra to measured spectrum. The theoretical spectrum producing the best fit identifies the temperature at the measurement point. Alternative approaches to temperature measurements employ spectral band ratio strategies, where various portions of the Raman spectrum can be monitored and the temperature determined from the resultant intensity ratio. For example there are four common methods of determining temperature from N_2 vibrational Raman scattering; (a) band area method, (b) contour fit method [69], (c) band peak-intensity method and (d) Stokes/anti-Stokes method [70, 71]. All these techniques rely on the increased population in the upper N_2 vibrational levels with rising temperature.

Thermometry by pure rotational Raman scattering is more precise than thermometry by vibartional Raman scattering, also it is ideally suited to lower temperatures because of the smaller spacing between rotational levels compared with that for vibrational levels [68]. The substantial increase in precision for rotational versus vibrational Raman reflects its inherent advantages: (1) higher sensitivity due to a larger differential cross section, (2) lower uncertainty because of a larger number of measurable transitions, and (3) greater dynamic range because of an increased spectral sensitivity to substantial variations in temperature. However, an important disadvantage of rotational Raman spectroscopy compared to vibrational Raman

spectroscopy is the propensity for overlapped spectral signatures in gaseous mixtures [72].

Raman scattering occurs with any laser excitation wavelength and has the advantage that the interaction time is very short (on the order of femtosecond), so that quenching effects are not encountered. In practical combustion situations, Raman scattering diagnostics are typically plagued by very low signal to noise ratio (SNR) [70, 73].

2.4.6 Thermometry by Rayleigh Scattering

As the Rayleigh scattering is an elastic process, after interaction with the incident light quanta, the molecules return to the same state they were in previously. Because there is no energy exchange, the scattered photons reside at the same frequency as the incoming light quanta and, therefore, the scattered signal is not specific to any particular species in a spectral sense. The total scattered power for a single gaseous species is the summation of the contributions from the number density in each rovibronic level. The inverse dependence of σ (in Eq. 2.1) on the fourth power of the wavelength mandates the use of visible or UV lasers to obtain sufficient signal-to-noise ratio (SNR) for effective scattering measurements [74, 75].

Temperature measurement by Rayleigh scattering may be obtained by interpreting the total Rayleigh scattered light intensity directly, if the gas pressure, mixture composition, or Rayleigh scattering cross section of the mixture is known. Since the gas pressure can be measured precisely by pressure transducer, the main difficulty for accurate interpretation of the temperature lies in the precise determination of the scattering cross section of the mixture. In a homogeneous non-reacting flow, the scattering cross section of the mixture remains constant, and the charge temperature can be determined accurately. However in reacting flow field, since both the mixture number density and the gas composition vary simultaneously, the application of Rayleigh scattering techniques to temperature measurement becomes difficult. From a practical viewpoint, Rayleigh diagnostics suffer from Mie interferences and spuriously scattered laser light and can only be used in very clean, particle-free situations. Thus, the technique is not suitable for most practical combustion device probing. However, due to its high signal strength (strongest of the molecular light

scattering techniques), simplicity and ease of implementing it has been used in some applications [76-78].

2.4.7 Laser Induced Fluorescence

In this review, fluorescence is considered as the sequence of an optical absorption process followed by a spontaneous emission event. The precise definition of fluorescence requires that emission occur between electronic energy states of the same multiplicity, i.e., same electronic spin states. Emission between states of different electronic spin is termed phosphorescence. In general, fluorescent lifetimes vary between 10^{-10} to 10^{-5} sec, much shorter than the phosphorescence lifetime of 10^{-4} sec. The light emission may be shifted in wavelength from the incident light, fluorescence, or occur at the same wavelength, resonance fluorescence. It is desirable to examine shifted emission to avoid potential interferences from particle (Mie) or spurious laser scattering.

2.4.7.1 Thermometry by Excitation or Fluorescence Scans

For laminar flow systems, slow excitation or fluorescence scans can be used to determine the rotational temperature of molecular species. The procedure is quite similar to absorption spectroscopy, with the advantage that the fluorescence method provides a local temperature rather than a line-of-sight temperature. For excitation scans the spectral bandwidth of the detector is fixed, while the excitation wavelength is varied. For fluorescence scans the excitation frequency is fixed, and the grating of the monochromator is rotated to determine the spectral distribution of the emissive signal. In both cases an accurate temperature requires that the fluorescence spectrum be uncontaminated by self-absorption; for the excitation case, optically thin conditions are also needed to avoid variations in laser beam absorptivity with changes in excitation wavelength [79, 80]. Excitation spectroscopy samples the rotational distribution in the ground electronic state, so thermal equilibrium is usually assured. Fluorescence spectroscopy, on the other hand, samples the rotational distribution in an excited electronic state. Therefore a reliable temperature necessitates sufficient rotational relaxation to ensure equilibration [81-83]. Because of the time required to perform an excitation/fluorescence scan, they are most often

employed for steady flame applications. The excitation case also requires that collisional quenching not vary with excitation wavelength, while the fluorescence case mandates that collisional quenching not vary with fluorescence wavelength. These requirements can usually be achieved at high temperatures, since the collisional cross section varies rather weakly with rotational quantum number in the excited electronic state, especially for molecules with small rotational constants [84]. Therefore, these methods are not suitable for engine applications where collisional quenching is high and often difficult to predict.

2.4.7.2 Thermometry by Single-line Fluorescence

The most straightforward monochromatic method is Thermally Assisted Fluorescence (THAF). In this technique the laser-induced populations of those equilibrated, so that an electronic, vibrational or rotational temperature can be extracted from the resulting fluorescence spectrum [85]. A second monochromatic method relies on the inherent temperature dependence of the fluorescence signal. This Absolute Fluorescence Method (ABF) requires that the mole fraction of the absorbing species, χ_s, be constant; hence best results will be obtained for nonreactive flows [86].

2.4.7.3 Thermometry by Two-line Fluorescence

Two-line fluorescence thermometry has evolved in response to the slow and tedious nature of excitation or fluorescence scans, which also prevents utilization of the latter in turbulent flows. In the two-line method, a pair of laser wavelengths is used to generate two broad band fluorescence signals from atomic (in TLAF[12]) or molecular (in TLMF[13]) species. The TLAF thermometry can be achieved at much lower laser power than TLMF thermometry as the atomic species have much higher oscillator strength. However, measurements at temperatures below 500 K are not feasible due to low vapour pressure of atomic seeds. Kaminski et al. demonstrated temporally resolved TLAF thermometry in a SI engine using indium as an atomic

[12] Two-line Atomic Fluorescence

[13] Two-line Molecular Fluorescence

additive for a temperature range of 800 to 2800 K. A precision of 14% on single-shot temperature distributions was claimed [87, 88].

2.4.7.4 Planar Techniques

Thermometry by light-scattering methods has been extended to linear and planar imaging of both laminar and turbulent flow fields. Planar techniques are particularly important because of the inhomogeneous temperature distributions inside the combustion chamber. The differential cross sections for both vibrational and rotational Raman scattering are too low for such applications, but temporally resolved measurements are possible via Rayleigh and fluorescence techniques [89]. In this technique, sheet illumination is employed with right angle detection of scattered light using a two-dimensional array detector, with or without a microchannel plate image intensifier. Temporal resolution is normally set by the laser source, while spatial resolution is determined by the pixel density of the array detector.

2.5 Two-line PLIF Literature Review

2.5.1 Choice of Tracer

Following a thorough investigation of thermometry techniques, the 2-line Planar Laser Induced Fluorescence (2-line PLIF) was considered to be the most suitable candidate for this work. Both qualitative and quantitative PLIF measurements have been performed in optically accessible engines using a variety of laser excitation wavelengths and collection strategies. Many studies of fuels and tracers for use with PLIF have been reported. Fluorescence from combustion intermediates such as the OH radical [90, 91], commercial-grade gasoline [92] or even iso-octane without tracer [93] has been used. However, the use of gasoline has some drawbacks and also the use of iso-octane without any tracer limits the capabilities of the PLIF technique. Researchers have surveyed numerous candidates in an effort to find an ideal tracer species for iso-octane. However the choice of a suitable combination of fuel and tracer depends on the desired application and conditions of that application as well as availability of lasers and detection equipment.

The most frequently used tracers in iso-octane are toluene, acetone and 3-pentanone. Applications of aromatic tracers like toluene in comparison to the ketones such as acetone and 3-pentanone are restricted mainly due to oxygen quenching. However the high sensitivity to oxygen can be exploited in applications such as measurements of the fuel-air ratio in SI engines. This significant finding was first noted by Reboux [94]. Also toluene's prevalence in a variety of fuels and fuel surrogates makes it a suitable candidate for a range of combustion-related mixing applications.

Acetone was first recommended by Lozano et al. [95, 96] for nonreactive gas phase mixing applications because it is safe, cheap, easy to handle and it also has;

- high vapour pressure which is desirable for seeding into the gas phase
- broad absorption spectrum where high-power lasers are available
- strong, non-resonant fluorescence spectrum in near-UV/visible where detector quantum efficiencies are high
- short fluorescence lifetime which enables measurements of fast flows without blurring effects
- high resistance to collisional quenching or bath gas effects.

These properties made the acetone PLIF one of the popular laser diagnostics for studying basic fluid mechanics and a variety of other engineering applications [97-102]. However it was soon realized that acetone is not the ideal tracer for all the applications. This was mainly due to the fact that it has a different mixing rate compared to iso-octane. Iso-octane is much heavier compound than acetone and therefore it tends to remain in the liquid phase much longer than acetone. As a result acetone PLIF measurements could not present for example fuel concentration.

3-pentanone was the next ketone proposed by researchers for the PLIF measurements. It has many of the same attractive photo-physical characteristics as acetone but it is heavier. The higher boiling point of 3-pentanone (102 °C) which is close to iso-octane's (99 °C) has made it more suitable for the PLIF measurements in SI engines. For heavier fuels such as diesel and jet fuels with boiling point around 200 °C, higher aliphatic ketones like heptanone and nonanone are obvious candidates. The physical and thermodynamic properties of the most frequently used organic tracer molecules in comparison to iso-octane are presented in Table 2.6.

Property	iso-octane	Toluene	Acetone	3-Pentanone
Molecular weight (g/mol)	114.2	92.1	58.1	86.1
Density at 25 °C (g/cm^3)	0.69	0.87	0.79	0.81
Boiling point (°C)	99.2	110.6	56.1	102.0
Heat of vaporization at 25 °C (kJ/mol)	35.1	38.0	31.0	38.5
Heat of combustion (MJ/mol)	5.50	3.95	1.82	3.14
Max. burning velocity at 25 °C and ϕ =(cm/s)	41.0 at 0.98	–	44.4 at 0.93	–
Flash point (°C)	-12 to 22	4.5-7	-18	7
Autoignition temperature in air (°C)	415-561	480-810	465-727	425-608
Flammability limits in 1 bar air (% vol)	0.95-6.5	1.2-7.1	2.6-13	1.6-8
Gas-phase viscosity at 100 °C (µPa s)	7.7	8.8	9.5	8.2
Gas-phase diffusion coeff. (1 bar air, 100 °C) (cm^2 s^{-1})	0.102	0.132	0.166	0.129
Gas-phase diffusion coeff. (8 bar air, 130 °C) (cm^2 s^{-1})	0.0148	0.0190	0.0239	0.0187
Octane number (RON/MON)	100/100	111/95	_	_
Heating Value (LHV) (MJ/kg)	44.31	40.58	28.55	_

Table 2.6 The physical and thermodynamic properties of iso-octane, toluene, acetone and 3-Pentanone [103-108].

2.5.2 Two-line PLIF Measurements

Grossmann et al. [109] studied the temperature and pressure dependences of the LIF signal of gas-phase 3-pentanone. They showed for the first time that after excitation at two different wavelengths (combination of KrF excimer laser at 248 nm plus 277 or 312 nm radiations which were obtained by Raman shifting the KrF excimer wavelength to the first and second Stokes lines of H_2, respectively) the ratio of the fluorescence signal intensities reflects the local temperature. Since this temperature measurement is based on the ratio of signal intensities it is independent of local tracer concentrations and therefore allows measurements of 2D-temperature distributions in non-homogeneously mixed systems. They compared the PLIF calculated temperature values with the thermocouple readings and reported a satisfactory precision up to 550 K. However at the higher temperatures, the calculated values tended to underestimate the thermocouple readings e.g. by 40-50 K around 600 K. They suggested that the deviation at higher temperatures may be due to uncertainties of the calibration curve.

The first application of the two-line PLIF technique for temperature distribution measurements in a SI engine was reported by the Einecke et al. [110]. In this report measurements were carried out in an optically accessible two-stroke engine fuelled with iso-octane and doped with 3-pentanone. Temperature distribution fields were obtained for both the compression stroke and the power stroke (from unburned gases). The use of two different excitation wavelengths (308 nm and 248 nm from XeCl and KrF excimer lasers respectively) simplified the otherwise complicated relation between LIF signal intensity and system parameters. This work was continued by measurements of the absolute concentration and the fuel/air equivalence ratios. Instantaneous temperature distribution fields obtained from the two-line technique were used to evaluate quantitative fuel distributions in terms of number densities and fuel/air equivalence ratio The measurements were performed at an engine speed of 1000 rpm and overall equivalence ratio of ϕ=0.62. The low equivalence ratio was chosen as it leads to very slow combustion and thus produces small pressure increase compared to the motoring test. This was necessary to ensure some of the tracer left for temperature measurements, late during the compression stroke. They reported $\pm$25 K uncertainty for temperature measurements of up to 600 K [111]. Strand et al. [112] exploited the PLIF technique using 3-pentanone and

Hydroxyl radicals (OH) for flame structure visualization of stratified combustion in a DISI engine. OH radicals were used to show the location of burned gas, and 3-pentanone was used to show the location of unburned fuel. By imaging during the expansion stroke long after the major heat release, lean flame quenching was directly observed by presence of 3-pentanone in the end gas. Kakuho et al. [113] experimentally investigated the relation between in-cylinder mixture temperature distribution and auto-ignition in HCCI combustion. In this report two types of fluorescent tracers, 3-pentanone and triethylamime (TEA), were used with one excitation light source of frequency-quadrupled YAG laser at 266 nm. The results of this study showed that applying in-cylinder temperature distribution is an effective way of controlling HCCI combustion.

Rothamer et al. [114] optimised the PLIF of 3-pentanone for simultaneous imaging of temperature and EGR of an HCCI engine. They exploited the 2-line PLIF with a single tracer and a single interline ICCD camera. By comparing the experimental average temperatures and the values computed (assuming isentropic compression), they reported an absolute accuracy of the temperature measurements of ± 5%. The diagnostic was tested during fired HCCI operation and was used to investigate the mixing of hot EGR with fresh intake charge [114, 115]. This work has been followed in similar researches to study the negative valve overlap (NVO) strategy in HCCI engine operation [116, 117]. Snyder et al. employed Single-line and two-line 3-pentanone PLIF diagnostics to study the distribution and evolution of naturally occurring thermal stratification (TS) in a HCCI engine under fired and motored operation. The two-line diagnostic was first applied during intake and early compression to provide simultaneous temperature and air mole fraction measurements. Subsequent single-line temperature measurements characterized the thermal stratification development during the latter part of the compression stroke. PLIF images were used to investigate the similarities and differences in the development of temperature stratification between motored and fired operation and to investigate the impact of direct fuel injection and cylinder wall temperature on TS [118, 119].

2.6 Summary

The first section of this chapter reviewed the introduction of the emission legislations and the current and future standards for the automotive industry. Section two assessed the current GDI engine technologies and the R&D trends. In section three a survey of the combustion measurement techniques was carried out. Disadvantages of the non-optical techniques along with advantages of the laser-based techniques were discussed. Incoherent techniques were compared and their similarities and differences were presented. The survey has shown that in recent years, various methods of measuring in-cylinder charge temperature have been developed for IC engine applications. The two-dimensional imaging techniques are particularly important because of inhomogeneous temperature and mixture distributions inside the combustion chamber. Such planar techniques favour fluorescence methods because of their intrinsically high signal to noise ratios. In this work the 3-pentanone 2-line PLIF approach was chosen because of its demonstrated potential for precise two-dimensional quantitative temperature and EGR measurements. In addition, the literature review has shown limitations of the 2-line PLIF works performed previously. Therefore the current work was carried out to further develop and optimise the technique through:

- Developing and applying alternative calibration technique
- Enhancing the fluorescence SNR
- Improving precision of calibration measurement (relative standard deviation of < 3%)
- Improving precision of PLIF measurement
- Improving temporal (5 μs) and spatial resolutions (13 Pixels/mm)
- Increasing the measurement area (>55 mm diameter of the imaging area)

This would allow the applications of the 2-line PLIF technique to be further expanded to measurements of other combustion phenomena such as flame thermal stratification.

Chapter 3

Experimental Test Facilities

3.1 Introduction

This chapter describes the experimental test facilities utilised in this work. A short description of the engine test bed, single cylinder research engine with its components and control units, air inlet and exhaust systems, ignition and injection systems and the data acquisition system are presented. Engine operation and maintenance are briefly explained. Engine modifications and design of new components including sandwich plates to adapt optics are discussed. Finally the experimental setup and test procedure for measuring the fuel/tracer injection quantity and intake air flow rate are described.

3.2 Engine Test Bed

The test bed comprises a Ricardo Hydra single cylinder research engine block mounted on Cussons single cylinder engine test bed, cooling modules, dynamometer and a control console.

3.2.1 Dynamometer

A McClure dynamometer (rated at 400 volts, 70 amps, 30 kW with a maximum speed of 6000 rpm) is operated through a KTK thyristor convertor unit (type 6P4Q30) so that it can act as a d.c. motor to drive the engine during starting and motoring operations, or as a d.c. generator when loaded by the engine. During

loading the d.c. power from the dynamometer is converted to 3 phase a.c. by the convertor unit and fed back into the mains supply. The unit is force ventilated by an electrically driven fan mounted on the base frame. A speed signal is provided by a tachogenerator mounted on the motor so that the speed selected at the control console is maintained (< ±5 rpm) by automatic adjustments to the motoring or loading torque.

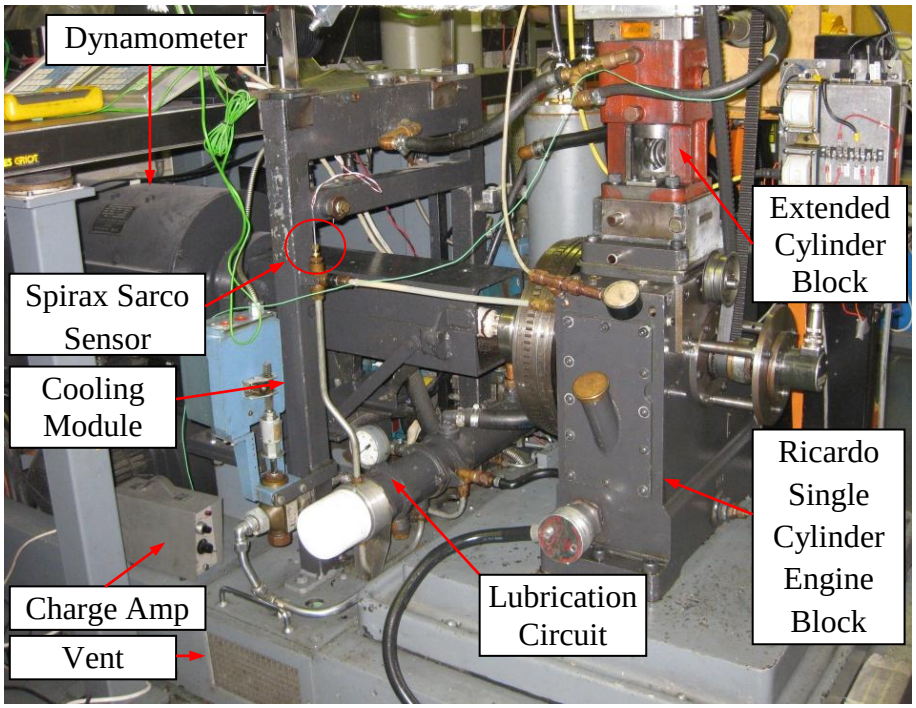

Figure 3.1 Engine test bed

3.2.2 Coolant and Oil Systems

The lubrication and coolant circulation pumps are mounted inside the test bed base fame. The engine coolant is a mixture of de-mineralised water and commercial anti-freeze (ratio of 3:1). It is drawn from the bottom of the header tank and pumped through the heat exchanger before passing out to the engine block and cylinder head. The electrical heater is used to maintain the coolant temperature during motoring tests. The coolant is returned to the top of the header tank by separate return pipes from the head and block. The coolant temperature is controlled by a Spirax Sarco sensor in the vertical leg of the header tank.

The lubrication system also includes a pressure pump and AC motor, a heat exchanger fitted with a closed loop control system that monitors the oil temperature

by a Spirax Sarco sensor. Both the coolant temperature (< ±2 °C) and oil temperature (< ±4 °C) can be adjusted on the engine control console.

3.3 Single Cylinder Research Engine

3.3.1 General Description

A single cylinder research engine based on Ricardo Hydra engine block was used throughout the research. The engine swept volume is 450 cc and its bore and stroke are 80 mm and 89 mm respectively. This engine is a robust research engine capable of operating at conditions representative of modern car and light commercial vehicle engines. The engine is mounted on a Cussons single cylinder engine test bed with integrated oil/coolant conditioning unites and the 30kW d.c electric motor.

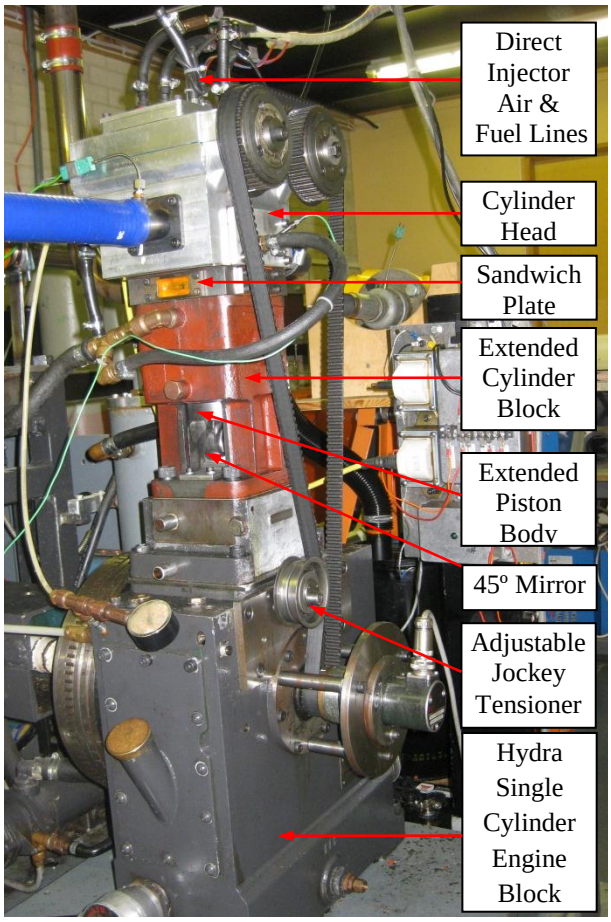

Figure 3.2 Single cylinder research engine

Combustion chamber	Pent-roof
Displaced volume	450 cc
Bore	80 mm
Stroke	89 mm
Inlet valves diameters	29.5 mm
Exhaust valves diameters	21 mm
Valve lift	9 mm for SI with 220° CA duration 4 mm for CAI with 110° CA duration
Compression Ratio	8:1 to 12.4:1

Table 3.1 Engine specifications

3.3.2 Cylinder Head

The engine employs a prototype cylinder head, supplied by Orbital Engine Corporation Ltd. It is a single cylinder, direct injection cylinder head featuring a pent-roof combustion chamber with four valves operated by double overhead camshafts housed in an aluminium cambox carrier. Figure 3.3 shows the combustion chamber, the positions of the valves, spark plug, fuel injector and the pressure sensor.

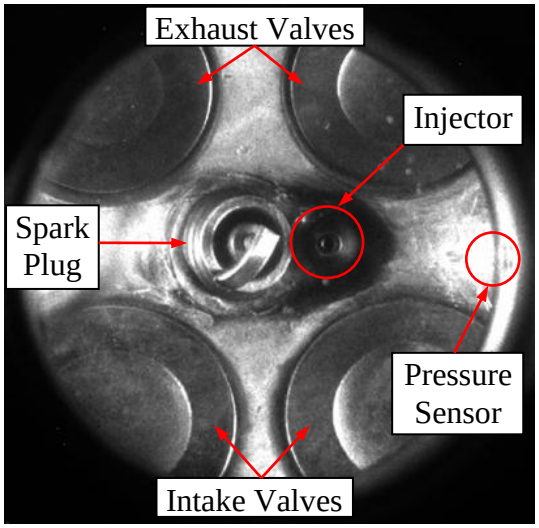

Figure 3.3 Combustion chamber of the prototype Orbital cylinder head

3.3.3 Camshafts

Two sets of camshafts (Figure 3.4) were used throughout this research. The first set has a high valve lift (9 mm) with 220 °CA duration[1] and was used for the SI operation with both normal and positive valve timing. The second set has a low valve lift (4 mm) with 110° CA duration and was used for internal exhaust gas recirculation (iEGR) with negative valve overlap (NVO) to achieve CAI operation as it had been demonstrated in other works [43, 44]. In this method, the exhaust valves are closed early to tarp large amount of residual gases in the cylinder while the intake valves opening are delayed to avoid unwanted back-flow of the residual gases into the intake port. Further description of the NVO operation will be provided in Chapter 6.

The overhead camshafts are driven from the crank-shaft by a two-point belt drive with an adjustable jockey tensioner. The camshaft timing is manually adjustable by using slotted holes provided in the camshaft pulley wheel and monitoring valves lift on a dial gauge as it shown in Figure 3.4. The detailed description of the valves retiming procedure can be found in Ricardo/Cussons Standard Engine Manual [120].

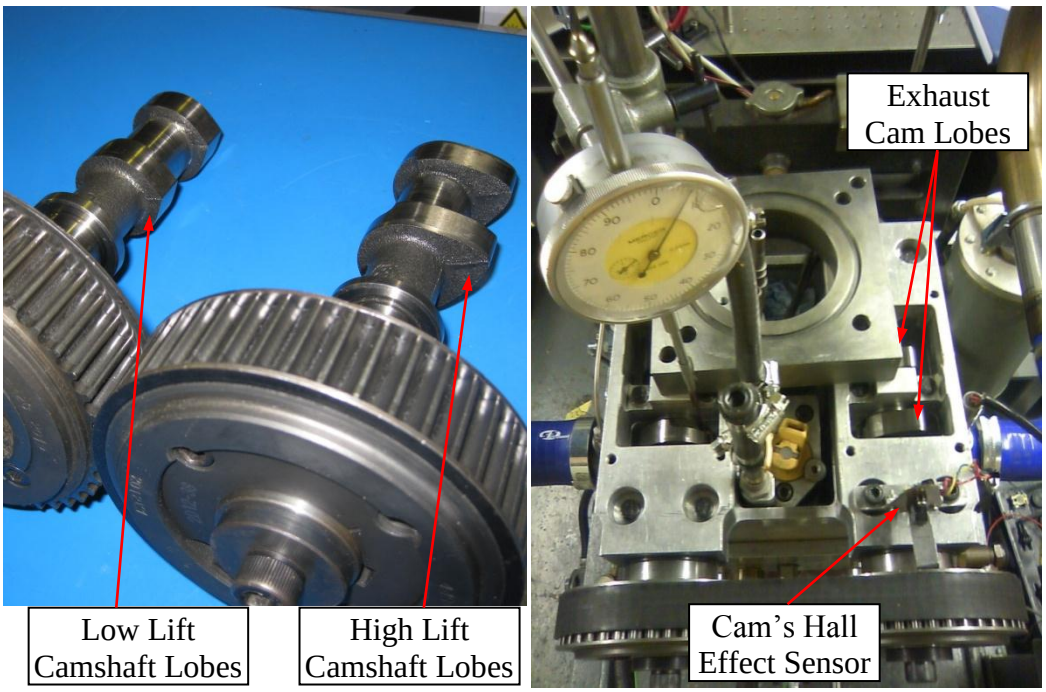

Figure 3.4 Left: High/low valve lift camshafts; **Right**: Adjusting the valve timing

[1] 0.5 mm valve lift was considered as the start/end point in this measurement.

3.3.4 Extended Cylinder Block and Extended Piston

The extended cylinder block is a cast iron barrel with centrifugally cast iron wet liner. It is mounted on a lower cylinder block which is attached directly to the engine crankcase. The extended piston is mounted on the lower piston ran in the lower block utilizing two compression rings and one oil control ring. The extended cylinder block and extended piston were designed to allow optical access to the cylinder bore and combustion chamber. This was accomplished by using sandwich plates that house either four optical windows on the sides or an optical annulus, piston top quartz window and a 45° mirror. The mirror allows the view from below the combustion chamber, via the piston window, to be captured.

3.3.5 Compression Ratio

The extended piston has an aluminium piston crown[2] which is screwed on the piston body. A 55 mm diameter quartz window or an aluminium window dummy can be fitted into the cavity of the piston crown. A spacer and a threaded lock ring secure the window in its place from below. With this configuration (shown in Figure 3.5) it was possible to vary the compression ratio from 8:1 to 12.4:1 using spacers with different lengths.

For the optical experiments where the quartz window should be used, a soft gasket (Chieftain Gasket Jointing 1 mm thick) was placed on either side of the window inside the piston crown. The Chieftain Gasket's formulation contains an advanced carbon fibre material and a Nitrile Butadiene Rubber (NBR) binder which improves its strength and stability. Also an anti-stick finish on its both surfaces is essential when using optical components. These gaskets should be checked and replaced after each engine disassembling. The copper spacer was placed after the soft gasket and cushioned the window from the threaded screw.

[2] The piston crown diameter was initially 79.6 mm which was later tapered for 200 μm.

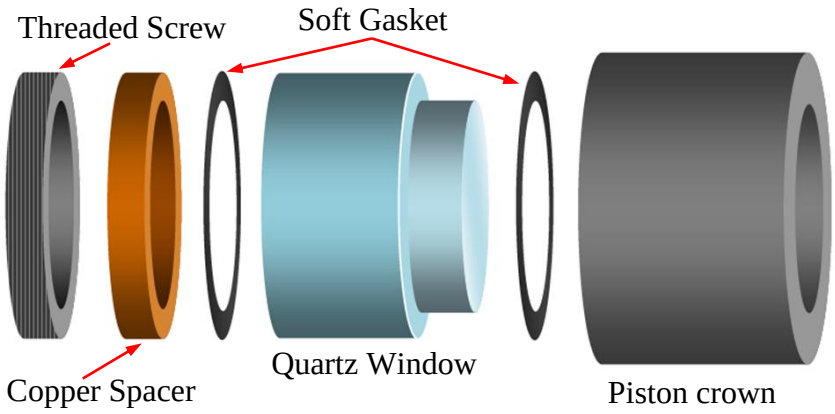

Figure 3.5 Piston window assembly arrangement

3.4 Air Inlet and Exhaust Systems

The inlet system (shown in Figure 3.6) consists of a 3kW intake air heater (Secomak), throttle body assembly and a Bosch multipoint port fuel injector installed on the inlet manifold. The position of throttle butterfly is controlled manually. Two K-type thermocouples are installed on the intake port. One is placed right after the electric heater and provides the feedback for the temperature controller (West 6100 Solid State Controller). The other one is installed just before the inlet ports to read the intake temperature. To reduce the heat loss from air inlet system and to increase the intake air temperature, all the intake pipes are wrapped with high temperature heat resistant knitted fiberglass tapes. An air flow meter (Romet Rotary Gas-meter) was used to measure (0.2% maximum error) the air flow rate when it was needed.

The exhaust system is a short steel pipe connected to a vertical extension pipe attached to a silencer. A K-type thermocouple to read the exhaust temperature and a lambda sensor are mounted on the exhaust port at 2 and 4 cm from the cylinder head respectively. Both the intake and the exhaust pipes are connected to the cylinder head by heat resistance rubber tubes that accommodate engine movement. The rubber tubes are hold and sealed on the pipes by metal jubilee clips.

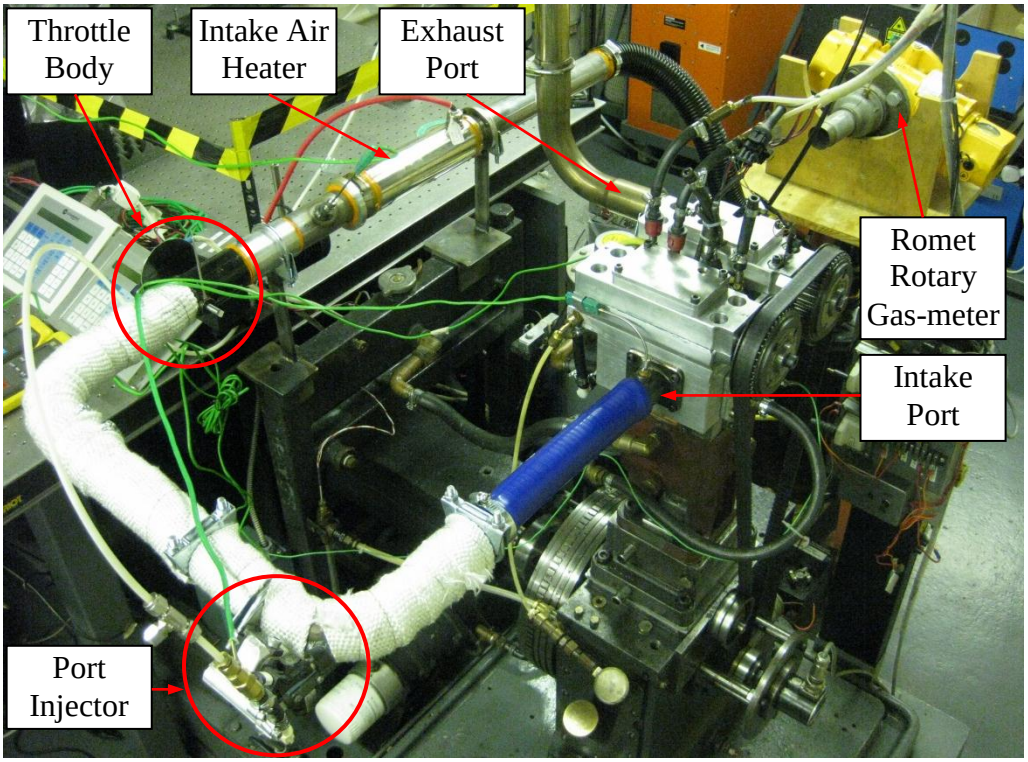

Figure 3.6 Air inlet and exhaust systems

3.5 Spark Ignition System

The engine ignition system (shown in Figure 3.7) is a conventional coil and spark plug arrangement with the primary coil circuit operated by a Lucas "Dial-A-Time" electronic ignition unit which enables manual control of the ignition timing as well as the coil-on (dwell) time. The signals from the flywheel and the camshaft are processed by an And Gate Logic unit. As this unit was set to provide a reference signal at 80°CA bTDC on the compression stroke, the range of ignition timing available was from 79.5°CA bTDC to 45°CA aTDC in 0.5° increments. The ignition signal from the Dial-A-Time was amplified by the ignition driver and the output was used to charge ignition coil primary winding. As soon as the current is switched off, the magnetic field begins to collapse; the coil tries to resist the drop in current causing the voltage in the secondary winding to rise rapidly. This high voltage breaks down the air/fuel mixture in the spark gap allowing a spark to pass, causing ignition of the air/fuel mixture.

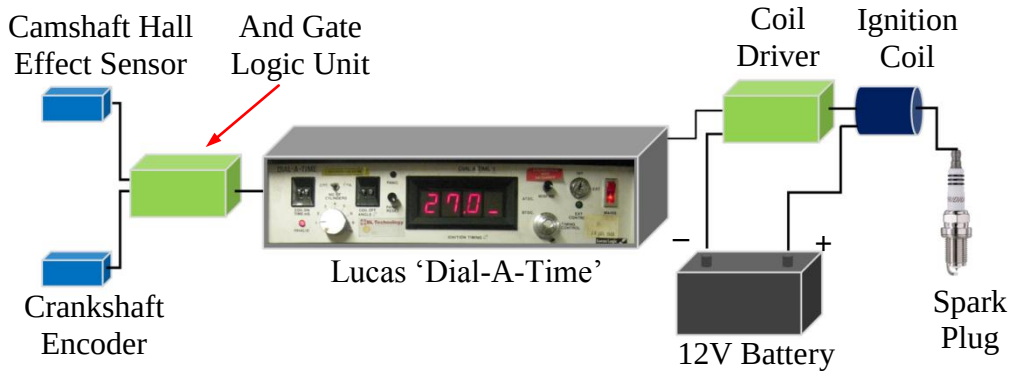

Figure 3.7 Schematic diagram of spark ignition system

3.6 Fuel and Tracer Injection Systems

A direct fuel injector (DI) and a port injector (PI) were used for different experiments in this work. The direct injector was used to inject the fuel or fuel plus tracer into the combustion chamber. The port injector was used to inject the tracer into the intake manifold in order to provide a homogenous trace/air mixture to capture calibration images for the PLIF tests.

3.6.1 Air-Assisted Direct Fuel/Tracer Injection System

The engine utilizes an air-assisted direct fuel injector supplied by Orbital Engine Corporation Ltd which was initially introduced for 2-stroke engines [121, 122]. It exploits a conventional port injector (PI) for fuel metering, and a main injector for direct injection of fuel plus air into the combustion chamber. The injection timing as well as the injection quantity of each of these two injectors can be set individually by control units made at Brunel University. A Dual Output Angle Delay unit receives the engine reference signal from the And Gate Logic unit. The crank angle delay between this reference signal and each of two injection events can be set on this unit. Then the injection timing signal is sent to a Dual Output Injector Timer unit where the injection duration of each of two injectors can be set. Finally the injection timing and duration signals are sent to the corresponding Driver units and from there to the injectors. Figure 3.8 shows the Orbital air-assisted injector and its typical injection

sequence. Figure 3.9 shows a schematic diagram of air-assisted injector control system.

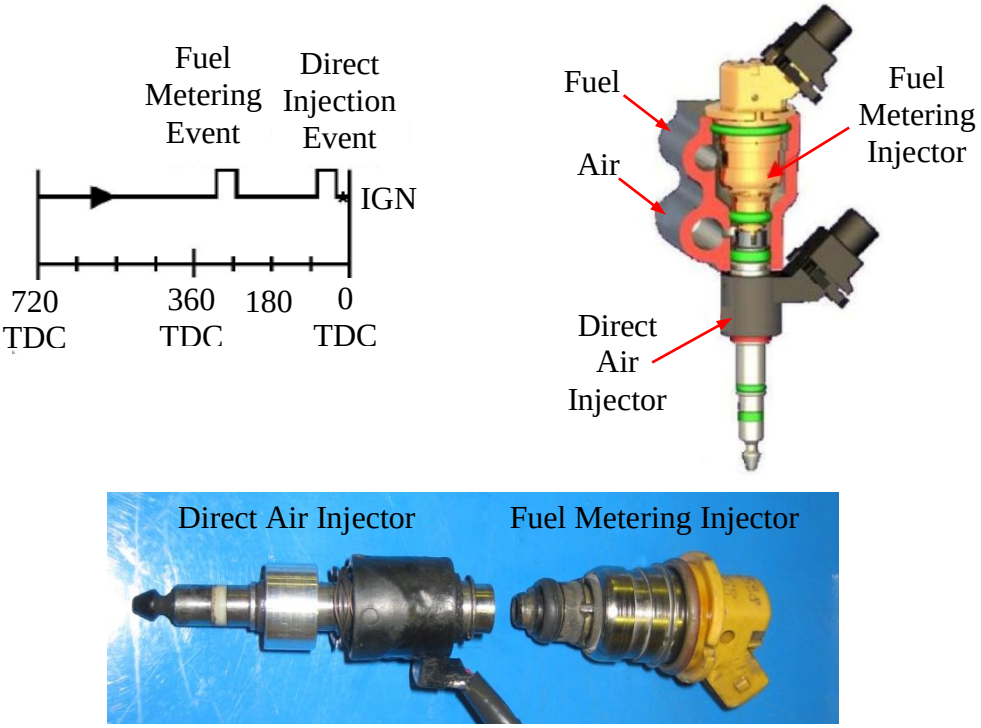

Figure 3.8 Top: Schematic diagram of Orbital air-assisted injector with typical injection sequence [123]; **Bottom**: Orbital air-assisted injector

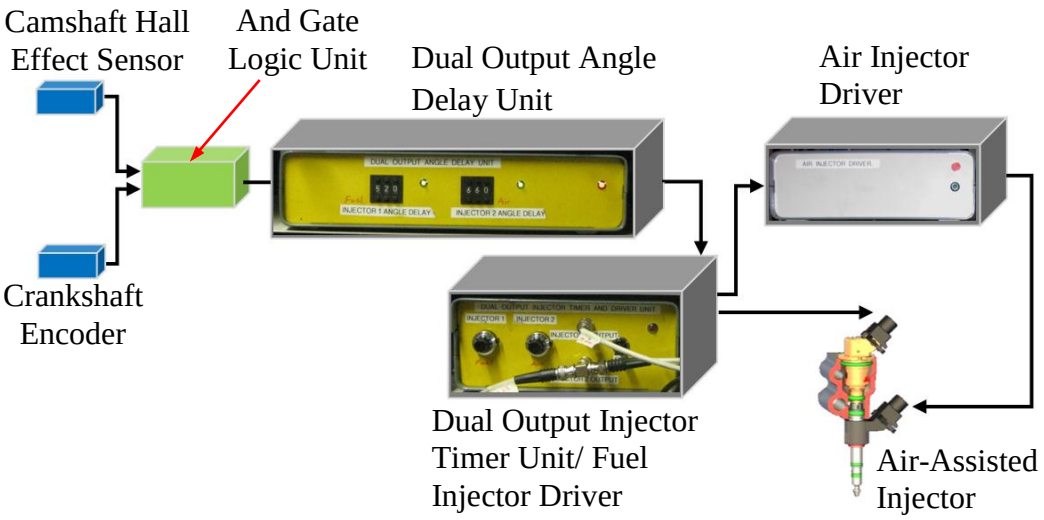

Figure 3.9 Schematic diagram of the air-assisted injector control system.

The advantage of the air-assisted injector is the fact that it utilizes pressurized air at 6.5 bar (gauge pressure) to break up the liquid fuel, which results in good

atomization with small droplet size at a low fuel pressure. However the injection timing is limited due to this low fuel injection pressure and high in-cylinder pressure during the piston moving up to TDC.

3.6.2 Tracer Manifold Port Injection System

A Bosch multi-point fuel injector (MPFI or MPI) was installed to inject the tracer into the intake air at about 50 cm from the intake port. This injector is currently used on the 1.2 litre, 4l Opel Corsa engine (2005). The injection timing and fuel quantity delivered per engine cycle were controlled and manually adjusted by the Dual Output Injector Control unit triggered with the engine reference signal at 80° CA bTDC. The corrosive and degrading effects of 3-pentanone used in this research do not allow the use of a conventional fuel pump, Instead, the tracer was supplied by an accumulator type system where a compressed nitrogen bottle was used to pressurise a sealed tank of tracer that was connected to the port injector. Nevertheless the injector o-rings should be checked and replaced after each engine dissembling.

3.7 Fuel and Tracer Supply Systems

A simple and flexible fuel and tracer supply system was designed and used in this work. The system is capable of providing fuel and tracer to both direct and port injectors during the motoring and firing tests. It was also used during temperature calibration measurements in the constant volume chamber (CVC).

In this configuration the air bottle (cylinder regulator set at 6.5 bar gauge pressure) is connected directly to the air-assisted injector. The N_2 bottle (cylinder regulator set at 8 bar gauge pressure) is connected to the fuel tank to supply pressurized fuel to the direct injector. The N_2 bottle is also connected through a brass union Tee to a second pressure regulator. This pressure regulator is connected to the tracer tank which feeds the port injector (at 3 bar gauge pressure) and the constant volume chambers (at 1 bar gauge pressure).

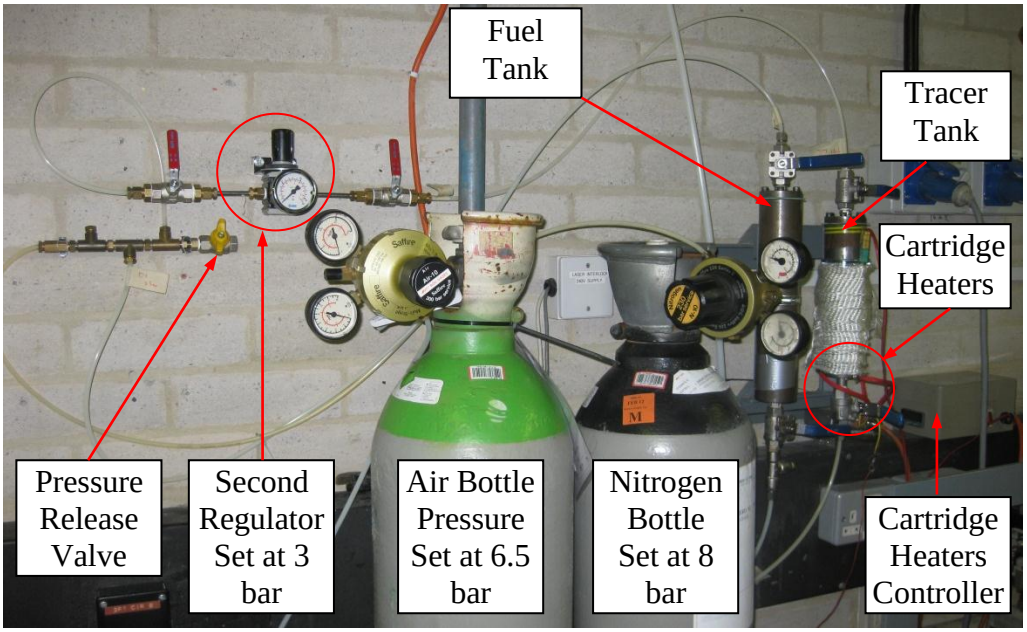

Figure 3.10 Fuel/tracer supply system

3.8 In-Cylinder Pressure Measurement

In-cylinder pressure is a curial parameter to analyse the combustion characteristics. In-cylinder pressure data is an indicator of cycle-to-cycle variation and can clearly show any misfiring or knocking combustion. It can be used for the engine performance analysis such as engine load measurement or for heat release analysis such as mass fraction burnt measurement.

Instantaneous in-cylinder pressure data acquisition was achieved by using a Kistler type 6055B80 piezo-electric pressure transducer, connected to a charge amplifier Kistler type model 568 via a high impedance cable. The charge output of the sensor is converted to a proportional voltage and amplified within the charge amplifier. This analogue signal is then converted to a digital signal by the analogue-to-digital (A/D) converter in the Data Acquisition System (DAQ). The in-cylinder pressure data acquisition system is capable of measuring pressure up to 250 bar with a sensitivity of 19.4 pC/bar and uncertainty of ± 0.1%.

For an accurate in-cylinder pressure measurement, the system should be checked and calibrated so it produces a known voltage for a known pressure applied to the transducer. A dead weight pressure gauge testing rig was used for this purpose. The

pressure transducer was first cleaned in an ultra-sonic bath and then was coupled to the end of a hydraulic circuit of the test rig. This hydraulic circuit is pressurized by placing weight on the circuit piston. The linearity of the transducer response over the measurement range can be determined by applying a range of weights and measuring the amplifier output voltage with an oscilloscope. As the in-cylinder maximum peak pressure is below 70 bar the system were tested up to 100 bar with the amplifier time-constant set at "long" (this should be set at "short" to account for the rapid change in pressure during the in-cylinder measurements). The Pressure-Voltage slope was found to be 10.03 bar/V and this was set in the data acquisition software.

3.9 Data Acquisition System

The Data Acquisition System (DAQ) used in this research consists of a National Instrument board type NI USB-6251, a host computer and a LabView based program written by a former Brunel University PhD student. This program is capable of real-time data acquisition as well as some calculations including IMEP and COV of IMEP. The NI USB-6251 is a multifunction data acquisition card with 16-bits resolution and a sampling rate of 1.25 MS/s. It has 3 inputs which receive the pressure charge amplifier output signal, the engine clock signal and engine reference signal. The card was connected with a USB cable to the host computer which was used to store the data and perform the calculations.

3.10 Engine Reference signal

A reference signal is required to synchronize the data acquisition system, laser diagnostic system and engine control units (including the MPI and DI injection systems and ignition system) with the engine crank angle. This reference signal is provided by the And Gate Logic unit at 80° CA bTDC. This unit receives a signal from a shaft encoder (clock signal) with 1° CA resolution and a signal from hall-effect cam sensor. The hall-effect sensor was attached on the exhaust camshaft pulley and provides a signal for each cycle at 80° CA bTDC. The connection diagram of all the engine control units and NIDAQ system is presented in Appendix A.

3.11 Engine Maintenance and Operation

In order to avoid fluorescence emission of the conventional engine lubricants as well as optical windows fouling, the extended piston and cylinder block were lubricated by non-fluorescence lubricating paste. This shortens the experiment duration as continued lubrication is not possible. The piston, piston rings and cylinder wall should be cleaned and re-lubricated using this paste after a few minutes run. A list of engine components' gaskets and sealants that should be replaced for each engine build up is presented in Appendix B.

Before starting the engine, coolant and oil levels should be checked and topped up if required. Fuel and tracer tanks should be filled with fresh iso-octane and 3-pentanone respectively, as their spectroscopic behaviour would change in time [78]. The tanks and supply lines should be purged after each experiment as they can be damaged by the remaining fuel and tracer. The engine battery should be checked and charged if it is required to ensure accurate operation of the fuel injectors and the spark plug. Also inspection of the pressure transducer, fuel injectors and spark plug should be carried out regularly.

To start the engine, first the water pump and water heater should be switched on. When the water temperature reached near 70 °C, the oil pump should be switched on. It takes about half of an hour for the coolant and oil to reach the setting values of 90 and 40 °C respectively. It should be noted that the calculated major half order torsional speed for the engine is 700 rpm (11.8 rev/s) and the engine must not be run at or near to this speed [120]. On starting the engine must be motored up to 1200 rpm as quickly as possible and not fired until this speed is attained.

Figure 3.11 Left: KTK thyristor convertor unit; **Right**: Hydra control console

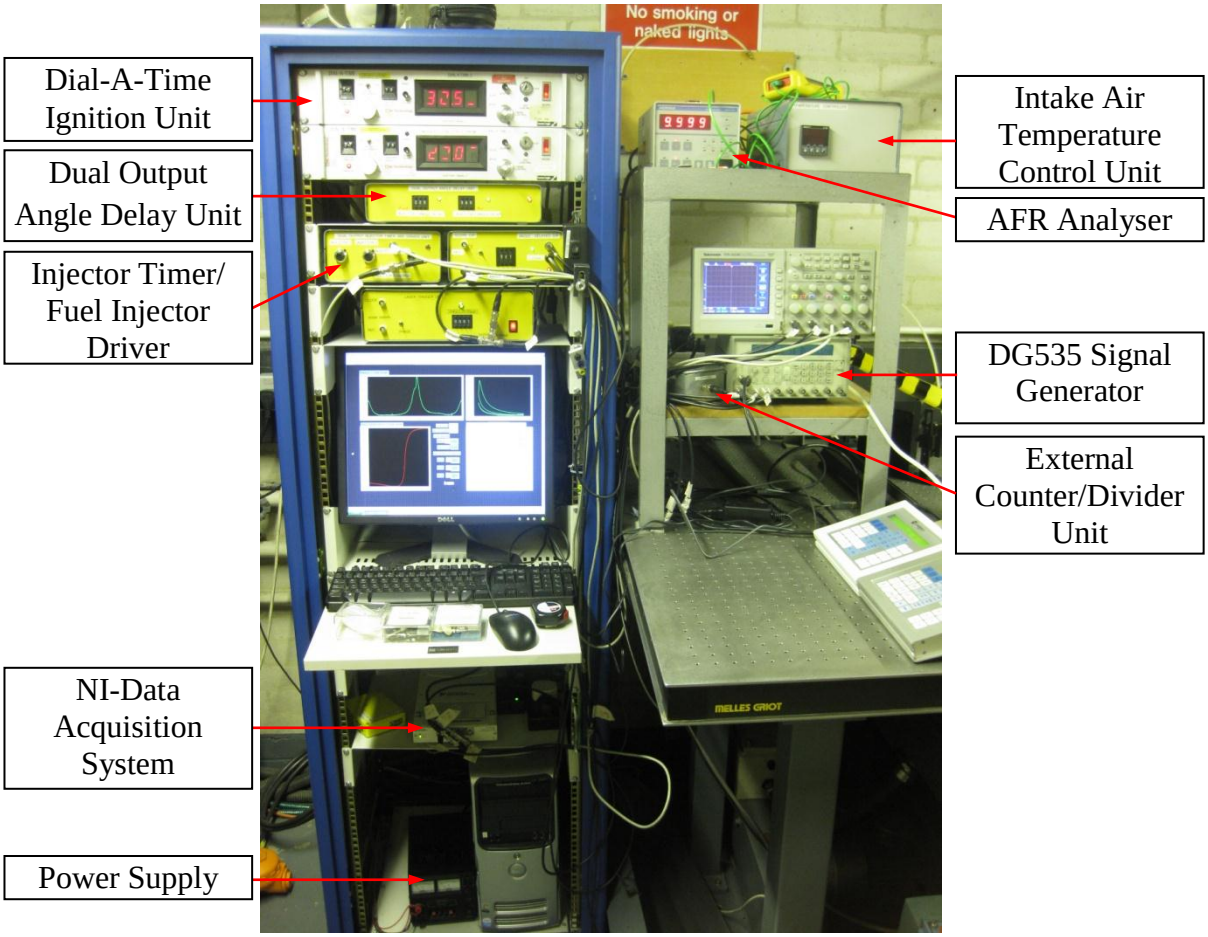

Figure 3.12 Engine control unites

3.12 Engine Modifications

Two different engine configurations have been used throughout this work. The first configuration was all metal components with no optical access to the engine which allowed extensive tests to be carried out on the engine. For the second configuration which was used during the optical experiments, some of the engine metal components have been modified to adapt optical windows. These changes are explained in this section.

3.12.1 New Sandwich Plates Design

Three different sandwich plates (shown in Figure 3.13) were designed and manufactured at Brunel University workshop for different experiments in this work. The all-metal sandwich plate was used for non-optical experiments to adjust engine

operation parameters such as injection timing and quantity, ignition timing, throttle position (SI operation) and intake air temperature.

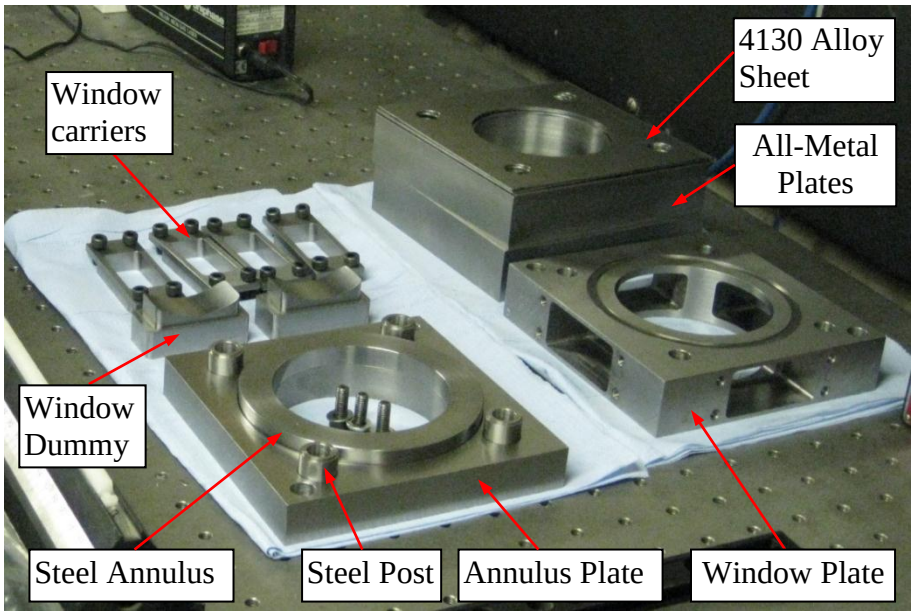

Figure 3.13 Three different manufactured sandwich plates

The second sandwich plate accommodates an optical annulus and allows laser illumination of the engine up to top dead centre. This plate was used for Near Infra-Red Absorption Tomography (NIRAT) experiments with a team from University of Manchester. The engine coolant channels that run through the cylinder head, sandwich plate and piston block were modified in order to have the maximum number of IR send and receive fibres around the cylinder. This was to improve the NIRAT measurements resolution.

The optical annulus made of fused silica was 10 mm long with inside and outside diameter of 80 mm and 110 mm respectively. As any unbalanced force on the ring or poor sealing results in a breakage, a great care should be taken during the mounting and sealing process. One important factor that could cause the breakage was the thermal expansion of metal components including the aluminium cylinder head, copper gaskets and steel sandwich plate. Any non-uniform expansion of these metal parts applies an unbalanced force on the annulus and results in a brakeage. A 1 mm thick sheet of 4130 alloy was placed on the cylinder head copper gasket. The 4130 is a low alloy steel containing molybdenum and chromium as strengthening agents and has a very low thermal expansion coefficient (compare to copper, aluminium and

steel) that can protect the ring from non-uniform thermal expansion of the metal components.

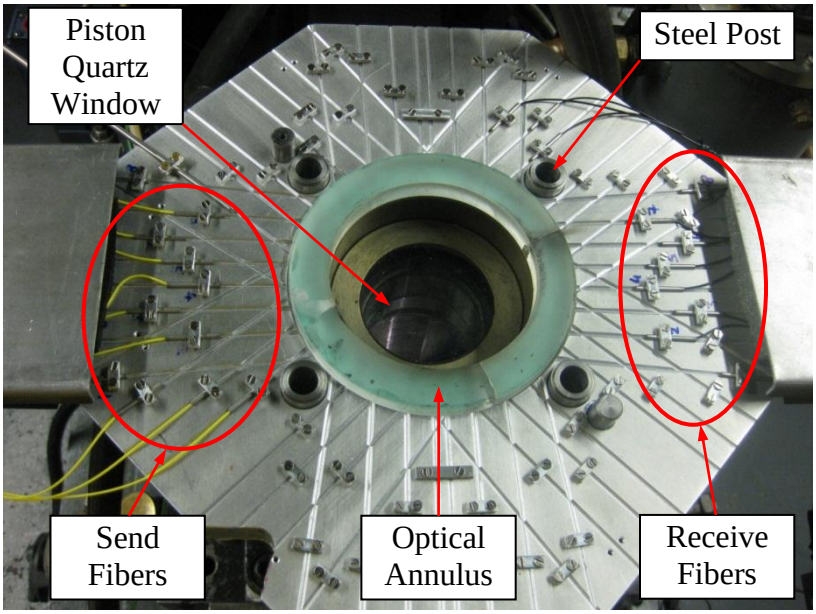

Figure 3.14 NIRAT array mounted on the engine

After a couple of experiments it was decided to further modify and improve the sandwich plate design. The new design was to provide a better sealing and even force distribution as well as to make the assembly process easier. In this arrangement the optical ring sits on a floating metal disk that was placed on an ERIKS Viton O-ring (Viton BS 342, cross section 5.3 mm). The floating metal disk (2.5 mm thick 4130 alloy) was to allow the optical ring to find its place before tightening up the cylinder head bolts. The Viton O-ring was to seal the gap between this metal disk and the sandwich block. The mounting and sealing details of the ring between the cylinder head and the sandwich plate are shown in Figure 3.15. As it can be seen in this figure, the cylinder head sits on four steel spacer posts. This was to ensure that no excessive load is passed to the ring. The length of these posts together with the thickness of the gaskets combination, metal floating disk and the O-ring were chosen that during cylinder head assembly the upper and lower gaskets were each compressed by 0.12 mm before the posts became clamped. It should be noted that the cylinder head bolts' tightening torque (that provides the clamping force) was reduce to 23 N.m (from 25 N.m).

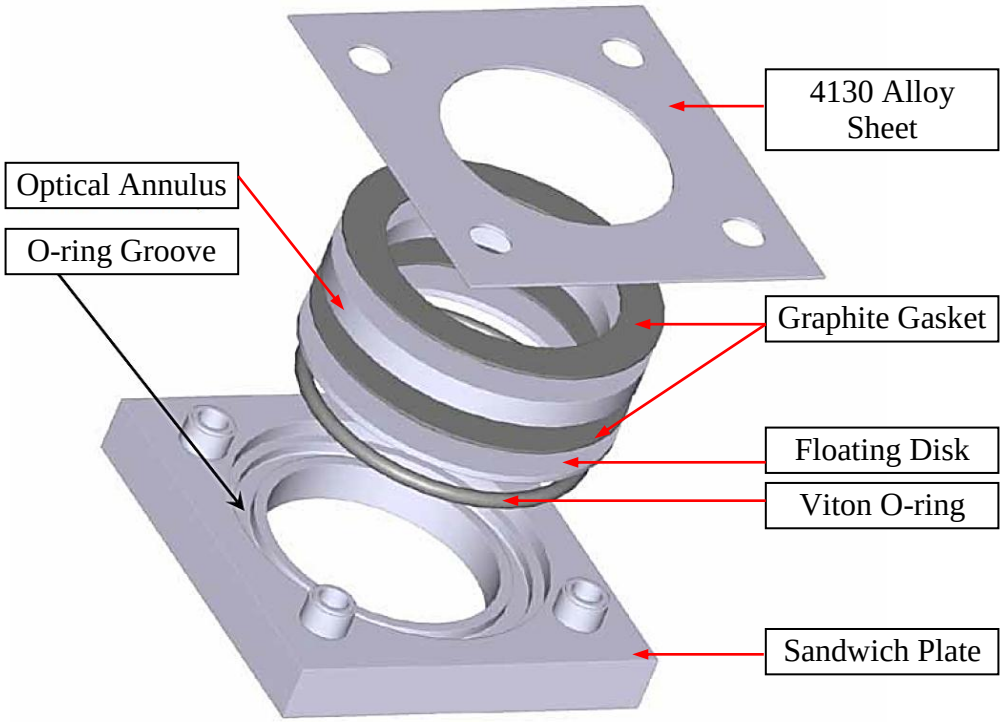

Figure 3.15 Mounting and sealing details of the optical ring

The third sandwich plate had four viewports on its sides for the quartz windows or metal dummies and allowed laser illumination of the engine up to 25°CA bTDC. As the quartz windows or metal dummies were held in their positions by the carriers, it was possible to easily remove them by unbolting the clamps. This allowed an easy access to the combustion chamber which was required to clean the engine optics during the tests. Being robust, having much quicker mounting and sealing procedure, and providing an easy access to the combustion chamber, made this design the primary plate in this work. The technical drawings of all these sandwich plates are presented in Appendix C.

3.12.2 Extended Cylinder Block and Piston Lubrication

The conventional lubricating techniques cannot be used for the extended cylinder block and the extended piston as they result in optical windows fouling. Therefore a different piston ring arrangement was used throughout the research. This arrangement consists of a single steel compression ring and two self-lubricating rings. A set of PTFE (known as PEEK) rings as well as Carbon Graphite (Lecarbon

grade 5890) rings were tested. The latter found to be a better choice as it is capable of many hours of operation before replacement.

The use of a steel compression ring necessitates the use of a lubricant. This lubricant should be a non-fluorescence agent and should not contaminate the windows. Rocol Dry Moly ASP (Anti-Scuffing Paste) was found to be a suitable lubricant for this job. It contains high contents of Molybdenum Sulfate which can provide an almost dry thin film with exceptional strength for surface lubrication of moving parts.

3.12.3 Engine Coolant Channels

The engine coolant channels originally run from the cylinder head through the sandwich plate to the piston block. To be able to use the new plate with the optical annulus, it was required to block and reroute the channels that go through the plate. To do this the coolant channel on the cylinder head/sandwich plate contact surface was measured and a steel ring was machined and placed 6 mm inside this channel. Then the remaining space was fitted with the J-B Weld, which is a two-part epoxy adhesive that can withstand high-temperature (up to 500 ºC). This filler is water-proof, petroleum/chemical-resistant and resists vibration, therefore suitable filler for this application. The metal ring was used to stop the paste to get further into the cylinder head and block the channels inside the cylinder head. Also it can protect the channels if the paste has to be drilled out anytime later. Then a copper gasket (0.4 mm thickness) and a 4130 alloy sheet (1 mm thickness) were attached to the cylinder head using VHT Copper Gasket Cement. The VHT adhesive provides a high-performance coating for sealing the sheets under pressure and heat fluctuation.

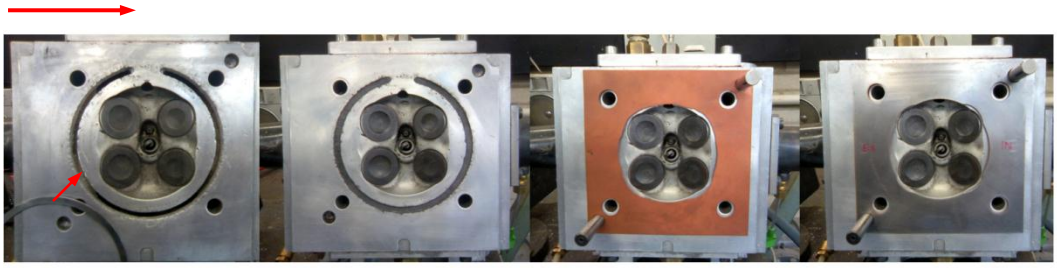

(a) **(b)** **(c)** **(d)**

Figure 3.16 **(a)** A metal ring was placed inside the coolant channel **(b)** The remaining space was filed with an adhesive. **(c)** and **(d)** copper gasket and 4130 alloy sheet were attached to the cylinder head.

3.13 Fuel/Tracer Injection Quantity and Intake Air Flow Rate Measurements

For this work, it was necessary to calibrate the direct and port injectors as well as to measure the engine intake air flow rate as:

a. The fluorescence signal is a function of the tracer mole fraction and the PLIF measurements are based on assumption that the fluorescence signal is in a linear region. A very lean tracer mixture will result in low fluorescence signal intensity which reduces the SNR and accuracy of the measurements. On the other hand a very rich mixture increases the absorption of the laser beam which results in non-homogenous illumination of the measurement area.

b. As it is described later in this thesis, comprehensive tests were carried out to study the direct injection charge cooling effects. And therefore a precise calibration of the direct injector was required to obtain quantitative assessments.

c. For the calculations of the exhaust gas mole fraction, it was required to know the exact quantity of the intake air.

Therefore a series of tests were carried out to measure the engine intake air flow rate and calibrate the port and direct injectors which are described in the following sections.

3.13.1 Manifold Port Injector Calibration

The MPI calibration was performed using a DG535 Signal Generator to provide a burst of 1000 pulses at 10 Hz which is the actual MPI injection frequency during the engine tests. The DG535 signal was used to trigger the injector control unit and driver. The injection quantity could be set by altering the injection pulse duration using the appropriate knob on the control unit. The pulse duration was monitored on oscilloscope (Tektronix TDS2024B). The injected tracer was collected in a small plastic bottle by pushing the injector nozzle into hole made on the lid of the bottle. 1000 injections were accumulated and weighted using a precise balance (Ohaus Analytical Plus) with accuracy of ±0.01 mg. The procedure was then repeated at different pulse durations to determine the injector calibration line (Figure D.1 in Appendix D).

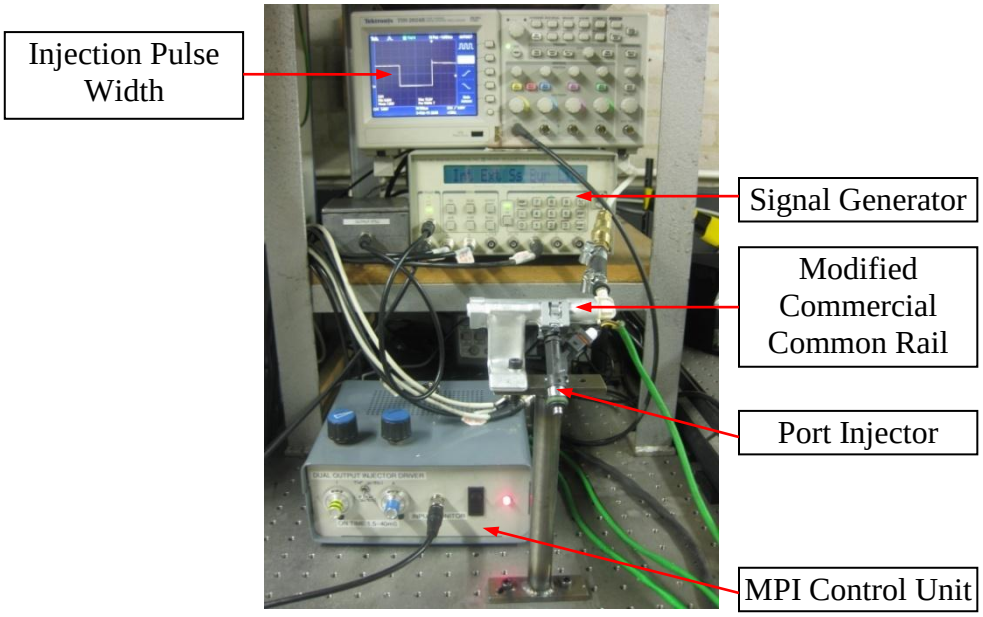

Figure 3.17 Experimental setup for manifold port injector calibration

3.13.2 Air-Assisted Direct Injector Calibration

As in the air-assisted direct injector fuel metering is done by the port fuel injector installed on it, the calibration tests were only carried out on this injector. During engine operation the And Gate Logic Box's reference signal is sent to the DI control units and drivers through a 15 pin D-SUB connectors. Therefore for the static calibration (without the reference signal) it was required to find the connecting cable's PIN definition to the trigger the injector using a signal generator and a BNC cable.

The air-assisted injector was removed from the engine and mounted on a testing board and connected to the fuel line. It should be noted that as the air line was attached unpressurized, the fuel pressure was reduced to 1.5 bar to provide the same pressure difference across the port injector as during NVO operation with SOI at 80 °CA bTDC. The calibration measurements were performed similar to the MPI calibration test. The injection pulse duration was varied from 2 ms to 9 ms with 0.6 ms increment (representing 0.2 degree on the injector's control unit knob). For pulse durations below 2 ms the injected fuel mass dropped dramatically which indicates the minimum operational pulse duration for the Orbital air-assisted direct injector. Figure D.2 in Appendix D shows the DI injector calibration line.

3.13.3 Intake Air Flow Rate Measurements

The intake air flow rate was required to calculate the engine volumetric efficiency for both the normal and negative valve timing operations as well as the tracer seeding mole fraction. This was accomplished by using a gas meter (Romet Rotary Gas Meter) connected to the intake port through a surge tank. The surge tank was designed to stabilize the flow since without it; the engine intake back flow would result in a false reading. For accurate measurements, engine was run for 1 minute and the intake air heater, port and direct injectors were operated as during the PLIF diagnostics. The flow rate was measured to be 0.24 m^3/min during firing operation with normal valve timing and 0.08 m^3/min for negative valve timings.

To calculate the engine volumetric efficiency it was required to know the total cylinder volume (displaced volume (V_d = 450 cc) + clearance volume (V_c)). To measure the clearance volume, cylinder head was placed upside down. A piece of transparent plate was placed on the combusting chamber and the inside volume was filled with diesel using a burette. To stop diesel from leaking, some grease was applied around the valves and cylinder bore as it shown in Figure 3.18. It should be noted that as the extended piston length was adjustable, the volume between piston top (at TDC position) and top of the cylinder block should be considered in V_c calculation. The engine volumetric efficiency (η_v) was calculated to be 88% for firing operation with normal valve timing (wide open throttle) and 31% for NVO.

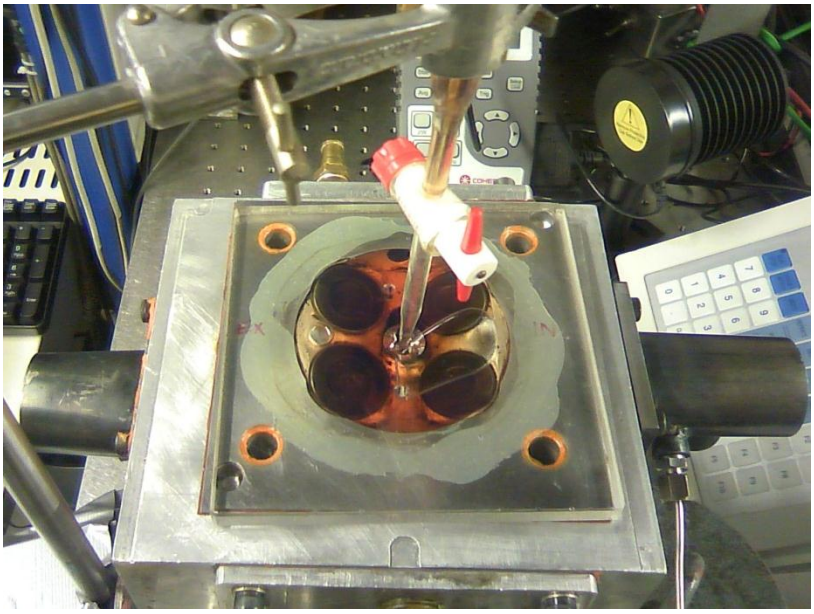

Figure 3.18 Measurements of the clearance volume

3.14 Summary

In this chapter a description of experimental test facilities used in this work has been given. The single cylinder engine and its test bed, air inlet and exhaust systems, ignition system, fuel and tracer injection and supply systems and data acquisition system were described. The engine maintenance and operation were briefly explained. The modifications and additions made for performing the 2-line PLIF technique on the research engine were discussed. Finally the experimental setup and test procedure for calibrating the port and direct fuel injectors as well as measurements of intake air flow rate were described.

Chapter 4
Development of the Two-line PLIF Diagnostic Technique

4.1 Introduction

This chapter focuses on development of the 2-line PLIF diagnostic system. The principles of the technique and its implementation requirements are explained. The laser diagnostic experimental setup including light sources, beam delivery and shaping systems as well as imaging systems are described. Study of Excimer lasers' beam divergence, profile and shot-to-shot energy fluctuation is presented. Synchronization of the PLIF diagnostic with engine crank angle and time budgeting of the system are discussed. Different techniques for improving the 2-line PLIF imaging quality are introduced. Finally the experimental tests and results for engine vibration and Raman convertor conversion efficiency measurements are presented.

4.2 Principle of Two-line PLIF Thermometry

The 2-line PLIF technique can be applied to both atomic and molecular systems. Figure 4.1 shows the principal feature of the 2-line molecular fluorescence thermometry (TLMF). The temperature is calculated via the Boltzmann expression and measurements of the relative populations of two states. These measurements are mostly based on a semi-classical rate equation analysis developed by Piepmeier [124]. The rate equations are conceptually and mathematically more tractable than the quantum mechanical approach.

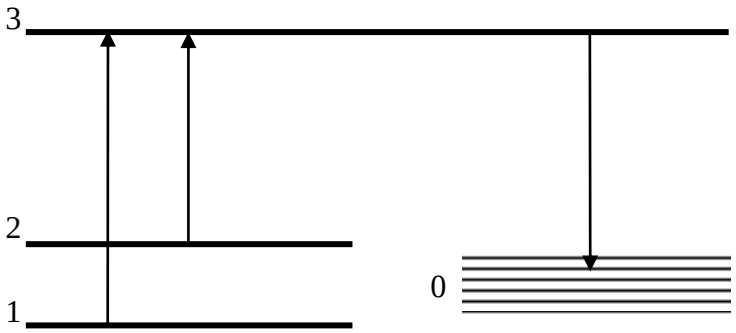

Figure 4.1 Energy diagram of molecular system

Level 3 (a single rotational level or a vibrational band) is pumped from level 1 and level 2 (two rotational levels in the *V*=0 level of the ground electronic state), and the broadband fluorescence signals from level 3 to the ground electronic state are measured sequentially for each excitation. For molecules with closely spaced rotational levels, the broadband fluorescence to the ground electric state does not depend on a particular rotational level [125, 126]. Performing both excitations in a rapid succession allows measurements to be carried out in a frozen turbulence. Also the dependence on quenching can be avoided by exciting lower levels to a single upper level. The rate equation for level 3 via optical absorption from level 1 is given by

$$\frac{dN_3}{dt} = N_1 B_{13} I_{13} - N_3 (B_{31} I_{13} + A + Q) \tag{4.1}$$

where N is total number density of each level (cm^{-3}), B_{13} and B_{31} are the Einstein coefficients for stimulated absorption and emission, A is the Einstein coefficients for spontaneous emission, Q is the non-radiative loss and I_{13} is the laser spectral intensity ($Wcm^{-2}Hz^{-1}$). Similarly, the rate equation for pumping level 3 from level 2 is given by

$$\frac{dN_3}{dt} = N_2 B_{23} I_{23} - N_3 (B_{32} I_{23} + A + Q) \tag{4.2}$$

The fluorescence from level 3 following the excitation from level 1 and 2, assuming steady state, can be written as

$$P_{13} = \eta_{13} N_3 A \left(\frac{h\bar{\nu}}{c}\right) = \eta_{31} \frac{N_1 B_{13} I_{13}}{(B_{31} I_{13} + A + Q)} \left(\frac{h\bar{\nu}}{c}\right) \tag{4.3}$$

$$P_{23} = \eta_{23} N_3 A \left(\frac{h\bar{\nu}}{c}\right) = \eta_{32} \frac{N_2 B_{23} I_{23}}{(B_{32} I_{23} + A + Q)} \left(\frac{h\bar{\nu}}{c}\right) \tag{4.4}$$

where $\bar{\nu}$ is the wavenumber (cm^{-1}). In the linear fluorescence regime, $B_{ij} I_{ij}$ is much less than $(A + Q)$ and can be ignored. Using the Boltzmann fraction[1] equation and radiative relations, the fluorescence ratio is obtained [64]

$$\frac{P_{13}}{P_{23}} = \frac{\eta_{13}}{\eta_{23}} \frac{I_{13}}{I_{23}} \frac{B_{13}}{B_{23}} \left(\frac{2J_1 + 1}{2J_2 + 1}\right) \exp\left(\frac{hc\Delta E}{kT}\right) \tag{4.5}$$

where h is Planck's constant [Js], c is the speed of light in vacuum [cm/s], k is the Boltzmann constant [J/K]. Equation (4.5) provides the direct relationship between the ratio of fluorescence signals and the desired temperature on the basis of excitation of two single transition lines to vibronic levels closely distributed in the excited electronic state. In the case of 3-pentanone, overlapping vibrational rotational bands in the absorption spectra means that multiple vibronic levels are excited simultaneously from the ground electronic state to many different vibronic levels. The fluorescence signal in the linear regime is given by

$$S_f = \frac{E}{hc\upsilon} dV_c \left[\frac{X_{tr} P}{kT}\right] \sigma_\lambda(T, P, X_{tr}) \phi_\lambda(T, P, X_{tr}) \frac{\Omega}{4\pi} \eta_c \tag{4.6}$$

where S_f is the number of photons incident per pixel at the detector or the photocathode of an intensified camera [photons/pixel], E is the laser fluence [J/cm^2], υ is the spatial frequency of the incident laser radiation [cm^{-1}], dV_c is the excited volume [cm^3], X_{tr} is the tracer mole fraction, P is the total pressure [MPa], T is the temperature [K], σ is the absorption cross section [cm^2][2], ϕ is the Fluorescence Quantum Yield (FQY), Ω is the collection solid angle of the optics used for imaging the florescence, and η_c is the transmission efficiency of optics and filters used in the imaging setup.

[1] The Boltzmann fraction is the fraction of the population at the initial vibrational rotational level of the ground electric state.

[2] Influence of temperature and tracer mole fraction on the absorption cross section is negligible.

The absolute Fluorescence Quantum Yield (FQY) of 3-pentanone has been published by Hansen et al. [127]. The measurements were made relative to acetone FQY using Heicklen's [128] value as a calibration standard. In 2003 Koch et al. [129] measured the absolute value of the FQY at a reference condition as a function of temperature using Rayleigh scattering as a mean of calibrating the optical system. It was shown that the FQY for all excitation wavelengths drops as the temperature goes up. However this is more significant for shorter excitation wavelengths.

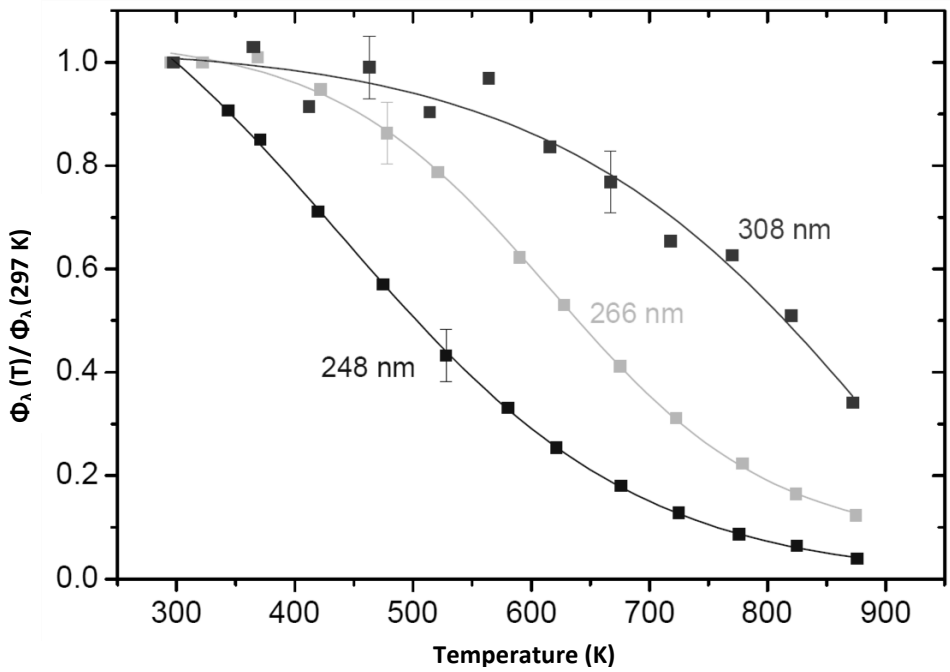

Figure 4.2 Relative fluorescence quantum yield for 3-pentanone at 1 bar excited with 248, 266, and 308 nm [129].

Figure 4.3 shows the absorption cross section of 3-pentanone for different excitation wavelengths at different temperatures. The 3-pentanone absorption band extends from 220 to 340 nm with a peak near 280 nm at room temperature [109]. As the temperature goes up, the peak intensity red-shifts so e.g. at 1000 K, the peak occurs at ~290 nm. This spectral shift of the absorption spectra can be used for measuring temperature by choosing two excitation wavelengths on different wings of this band. Temperature can be calculated by taking the ratio of fluorescence signals from these two excitation wavelengths.

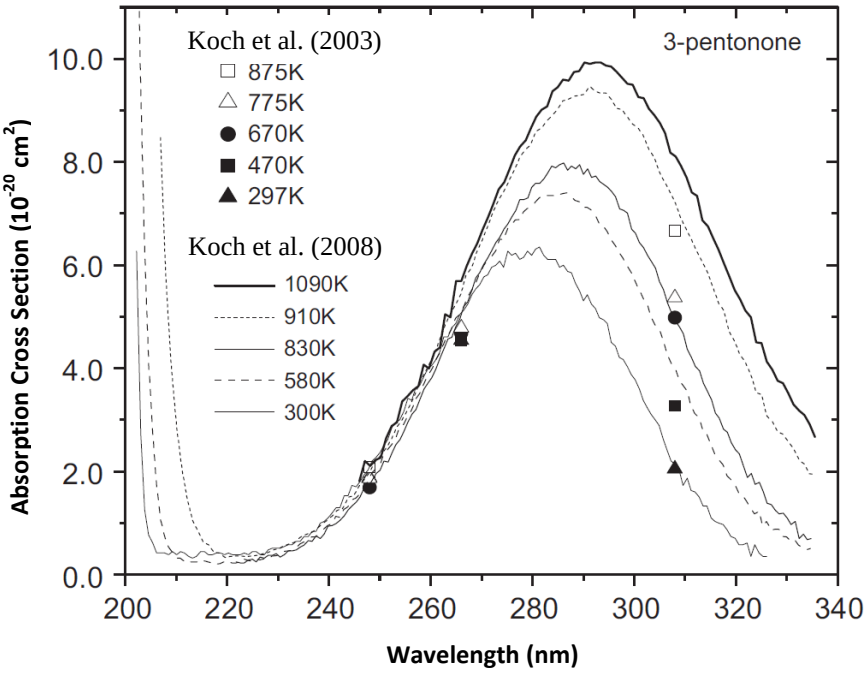

Figure 4.3 Absorption spectra of 3-pentanone at elevated temperatures [130]

In the previous two-line PLIF thermometry techniques such as [117], to calculate the absolute temperature values, the signal at each of the two excitation wavelengths is normalized by a calibration measurement signal taken at a known uniform temperature condition. The collection volume and optical collection efficiencies remain constant between the data and calibration measurements if the calibration and data images are taken at similar condition and relatively close together in time. The fluorescence signals ratio is given by

$$\frac{S_{f2}/S_{f2-Cal}}{S_{f1}/S_{f1-Cal}} = \frac{E_2}{E_1}\frac{E_{1-Cal}}{E_{2-Cal}}\frac{\sigma_2(T)}{\sigma_1(T)}\frac{\phi_2(T,P,X_{tr})}{\phi_1(T,P,X_{tr})}\frac{\sigma_1(T_{Cal})}{\sigma_2(T_{Cal})}\frac{\phi_1(T_{Cal},P_{Cal},X_{tr-Cal})}{\phi_2(T_{Cal},P_{Cal},X_{tr-Cal})} \quad (4.7)$$

where variables with the subscript '*Cal*' correspond to the conditions of the calibration measurements. Also by assuming a small laser pulse to pulse variation, $\frac{E_2}{E_1}$ cancels out with $\frac{E_{1-Cal}}{E_{2-Cal}}$. In this work an alternative approach was utilised which will be discussed in details in Chapter 5.

4.3 Implementation of Two-line PLIF Diagnostic Technique

Figure 4.4 shows a timing event of lasers output, fluorescence signals and camera gate widths for the 2-line PLIF technique. The laser pulse widths are usually10-20 nm (at FWHM) and fluorescence signals' life time are a few hundreds of nanoseconds, therefore camera gate widths of sub microsecond are typically exploited.

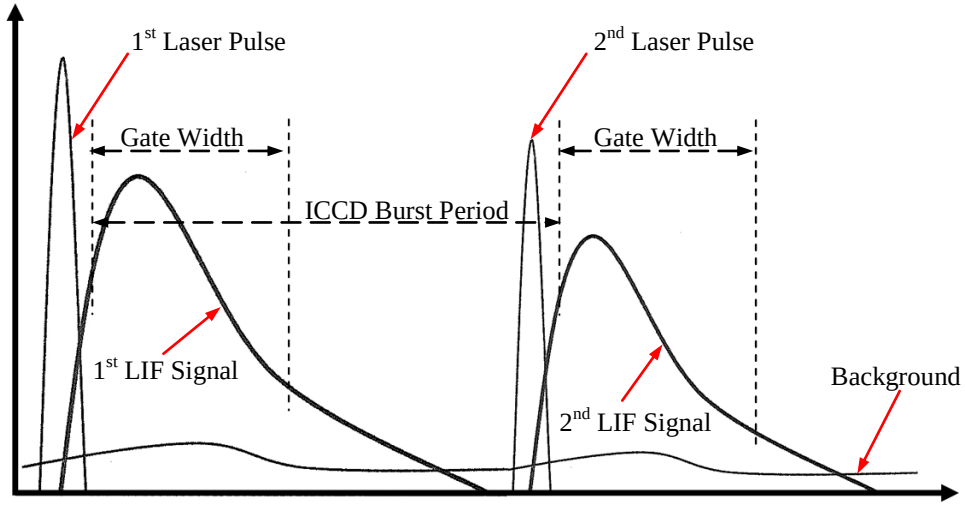

Figure 4.4 The timing event of 2-line PLIF technique [59]

High-energy pulsed UV lasers such as Excimer, Nd:YAG or tuneable dye are employed to generate two laser pulses at specific engine crank angles. The laser pulses are formed into thin (sub millimetre) laser sheets and steered to the sampling area inside the engine by the ancillary optics. The fluorescence signals are intensified and captured by ICCD camera(s) through the piston top window and a 45° mirror. The time delay between camera gates are typically kept as short as a few microseconds. This is to ensure that the frames are taken at a frozen condition with minimum change in thermodynamic state of the measurement area between two frames. In this technique precise time budgeting and synchronization of engine crank angle with the lasers and camera(s) are essential.

4.4 Laser Diagnostic Experimental Setup

This section describes the laser diagnostic experimental setup used throughout this work. The equipment consists of light sources, beam steering and shaping system and light capturing devices.

4.4.1 Light Sources

Use of suitable excitation sources is a key to high precision 2-line PLIF. The light sources should provide high intensity beams with minimum pulse to pulse variation in energy, profile and direction. Three different wavelengths were employed in this study. 248, 277, and 308 nm. 248 and 308 nm pulses were provided by Excimer lasers. The 277 nm beam was selected from the output of the Raman Convertor.

4.4.1.1 Excimer Lasers

Excimer (short for ‘excited dimer’) lasers or more correctly called Exciplex (short for ‘excited complex’) lasers are type of ultraviolet gas lasers that use a combination of a noble gas (in this case xenon and krypton) and a reactive gas (chlorine and fluorine). Excimer lasers usually operate with a pulse repetition rate of around 10s Hz and pulse duration of 10s ns. A Xenon Chloride (XeCl) and a Krypton Fluoride (KrF) lasers were exploited for this work to supply the excitation wavelengths at 308 and 248 nm respectively. Table 4.1 presents specifications of these two lasers. While the output of the XeCl laser at 308 nm was directly used for the measurements, the KrF laser output at 248 nm was Raman shifted to 277 nm. The 308 and 277 nm excitation wavelengths provide the best combination for simultaneous in-cylinder charge temperature and exhaust gas residual measurements [114].

Type	XeCl	KrF
Model	COMPexPro 102	COMPexPro 102
Max Output Power	4 W	8 W
Wavelength	308 nm	248 nm
Pulse Energy	200 mJ	400 mJ
Pulse Length	20 ns	20 ns
Pulse Repetition Rate	Max 20 Hz	Max 20 Hz
Beam Size (V×H)	24×10 mm^2	24×10 mm^2
Beam Divergence (FWHM)	3 mrad Vertical 1 mrad Horizontal	3 mrad Vertical 1 mrad Horizontal

Table 4.1 Excimer lasers specifications

4.4.1.2 Raman Convertor

Following a study of parameters affecting the Raman conversion efficiency and a review of all off-the-shelf Raman converters, it was decided to have a customised Raman convertor for this work. As the KrF laser output beam is 10 mm×24 mm (H ×V), by using off-the-shelf convertor (with typical aperture size of about 10 mm), it was required to reduce the laser beam dimension. This can be done by using a reverse Keplerian beam expander or a reverse Galilean telescope (Figure 4.5). The former causes air to breakdown and is more suited for low power lasers. Instead, the reverse Galilean setup is more suited for high power laser applications. It consists of a positive (biconvex) lens and a negative (plano-concave) lens that are separated by the sum of their focal lengths. Also as this telescope provides a parallel output beam, it was then required to use two other convex lenses before and after the Raman convertor to focus the beam inside the cell and to re-collimate it after it.

However, the external lenses for the Galilean telescope setup were replaced in the present setup by bespoke lenses installed on the convertor's input and output windows for focusing and collimating the laser light. A 60 cm long convertor (internal volume 1.3 litre) with a large aperture size of 1 inch, accompanied with an internal recirculation system was ordered from Light Age Inc. Two Lithosil lenses with anti-reflection coating from 248 nm to 277 nm and focal length of 33.3 cm (nominal) with a thickness of 15.8 mm (5/8 inch) were ordered. Using Lithosil lenses with large aperture of 38.1 mm (1.5 inch) as the convertor's input and output

windows eliminated the Galilean telescope and external lenses for focusing and re-collimating the laser beam. This not only reduced the overall costs of the experimental setup and simplified the optical alignment procedure, but it also removed the adverse effects of the extra lenses including aberrations and pulse energy reduction.

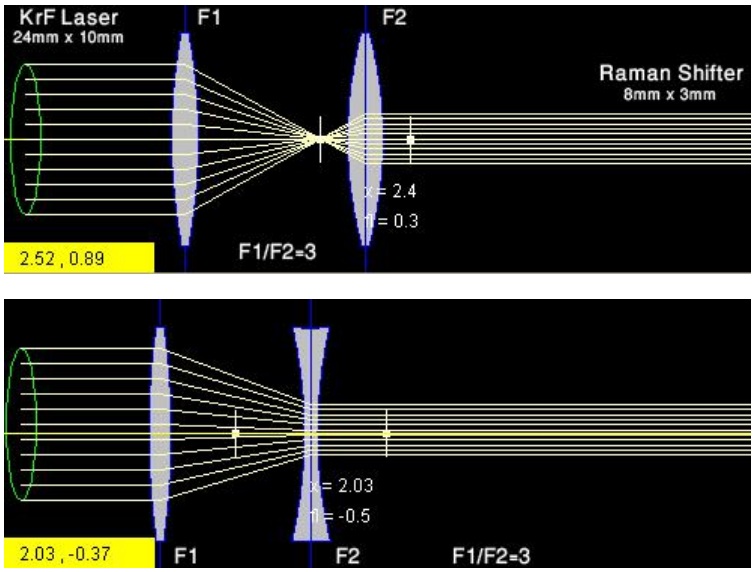

Figure 4.5 **Top:** A reverse Keplerian beam expander; Bottom: A reverse Galilean beam expander

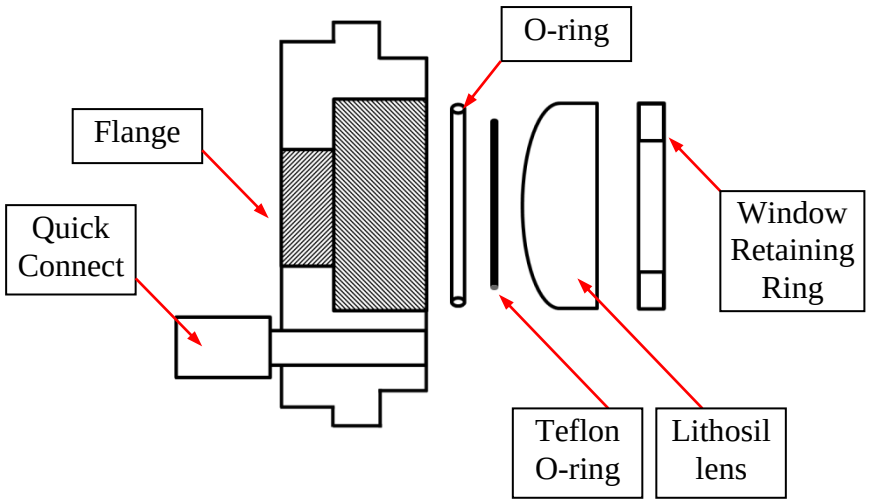

Figure 4.6 Raman convertor lens assembly

4.4.1.1 Raman Convertor Filling and Purging Facilities

As the Raman convertor was designed to operate at high gas pressures of up to 70 bar, special caution should be exercised during the tests as well as during filling and purging processes. A hydrogen filling and purging facility (shown in Figure 4.7) was designed and installed in a vented area outside the laboratory. In this setup, the Raman convertor is placed and secured inside a wooden crate that is anchored down to the ground (so it will not move when reasonable force is applied to it). A tube to VCO® connector connects the 1/4" stainless steel tubing to the RC Quick Connector through a Fill Valve Assembly. The other end of tubing is connected to the hydrogen regulator (a brass regulator with a reverse-thread) through a tube to MNPT connector. The tubing coil in this configuration is to reduce the stress on the connections at the convertor and the gas tank. The cell gas pressure can be monitored by coupling a pressure gauge (0-150 bar) to the second RC Quick Connector. Following a series of conversion efficiency tests, and as it was decided to use the cell with the gas pressure below 55 bar, a high pressure release valve (set at 60 bar) was installed before the cell.

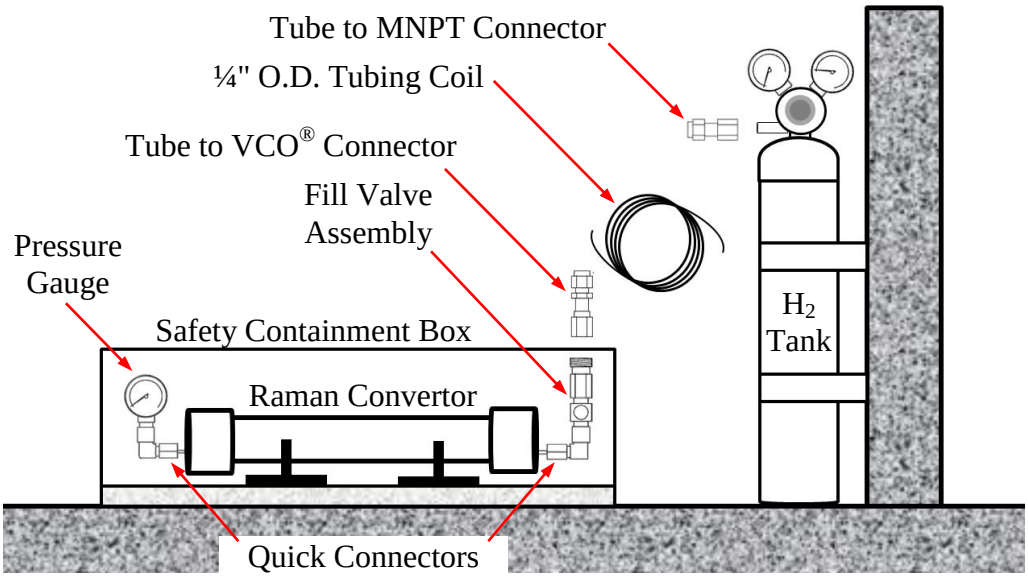

Figure 4.7 Raman convertor filling/purging facilities

It should be noted that the proper inspection of all fittings and optics before filling process as well as following the filling/purging instruction is of high importance. For future reference, this instruction is presented in Appendix E.

4.4.2 Beam Delivery and Shaping System

The 2-line PLIF technique requires generation of two thin, high intensity laser sheets in order to illuminate the measurement plane within the cylinder. These two laser sheets should be precisely spatially overlapped. Considering the rectangular shape of the Excimer lasers' output and the distance between the lasers and the sampling area, additional optical components were required for shaping beams and steering them into the combustion chamber. Some of the important factors that were considered for the design of this system include: the components' material and coating, laser damage threshold (LDT)[3], overall transmission efficiency, capability and precision of the system for beam shaping and steering, ease of alignment process, number of required optics and the overall costs.

The designed optical system consists of a beam splitter, mirrors, cylindrical lenses, equilateral dispersing prism with their mechanical holder/mounts and it was arranged on two anti-vibration optical tables as shown in Figure 4.8. The lower optical table utilizes levelling fits that allow alignment of the table height with the Excimer lasers' output. The output of the XeCl laser goes through a beam splitter while the KrF laser beam is sent through the Raman convertor and passes a dispersive prism. Then both laser beams are lifted and flipped by high reflective mirrors, combined by a dichroic mirror and finally focused on their vertical axes by a cylindrical lens. The detailed descriptions of the optical system components are presented in following sections.

[3] A laser damage threshold of 1 J/cm^2 (20 ns, 10 Hz at 248 nm) considering a safety factor of 3 to accommodate the hot spots in the laser beam was calculated to be suitable.

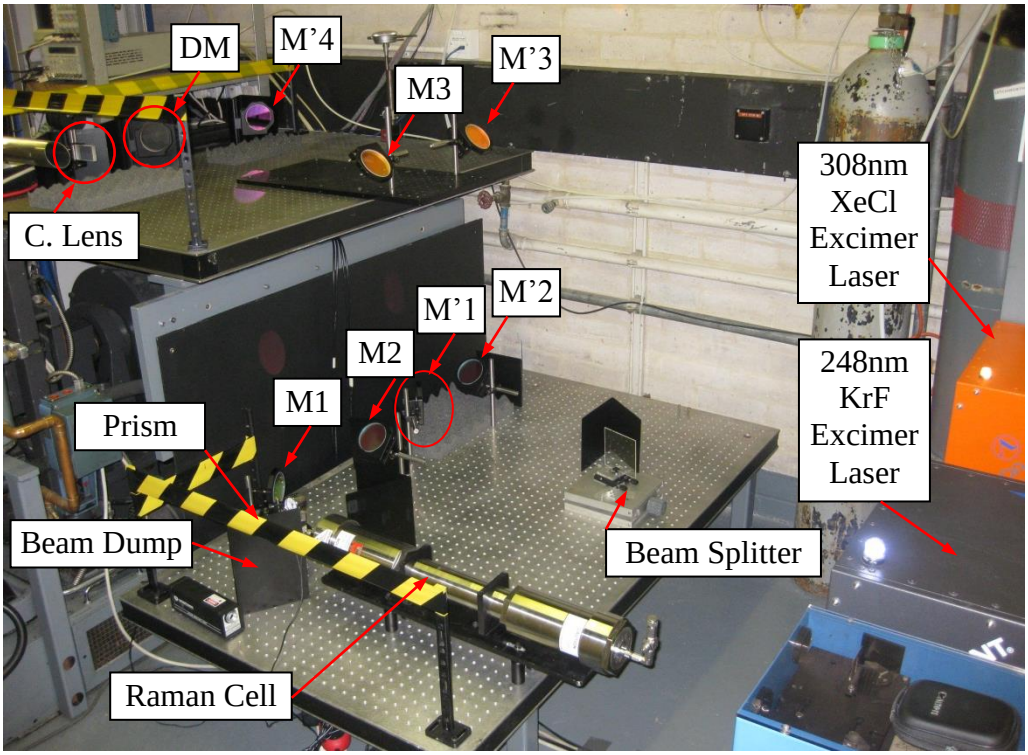

(a)

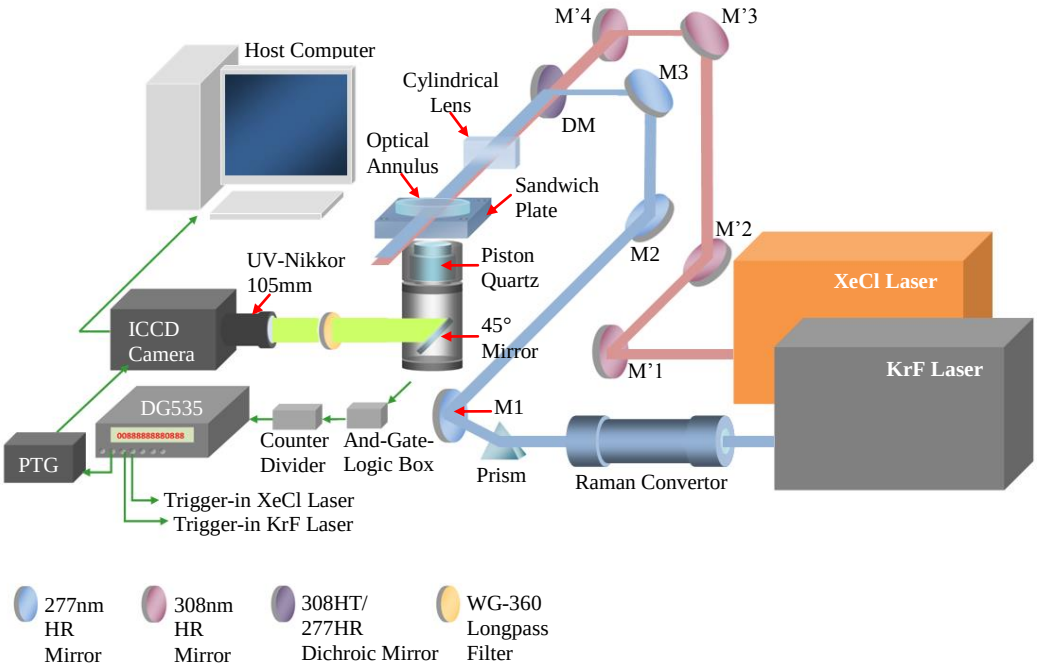

(b)

Figure 4.8 Beam delivery and shaping system (a) picture of the setup (b) schematic diagram of the setup

4.4.2.1 Equilateral Dispersing Prism

An equilateral dispersing prism was placed right after the Raman convertor to separate higher Stokes and anti-Stokes from the desired wavelength. In this prism, as shown in Figure 4.9, the beam deviation, ϵ, depends on the apex angle, A, the angle of incidence, α, and is given by

$$\epsilon = \alpha + \delta - A \tag{4.8}$$

where δ is the angle of refraction exiting the prism, γ is angle of incident at second surface, β is angle of refraction at first surface and given by

$$\delta = sin^{-1}(\text{n sin}\gamma) \tag{4.9}$$

$$\gamma = A - \beta \tag{4.10}$$

$$\beta = sin^{-1}\big((sin\alpha)/n\big) \tag{4.11}$$

where, '*n'* is the refractive index of the prism material and is given by Sellmeier equation

$$n^2(\lambda) = 1 + \frac{B_1\lambda^2}{\lambda^2 - C_1} + \frac{B_2\lambda^2}{\lambda^2 - C_2} + \frac{B_3\lambda^2}{\lambda^2 - C_3} \tag{4.12}$$

'λ' is the incident beam wavelength, '$B_{1,2,3}$' and '$C_{1,2,3}$' are experimentally determined Sellmeier coefficients of the fused silica. The angular dispersion of the prism is given by

$$\frac{d\delta}{d\lambda} = \left(\frac{\sin A}{\cos\delta\cos\beta}\right)\left(\frac{dn}{d\lambda}\right) \tag{4.13}$$

This equation allows to calculate the minimum distance required (from the prism to the first 277 nm mirror) to separate the 1st and 2nd Stokes.

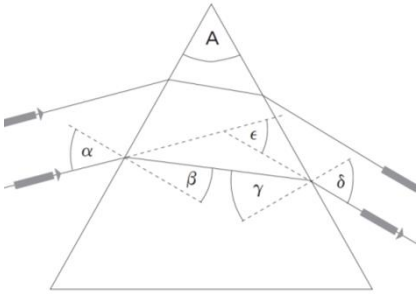

Figure 4.9 Diagram of dispersing prism [131]

4.4.2.2 Beam Splitter

A beam splitter (10×10 cm^2) was placed right after the XeCl laser to reduce its output pulse energy. This was to produce a ratio of the 2:1 for the 308 nm (XeCl) to 277nm (Raman shifted KrF output) laser pulse energy at the sampling area. Although the maximum pulse energy of the XeCl laser (200 mJ) is less than the KrF laser (400 mJ) but due to a low Raman conversion efficiency and the fact that it was not possible to run the KrF laser continuously at its peak pulse energy, the maximum pulse energy at 277 nm available at the measurement area was less than 30 mJ. One solution was to run the XeCl at lower pulse energy but it was found that this (same as running the laser at its peak pulse energy) results in a very high pulse to pulse energy fluctuation. Therefore the XeCl laser was run at high output pulse energy and the beam splitter was used to reduce the energy. The beam splitter was coated for the 50% transmission of 308 nm beam at 45° incident angle and it was possible to alter the transmission by rotating the beam splitter.

4.4.2.3 High Reflective and Dichroic Mirrors

Having a relatively long distance from the lasers to the sampling area and sending the beams through several optical components (which each can alter the properties of the laser beam), it was required to calculate the shape and dimension of laser lights at different points of the optical path so the components with appropriate size could be selected. These calculations can be done manually or by using commercial programs, knowing the properties of the optics and laser outputs. One of the crucial properties that dictate the size of the optics is the laser divergence. The laser divergence should be measured as the manufacturer's specification does not necessarily provide the actual values (usually different measurement methods are applied by the manufacturers). The current optical system was designed so it utilizes minimum number of components to reduce the overall costs, pulse energy loss and to make the alignment process easier and quicker. The system was made up of four high reflective (HR) mirrors at 308 nm and three HR mirrors at 277 nm beam, while a minimum of three mirrors were required to raise and flip the beams at each wavelength (illustrated in Figure 4.10). The main reason for flipping the beams was the fact the lasers' divergence on the vertical axis was much higher than on the

horizontal axis and as a result the beams could rapidly expand vertically while for the measurements, laser sheets (expanded horizontally but very thin on vertical axis) were required.

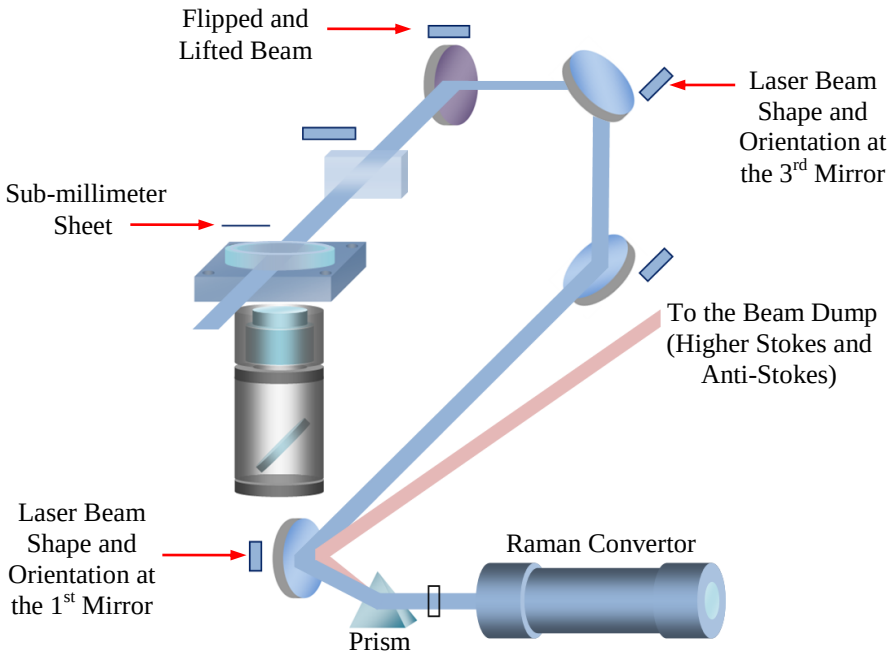

Figure 4.10 Illustration of the beam lifting and flipping steps

A key component of the optical system that allowed the spatial overlap of the two excitation beams was the dichroic mirror (DM). This mirror utilizes the same dimensions as the other HR mirrors but with special coating that allows transmission of one wavelength and reflection of the other. Although the two beams were un-polarized and relatively close in wavelength, the tremendous improvement in optical coating technology (such as improved deposition technologies) in recent years allowed to have a dichroic combiner that transmits one laser beam at 308 nm with >90% efficiency while reflects the other wavelength 277 nm with >97% efficiency.

4.4.2.4 Cylindrical Lenses

Rectangular cylindrical lenses 76.2 mm by 38.1 mm (3"×1.5") were required to focus the expanded laser beams on the vertical axis and provide the laser sheets. The suitable focal length of the required plano-convex lenses was calculated to be 1500 mm. As Equation 4.14 shows, the focal length of the lens is a function of the

refractive index of the lens material, *n*, which in turn is a function of the incident wavelength.

$$\frac{1}{f} = (n-1)\left(\frac{1}{R_1} + \frac{1}{R_2}\right) - \frac{(n-1)^2 d}{n R_1 R_2} \qquad 4.14$$

R_1 and R_2 are the curvature radii on the two lens surfaces. The curvature radii are taken positive for convex surfaces and negative for concave surfaces (here $R_2 = \infty$). Therefore in theory a separate lens should be used for each wavelength to avoid the chromatic aberration. However in practice as the illumination wavelengths were close (277 and 308 nm) and to simplify the optical system and reduce the costs, a single cylindrical lens with a proper AR coating was utilized. The CVI Melles Griot BBAR[4] 248-355 coating was selected for this lens. The coating provides both a very low reflection of ≤0.5% over a broad UV range from 248 nm to 355 nm and also a very high damage threshold[5]. The performance curve of this coating as well as detailed specifications of all the optical components including material, size, clear aperture, coating, LDT, supplier and cost are presented in Appendix F.

4.4.3 Imaging System

For the high speed imaging or during the PLIF measurements, under conditions where the camera's gating time is extremely short and signal levels are low, the signal to noise ratio (SNR) of the measured signal is one of the primary parameter limiting the precision of the measurements. To optimise the precision of the diagnostic, the imaging systems should be able to give the maximum SNR for a given number of incident photons. The imaging system used in this work consists of two different cameras, optical lenses and filters.

[4] Broad Band Anti Reflection

[5] Up to 10 J/cm^2 for 20 ns, 20 Hz pulse at 1064 nm and 1 MW/cm^2 for a CW at 1064 nm [132]

4.4.3.1 PI-MAX III Intensified CCD Camera

Most of the optical data acquisition works in this research including high resolution flame propagation imaging, fuel spray visualization, charge cooling effect and EGR/T measurements were carried out with a Princeton Instrument PI-MAX III intensified CCD camera system. This camera is designed for general macro-imaging and its ideal for applications involving ultra-low light measurements, or measurements of transient effects. The system components are the camera head (houses the CCD, intensifier and a multi-stage Peltier cooler), ST-133 controller with the Programmable Timing Generator (PTG), host computer with an interference card and Princeton Instrument WinView/32 software. The image intensifier (illustrated in Figure F.4 in Appendix F) is a proximity-focused micro channel plate (MCP) fibre-optically coupled to a CCD array [134]. The CCD array provides a low noise, high dynamic range readout that can be scanned at variety of pixel rates. To capture 2-line PLIF Double Image Frames (DIF), the Overlapped Interline read out was exploited. The overlapped operation allows a new exposure begins while the readout of the previous one is still in progress, enabling the camera to capture two frames with an extremely short interval. Figure 4.11 illustrates exposures and how pixel charge is shifted and digitized in this read out mode.

1. Empty Readout Register. Exposure has ended and image is being transferred to storage cells.

2. Image has been shifted to storage cells, first line has been shifted to Readout Register and second exposure begins.

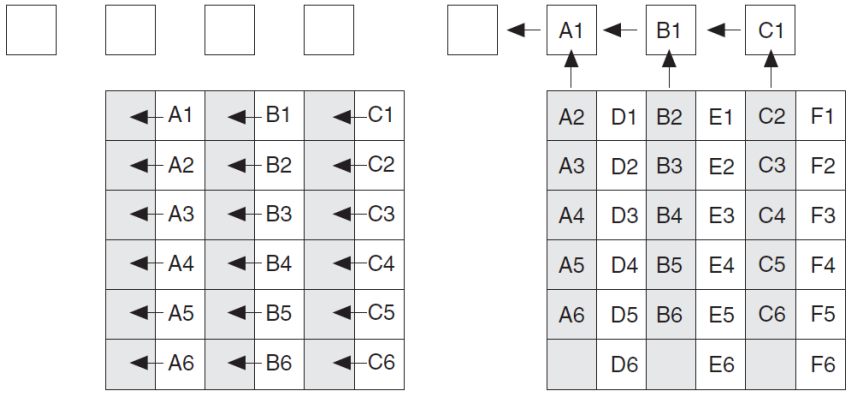

3. Charge from first cell has been shifted to Output Node

4. After first image is read out, storage cells are empty. Second exposure continues.

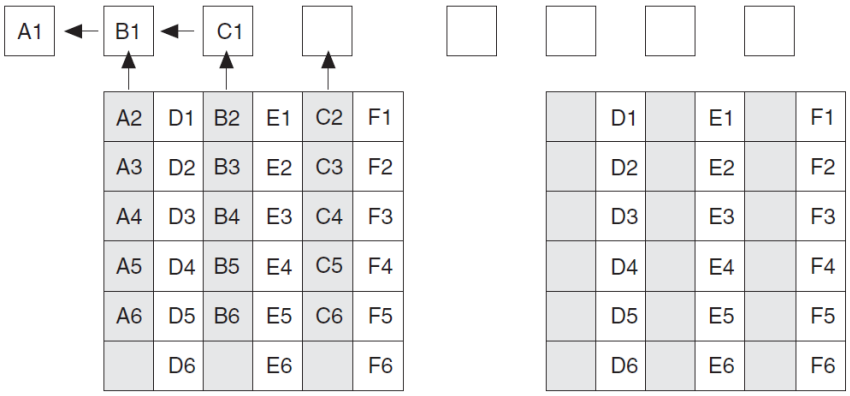

Figure 4.11 Exposure and readout in overlapped mode [134]

The time needed to take a full frame at full resolution in non-overlapped timing mode is

$$t_{exp} + t_R \qquad 4.15$$

where t_{exp} is the exposure time and t_R is the CCD readout time. This time for the interline array running at 5 MHz for the full CCD (1024×1024 pixel) is 4 frames per second, but it can be reduced by pixel binning (2×2 to 16×16) or by selecting a

smaller Region of Interest (ROI) on the CCD which both are explained later in this chapter.

4.4.3.2 Camera Lenses

A UV-Nikkor 105 mm *f*/4.5 and a Micro-Nikkor 60 mm *f*/2.8 lenses were used in this work. Both lenses are considered as a macro photography lens. Macro photography refers to taking pictures in which the image appears at least as large as it does in reality[6] [135]. The UV-Nikkor lens was coupled with the PI-MAX III camera mainly for the PLIF imaging. Due to an appropriate choice of materials, this lens provides a high transmission (of up to 70%) on a broad spectral range from 220 to 900 nm. The Micro-Nikkor was used on the Memrecam fx-6000 camera for high-speed combustion imaging. The technical specifications of both lenses are presented in Table 4.2.

Figure 4.12 UV-Nikkor 105 mm *f*/4.5 and its lens construction [136]

Figure 4.13 Micro-Nikkor 60 mm *f*/2.8 and its lens construction [137, 138]

[6] Traditionally, macro photography is defined as any photo in which the subject has a 1:1 ratio with the photo negative.

Specifications	Micro-Nikkor 60mm f/2.8	UV-Nikkor 105mm f/4.5
Focal Length	60mm	105
Aperture (min to max)	f/32 to f/2.8	f/32 to f/4.5
Maximum Angle of View	26°30'	23°20'
Reproduction Ratio	1:1	1:10 to 1:2
Lens Elements	8	6
Lens Groups	7	6
Filter Size	62 mm	52 mm
Dimensions (dia. x Length)	70 × 74.5 mm	68.5 × 108 mm
Weight	440 g	515 g

Table 4.2 Technical specifications of Micro-Nikkor and UV-Nikkor [136,138]

4.5 Study of Excimer Lasers' beam Characteristics

Excimer lasers are the heart of the illumination system in the 2-line PLIF diagnostics. These are gas lasers that produce pulsed outputs in the ultraviolet region of the spectrum, where the output wavelength depends upon the active gas fill of the laser. The pulse generation is through an electric high voltage discharge in the lasing medium. In order to avoid a spark during the discharge process the gas mixture has to be pre-ionized. Also a heat exchanger is required, as the main part of the energy supplied has to be carried away in the form of heat. Although the energy efficiency of the Excimer lasers is of the order of a few percent, they are widely used as they are able to irradiate ultraviolet rays with ultra-short pulse width and very high peak power density (tens of MW/cm^2). For a precise quantitative measurement it was required to analyze lasers' output pulse energy variation and propagation characteristics of which, the beam divergence and profile are discussed in this section.

4.5.1 Divergence

One of the three unique features of the lasers is to provide a highly directional beam, a well collimated beam that travels over long distances with very little spread. This is described as the beam divergence which is an angular measure of the increase in beam diameter or radius with distance from the beam waist. For a diffraction-limited Gaussian beam (M^2=1), the $1/e^2$ beam divergence half-angle is given by

$$\theta = \frac{\lambda}{\pi w_0} \tag{4.16}$$

where w_0 is the beam radius at the beam waist. For the laser beams with higher divergence the M^2 factor or the beam quality is used and the divergence half-angle is given by

$$\theta = M^2 \frac{\lambda}{\pi w_0} \tag{4.17}$$

The above equations are for circularly symmetric beams. For the rectangular beams of the Excimer laser, the M^2 can be different for each axis. In case of Excimer lasers, the x and y values of beam quality can differ by an order of magnitude, which basically means a different focusing limit on each axis. Although this is not desired for the beam delivery system but preferentially the axis with lower spatial coherence can be utilised to achieve a more homogeneous illumination over a larger area which are crucial for 2-line PLIF diagnostic.

The Excimer lasers beam divergences were measured to be 9 mrad on the vertical axis (longer axis) and 1 mrad on horizontal axis for both lasers. The beam divergences were determined by sending the beams on a 4 m long path and measuring the pulse energy at different distances from the lasers using a pulse energy meter[7] and knife edge technique.

[7] Coherent J-50MUV-248 energy sensor coupled with Coherent FieldMaxII-TOP energy meter.

4.5.2 Shot-to-Shot Pulse Energy Variation

To eliminate the effect of laser energy variation by time from the captured fluorescence images, usually laser shot-to-shot pulse energy are logged during the tests and used to correct images in post processing. Nevertheless this technique only indicates the peak intensity fluctuation and does not provide any information regarding the small but significant shift in the laser output pulse direction and energy distribution.

Figure 4.14 shows the energy variation of 700 pulses. For this test both lasers were filled with fresh gas and run at 10 Hz at the required output pulse energy ratio (2:1 for XeCl to KrF). The pulse energies were measured[8] right after the beam exits. As it can be seen from the data, both lasers show a relatively low energy fluctuation (1.89% and 0.74% standard deviation for XeCl and KrF lasers respectively). However the pulse energy variation of both lasers were monitored and recorded prior to each test to make sure they are in an acceptable range. To achieve the maximum pulse energy with lowest fluctuation, Excimer lasers should operate with fresh gas (this was done by purging lasers' resonator and refilling it with fresh premix gas prior to each test). Also both lasers were run at constant energy mode. In this mode, lasers' internal energy meter monitor the output pulse energy and vary the resonator high voltage to keep the output pulse energy constant.

[8] Overall accuracy of the energy measurement system was calculated by $\sqrt{(V^2 + W^2)}$ where $V = \pm 3\%$ and $W = \pm 1\%$ are the energy sensor and energy meter uncertainties respectively [139].

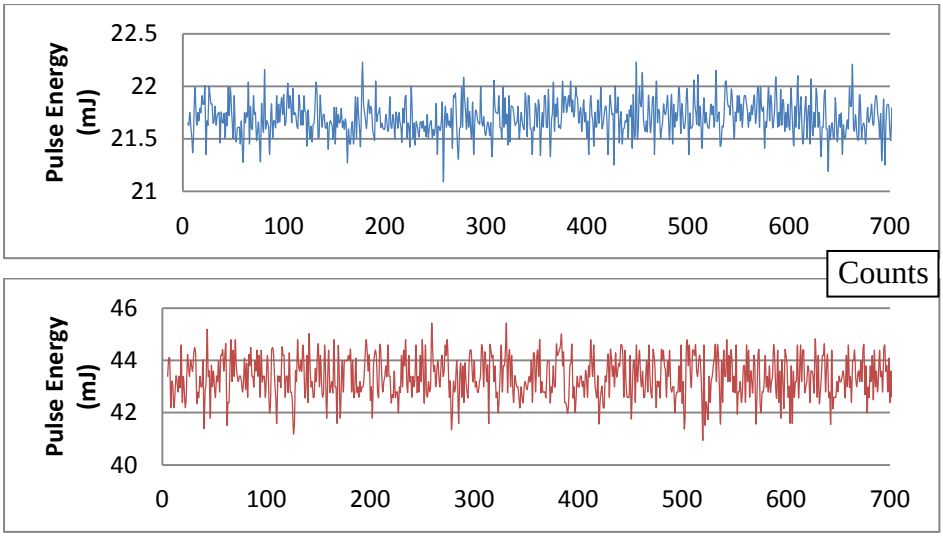

Figure 4.14 Sample measurements of Excimer lasers pulse energy variation, **Top**: KrF; **Bottom**: XeCl[9]

4.5.3 Beam Profile

The beam profile is the 2D intensity plot of a beam at a given location along the beam path which indicates hot spots in the beam. Figure 4.15 shows the typical beam profile of the Excimer laser which is similar for both 308 and 248 nm wavelengths. As it can been from this figure, the short dimension has a Gaussian intensity distribution while the large dimension shows a top-hat profile which explains the different divergence values on these two axes.

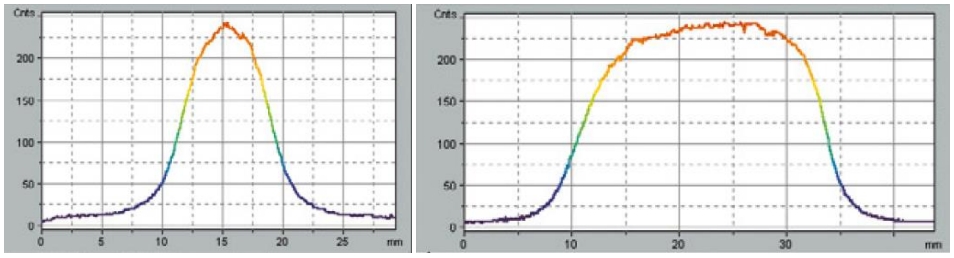

Figure 4.15 Typical beam profile of a 248 nm Excimer laser on X and Y axes [140]

[9] KrF laser pulse energy: Min=21.2 mJ, Max=22.21 mJ, Mean=21.74 mJ. Standard Deviation= 162 μJ – 0.74%

XeCl laser pulse energy: Min=40.99 mJ, Max=44.79 mJ, Mean=43.31 mJ. Standard Deviation= 819 μJ – 1.89%

The beam profile is an important factor in quantitative PLIF as its spatial variation result in false measurements. To reduce the spatial intensity fluctuations, different techniques have been exploited. In one of the most effective techniques, the output beam is split in several sections which are then overlapped in the focal plane of an imaging lens. This technique is usually based either on microlens arrays [141, 143], random phase plates [144], or a combination of these [145]. In this work, a set of calibration images were captured just before data images which were used to remove the spatial and temporal variation of the beam profile. This technique is explained in detail in chapter 6.

4.6 Two-line PLIF System Trigger-in Signal

For the engine-PLIF system synchronization, the And Gate Logic Box reference signal which triggers the ignition and injection systems was used to trigger the illumination and light capturing systems. This reference signal which is at 80 °CA bTDC compression stroke (it can be phase shifted to 80 °CA bTDC intake stroke) has 10 Hz frequency at engine speed of 1200 rpm. The Excimer lasers maximum repetition rate is also 10 Hz and therefore this signal can be used to trigger the lasers. But the PI-Max III camera readout frequency at full CCD (1024×1024 pixels) is 4 Hz. Therefore to be able to use the 10 Hz trigger-in signal for the imaging system, either a Region of Interest (ROI) should be assigned on the camera CCD or the imaging pixels binned together (at 2×2 to 16×16).

A Region of Interest (ROI) may be the entire CCD array (Full Chip) or it may be a rectangular sub-region of the array. The PI-Max III allows up to 10 ROIs (each with a different width and length) to be assigned on the CCD for data acquisition. However the actual size of the measurement area on the CCD is dictated by the optical lens aperture size and its focal length, and setting a smaller ROI results in shrinking the actual measurement area.

On the other hand in the binning process, the data from adjacent pixels (vertically or horizontally) are added up together to form a single (super) pixel. On the PI camera binning can be set up to occur during data acquisition (hardware binning) or after the data has been sent to the host computer (software binning). The hardware binning

improves the signal to noise ratio (SNR)[10] and as it is performed before the signal is read out by the preamplifier, the readout time and the load on computer memory are reduced. However this scarifies the resolution and may result in pixel saturation and blooming. The blooming (spilling charge into adjacent pixels) is due to fact that the shift register pixels typically hold twice as much charge as image pixels[11]. In this case the software binning can be exploited but this binning process is not as fast as the hardware binning and does not improve the S/N ratio while decrease the resolution.

An alternative technique was to use an external Counter/Divider unit that receives the 10 Hz engine reference signal and provides a trigger-in signal for the camera at lower frequencies. Therefore an electronic board was designed and built to meet this requirement. In order to use this Counter/Divider for the skip injection tests[12], the board was installed in the Dual Output Angle Delay unit that controls the air and fuel injectors of the Orbital direct injector.

[10] Pixel binning improves the SNR for low signal levels (readout-noise limited) linearly with the number of pixels grouped together and proportional to the square-root of binned pixels for large signals (camera is photon shot noise limited) [134].

[11] As the digital conversion factor of CCD used in the camera was 16 bits, it can convert the analogue signal into 2^{16} or 65536 digital steps. And any light intensity over this saturates the pixel.

[12] In the skip injection strategy the fuel injection takes place only on desired cycles which can be set on the Counter/Divider unit. The main application of this injection strategy is to reduce contamination of the optical windows, especially during the motoring operation with direct fuel injection.

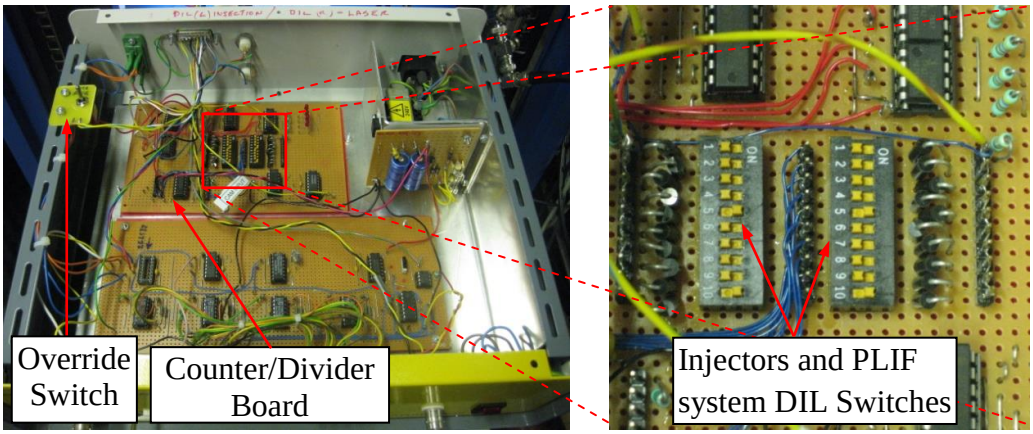

Figure 4.16 Counter/Divider Board Installed in the Dual Output Angle Delay Unit

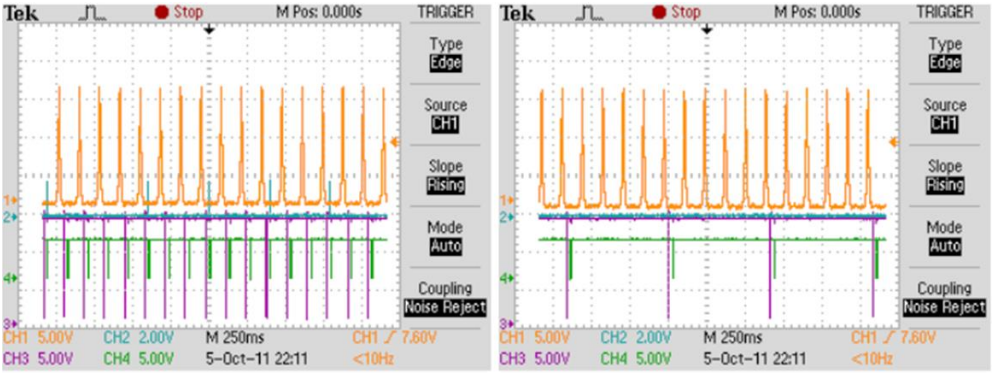

Figure 4.17 Oscilloscope screen shots, **Left**: override mode; continues injections; **Right**: 4 cycles OFF, 1 injection (yellow=pressure, pink=fuel injection green=air injection)

4.7 Time Budgeting and Synchronization

A precise PLIF measurement requires capturing two frames with delays of a few micro seconds. At the engine speed of 1200 rpm each crank angle takes 139 µs. The Excimer lasers pulse width and tracer fluorescence signal life time are 20 ns and few hundreds of nanosecond respectively. These numbers indicate that the diagnostic system should have an extremely high temporal resolution while precisely synchronized with the engine. Therefore an accurate study of signal delays within and between all the system's units should be carried out. Having calculated the total delay in the illumination[13] and light capturing systems (summarized in Table 4.), one

[13] To measure the "trigger-in signal to laser pulse" delay, each laser was triggered separately with the camera using a same signal from the delay generator. The delay

can synchronize them using external delay generators. For this purpose a DG535 Delay Generator and the Programmable Timing Generator (PTG) installed in the ST-133 Controller were utilised.

The Counter/Divider output signal was sent to DG535. The T_A and T_B were used to trigger the XeCl and KrF lasers respectively, while T_C was sent to the camera controller. The T_A to T_B delay was used to fire KrF laser after XeCl laser on desired moment and the delay between T_0 to T_A and T_C were used to activate the PLIF system for measurements at any interested engine crank angle. The PTG was used for adjustment of the camera gating time in both repetitive and sequential imaging.

Delay in Illumination System	
Delay in BNC cable from DG535 to lasers (4.9 ns/m [146])	34 ns (C)
Trigger-in signal to laser pulse delay in Excimer lasers without Charge on Demand (COD)	800 ns for XeCl (M) 1500 ns for KrF (M)
Laser pulse delay from laser out put the measurement area (3.3 ns/m)	20 ns (C)
Fluorescence signal delay from the measurement area to the camera CCD (3.3 ns/m)	5 ns (C)
Total delay	859 ns for XeCl 1559 ns for KrF
Delay in Light Capturing System	
Delay in BNC cable from DG535 to PTG (4.9 ns/m)	15 ns (C)
Trigger-in signal to start of gate open delay in PTG	25 ns (S)
Delay in cable from PTG to the camera CCD (4.9 ns/m)	22 ns (C)
Detector insertion delay	15 ns (S)
Total delay	77 ns
There is also 85 ns (S) internal delay between trigger-in to output pulse in DG535 and ±10 ns jitter for trigger-in to laser pulse for the Excimer lasers.	

Table 4.3 Delays in the 2-line PLIF System; (C)=Calculated, (M)=Measured, (S)=Device Specification

was measured using an ultra short gate width of 2 ns and varying the gate delay (on camera PTG) to see the start of illumination.

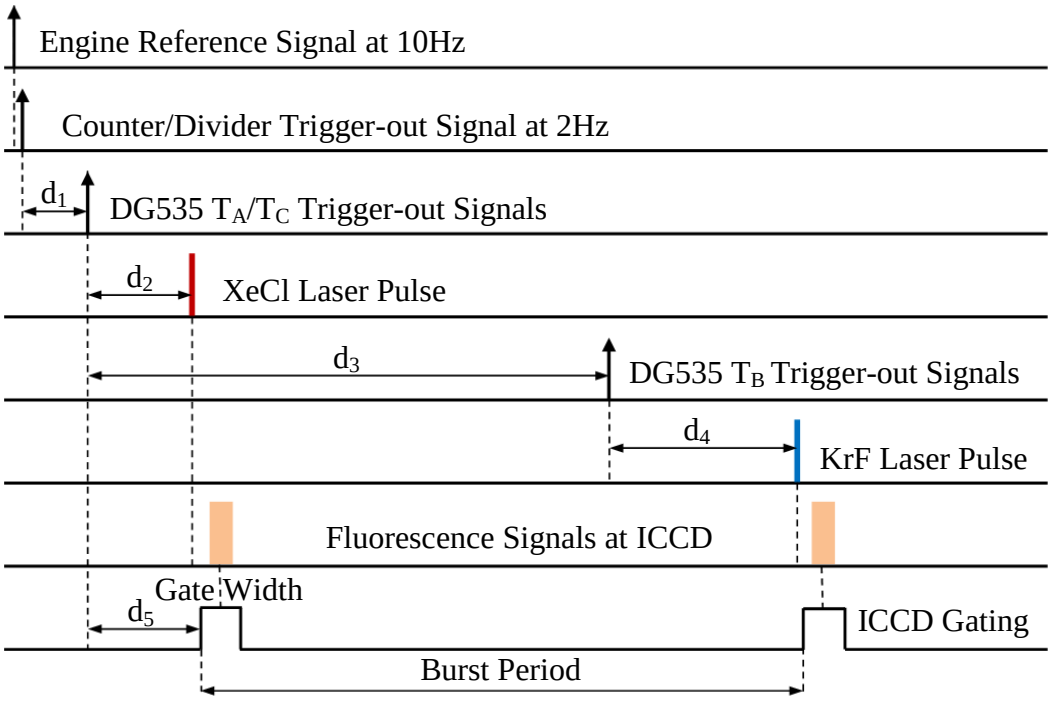

Figure 4.18 Timing diagram of various camera and laser events and adjusted delays for capturing a double image frame (DIF)**,** d_1= T_0 to T_A and T_C, d_2= delay at XeCl laser, d_3= T_A to T_B, d_4= delay at KrF laser, d_5= d_2 + delay at PTG

4.8 Engine Vibration Measurements

Although the engine runs steadily above 900 rpm during motoring operation, it was necessary to measure the engine horizontal and vertical vibrations and study their effects on the diagnostic system. For this reason the Memrecam fx-6000 high speed video camera was exploited. A piece of scaled paper was attached on the cylinder head above the sandwich plate optical access and illuminated with 250 W halogen lamp. The engine was motored at 1200 and 1500 rpm and the videos of 100 cycles were captured at 500 fps. A reference point was assigned on the scaled paper and its vertical and horizontal displacements were measured in the captured frames using a MATLAB program. The horizontal and vertical displacements were calculated as ±120 μm and ±230 μm (respectively) at 1200 rpm and as ±110 μm and ±230 μm (respectively) at 1500 rpm. This engine vibration does not affect the 2-line PLIF measurements as it exploits ultra-short gate widths for imaging.

4.9 Improving Two-line PLIF Imaging Quality

Following some preliminary CVC calibration tests, it was found that the DIF (Double Image Frame) mode of the PI MAX camera introduces a noise on captured images. Also it was discovered that the light reflection from the combustion chambers' roof and cylinder walls affected the quantitative measurement. Therefore it was necessary to remove these sources of interference before proceeding to the motoring and firing tests.

4.9.1 Eliminating DIF Mode Noise

As for the temperature and EGR measurements it was required to capture two images in a rapid succession and hence the camera should be set at the Double Image Frame (DIF) mode. However it was found that changing the gating mode from the Interline to DIF introduces a strong noise on images. Figure 4.19 shows the level of this noise on the first and second images of a single DIF. This pair of DIF was captured using both lasers while the WG360 filter was removed.

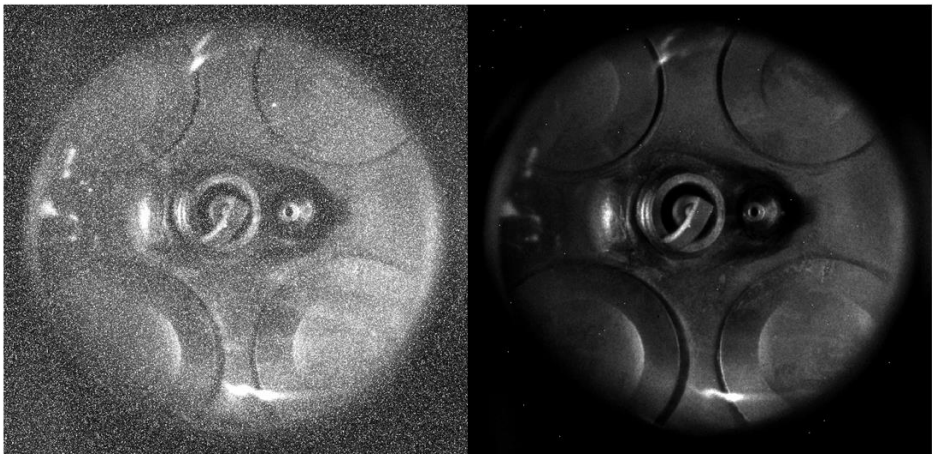

Figure 4.19 Noise level on the first (left) and second image (right) of a single DIF

After different experiments and investigations, it was discovered that the noise was due to ST-133 controller fault and was related to the PTG trigger-in signal. It was found that triggering the PTG with odd frequencies (e.g. 1 Hz, 3 Hz, etc.) or frequency with decimal values (e.g. 1.2 Hz, 3.5 Hz, etc.) introduces the noise and that this could be easily avoided by using trigger-in signals at even frequencies (e.g. 2 Hz, 4 Hz, etc.). To quantify this noise, 40 DIFs were captured (while the camera

lens was covered) at six different PTG trigger-in frequencies. The DIFs were divided into two stacks of even and odd images and the noise level was investigated for both averaged image of each stack and the first image of each DIF series. The first image of each DIF series had a relatively higher noise compare to other images. This was due to dark charge accumulated on the CCD and consequently had a higher value at lower trigger-in frequencies. Both the averaged and single images (SPE format) were converted to unit 8 TIFF format and processed in MATLAB. The TIFF files (with pixel intensities between 10 to 245 counts) were binarised by 'greythresh' function using Otsu's method. And number of non-zero pixels which represent noise were counted and compared.

PTG trigger-in frequency (Hz)	Number of non-zero pixels (average of 40 images) in full CCD	Number of non-zero pixels (first image) in full CCD
10	138	201
5	276	300
4	137	332
2.5	399	420
2	137	492
1	540	95078

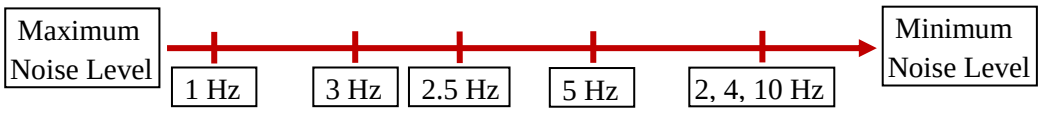

Figure 4.20 DIF noise level dependency on PTG trigger-in signal frequency

4.9.2 Eliminating Unwanted Wavelengths

Although the PLIF light capturing system was designed and optimised to capture the fluorescence signal (inelastic scattering from the tracer molecules), it also sees other types of scattering. Therefore it was required to study different sources of scattering that may affect the measurements.

Figure 4.21 shows the regimes of Mie, Rayleigh and geometric scattering which all are elastic scattering as the wavelength of the scattered light is the same as the incident light (in this case Excimer lasers). These regimes are defined by

$$x = \frac{2\pi r}{\lambda} \tag{4.18}$$

where 'x' is a non-dimensional size parameter, 'r' is the radius of a scattering particle and 'λ' is the wavelength of the incident radiation. Knowing the size of the in-cylinder particles, one can associate its relative scattering type and study its influence on the measurements. For a UV excitation source, the most dominant scattering type for the 'x' values is shown in Table 4.4.

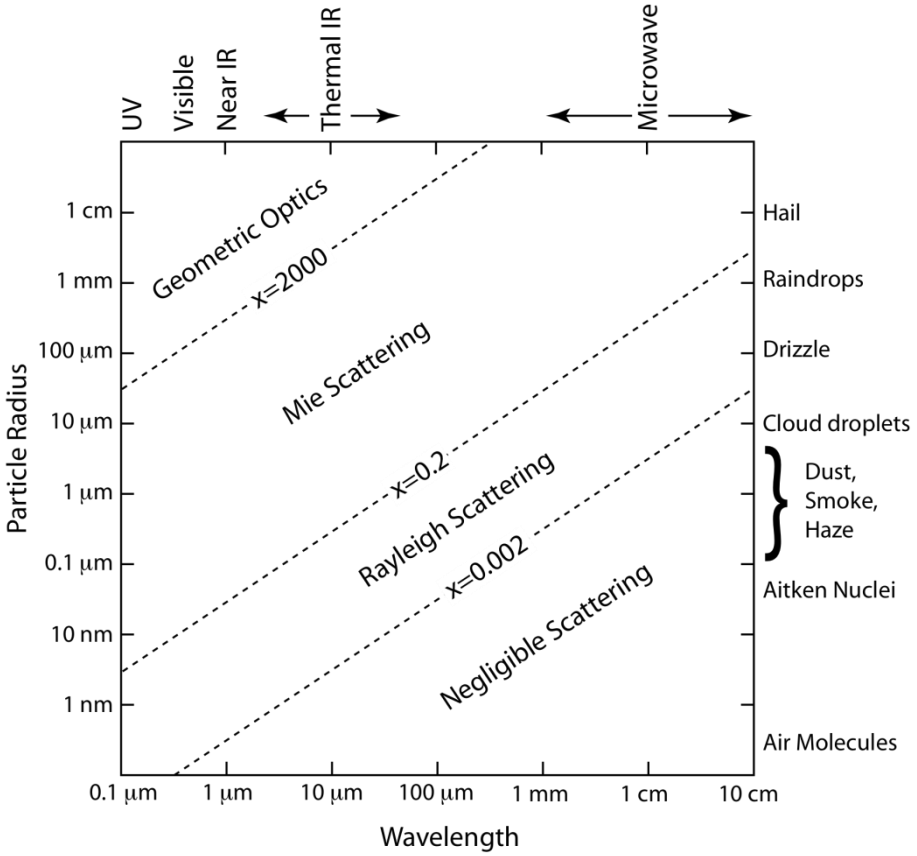

Figure 4.21 Scattering regimes [147]

Size parameter	Scattering Particles	Most dominant scattering
$x << 1$	Gas (nm)	Rayleigh scattering
$x \sim 1$	Liquid (µm)	Mie scattering
$x >> 1$	Cylinder wall (cm)	Geometric scattering

Table 4.4 Most dominate scattering type of different particle size parameter regimes

As it is described in Chapter 2 the relative signal intensity for each scattering type depends primarily on the differential cross section. By comparing the differential cross section of each scattering it is obvious that the Mie and geometric scattering signal intensity are much stronger than the fluorescence signal and can significantly affect the diagnostic system. The post processing techniques such as background subtraction cannot eliminate all these light sources on their own and therefore they should be combined with appropriate techniques during the data acquisition.

As the fluorescence signal has a different wavelength from elastic scatterings, it was possible to reduce the intensity of the elastic scatterings by placing a proper optical filter in front of the camera lens. However a single filter cannot completely block all unwanted wavelengths and using couple of filters in a series reduces the fluorescence signal intensity. As a result, other techniques should be applied for further reduction of unwanted wavelengths.

4.9.3 Eliminating In-cylinder Reflections

To reduce in-cylinder reflections, the cylinder head is usually tinted with high temperature resistance (HTR) paints or covered with soot or anodized. As the latter method is an expensive and time consuming technique, it was decided to compare the HTR paint with the candle soot.

For this experiment a small section of a thin aluminium sheet was covered with HTR paint and a strip of candle soot was deposited near the painted area (Figure 4.22). The aluminium sheet was then illuminated with both Excimer lasers at different pulse energies and the reflection was recorded by the PI-Max camera. It was found that candle soot is a suitable choice as it can significantly reduce reflections for incident beams with pulse energies below 50 mJ while the HTR paint, red shifts the Excimer lasers' wavelength and requires a different band pass filter.

The other technique which was utilised to reduce in-cylinder reflections was focusing laser sheets behind the cylinder block. Figure 4.23 compares two different alignments for up to two internal reflections. As it can be seen, focusing laser beams behind the cylinder block can significantly reduce the internal light scattering. This alignment can be achieved by placing the cylindrical lens closer to the engine or

exploiting a lens with a longer focal length. The later was utilized in this work due to engine position relative to the optical table.

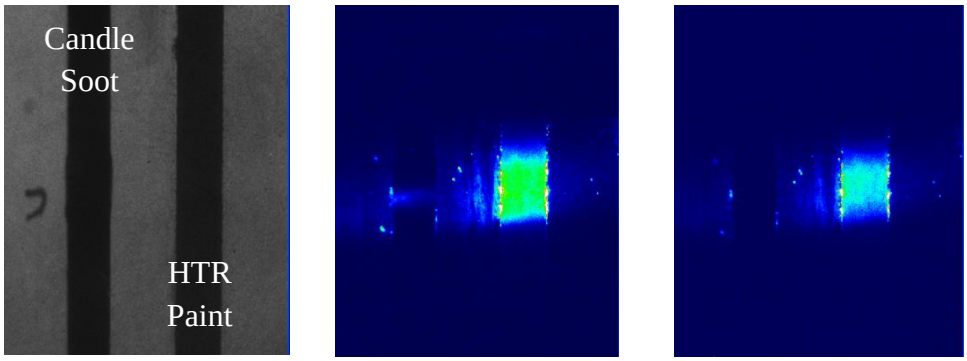

(**a**) (**b**) (**c**)

Figure 4.22 Comparison of the candle soot and HTR paint reflection for incident beam at 308 nm with pulse energy of (b) 50 mJ, (c) 25mJ

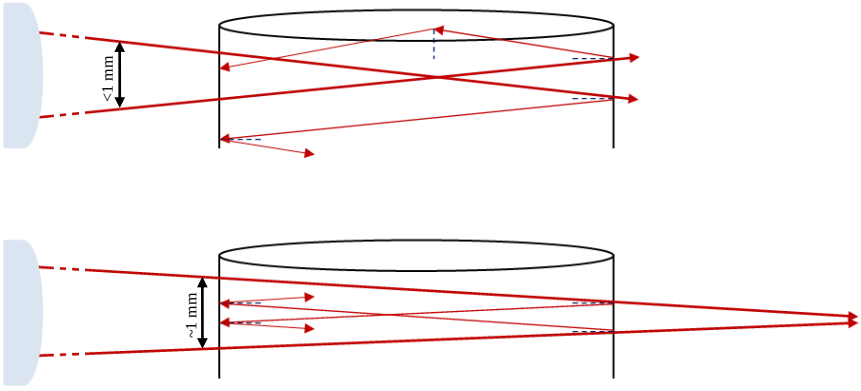

Figure 4.23 Comparison of up to two internal reflections of the laser sheet inside the engine for the sheet focused, **Top**: Inside the cylinder; **Bottom**: Behind the cylinder

It should be noted that another powerful tool for eliminating unwanted light sources is the camera CCD gating. As the fluorescence signal life time is in the order of few hundreds of nanosecond, it was possible to significantly reduce the non-fluorescence light intensities by shortening the gate width and triggering the camera on a precise moment. This technique has also been exploited in conjunction with above mentioned methods throughout this work.

4.9.4 Eliminating CCD Accumulated Dark Charge

The PI-Max CCD array captures a signal of interest only when the intensifier is being gated to take an exposure by the controller. However as soon as the CCD array is connected to the controller even with the photocathode being biased off, dark charge –thermally induced charge– will be accumulated on the array. To counteract this, the array temperature should be reduced as much as possible. In this work before each data acquisition, the CCD temperature was set to -20 °C (lowest temperature possible for the test conditions) and enough time was allowed so the internal Peltier device could fix the array temperature at the setting value. Also clean cycles were programmed on the controller to repeatedly shift and discard any integrated signal on the array while the intensifier is waiting for Start Acquisition command. For further reduction of accumulated charge it was possible to set the camera to perform a final clean cycle just before exposure begins. However as this technique delays[14] the start of exposure, it was not applied during DIF operation. Table 4.5 summarizes the above mentioned techniques that have been exploited in this work to enhance the 2-line PLIF SNR.

1.	Exploiting appropriate band pass filter
2.	Avoiding Mie scattering from fuel droplets by considering injection timing and droplets life time
3.	Covering the cylinder head with candle soot
4.	Focusing laser sheets behind the cylinder block
5.	Fine adjustment of the ICCD gating time, and exploiting extra short gate durations
6.	Operating the camera at the lowest CCD array temperature (-20 °C)
7.	Utilising the CCD clean cycles
8.	Background subtraction during image post processing

Table 4.5 Summary of techniques used in this work for improving the 2-line PLIF signal to noise ratio

[14] This delay depends on the number of strips on the CCD that are set to be emptied on each clean cycle.

4.10 Raman Convertor Conversion Efficiency Measurements

In order to measure the conversion efficiency of the Raman Convertor (RC) used in 2-line PLIF setup, a series of tests were carried out on the vessel. The Raman convertor was filled with grade 5 hydrogen (BOC Special Gases, purity 99.999%) at 55 bar (800 psi) at the outside facility (described earlier in this chapter) and brought into the lab cell. The KrF laser was used to pump the RC at 10 Hz repetition rate with different pulse energies. In order to measure the conversion efficiency of the 1st Stoke of H_2 (conversion of 248 nm to 277 nm), it was required to eliminate the pump beam as well as the higher Stokes and anti-Stokes from the RC output. Two techniques could be applied for this purpose; the first technique exploits three HR coated mirrors at 277 nm while the second technique utilizes angular deviation of a dispersive prism.

Figure F.1 in Appendix F shows reflectivity versus incident beam wavelength of a 277/633 nm HR coated mirror. As it can be seen in this figure the reflectivity of this mirror drops from 99% at 277 nm to less than 30% below 250 nm and above 320 nm. Therefore it was possible to significantly reduce the pump beam at 248 nm and unwanted Stokes and anti-Stokes beams by placing three such mirrors before the pulse energy meter, which could be done by simple rearrangement of the beam delivery system. In the second technique the spectral filtering of the unwanted laser beams was achieved by placing the equilateral dispersive prism in front of the RC exit window and sending the laser beam into a relatively long optical path which allows the angular deviation of the prism to separates all the wavelengths in the RC output pulse. The minimum required optical length can be calculated from the Snell's Law (Eq. 4.9) and Sellmeier equation (Eq. 4.12).

Figure 4.24 shows the setup arrangement of the test. The Raman convertor was connected to the exhaust line through the Fill Valve Assembly and Quick Connector. This was to release H_2 into a vented area and perform the measurements at different fill pressures without moving the RC and rearranging the optics.

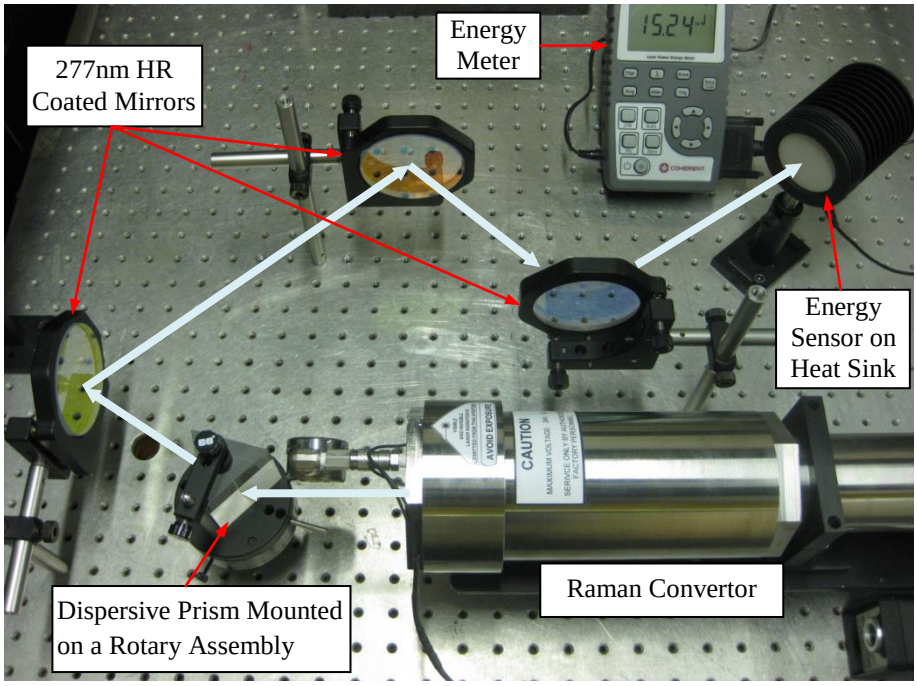

Figure 4.24 Raman convertor conversion efficiency measurements test setup

The H_2 pressure was reduced from 55 bar (800 psi) to 7 bar (100 psi) in 3.5 bar (50 psi) increments and at each step the KrF pulse energy was varied from 350 mJ to 150 mJ in 50 mJ increments. The output pulse energy at 277 nm and its standard deviation were measured and recorded using the FieldMax TOP pulse energy meter and its software installed on the host computer.

4.10.1 Results and Discussions

Figure 4.25 shows Raman convertor output pulse energy at 277 nm as a function of KrF laser input pulse energy at 248 nm at different fill pressures. The output of the Raman convertor was measured after eliminating unwanted higher Stokes and anti-Stokes. As it can be seen from this graph the RC output pulse energy increases with increase in both the pump pulse energy and H_2 fill pressure. However highest conversion efficiency of 13% achieved at the lowest pump energy (150 mJ) while it dropped to 10% at 350 mJ. Also the minimum required H_2 fill pressure was found to be 24 bar (350 psi).

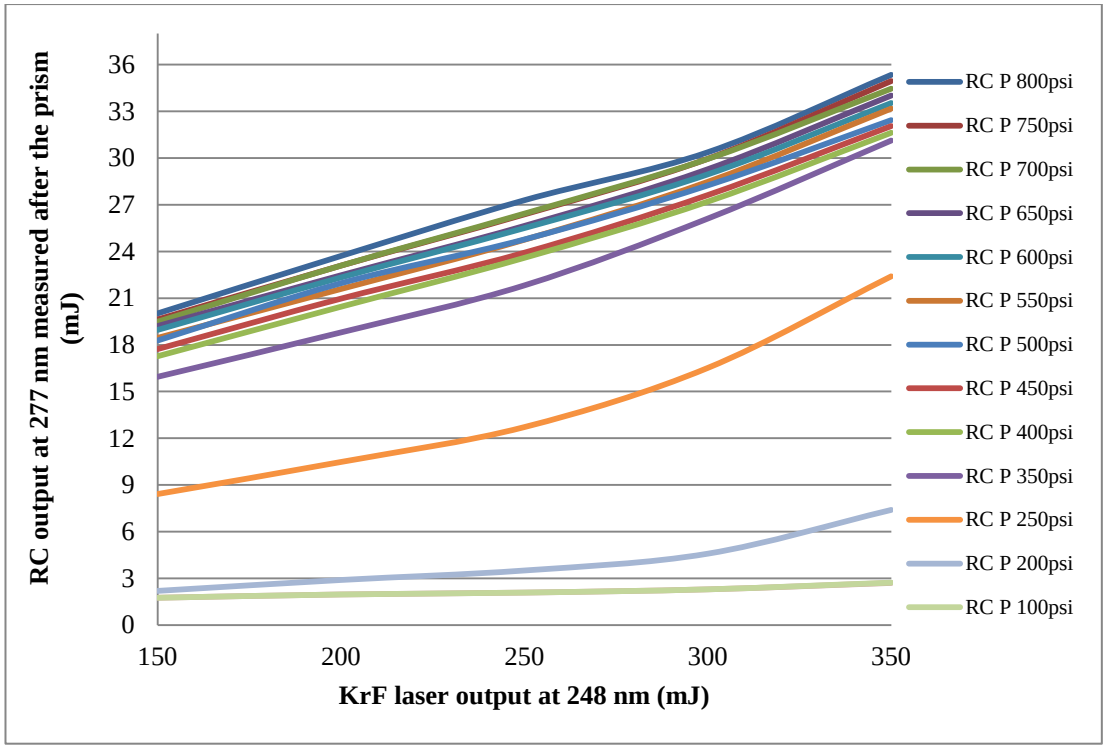

Figure 4.25 Raman convertor output pulse energy at 277 nm as a function of pump pulse energy and RC fill pressure

As the above measurements were performed after the prism, it was required to investigate effects of the prism on the results. Although both the RC optics and the prism exploited anti-reflection (AR) coatings at 248 and 277 nm respectively, measurements showed a 6% pulse energy reduction at the RC and additional 8% reduction at the prism. In case of prism there was 3% reduction due to external reflection at the first surface, 3% internal reflection at the second surface plus 2% reduction due to light absorption and scattering inside the prism. Consequently considering these losses, the actual RC conversion efficiency was found to be 12 to 15%.

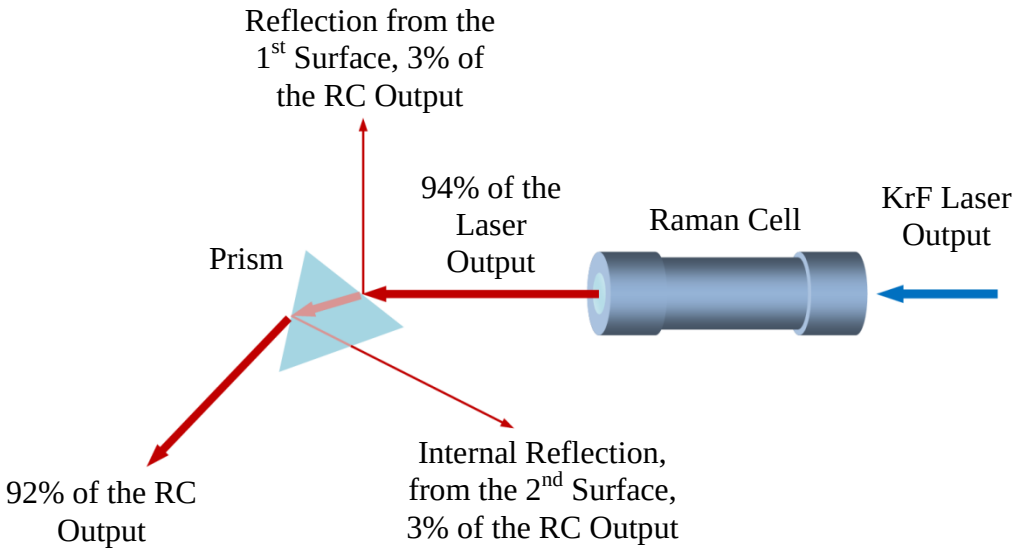

Figure 4.26 Output pulse energy reduction at RC and prism

Furthermore it was required to study and compare the RC output pulse energy variation with the KrF output. An energy sensor was placed right after the RC and energy variation of 200 shots at selected laser output pulse energies and RC fill pressures were measured. It was observed that increase in the KrF output pulse energy to up to 300 mJ reduces the RC output pulse energy fluctuation, which was due to the fact that the laser resonator operates in a more stable high voltage (HV) range. Also as it can be seen in Figure 4.27, increasing the RC fill pressure can further drop the RC output energy fluctuation to the laser limit.

As a result of the abovementioned tests, the RC was filled with H_2 at 55 bar (800 psi) for all the tests in this work as this high pressure can:

a. provide the maximum Raman conversion efficiency
b. provide the lowest output pulse energy fluctuation
c. suppress the unwanted higher Stokes and anti-Stokes [148-150]

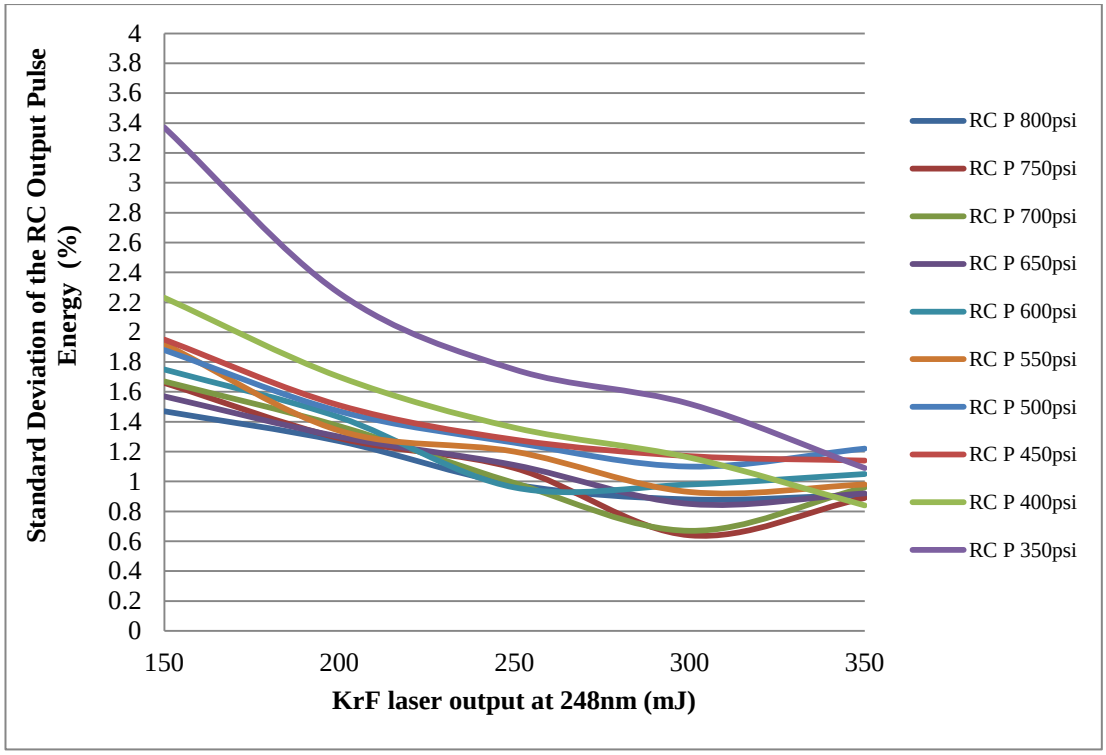

Figure 4.27 RC output pulse energy variation as a function of pump pulse energy and fill pressure

4.11 Summary

This chapter has included the background theory and implementation requirements for the 2-line PLIF technique. Description of the light sources, imaging systems and ancillary optics were presented. Due to the importance of the light illumination systems on the PLIF measurements, a study of Excimer laser beam characteristics has been carried out. Synchronization of the diagnostic technique with engine crank angle and time budgeting were discussed. Comprehensive description of different techniques utilized in this work to remove the DIF mode noise, unwanted wavelengths, in-cylinder reflections and the CCD dark charge was presented. Furthermore, the experimental setup and test procedure for engine vibration and Raman convertor conversion efficiency measurements were described.

Chapter 5
Calibration and Validation Measurements

5.1 Introduction

This chapter provides detailed description of the concept design and manufacturing of the constant volume chamber including its heating system, thermal insulation and tracer supply system. The experimental setup and test procedure for temperature calibration measurements using the constant volume chamber are explained and the results are discussed. In-cylinder charge temperature is calculated using in-cylinder pressure data. The experimental setup and test procedure for measurements of the average in-cylinder charge temperature for both motoring and firing runs are presented and results are compared and validated with the temperature values obtained from in-cylinder pressure data.

5.2 Constant Volume Chamber

For quantitative 2-line PLIF measurements it was required to calibrate the laser diagnostic system so the relation between the fluorescence signal intensity ratio of two beams and the temperature of the sampling area could be determined. This could also be done using theoretical models developed for the fluorescence quantum yield and absorption cross section of the tracer. However it was found that although extensive studies have been carried out to identify photo-physical properties of 3-pentonone, the tracer used in the PLIF measurement, these models still require further validation and adjustments. On the other hand, an experimental calibration technique that exploits same optics as in the measurement could provide the most accurate results. Therefore it was decided to design a Constant Volume Chamber

(CVC) and simulate the engine motoring conditions for the most precise calibration measurements.

An ideal chamber can simulate the in-cylinder thermodynamic state by adjusting variables such as temperature, pressure and volume. However design and manufacturing of such a device is not straight forward and will be expensive to make. Also some of these thermodynamic parameters have negligible effect on the tracer fluorescence signal. A constant volume chamber with a working pressure of up to 3 bar and maximum temperature of 850 K was designed and manufactured at the Brunel University workshop. The pressure and temperature upper limits were imposed by the safety factor and the CVC material (aluminium with melting point 933 K). The chamber was designed to exploit the same optical components (side windows and piston window) as the engine. This was to reduce the overall cost and to have exactly the same optical properties for both the engine and chamber. Of these optical properties, the light transmission efficiency and surface flatness[1] are of paramount importance. Both of these two parameters can alter the signal intensities on the CCD and result in false measurements [151]. The other factor considered in chamber design was that it allows calibration measurement to be performed with the same 2-line PLIF setup as the engine measurements.

[1] An optic with a bad rating on surface flatness introduces some wave-front distortions, resulting in aberration and power drop. This power drop is expressed by the Strehl ratio (ratio of the observed peak intensity at the image plane compared to the theoretical maximum peak intensity) which is given by [152, 153]

$$Strehl \cong 1 - (\frac{2\pi}{\lambda})^2 \, rms^2$$

where *rms* is the root mean square value of the surface flatness.

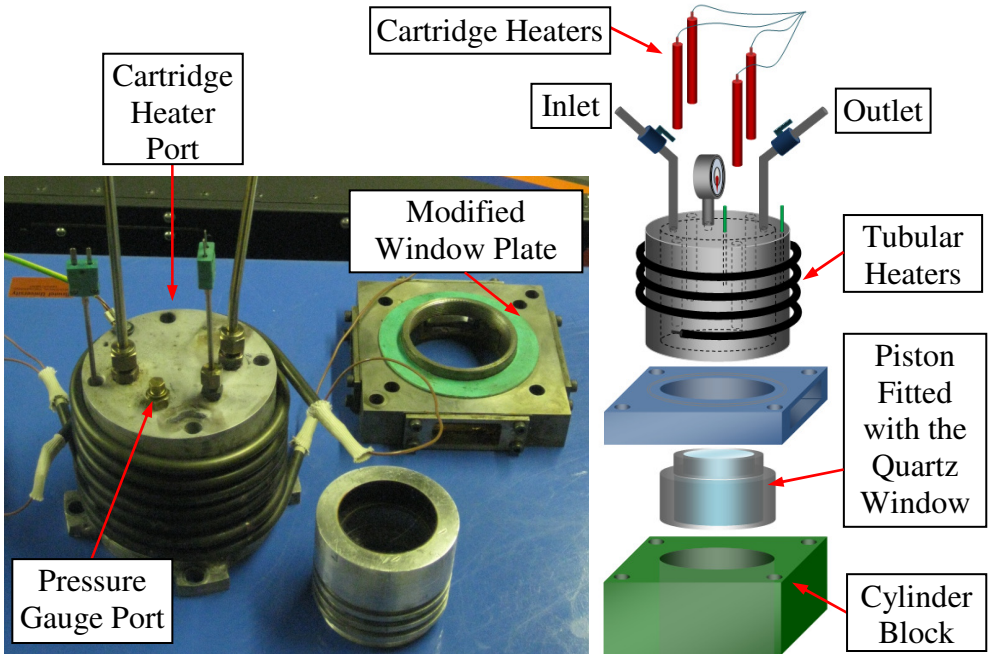

Figure 5.1 Constant volume chamber components

As can be seen in Figure 5.1, a spare aluminium piston crown and a steel sandwich plate redesigned and modified for the CVC assembly to ease the manufacturing effort. A quartz window with the appropriate gasket combination (as described in section 3.3.5) was fitted into the piston crown. The modified piston crown was then screwed to the sandwich plate (using PTFE tape for sealing) and the plate was mounted on the cylinder block. A Klinger TSM-AS graphite gasket (2 mm thickness) was place on the sandwich plate to seal and provide thermal insulation between the chamber and plate[2]. Then the chamber was placed on the graphite gasket and bolted to the cylinder block.

Using the same engine components on the CVC allowed the same piston window and side windows to be used on both the CVC and engine. Also the CVC assembly was designed so it can be mounted on the cylinder block using the cylinder head bolts. Therefore the calibration measurements can be performed right after disassembling cylinder head without requirements for any adjustment to the PLIF setup including the laser sheets and camera.

[2] This gasket has an outstanding heat resistance (460 °C in oxidising atmospheres, 3000 °C in non-oxidising atmospheres) and a good leakage property also the anti-stick finish on its both sides makes it an ideal gasket for this application.

5.2.1 Heating System

The CVC heating system consists of four cartridge heaters (12.5×100 mm, 250 W) and two tubular heaters (heating element, 1 kW). Three holes were drilled in the chamber's wall to house the cartridge heaters. The tubular heaters were wrapped around the chamber. To minimize the gap between tubular heaters and chamber wall, the heaters were first tightly fit around the chamber and then switched on to expand to their full length and were tightened up again. A separate control unit (West 6100 solid state temperature controller) was made for each of two types of heater to set the desired temperature. Three K-type thermocouples were installed on the CVC. Two were placed into the chamber wall to monitor the wall temperature and provide feedback to the controllers. The third thermocouple was placed in the middle of the cavity inside the chamber for the gas temperature measurements. Three ports were machined on the top of the chamber, to allow gas flow in and out of the cell and to connect the pressure gauge.

5.2.2 Thermal Insulations

For safety as well as to be able to reach the maximum temperature in a short time, it was necessary to use a suitable insulation system. A thin (0.5 mm thick) copper foil was wrapped around the chamber before fitting the tubular heaters. By shaping this copper foil after installation of the tubular heaters, it was possible to increase the surface contact. Also the copper foil could distribute the heat more evenly on the CVC wall and prevents the excess heat transfer to a point. Then the tubular heaters were covered with a thick (1.5 mm) copper sheet. This was to hold the heaters around the chamber and to prevent the heaters' bits to fly around if the heaters brake into pieces. Then four layers (0.5 cm thickness) of Rockwool were used to insulate the copper sheet and a fibre glass tape was used to hold these layers and to provide extra thermal insulation as well as protection. The fibre glass tape was heat, flame and fire resistant and could withstand continuous exposure to high temperatures.

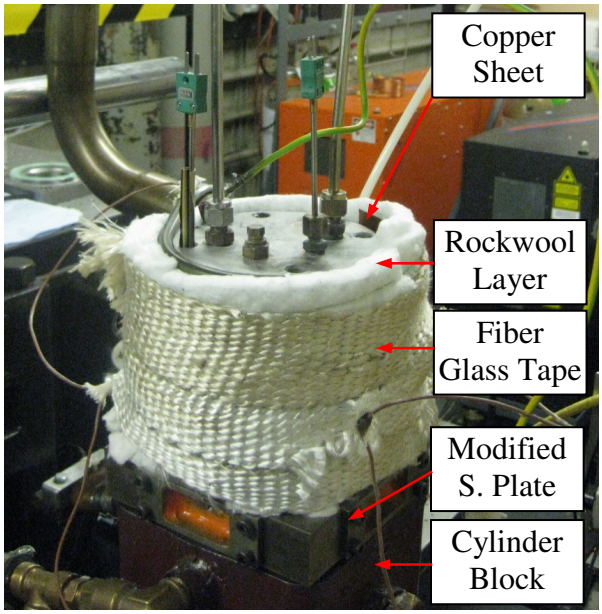

Figure 5.2 Insulation layers of the CVC assembled on the cylinder block

5.2.3 Tracer Supply System

The initial plan was to provide batches of seeding to the CVC during each calibration measurement. But due to the fast decomposition of the tracer at high temperatures and leakage this was not a practical technique. Therefore, the engine fuel/tracer supply system was modified with a simpler and easier arrangement to provide a continuous homogenous mixture of the tracer and bath gas. In this configuration a second tank was filled with liquid 3-pentanone, three cartridge heaters were used to heat up (318 K) and evaporate the tracer inside the tank, the bath gas bottle (air or N_2) was connected to the bottom of this tank through a second regulator. By setting the bath gas pressure and adjusting the inlet and outlet valve openings on the chamber, one can introduce a homogenous mixture of the tracer and the bath gas into the chamber. As the tracer partial pressure is a function of temperature it was possible to increase or decrease the tracer mole fraction by applying different temperature to the tracer tank.

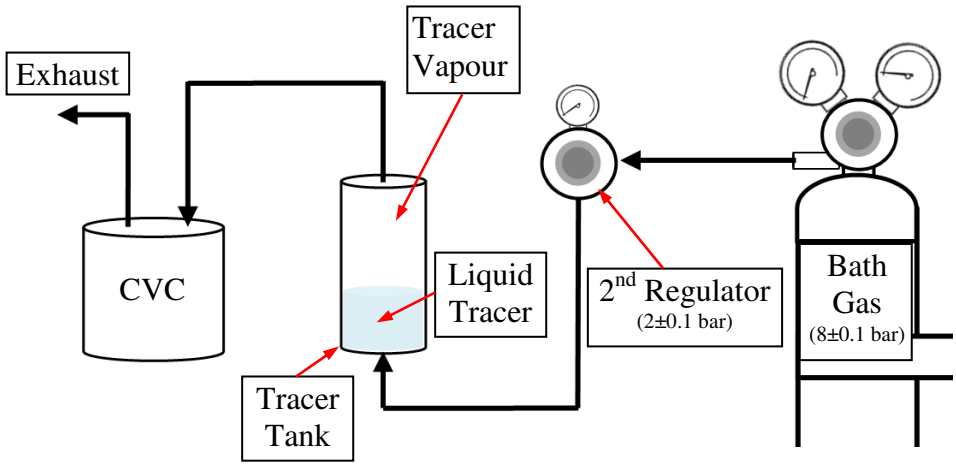

Figure 5.3 Tracer supply system

5.3 Constant Volume Chamber Temperature Calibration Measurements

5.3.1 Experimental Setup and Test Procedure

For quantitative temperature measurements it was required to calibrate the 2-line PLIF signal intensity. This was accomplished by a series of tests on the constant volume chamber (CVC) to determine the temperature dependency of fluorescence signals at both excitation wavelengths. To ensure both Excimer lasers experience minimum pulse to pulse variation throughout the measurements, their resonators were flushed and filled with the fresh premix gases prior to each test. Then they were run continually for a few minutes, this allowed the resonators to reach a stable temperature which in turn fix the output beam direction. Using a low power (4 mW) HeNe laser the optical components of the beam delivery system were approximately aligned to steer the Excimer lasers output to the CVC. Then for the fine alignment, Excimer lasers were triggered at 1 HZ repetition rate (once at a time) and the optical components were aligned so they could provide two precisely spatially overlapped horizontal laser sheets with thickness of <0.5 mm at the measurement plane. By attaching scaled papers on the CVC's inlet and exit windows it was possible to check if both laser sheets have a same height and to see if they cross the measurement plane parallel to each other.

It should be noted that it was always required to check the Excimer lasers resonator's mirrors alignment. This can be done by using a beam profiler or simply by placing a

thermal fax paper right after the laser beam shutter. In the latter technique, the laser beam burns a region on the fax paper that represents its exact geometry. If any variation from the original rectangular shape is observed, then the resonator mirrors should be aligned. Also as the light delivery system exploits number of optics in a quite complex geometry the rectangular shape of output beam can be easily changed at the end of the light delivery system. Therefore it was important to check the lasers beam profile right before the measurement area to ensure a homogeneous illumination of the region of interest.

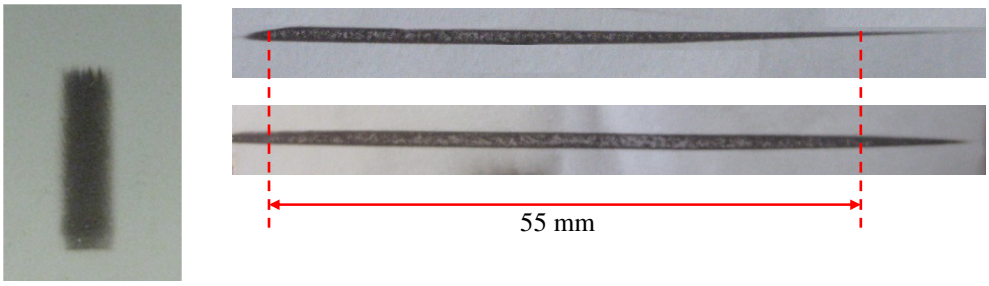

Figure 5.4 Left: Excimer laser pulse rectangular shape (right after the beam shutter) burned on a thermal fax paper; **Right**: Laser marks at the end of the beam delivery system for; **Top**: Poorly aligned beam; **Bottom**: Accurately aligned beam

After a fine alignment of the laser sheets, the Excimer lasers output pulse energy were set and their shot-to-shot variation were investigated as described in Chapter 4. The UV Nikkor lens (*f*/4.5, 105 mm) was mounted on the PI-MAX camera head and focused using the camera Shutter Mode and a 200 W halogen lamp for illumination. For the fine focus of the lens, one of the sandwich plate metal dummies were removed and a transparent ruler was placed inside the chamber at the same level as measurement plane (shown in Figure 5.5) and the lens was focused on the ruler. Then the Schott WG-360 longpass (LP) filter was mounted on the lens and the camera mode was changed to the Double Image Frame (DIF) with a gate width and burst period[3] of 1 µs and 30 µs respectively. Considering the Excimer lasers' delay (trigger-in signal to laser pulse) of 0.8 µs and 1.5 µs for XeCl and KrF respectively, a 29.3 µs delay was set between the XeCl and KrF trigger-in signals on DG535 for

[3] gate delay between two images

the above mentioned DIF timing. For brevity, other signal delays and imaging parameters are presented in Table G.1 in Appendix G.

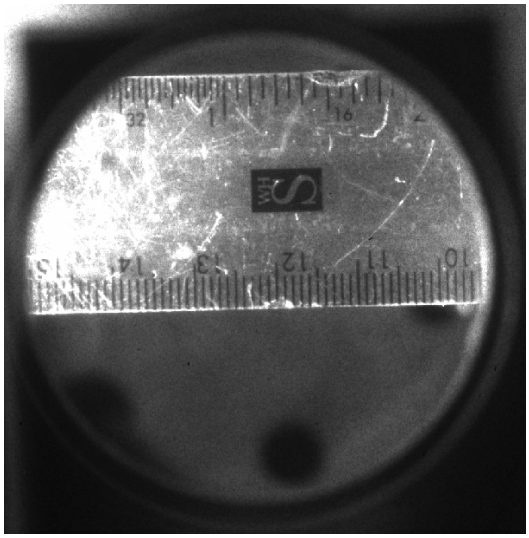

Figure 5.5 UV Nikkor lens focused on the measurement plane inside the CVC

The CVC was assembled and sealed as described earlier in this chapter and the tracer supply and exhaust lines were attached to the chamber. The tracer tank was filled with 200 ml of 3-pentanone (98% purity research grade, Sigma-Aldrich). A set of 40 background images (20 at 277 nm excitation and 20 at 308 nm excitation) were captured prior to seeding the chamber at the room temperature. Then the CVC cartridge and tubular heaters and tracer tank heater were switched on. The tracer tank regulator was set to 2 bar and the inlet valves were opened to deliver the tracer vapour mixed with nitrogen (99.995% purity research grade) to the chamber. The 2-line PLIF images were captured from room temperature up to 750 K with 10 K increment. In order to have enough time for imaging at each selected temperature, the CVC heaters' temperature was increased gradually in steps. However the temperature rise was still too fast for the imaging system (as the camera run at 4 Hz, it takes 10 s to capture 40 images on interline mode and ~ 7 s on DIF mode). It was found that it is better to heat up the CVC to the maximum temperature and then switch off heaters and start the PLIF measurements as the temperature drops. As the CVC temperature drops much slower than it goes up, this technique reduced temperature variation at each set of images from 2-4 K to less than 0.5 K.

5.3.2 Results and Discussion

The PI-MAX camera is programmed through WinView 32 software. It stores the captured images on the host computer with '.SPE' extension (a CCD image format used by Princeton Instruments). Although the WinView 32 is a powerful software in data acquisition, it has not fully been developed for post processing applications yet. Consequently some of the data processing steps throughout this work were carried out using separate macros programmed in Visual Basic, which are presented in Appendix H. Diagram 5.7 shows the data processing algorithm exploited for the CVC temperature calibration curve calculation. As was described earlier, two sets of background and data images were captured at each measurement point. The first macro code divides a single DIF stack of 40 images into two stacks of even images (laser illumination at 277 nm) and odd images (laser illumination at 308 nm). The second macro code gets the average of both even and odd stacks. Then the averaged background stacks were subtracted from their averaged data stacks. A region of interest (ROI), 600×600 pixels, was defined on the CCD and pixel values within the ROI were averaged. Finally the ratio of two averaged fluorescence signals was calculated.

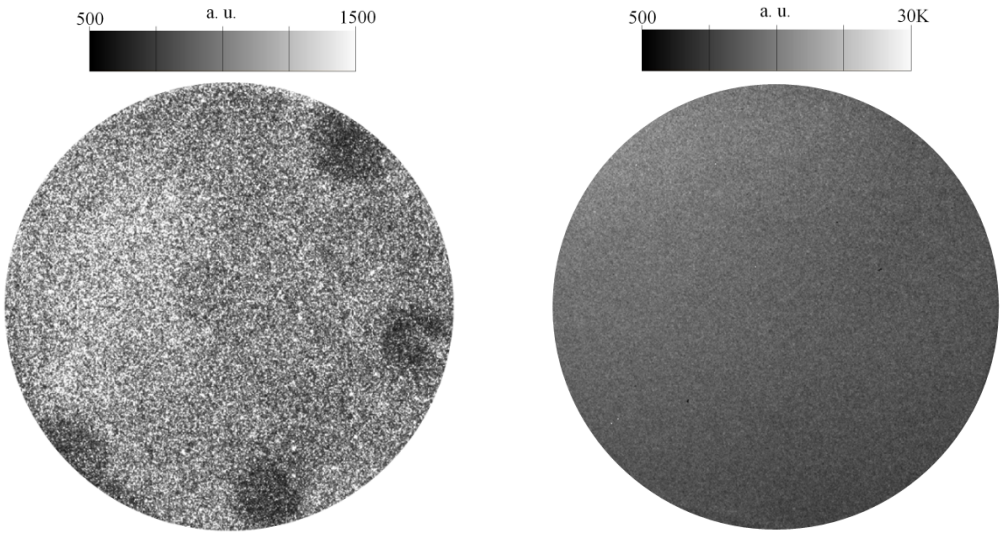

Figure 5.6 Left: single-shot background image **Right:** single-shot data image

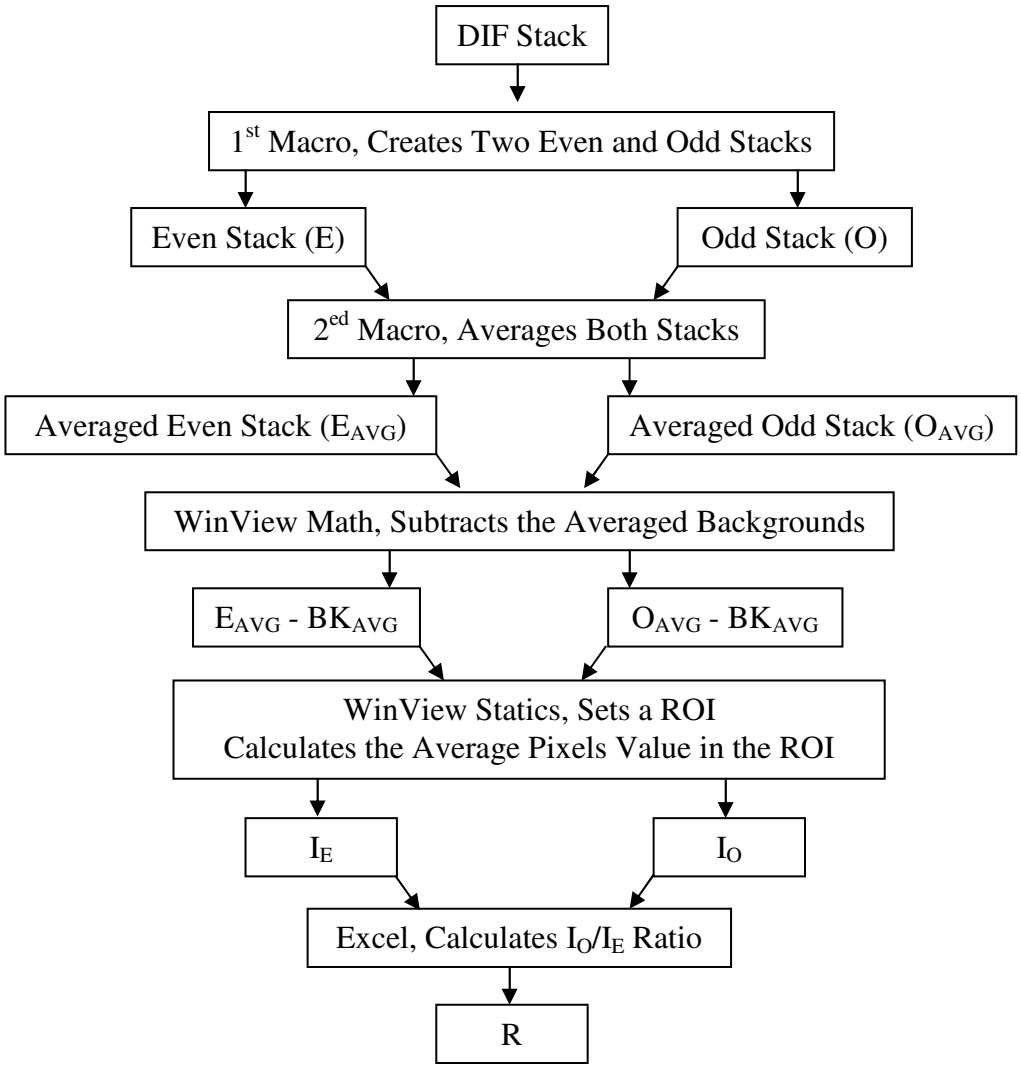

Figure 5.7 Image processing algorithm for the CVC temperature calibration curve

Figure 5.8 shows a sample CVC temperature measurement result. The red and blue markers represent fluorescence signal intensity as a function of CVC temperature for laser illumination at 308 nm and 277 nm respectively. The fluorescence signal intensity at each data point was calculated using the above-mentioned image processing algorithm. The temperature calibration curve was obtained by calculating the signal intensity ratio at each data point (green markers), and fitting a trend line (linear) on the data.

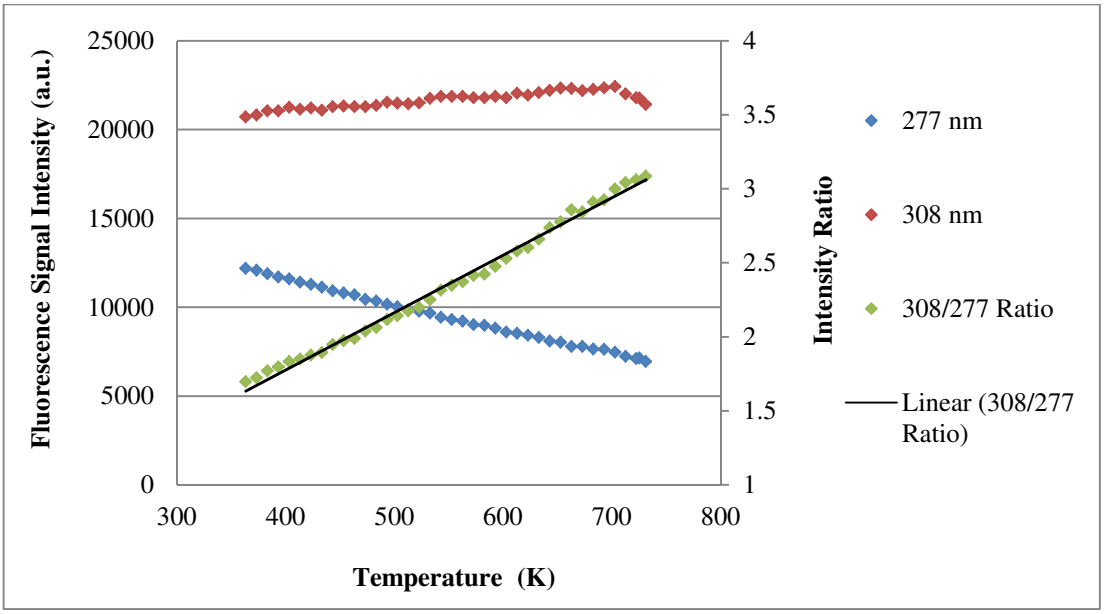

Figure 5.8 Two-line PLIF sample CVC temperature measurement result

It was observed that while the fluorescence signal intensity for the excitation at 277 nm (I_E) dropped as the temperature went up, the fluorescence signal intensity for the excitation at 308 nm (I_O) slightly increased. The test results showed a very good agreement with models recently developed for 3-pentanone which can be explained by simplifying Equation 4.6 as

$$S_f \propto \frac{1}{T}\sigma(\lambda,T,P,X_{tr})\phi(\lambda,T,P,X_{tr}) \tag{5.1}$$

As it will be discussed in Chapter 6, at a constant pressure as the temperature goes up, the frequency quantum yield of both excitation wavelengths drops while the absorption cross sections increase. However for the temperature range of 300 to 800 K, the increase in the absorption cross section for the excitation at 308 nm is almost three times more than the excitation at 277 nm, which is responsible for slight increase in I_O by temperature. It should be noted that the slight reduction in I_O for temperature above 750 K, seen in Figure 5.8, is due to the fast decomposition of 3-pentanone which can be avoided by increasing the flow rate of the fresh charge. However as the higher flow rates provide inhomogeneous mixture, a tubing coil and a surge tank should be added to the tracer supply system before the CVC. The absolute value of the coefficient of variation (COV) of the temperature calibration measurements was less than 3%. This was calculated by comparing the single DIFs

at each imaged temperature. This variation was mainly due to pulse to pulse energy variation of two the excitation wavelengths.

5.4 Two-line PLIF Average In-Cylinder Charge Temperature Measurements

It was necessary to validate the developed 2-line PLIF thermometry technique before further proceeding to other combustion measurements such as study of the charge cooling effect or flame thermal stratification. This could be done by using the 2-line PLIF system for measurements of average in-cylinder charge temperature during the compression stroke and comparing the results with the calculated temperature values from in-cylinder pressure data.

5.4.1 Average In-cylinder Charge Temperature Calculation from Pressure Data

The average in-cylinder charge temperature from the Intake Valve Closing (IVC) to the ignition timing on the compression stroke was calculated from the pressure data to compare with and validate the PLIF measurements. This was done by considering the engine as a closed thermodynamic system between IVC to the Exhaust Valve Opening (EVO) and taking the IVC timing as the reference point for the calculation. While for the operation with normal and Positive Valve Overlap (PVO) the fresh charge temperature slightly increases between the Intake Valve Opening (IVO) and IVC (due to heat transfer from the cylinder walls), for the Negative Valve Overlap (NVO) operation, it significantly increases (due to presence of a large amount of hot EGR). Therefore for the NVO operation one cannot simply take the intake port temperature as the in-cylinder charge temperature at IVC. The charge temperature at the start of compression (T_{IVC}) can be calculated by the enthalpy balance equation [154];

$$T_{IVC} = \frac{m_s \times c_{p,a} \times T_{in} + m_r c_{p,r} \times T_{ex}}{m_s \times c_{p,a} + m_r \times c_{p,r}} \tag{5.2}$$

where T_{in}, is the intake gas temperature measured at 5 cm above the intake port, T_{ex}, is the exhaust gas temperature measured at 2 cm above the exhaust port, m_s is the mass of scavenging gas ($m_s = m_{air} + m_{fuel} + m_{tracer}$) calculated by measuring air flow rate and fuel and tracer injection quantities, m_r is the mass of residual gas and

$c_{p,a}$ (air) and $c_{p,r}$ (residual gas) are the specific heats at constant pressure. The mass of residual gas m_r, is calculated by

$$m_r = \frac{PVM}{\tilde{R}T} \tag{5.3}$$

where P, V, T are at the EVO (T from exhaust thermocouple), $\tilde{R} = 8.3144 \frac{J}{kg.mol}$ and M is the molecular weight of residual gas. Having calculated the temperature at IVC, the average in-cylinder charge temperature from start of compression to ignition timing can be calculated using averaged in-cylinder pressure (e.g. of 100 cycles) and Equation 5.4 assuming a polytropic compression process

$$T_2 = T_{IVC}\left(\frac{P_{IVC}}{P_2}\right)^{\frac{n-1}{n}} \tag{5.4}$$

where n is the polytropic constant calculated from *log P-log V* diagram between IVC to IGN timing. A sample calculation of the in-cylinder charge temperature from pressure data is presented in Appendix I.

5.4.2 Engine Setup for Combustion Measurements

Before performing the firing measurements, it was required to operate the engine at stable conditions. The ignition timing, fuel and air injection timing as well as quantity, should all be adjusted for stable firing operation at λ=1. Therefore to avoid the potential risk of optical components breakage, they were all replaced with the metal parts. A throttle body was installed on the intake port after the electric heater (Figure 5.9) to regulate the airflow into the engine for normal valve overlap operation. The butterfly valve can be adjusted manually and secured in its place by tightening up an Allen screw at the top of throttle body. For the normal valve timing tests, the high lift camshafts were installed and secured with the cam covers. The intake/exhaust valves opening/closure were adjusted using a dial gauge (0.01 mm graduation). The EVC and IVO were set at 15 ºCA aTDC and 15 ºCA bTDC respectively. For negative valve timing tests, high lift camshafts were replaced by low lift camshafts. Then the EVC and IVO were set at 80º CA bTDC and 120º CA aTDC respectively.

It was necessary to investigate the ignition system components including the Dial-A-Time control unit, ignition coil and spark plug. Following initial investigation, it was found that it is required to increase the spark intensity. This is usually achieved by either increasing the coil dwell time or reducing the spark gap. The first technique shortens the spark plug lifetime and as it was not a problem for a research engine, the coil on time (COT) was increased to 7.0 ms. The second technique increases the chance of spark especially for the engines with high in-cylinder pressure or during lean operation. But at the same time the spark plug electrodes themselves can act as heat sinks and influence initial kernel development, quenching early flame development and promoting asymmetric flame propagation [155, 156]. Consequently the spark gap was not reduced more than 1 mm. It was also discovered that the ignition system generate a noise that can trigger the 2-Line PLIF system and disturb the NIDAQ system. Therefore an inductive filter and a relay switch were added to isolate the wirings from the ignition coil. Also a short earth lead for a quick local earth connection was provided.

Among the fuel injection strategies for normal valve overlap operation, the early injection (during intake) can provide a homogenous air/fuel mixture which in turn minimizes the cycle to cycle variation during firing tests. Therefore two injection timings of 90 and 180 ºCA aTDC (Int.) were chosen and studied for different ignition timing from 40 to 10 ºCA bTDC. For the Negative Valve Overlap (NVO) operation the injection timing was kept at 80 ºCA bTDC (Com.). The optimum ignition timing depends on engine design and operating conditions, as well as properties of the fuel, air and burned gas mixture. An early ignition increases the in-cylinder peak pressure and the compression stroke work transfer while a late ignition acts inversely and reduces the engine torque [27]. While on production engines the timing is typically set for the maximum brake torque, in this work the cycle to cycle variation was the primary concern. The DI air and fuel injection quantities were adjusted for stoichiometric combustion. A lambda sensor was first cleaned in an ultrasonic bath and attached to a Horiba Mexa-110 AFR Analyzer to monitor the lambda value. Following a series of firing tests, it was found that the ignition at 30 ºCA bTDC with fuel injection at 90 ºCA aTDC (Int.) provides the lowest cycle to cycle variation (IMEP of ~5.7 bar and COV_{IMEP} <2%). Injection at 180 ºCA aTDC lowered the IMEP to around 5 bar and increased the COV_{IMEP} which might be due to

unburned fuel. Ignition timing later than 20 ºCA bTDC resulted in some misfiring during the operation.

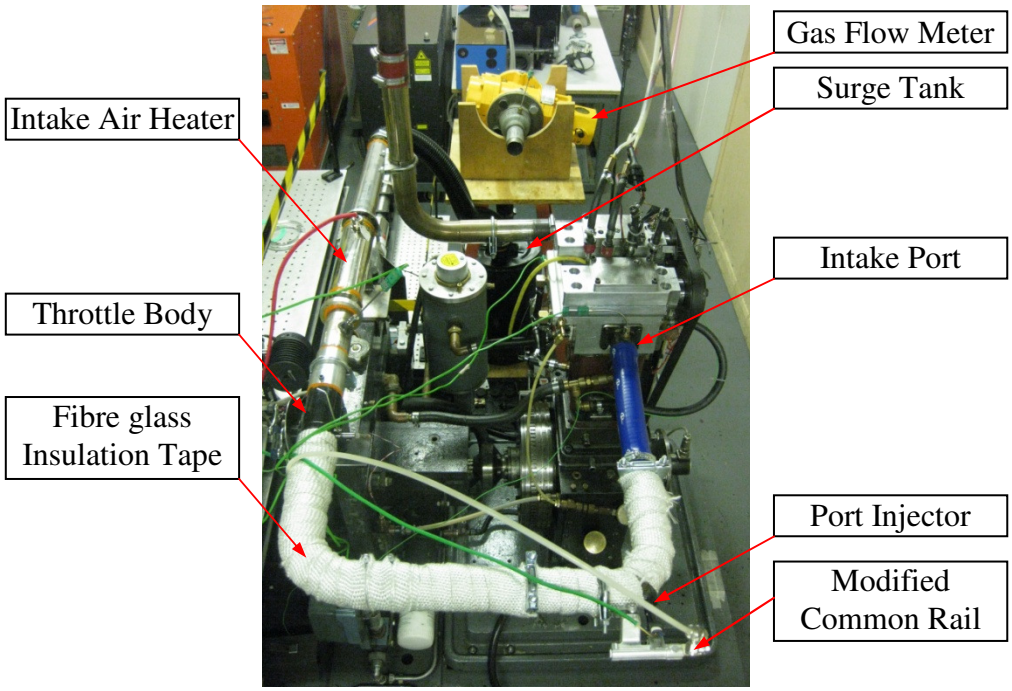

Figure 5.9 Intake port arrangements

5.4.3 Experimental Setup

The 55 mm diameter quartz window was installed into the piston crown and the sandwich plate with side windows was placed on the cylinder block. Then the cylinder head was placed on the sandwich plate and torqued down (25 Nm) with four M13 bolts to the cylinder block. Dowty washers were used to stop oil leakage from the cam box through the cylinder bolts' hole. An oval shape 45º mirror was positioned inside the extended cylinder block to provide the view of the combustion chamber for the camera. Figure 5.10 shows the experimental setup of the test.

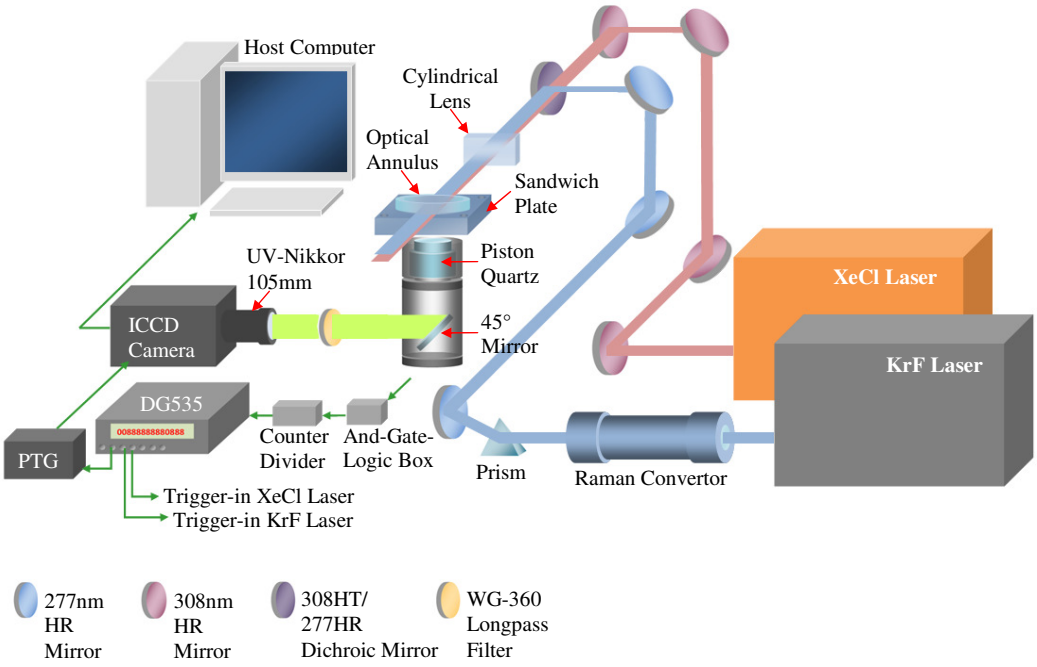

Figure 5.10 Experimental setup for average in-cylinder charge temperature measurements

The Excimer lasers and PI-MAX camera were set identical to that described in CVC temperature calibration tests. The laser sheets should be perfectly aligned not only to have a full spatial overlap but also to illuminate the combustion chamber at 30 ºCA bTDC. This can be checked as it described earlier in this chapter, or by hand cranking the engine to 30 ºCA bTDC and elevating the laser sheets so that they do not hit the piston crown and pass the sampling area. A homogenous mixture of tracer and air was provided by injecting the tracer into the intake port via a port injector. The fuel tank was filled with iso-octane and the tracer tank with 3-pentanone and were pressurized to 8 and 3 bar (gauge pressure) respectively. In order to facilitate the tracer vaporization, the intake port was insulated with heat resistant fibreglass tape and the intake air was heated to 318 K. Having calculated the engine volumetric efficiency (for both valve timings) and calibrated the port fuel injector, it was possible to set the injection duration for any required seeding mole fraction. In this work, a tracer mole fraction of 1% in the total cylinder charge was used.

5.4.4 Test Procedure

To increase the fluorescence SNR, the PI-MAX camera intensifier was set at maximum gain (255) and readout speed was set to the slowest setting of 100 kHz. Imaging at each required crank angle was accomplished by adjusting the DG535 T_0 delay. Three sets of 80 images (40 at 308 nm and 40 at 277 nm illumination) at each crank angle were captured. The first set was the background images with both lasers on but both MPI and DI injectors off. These images were later subtracted from the other two groups of images during image post proceeding. The second set was MPI data images in which both lasers and MPI were on but the DI injector was switched off. And finally the third set, was the DI data images in which both lasers were on and both MPI and DI were on as well. To minimize effects of windows fouling on the measurements, all three sets of images at each crank angle were captured following each other. After setting appropriate delays on DG535, first 80 background images were captured, then the port injector was switched on and 80 MPI data images were captured. This followed by switching on the DI injector and recording 80 DI data images. Measurements of in-cylinder charge temperature during the compression stroke was the main objective of these tests and therefore images were taken from 90 to 30 ºCA bTDC on compression stroke.

5.4.5 Results and Discussion

Figure 5.11 compares average in-cylinder charge temperature calculated from both the PLIF measurements and pressure data for the motoring and firing NVO operations. The acquired PLIF images were processed using the same algorithm as the CVC temperature measurements, except that before calculating the pixels' value in the ROI (501×501 pixels) of both averaged even and odd stacks of MPI data images, they were divided by averaged even and odd stacks of a MPI data image taken at 94 °CA bTDC (Com.). This was to remove the lasers' profile and effect of laser sheet attenuation across the imaged area from the motoring images. For the firing images averaged even and odd stacks of the same crank angle during motoring (MPI data images) were used for this purpose. Having calculated the charge temperature at IVC from the enthalpy balance equation, the fluorescence intensity ratio at IVC was matched to the value of PLIF ratio on the calibration curve at the

same temperature as the charge temperature at IVC. Then the PLIF images at later crank angles were converted into temperature readings by reference to the CVC calibration curve.

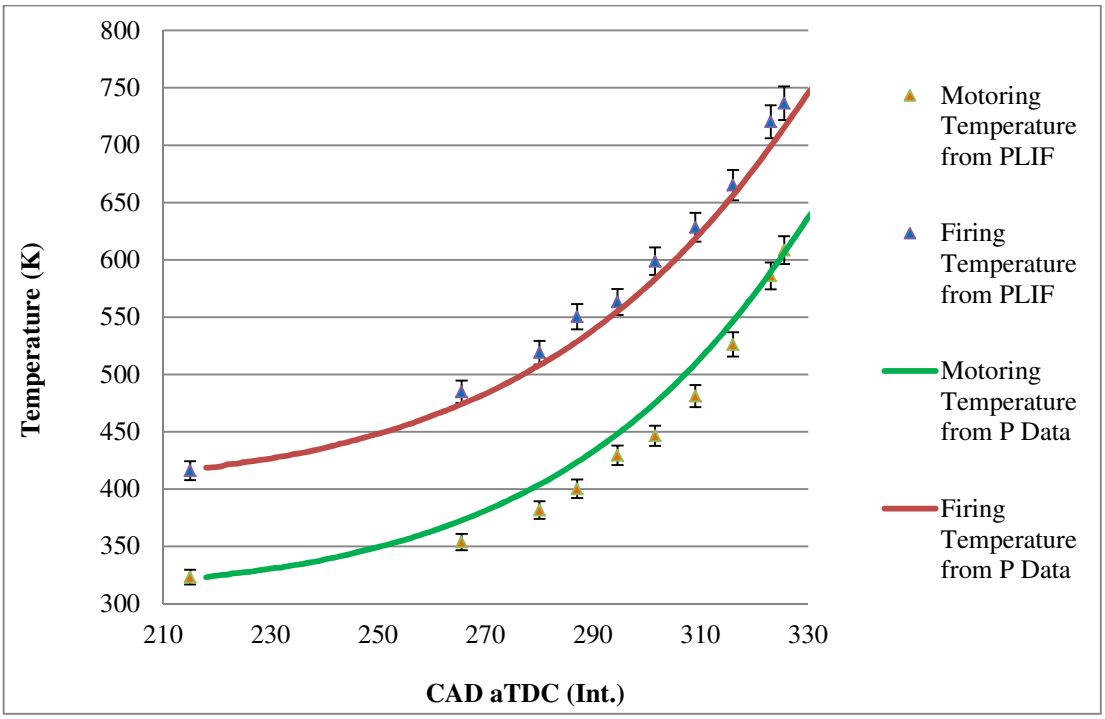

Figure 5.11 Average in-cylinder motoring and firing charge temperature calculated from both pressure data and 2-line PLIF images for the NVO operation

Table 5.1 shows calculated charge temperatures from both in-cylinder pressure data and PLIF images for selected crank angles. For the motoring case, average percent difference between the two methods was 3.5% with standard deviation of 2.4%, while for the firing test the average percent difference was 2% with standard deviation of 1.3%. The percent difference at each imaged crank angle was calculated by

$$\text{Percent difference} = \frac{\text{Absolute Difference}}{\text{Average Value}} \times 100 \tag{5.5}$$

where the *Absolute Difference* was calculated by subtracting the temperature value obtained from pressure data by the value obtained from the PLIF images and the *Average Value* was calculated by taking the average of the two temperature values. The standard deviation was then calculated to measure the dispersion. The higher

value of the average percent difference in the motoring cycle compare to the firing cycle is due to the image processing algorithm and the fact that the firing images were normalized by the motoring images of the same crank angle while all the motoring images were normalized with a single motoring image taken at 94 °CA bTDC (Com.).

CAD	Motoring In-cylinder Charge Temperature			Firing In-cylinder Charge Temperature		
	from PLIF	from P data	% Difference	from PLIF	from P data	% Difference
215	323	322.93	-0.02	416.02	418.66	0.63
265.5	353.6	371.72	5	484.81	475.05	-2.03
280	381.71	403.81	5.63	518.89	507.9	-2.14
287	400.15	423.48	5.67	550.33	528.66	-4.02
294.5	429.4	446.29	3.86	563.09	556.92	-1.1
301.5	446.4	468.78	4.89	598.74	580.91	-3.02
309	480.94	509.3	5.73	628.31	618.59	-1.56
316	526.14	546.45	3.79	665.04	656.25	-1.33
323	585.94	589.36	0.58	720.34	699.08	-3
325.5	608.31	609.28	0.16	736.64	718.66	-2.47
		Average Percent Difference =	**3.53%**		Average Percent Difference =	**2.00%**
		Standard Deviation =	**2.37%**		Standard Deviation =	**1.28%**

Table 5.1 Average in-cylinder motoring and firing charge temperature calculated from both pressure data and 2-line PLIF images for the NVO operation

5.5 Summary

This chapter was focused on the 2-line PLIF calibration and validation measurements. The design and manufacturing of the constant volume chamber were discussed. The experimental setup and test procedure for static measurements on the constant volume chamber, as well as motoring and firing tests carried out on the single cylinder optical engine, were presented. Using temperature calibration curve obtained from the constant volume chamber, 2-line PLIF average in-cylinder charge temperature measurements were compared and validated with the temperature values obtained from in-cylinder pressure data. It was attempted to provide a precise and detailed description of each test setup and procedure so it can be repeated and continued by following research students or staff.

Chapter 6
In-cylinder Fuel Injection, Mixing and Combustion Measurements

6.1 Introduction

This chapter presents applications of the 2-line PLIF technique and other laser diagnostics for in-cylinder fuel injection, mixing, and combustion studies. The experimental setup, test procedure, results and discussion for both motoring and firing tests are discussed. The motoring tests section covers Single-line PLIF fuel spray visualization and 2-line PLIF measurements of direct injection charge cooling effects. The firing tests section contains high-speed video imaging of combustion, flame formation and propagation visualization, 2-Line PLIF measurements of flame thermal stratification and simultaneous in-cylinder charge temperature and exhaust gas residuals measurements.

6.2 Motoring Tests

6.2.1 Single-Line PLIF Fuel Spray Visualization

In order to get a better insight into the behaviour of the air-assisted direct injector as well as to provide reference images for comparison with NIRAT (Near Infrared Tomography) frames, single-line PLIF fuel spray visualization was performed for both normal and negative valve timing at three different injection timing of 120 ºCA aTDC (Int.), 140 ºCA bTDC (Com.) and 90 ºCA bTDC (Com.). It should be noted that 140 ºCA delay between fuel and fuel/air mixture injection events of the air

assisted injector was kept constant throughout this work. This delay can affect the overall injection characteristics.

6.2.1.1 Experimental Setup

For fluorescence imaging, the direct injector fuel tank was filled with iso-octane (CHROMASOLV for HPLC, ≥99%, Sigma-Aldrich) premixed with 3-pentanone (9:1 volume ratio) and pressurized with nitrogen at 8 bar. Then the light illumination, delivery and capturing systems were set up as described in Chapter 5 for the temperature calibration measurements with few exceptions. First, for the fuel spray visualization tests a single illumination source was required and therefore only the XeCl laser was used. Secondly the cylindrical lens was removed from the end of optical path in order to have an expanded laser beam. As it can be seen in Figure 6.2, the expanded beam (thickness 21 mm) illuminates a larger volume inside the cylinder and results in a better fuel spray visualization compare to a focused (sub millimetre) laser sheet. Thirdly, the camera gating mode was changed to the interline mode to capture single image frames (SIF) on desired engine crank angles.

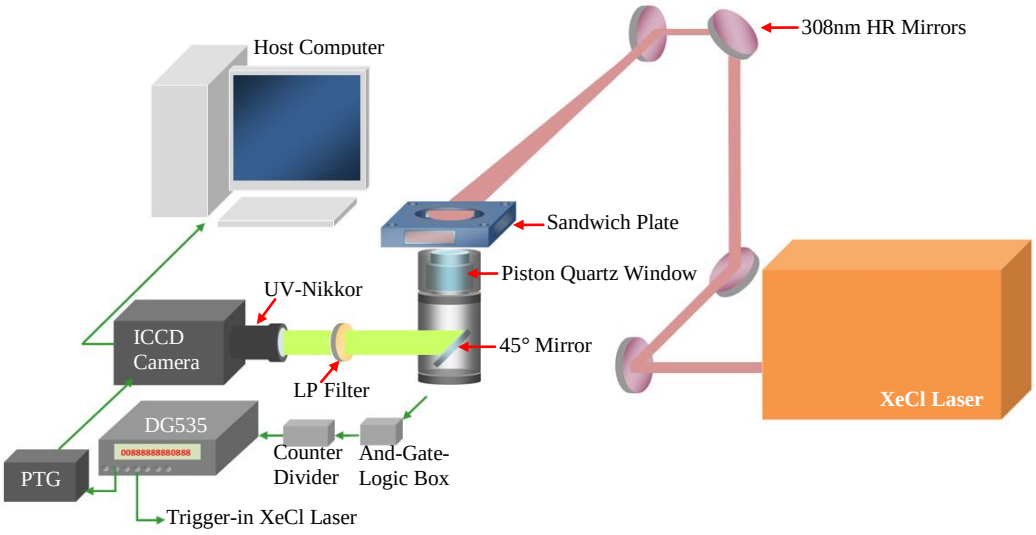

Figure 6.1 Single-line PLIF fuel spray visualization experimental setup

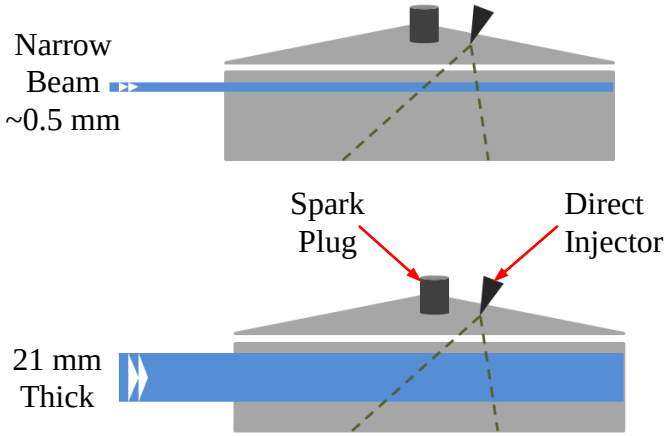

Figure 6.2 Comparison of focused and expanded laser sheets

6.2.1.2 Test Procedure

As the engine reference signal was at 80 ºCA bTDC (Com.) and fuel injection was set at 120 ºCA aTDC (Int.) for the first measurement, the injectors trigger-in delays on the Dual Output Angle Delay unit were set at 420 ºCA and 560 ºCA for the fuel and air injectors respectively. But for the imaging system, the engine reference signal was phase shifted to 80 ºCA bTDC (Int.) and as imaging from the start of injection (SOI) was desired, 27.8 ms (200 ºCA signal gap times 139 µs each CA duration at 1200 rpm) delay was set on the DG535 T_0 (between the trigger-in and trigger-out signals). Then the DG535 output signal was used to trigger the XeCl laser and PI-MAX camera. Also 0.8 µs gate delay was set on the camera PTG to compensate the laser 'trigger-in to pulse' delay.

To minimize engine optics' fouling, the engine was warmed up for about 30 minutes prior to the test. This allowed the engine coolant and oil temperature to get to 90 ºC and 40 ºC respectively to heat up the engine. Also the intake air was heated during the test to 80 ºC using a 3 kW electric heater (Secomak 571/4) mounted on the intake port. Nevertheless it was required to frequently clean the 45º mirror and piston top window during measurements.

To start imaging, XeCl laser and PI-MAX camera were put on the External trigger mode (ready to operate) while the DG535 was set on Single-Shot (requires a press of the execute key to send an output) which puts the whole system on the stand-by

mode. Then the engine was motored to 1200 rpm (20 rps), after its speed was steadied, the DG535 trigger mode was shifted from the Single-Shot to External mode. Following capturing 40 background images the direct injector was activated and 40 images of the fuel injection were recorded at the same crank angle. Imaging at later crank timing was accomplished by simply increasing the delay on the DG535. The same test procedure was repeated for injection at 140 ºCA bTDC (Com.) and 90 ºCA bTDC (Com.) with normal valve timings. For negative valve timing tests, high lift camshafts were replaced by low lift camshafts. Then the EVC and IVO were set at 80 ºCA bTDC and 120 ºCA aTDC respectively and fuel spray visualization tests carried out for the same injection timings.

It should be noted that the above mentioned injection timings are the values that were set on the Angle Delay unit which triggers the injectors' driver. In order to measure the delay between injectors' trigger-in signal and the injection event, a short CCD gate width of 1 μs was used and the gate delay on the Programmable Timings Generator (PTG) was varied. This delay was measured to be 1.2 ms (8 ºCA). Figure 6.3 shows fuel injection, intake and exhaust valves timings for both normal and negative valve timings.

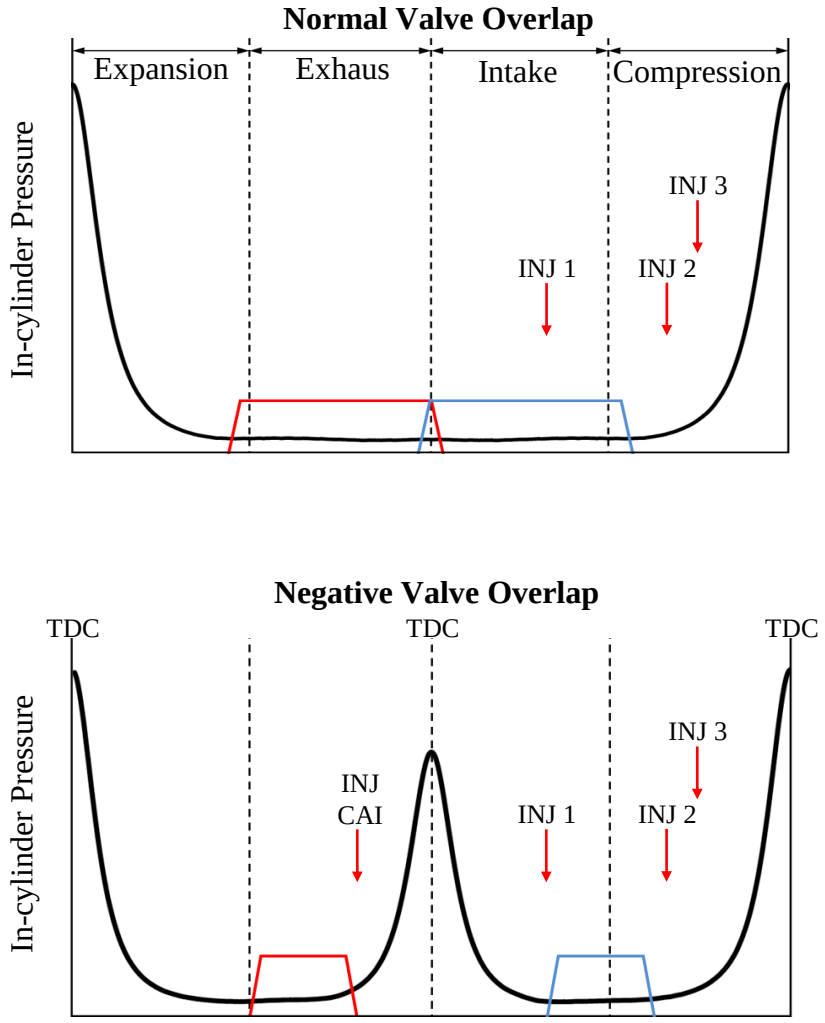

Figure 6.3 Intake and exhaust valves timing, fuel injection events for both normal and negative valve overlaps

6.2.1.3 Results and Discussion

Figure 6.4 shows the fuel injection event at 120 CA aTDC (Int.) during intake. The injection pulse width was 4 ms (on the scope) and injection quantity was 16 mg/cycle. Each image is an average of 40 single frames at the same crank angle without the background subtraction. The fully-opened intake valves can be seen at the bottom of these images. Considering 1.2 ms injection delay, the first image was taken 29 ms (instead of 27.8 ms) after the engine reference signal. The image shows a weak fluorescence signal from the injected fuel into the cylinder at 128 CA aTDC (Int.). The low fluorescence intensity is due to the fact that the spray is still above the unfocused laser beam and therefore only reflections of the laser beam illuminate the fuel droplets at this stage.

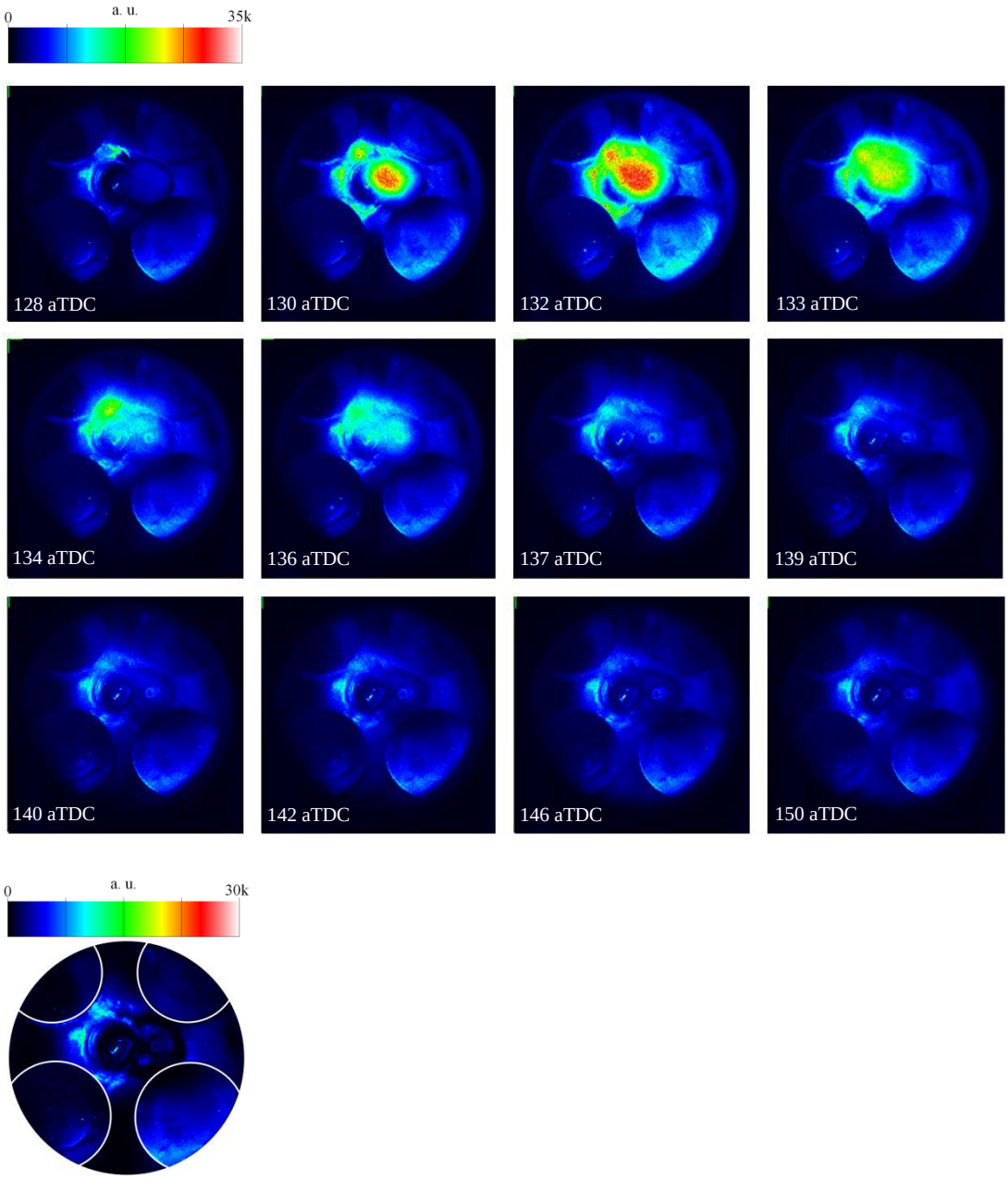

Figure 6.4 Top: Fuel injection event at 120 °CA aTDC (Int.) without background subtraction (average of 40 single frames at each crank angle), **Bottom:** Sample averaged background image at 128 °CA aTDC (Int.)

For further image processing, the intensity of the averaged background images was increased by a fraction before subtracting them from the data images. The reason was that for the background images only a very weak Rayleigh scattering (from the gas molecules) and laser light internal reflections were captured while for the data images due to high concentration of liquid droplets, two strong fluorescence and Mie scattering signals significantly increased the internal reflections.

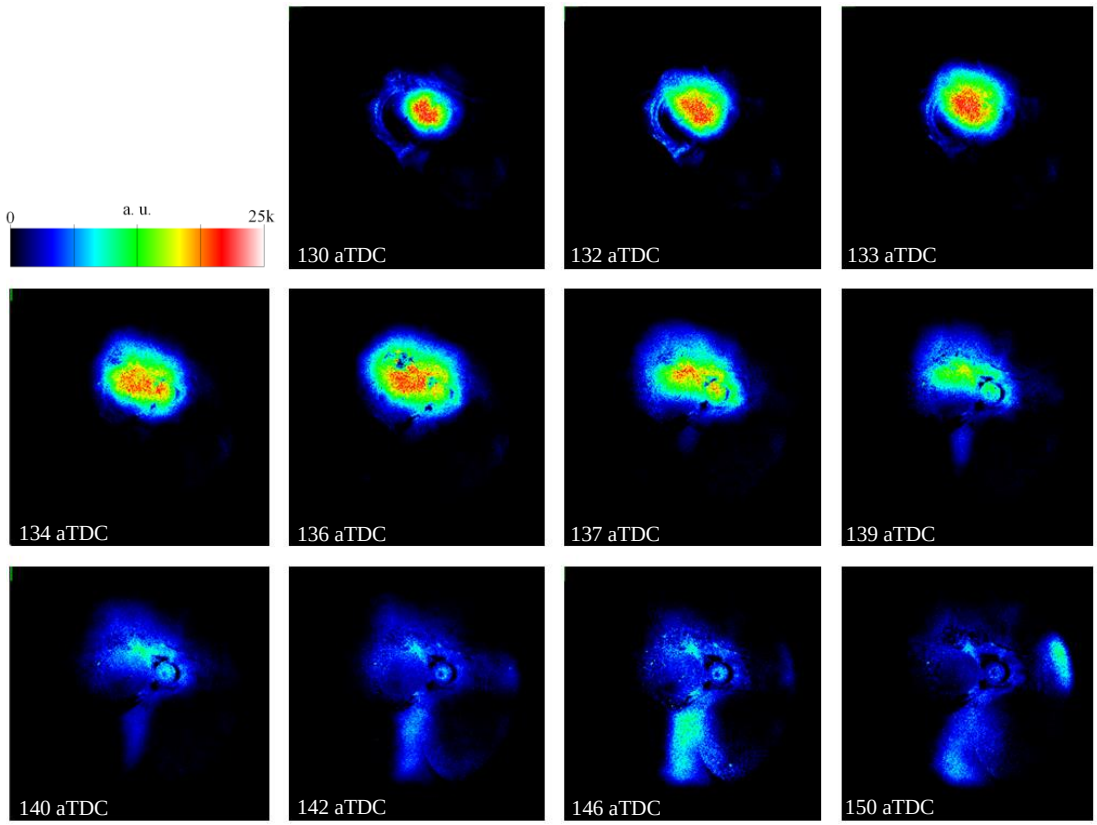

Figure 6.5 Fuel injection event at 120 °CA aTDC (Int.) after background subtraction (average of 40 single frames at each crank angle)

It was observed that although the injection signal is 4 ms long, but the main volume of the fuel is injected in the first two milliseconds. Also as the injection occurs during the intake, the introduced air rapidly disturbs the injection cone and mixes the fuel droplets. To better visualize and study the fuel spray pattern and mixing processes, the injection timing was advanced to 140 bTDC (Com.) when intake valves were closed.

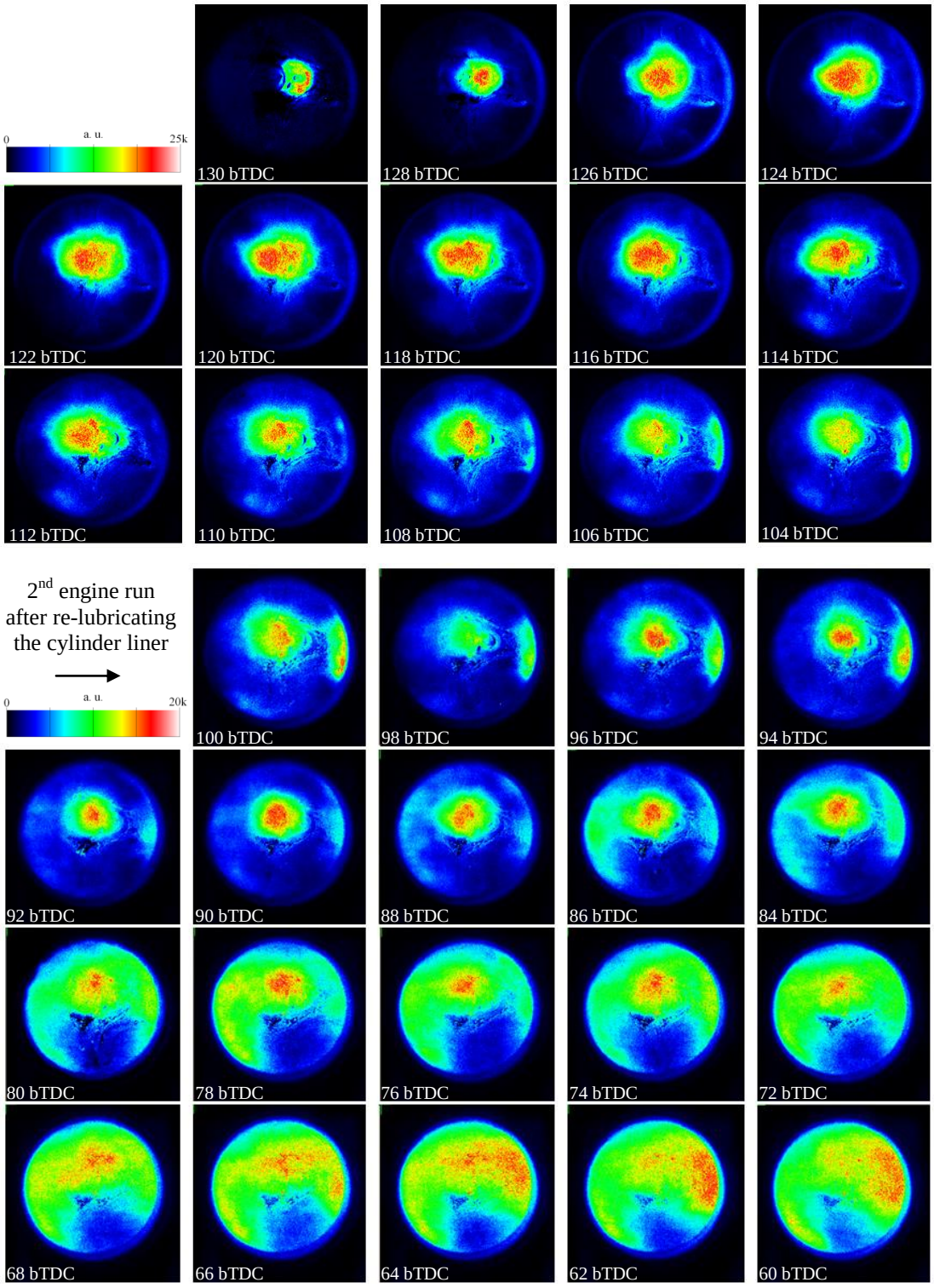

Figure 6.6 Fuel injection event at 140 °CA bTDC (Com.) after background subtraction (average of 40 single frames at each crank angle)

Figure 6.6 shows the fuel injection event at 140 °CA bTDC (Com.). As the injection occurs after the intake valves closure and due to lower in-cylinder large scale flow motion, an injection cone was developed. It was observed that the injection timing

cannot provide homogenous mixture prior to ignition due to insufficient mixing time and reduced flows. Although the air-assisted DI injector utilizes a very low injection pressure of 6.5 bar, fuel impingement was also observed around 100 °CA bTDC. This high fuel injection depth of penetration allowed us to further advance the injection timing and study a late injection strategy.

It should be noted that the fuel spray visualization tests were performed for both negative and normal valve timings at 120 ºCA aTDC (Int./Re.Com.), 140 ºCA bTDC (Com.) and 90 ºCA bTDC (Com.). For both valve timings, injection at 120 ºCA aTDC (Int./Re.Com.) occurs when the intake valves are opened while injection at 140 ºCA bTDC (Com.) occurs when the intake valves are fully closed. As a result no significant change in spray pattern was observed between the two different valve timings.

Figure 6.7 shows the injection event at 90 °CA bTDC (Com.) during the NVO operation with 1 ms imaging increment (~7 crank angle at 1200 rpm). Each image in this figure is an average of 40 frames after background subtraction. It can be seen that due to high concentration of tracer molecules in the measurement volume, most of photons were absorbed as they entered the cylinder. This resulted in an inhomogeneous illumination of the sampling area which in turn altered the actual spray pattern. The effect becomes more significant as the piston moves towards the TDC.

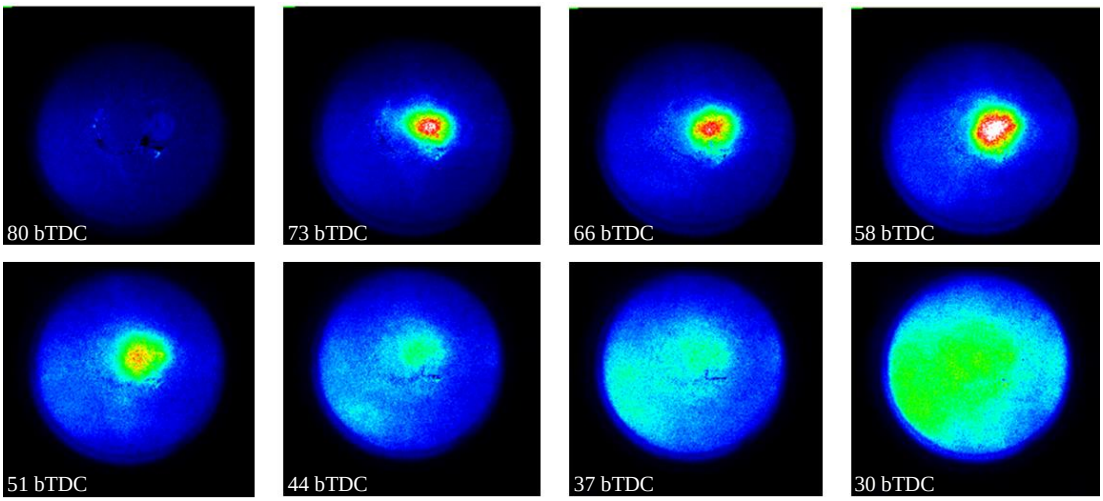

Figure 6.7 Fuel injection event at 90 °CA bTDC (Com.) after background subtraction (average of 40 single frames at each crank angle)

In order to remove the effect of inhomogeneous laser illumination, all images in Figure 6.7 were divided by a reference image at 80 °CA bTDC (Com.) The result is shown in Figure 6.8. During background subtraction some pixels get a negative value. Thus dividing other images by a background corrected image introduces the noise seen in Figure 6.8. A simple way to remove this noise is to find the largest negative value on the reference image and increase the intensity level of all pixels with this value so the lowest pixel value of '0' is achieved. Figure 6.9 shows the results after adjusting the lower intensity level (LIL) of the reference image.

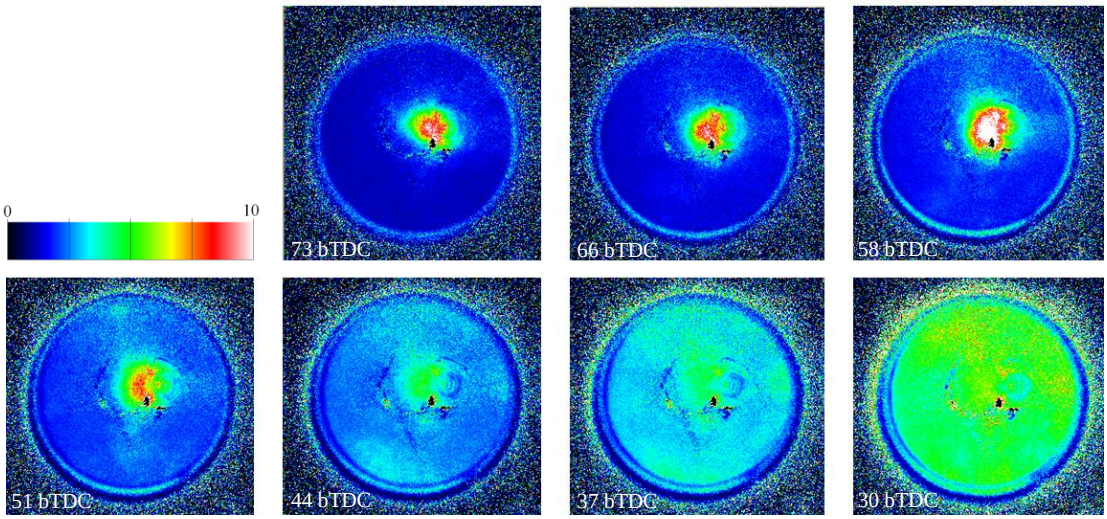

Figure 6.8 Fuel injection event at 90 °CA bTDC (Com.) after correction for inhomogeneous laser illumination

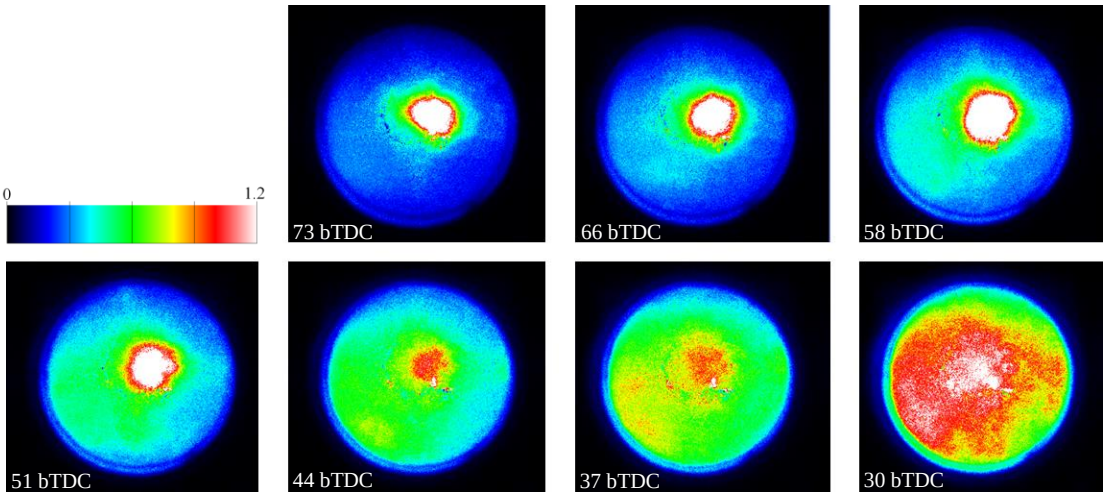

Figure 6.9 Fuel injection event at 90 °CA bTDC (Com.) after correction for inhomogeneous laser illumination using a lower intensity level-adjusted reference image ($\frac{\text{Avg 40 DT images} - \text{Avg 40 BK images}}{(\text{Avg 40 DT images @ 80 bTDC} - \text{Avg 40 BK images @ 80 bTDC})_{\text{LIL adjusted}}}$)

6.2.2 Two-line PLIF Study of Direct Injection Charge Cooling Effects

6.2.2.1 Experimental Setup Test Procedure

The experimental setup and test procedure were identical to the in-cylinder temperature measurement tests presented in Chapter 5. To study direct injection charge cooling effects, experiments carried out for two injection timings at 90 ºCA aTDC (Int.) and 110 ºCA bTDC (Com.). In general the 'early' injection strategy is used during a full load homogenous operation, while the 'late' injection strategy, intended to simulate a stratified, part load condition. Two injection quantities of 10 and 30 mg/cycle were studied at each injection timing. As the measurements were carried out during motoring operation with lower in-cylinder temperature and due to relatively long fuel droplets' lifetime (especially for the case of 30 mg injection per cycle) the late injection timing was advanced from its initial 90 to 110 ºCA bTDC.

6.2.2.2 Results and Discussion

Table 6.1 presents the in-cylinder averaged peak pressure (of 100 cycles) and peak temperature calculated from pressure data for five engine runs. For the motoring tests with no fuel injection and tests with only port injection, the variation in the measured averaged peak pressure is less than 0.07 bar. Switching on the port injector drops the peak pressure by 0.15 bar which is equivalent to ~6 K drop in calculated peak temperature. It should be noted that in order to utilise the PLIF diagnostic in this study the port injection quantity of 4.5 mg/cycle (tracer seeding mole fraction of 1%) was used. Switching on the direct injector significantly drops the peak temperature which was found to be a function of both injection timing and quantity. The later injection timing and larger injection quantity result in a lower in-cylinder peak temperature.

Motoring test with:	1st Run		2nd Run		3rd Run		4th Run		5th Run	
	no DI		DI at 90 aTDC (Int.) 10 mg/cycle		DI at 110 bTDC 10 mg/cycle		DI at 90 aTDC (Int.) 30 mg/cycle		DI at 110 bTDC 30 mg/cycle	
	P (bar)	T (K)	P (bar)	T (K)	P (bar)	T (K)	P (bar)	T (K)	P (bar)	T (K)
PI/DI off	18.82	765	18.79	762	18.84	765	18.77	764	18.78	762
PI on	18.67	759	18.64	758	18.69	761	18.62	756	18.63	757
PI/DI on	—	—	18.16	738	18.36	726	17.26	703	17.7	699
Difference between 'PI on' and 'PI/DI on' tests			0.48	19	0.33	34	1.36	53	0.93	58

Table 6.1 In-cylinder averaged peak pressure and peak temperature variation by direct injection timing/quantity

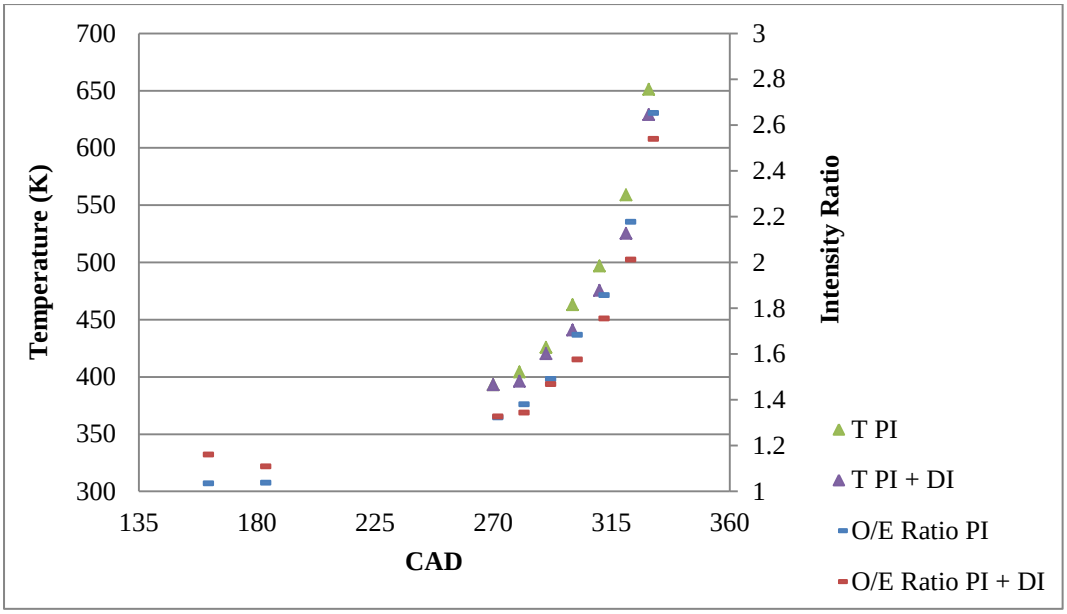

Figure 6.10 Fluorescence intensity ratio and temperature, 10 mg/cycle direct fuel injection at 90 CA aTDC (Int.)

The PLIF temperature measurements were also performed for all five runs and the results were compared with thermodynamic data. Figure 6.10 shows PLIF results for the second engine run with direct fuel injection at 90 °CA aTDC (Int.) and injection quantity of 10 mg/cycle. In this figure the 'PI' subscript stands for port injection and 'PI+DI' is for motoring while both port and direct injectors were switched on. The dash markers are the fluorescence intensity ratio of 308 to 277 nm (O/E) while the triangles are the calculated temperature at the same crank angles. The high intensity ratios of the red dash markers at 160 and 180 °CA aTDC (Int.) is due to a strong Mie scattering signal from the fuel droplets. The fuel droplets lifetime for this injection timing can be approximated from the PLIF data to be more than 90 °CA. Therefore neither of these two crank angles can be used as a reference point for in-cylinder temperature calculation. Consequently PLIF images taken at 90 °CA bTDC (Com.) were used to normalize images of the proceeding crank angles and calculate in-cylinder average temperature using the CVC calibration curve.

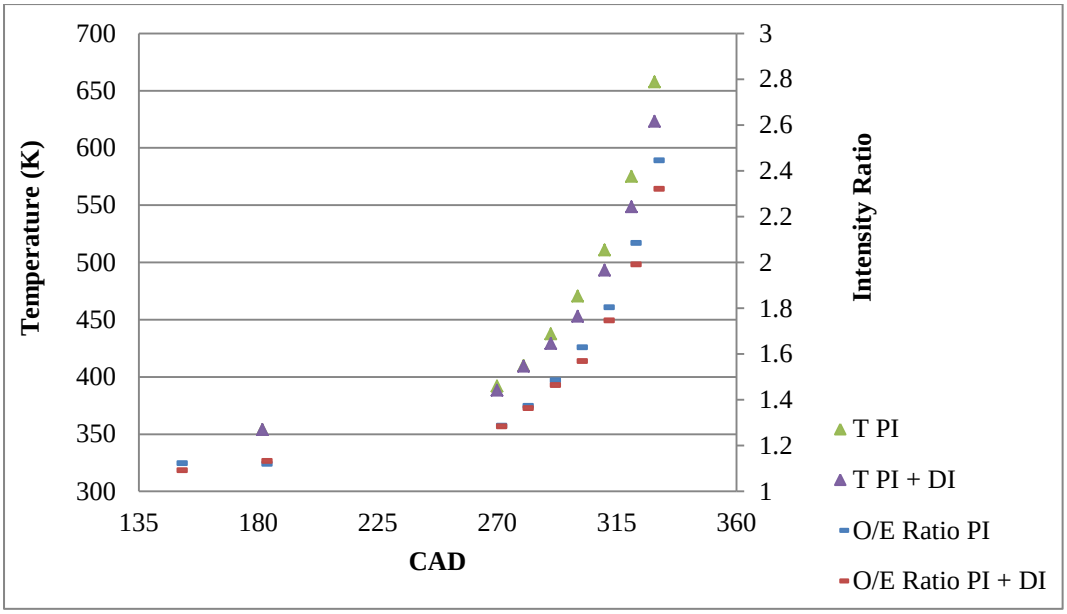

Figure 6.11 Fluorescence intensity ratio and temperature, 10 mg/cycle direct fuel injection at 110 °CA bTDC (Com.)

Figure 6.11 shows 2-line PLIF results for the third engine run with 10 mg/cycle injection at 110 °CA bTDC (Com.). By studying the O/E ratios at 90 °CA bTDC (Com.) for both 'PI' and 'PI+DI' runs, the fuel droplets lifetime was estimated to be less than 20 °CA for this injection timing. The much shorter droplet lifetime is due to a higher in-cylinder temperature at the injection timing. In this test, 180 °CA bTDC (Com.) timing was used as a reference point for in-cylinder temperature calculation.

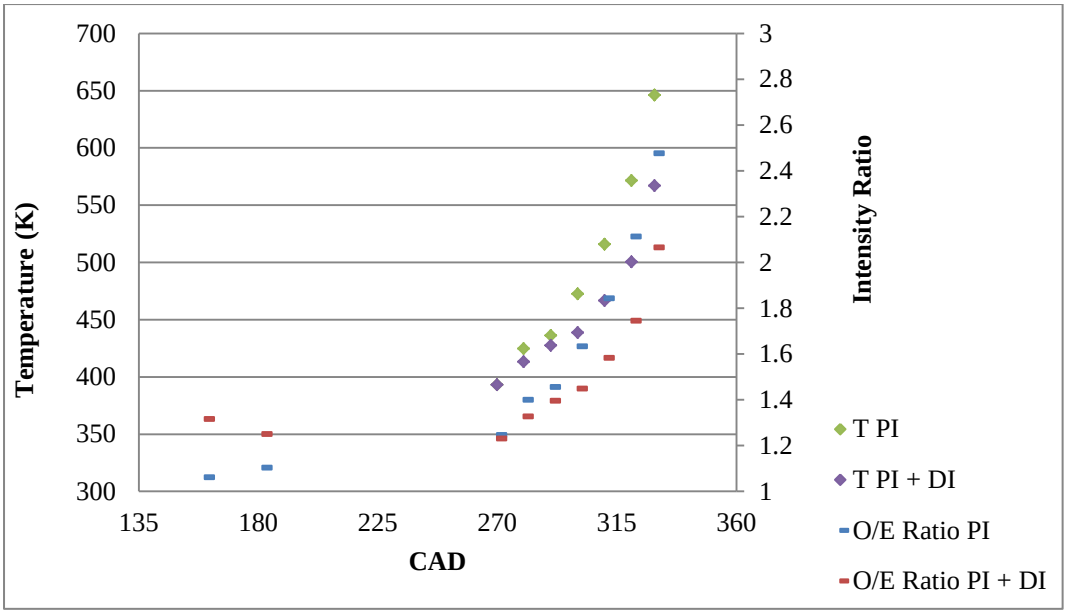

Figure 6.12 Fluorescence intensity ratio and temperature, 30 mg/cycle direct injection at 90 °CA aTDC (Int.)

Figure 6.12 shows 2-line PLIF results for the fourth engine run with 30 mg/cycle injection at 90 °CA aTDC (Int.). Similar to the second engine run, a very high O/E intensity ratio at 160 °CA aTDC (Int.) was observed for the 'PI+DI' run. As the fuel droplets evaporate, the Mie signal reduces and the O/E intensity ratio drops as it can be seen at 180 °CA bTDC (Com). In this test 90 °CA bTDC (Com.) timing was used as a reference point for in-cylinder temperature calculation due to a high Mie scattering signal at lower crank angles.

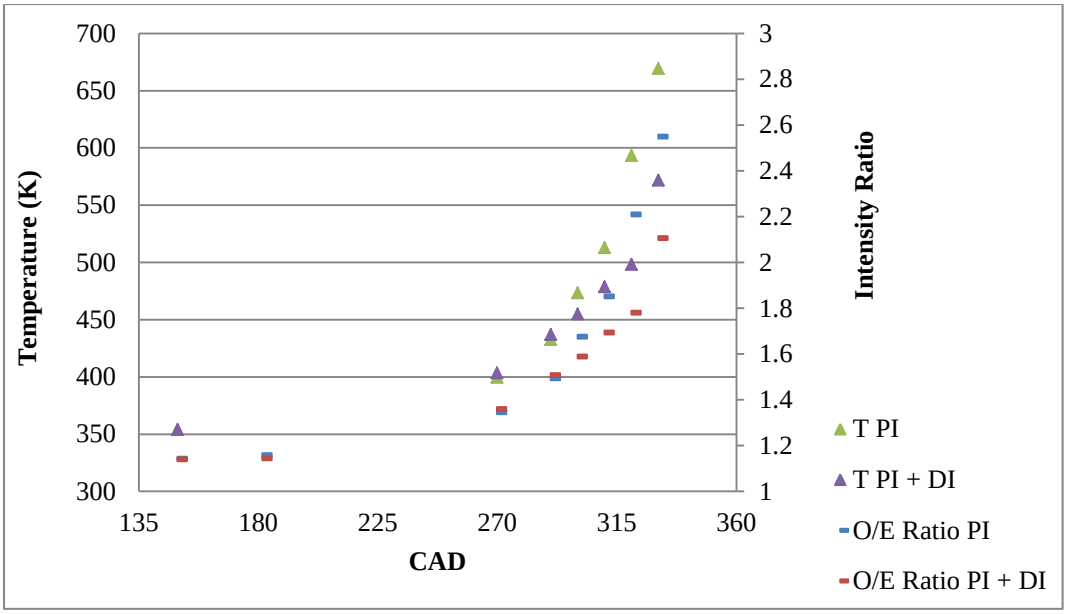

Figure 6.13 Fluorescence intensity ratio and temperature, 30 mg/cycle direct injection 110 °CA bTDC (Com.)

Figure 6.13 shows 2-line PLIF results for the fifth engine run with 30 mg/cycle injection at 110 °CA bTDC (Com.). It can be seen that the O/E intensity ratio at 70 °CA bTDC (Com.) for the 'PI+DI' run is still higher than 'PI' run which indicates the fuel droplets lifetime should be ~40 CA for this injection quantity and timing. In this test 160 °CA aTDC (Int.) timing was used as a reference point for in-cylinder temperature calculation.

Motoring test with:	**2ed Run** DI at 90 aTDC (Int.) 10 mg/cycle		**3rd Run** DI at 110 bTDC 10 mg/cycle		**4th Run** DI at 90 aTDC (Int.) 30 mg/cycle		**5th Run** DI at 110 bTDC 30 mg/cycle	
	From PLIF	**From P data**	**From PLIF**	**From P data**	**From PLIF**	**From P data**	**From PLIF**	**From P data**
PI on	651	642	657	644	646	641	659	642
PI+DI on	629	626	623	622	567	603	571	601
Temperature drop between 'PI' and 'PI+DI' tests	22	16	34	22	79	38	88	41
Temperature drop (%)	3.4	2.5	5.5	3.4	12.2	5.9	13.4	6.4

Table 6.2 Calculated temperature at 30 °CA bTDC (Com.) from both the PLIF and pressure data

Table 6.2 summarises the calculated temperature at 30 °CA bTDC (Com.) from both the PLIF and pressure data. The PLIF values are slightly higher than the values calculated from the polytropic compression relationship. For the low injection quantities both techniques showed a very good agreement with less than 2% variation in calculated temperature. For high injection quantities (in this case 30 mg/cycle), 7% deviation in the calculated temperature between the two methods was observed. This was mainly due to interference signals from the fuel droplets which can be reduced by considering the droplets lifetime and performing the PLIF measurement after that.

It was observed that the later injection results in higher temperature drop. This is due to fact that for the late injection timing after IVC, the in-cylinder mass is constant. As the fresh charge is injected into the cylinder, fuel droplets absorb heat from the gas mixture and evaporate which reduces the in-cylinder gas temperature. For the injection during the intake, the in-cylinder gas temperature drop is compensated by increased air into the cylinder.

6.3 Firing Tests

6.3.1 High Speed Imaging of Flame Propagation and Combustion

After setting the engine operation parameters for combustion testing, the sandwich plate with the four side windows was installed on the engine and the top quartz window was fitted into the piston crown. Before performing any quantitative measurement, it was considered to be beneficial to have a general view of ignition, flame formation and propagation, as well as exhaust gases development in the cylinder. This was required to study the feasibility of conducting quantitative 2-line PLIF measurements for firing operation.

6.3.1.1 Experimental Setup

A copper vapour laser (Oxford Laser CU15-A) was used to provide a high intensity light source during high-speed imaging of combustion. The imaging rate depends on the engine speed, crank angle resolution required and imaging application. This is usually in the range of a few thousand frames per second (fps). In this work as the

engine speed was 1200 rpm and a resolution of 1 °CA was required, an imaging rate of 7000 fps was chosen for high-speed imaging. At 7000 fps, the camera gating time is very short (tens of microseconds). This means that the camera CCD (Charged-Coupled Device) has a very short time to collect light photons for each frame, which results in dark frames. The solution is either to use a powerful light source such as a laser that provides more photons or to use an image intensifier that increases the intensity of available light under low light conditions.

A high speed colour video camera (NAC Memrecam fx-6000) with an intensifier (DRS Hadland Model ILS-3-11) and a Micro-Nikkor 60 mm *f*/2.8 were used to capture videos of flame propagation and combustion. The ILS-3-11 intensifier is designed to provide light intensification, high speed shuttering and UV to visible conversion [133]. Even though the intensified image formed on the output of the intensifier is focused onto the camera by means of a high efficiency, telecentric relay lens system, using the intensifier reduces the overall imaging resolution. The 45º aluminium coated mirror was mounted on the engine block and the Memrecam fx-6000 high speed video camera was placed in front of the mirror. To synchronise imaging with in-cylinder pressure, the engine reference signal was used to trigger both the NIDAQ system and camera. Also a series of tests was performed without the intensifier. In this case the copper vapour laser was used to illuminate the combustion chamber and the Micro-Nikkor lens was replaced with the UV-Nikkor. As the Micro-Nikkor has a shorter focal length and an almost the same aperture size, it exploits a smaller *f*-number ($f/= \frac{focal\ length}{aperture\ size}$) of *f*/2.8 compared to *f*/4.5 of the UV-Nikkor. The amount of light per unit area transmitted to the camera CCD decreases with the square of *f*-number ($\Omega_{lens} = \pi/4f^2$). Consequently halving the *f*-number reduces the necessary exposure time by a factor of four. This is crucial for high-speed imaging where very short gate widths are applied. On the other hand using a smaller *f*-number shortens the depth of field (DOF)[1]. As it can be seen in Figure 6.14 the DOF is inversely related to the *f*-number. When the light intensity is high enough a larger DOF is more favourable as it provides sharper images from the bottom dead centre to the top dead centre.

[1] The DOF is defined as the distance between nearest and farthest object locations in the scene with an acceptable image sharpness level.

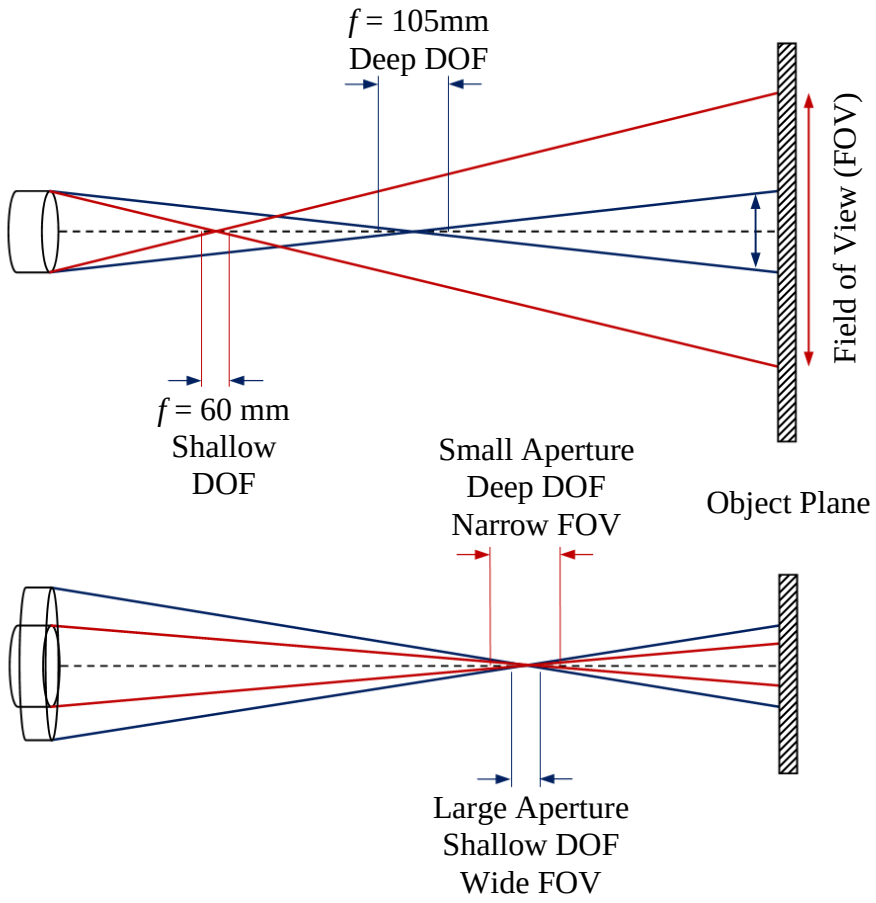

Figure 6.14 Effect of focal length and aperture size on field of view and depth of field. **Top**: same aperture size, different focal length; **Bottom**: Same focal length, different aperture size

6.3.1.2 Test Procedure

After the engine was motored and steadied at 1200 rpm, the in-cylinder pressure of 100 cycles was recorded and then the engine fired. The air and fuel injection quantities of the Orbital injector were adjusted to achieve λ=1 and again in-cylinder pressure of 100 cycles was recorded. To start the imaging the camera DRP (Digital Recording Processor) mode was change from the 'View' to 'Arm'. This puts the camera on the standby mode ready to receive the trigger-in signal and start of acquisition. The high-speed images were first stored on the camera's 4 GB on-board memory during the data accusation and then transferred and saved in the host computer. The Memrecam fx-6000 Link software allows saving files as the *.mcf or *.avi formats.

6.3.2 Study of Flame Formation and Propagation of SI and Spark-assisted CAI Combustion

Following the high-speed imaging of the combustion with Memrecam camera, and study of start of ignition, combustion duration and EGR formation, it was decided to use the PI-MAX camera to investigate the flame formation and propagation at much higher spatial resolution. The main objective of these tests was to measure non-fluorescence light intensities of flame and EGR to compare with the tracer's fluorescence signal intensities.

6.3.2.1 Experimental Setup

These experiments were carried out in two phases. In the first phase which was flame formation and propagation imaging, no external illumination system was used. A series of tests were completed to find the optimum gate width and intensifier gain for flame visualization. In the second phase for quantitative measurements of flame thermal stratification, the 2-line PLIF system was exploited.

During high-speed imaging it was found that there was a 0.7 ms (5 ºCA) delay in the ignition system. As a result although the ignition timing was set at 30 ºCA bTDC, the actual ignition was at 25 ºCA bTDC. On the other hand as the piston crown blocks the sandwich plate optical access for 25 ºCA either side of TDC (for the lower piston crown position), it was not possible to illuminate the combustion chamber at the start of flame formation. Therefore the ignition timing was retarded to 20 ºCA aTDC (setting value) so that flame kernel could be detected albeit at atypical timing.

6.3.2.2 Test Procedure

For flame formation and propagation imaging the CCD gate and intensifier gain were set at 50 µs and 100 respectively. The camera PTG was set on the Sequential mode. On this mode, unlike the Repetitive mode, the camera automatically increases the gate delay for each image following a pre-defined pattern. However it still requires a trigger-in signal for each gating and therefore it was not possible to have a sequence of images from a single cycle.

Similar to other experiments, the engine was motored to 1200 rpm and after the engine speed was steadied, it was fired. Having adjusted the injection quantities for lambda 1 (for ignition setting value at 30 ºCA bTDC), the sequential gating was exploited to capture single frame images from 25 ºCA bTDC to 135 ºCA aTDC. Then the gating mode was changed to Repetitive mode and 40 frames were recorded at each crank angle separately.

For the second phase of these experiments, the spark timing was retarded to 20 ºCA aTDC (setting value). The imaging parameters were set the same as for in-cylinder temperature measurements. DIFs were taken without excimer laser beams from 25 to 90 ºCA aTDC (with 5 ºCA increment) during the expansion stroke. While the first phase of experiments was performed for flame visualization, the second phase of imaging allowed measurements of non-fluorescence signal intensity and its comparison with fluorescence signals.

6.3.2.3 Results and Discussion

6.3.2.3.1 Spark Ignition Combustion

Figures 6.15 and 6.16 show flame formation and propagation for engine operation with normal valve timing from the start of ignition to 40 °CA aTDC. The start of ignition and the spark can be seen on the second image of Figure 6.15 at 25 °CA bTDC with 5 crank angle delay (~0.7 ms at 1200 rpm) from the actual setting value. For this test the direct fuel injection was set at 90 °CA aTDC (Int.). As the exhaust gas luminosity was stronger than the flame luminosity, for a better visualisation a dynamic intensity range was exploited and each image was scaled to 5%-95%. Although the early injection provides a homogeneous charge mixture prior to the ignition, it was observed that the flame kernel moves faster towards the exhaust side. This could be caused by the large scale air flow motion or due to the flame quenching at the cold areas as well as higher temperature at the exhaust side which can provide a better fuel/air mixture and can be investigated by applying the PLIF technique. The tendency of the flame to move towards the exhaust side was also confirmed by taking average of 40 single frames at each crank angle (shown in Figure 6.17). Starting from 10 °CA aTDC the exhaust gases become the major source of luminosity with the max intensity at 20 °CA aTDC.

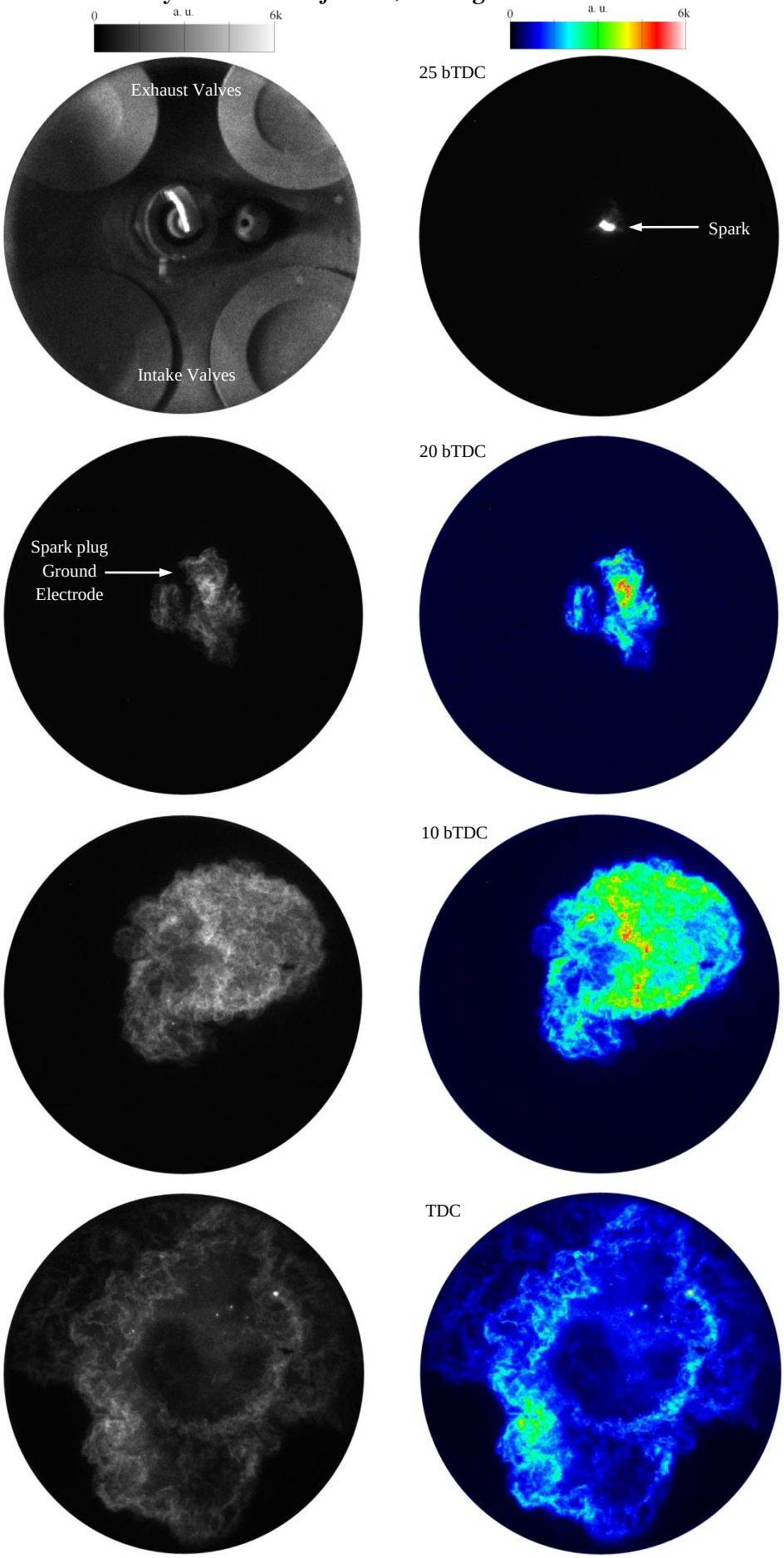

Figure 6.15 Single frame images of flame formation and propagation at selected crank angles

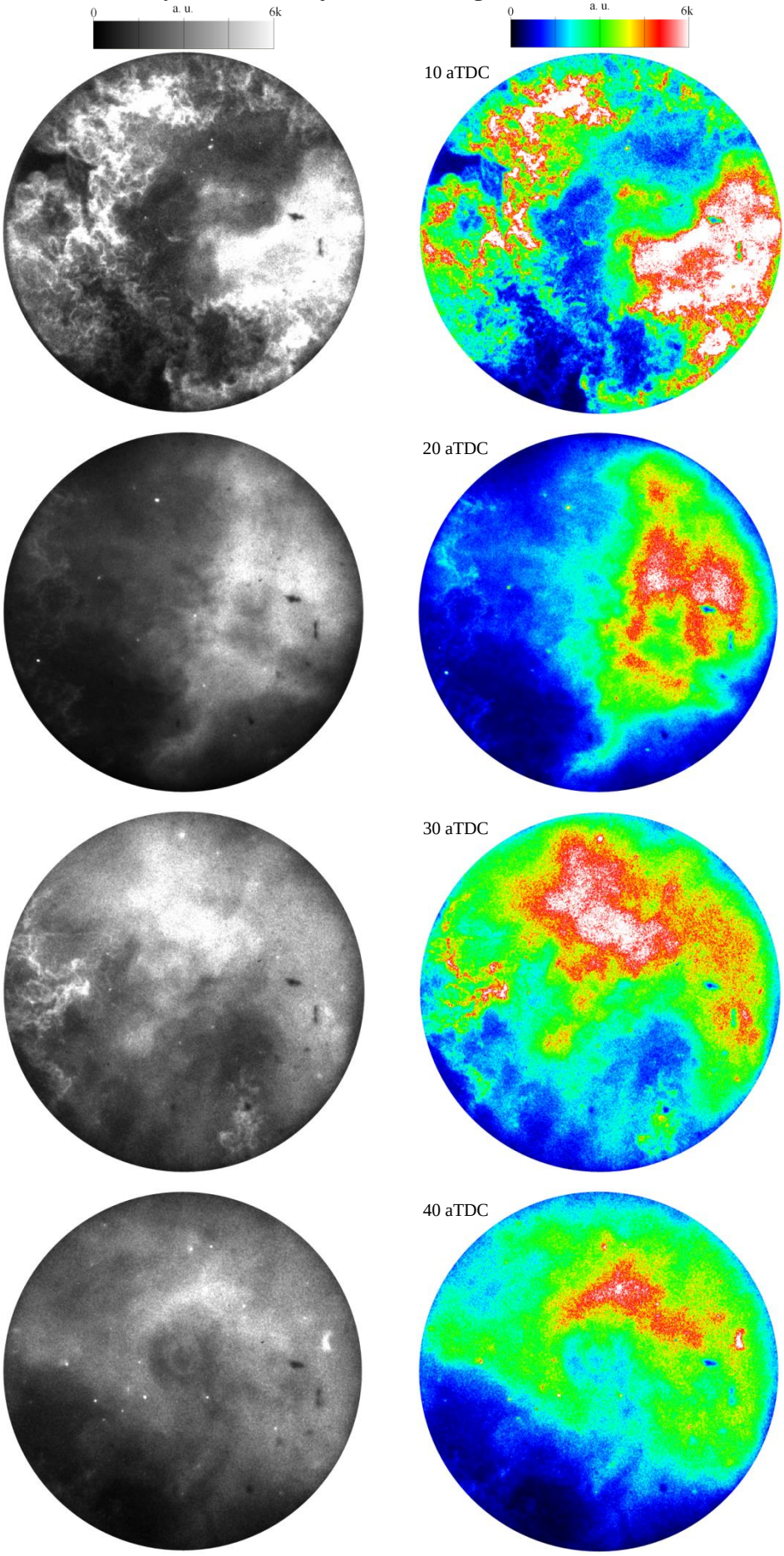

Figure 6.16 Single frame images of flame formation and propagation at selected crank angles

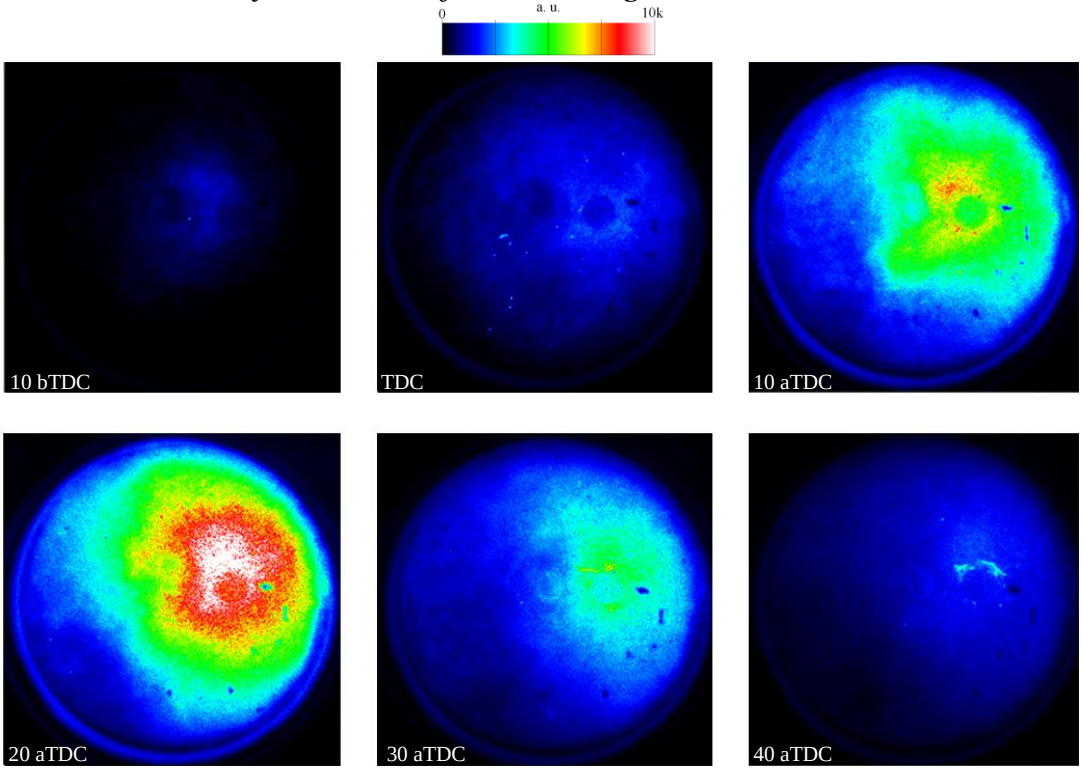

Figure 6.17 Averaged images of flame formation and propagation at selected crank angles

By investigating the images of early flame formation to 15 CA after the spark, it is noted that the flame moves away from the spark plug ground electrode. The Particle Image Velocimetry (PIV) technique can be utilized to study the in-cylinder flow motion which could be also responsible for the flame tendency to move towards the exhaust side.

6.3.2.3.2 Spark-assisted CAI Combustion

The three basic requirements for a gasoline engine to operate with CAI combustion are [13]:

1. a sufficient charge temperature for autoignition to occur
2. the presence of diluents (air or recycled exhaust gas) to restrict the heat release rate
3. a method to alter the combustion phasing

CAI combustion can be achieved through three major approaches as: thermal management [163-166], internal exhaust gas recirculation (iEGR) [167, 168] or residual gas trapping [40-44, 169,170]. In this work the spark-assisted CAI was

achieved by exploiting the residual gas trapping through the NVO strategy. The injection and ignition timings were kept at 80 and 30 °CA bTDC respectively. The injection quantity was reduced significantly to achieve λ=1. Figure 6.18 compares the flame formation and propagation of a SI and spark-assisted CAI operations. As it was expected the combustion duration of the CAI operation was found to be shorter than the SI operation. It was also observed that the autoignition stared mainly within the flame region. However on some cycles as it is shown in Figure 6.19 the hot spots can be found outside the flame area.

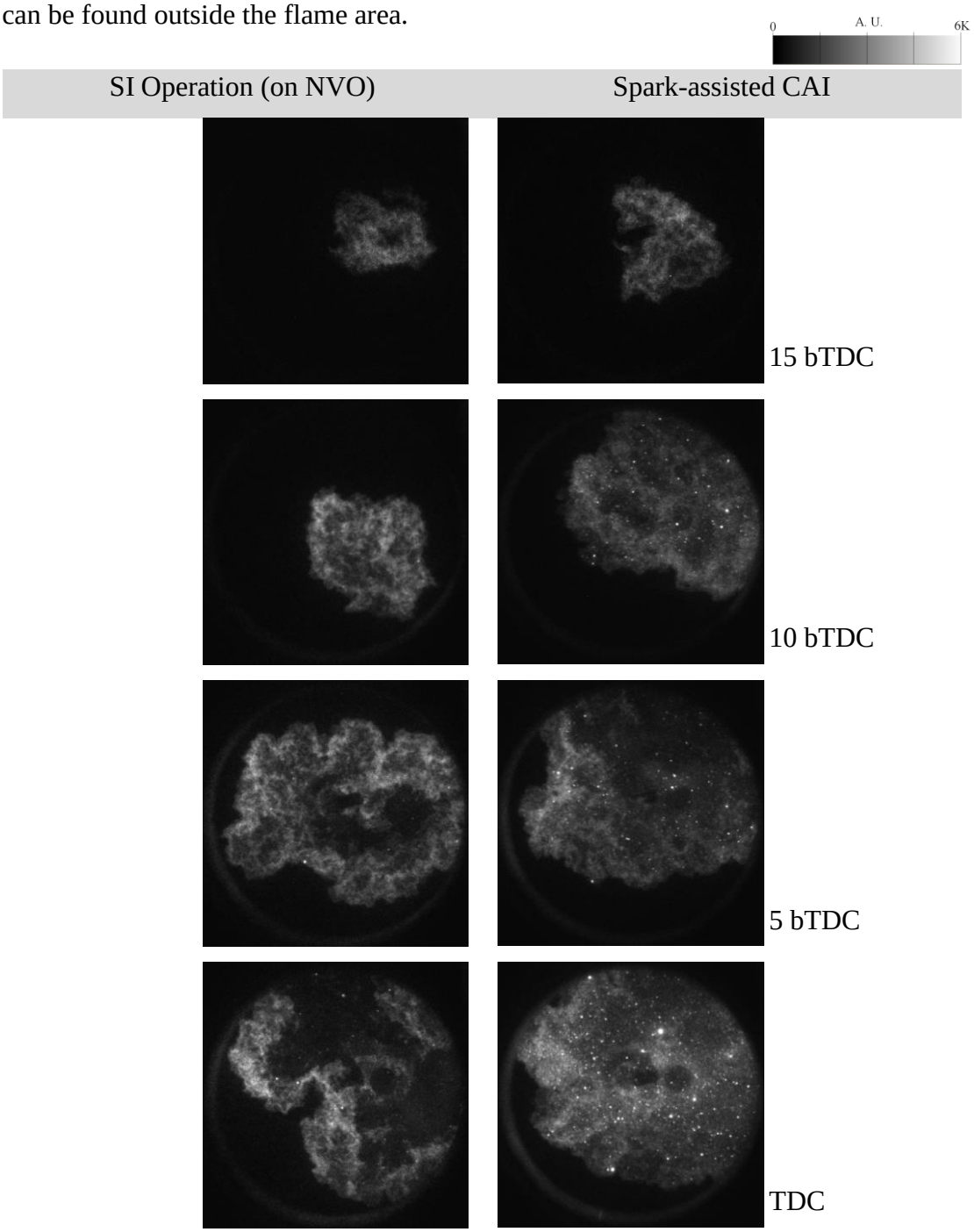

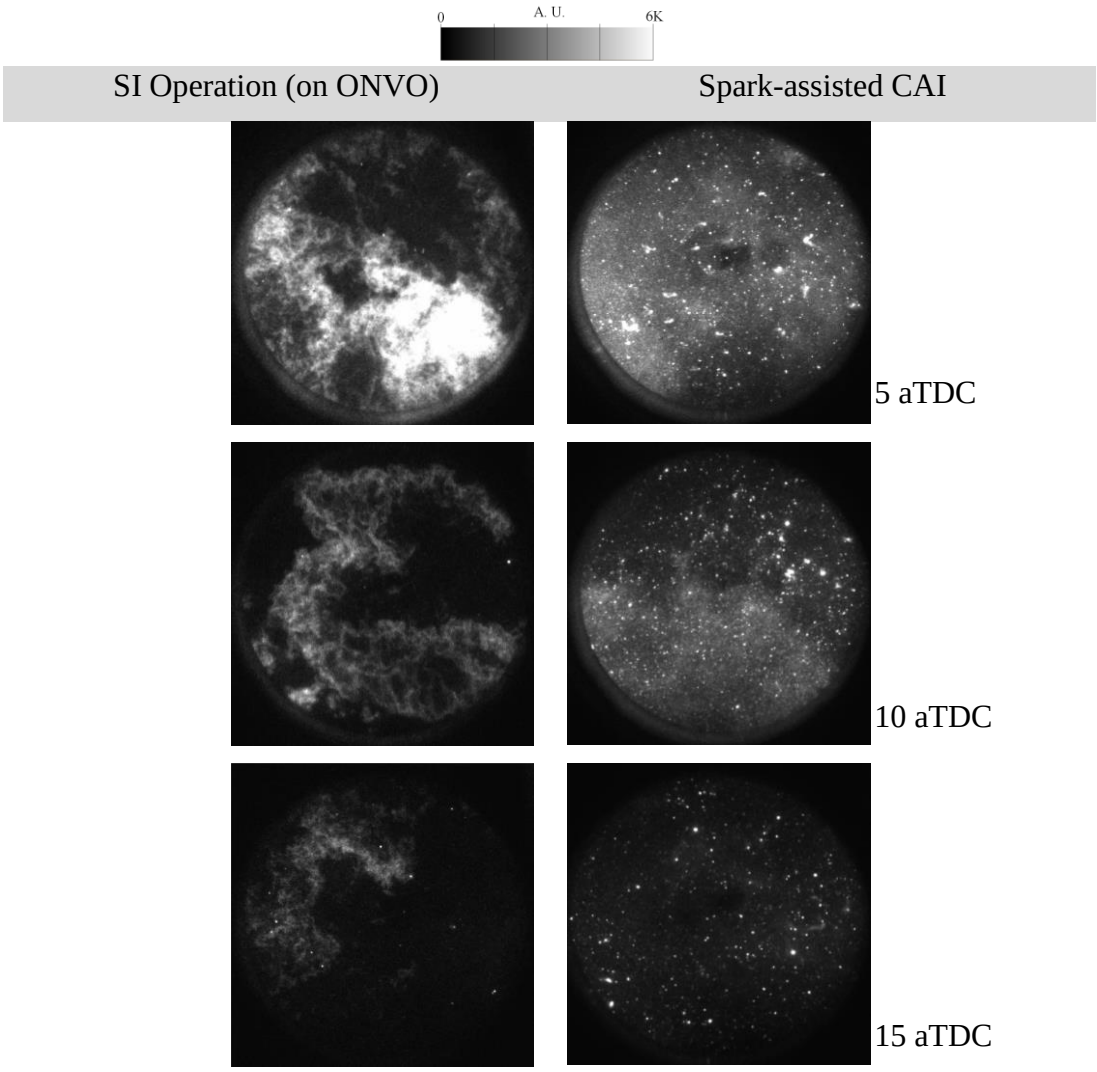

Figure 6.18 Flame formation and propagation in SI and spark-assisted CAI operations

In-cylinder pressure data can be used to further study spark-assisted CAI operation and knocking combustion. In this case, the NI DAQ system should be synchronized with the imaging system, using same trigger-in signal from the Counter/Divider unit. Also the LabView program should be modified so it automatically records in-cylinder pressure data for each imaging cycle. However as the quantitative comparison of SI and spark-assisted CAI operations was not objective of this study, the pressure data analysis was not performed.

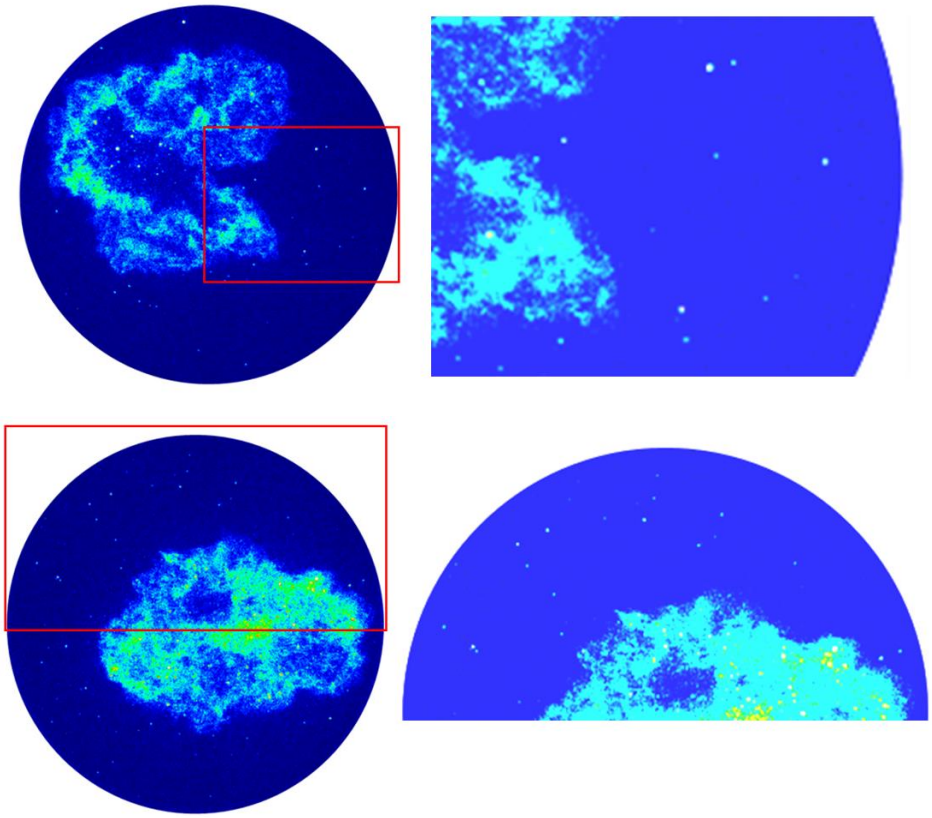

Figure 6.19 Autoignition in the end gas

6.3.4 Two-line PLIF Study of Flame Thermal Stratification

6.3.4.1 Experimental Setup and Test Procedure

Following the feasibility studies, experiments were carried out to study the flame thermal stratification. As the piston crown blocks the optical access for 25 °CA either side of TDC, it was not possible to illuminate the combustion chamber at the start of flame formation. Therefore a series of tests were carried out to find an ignition timing that allowed the 2-line PLIF to be carried out while providing a stable stoichiometric operation for the normal valve timings. It was found that ignition timings within 10 °CA either side of TDC resulted in unstable operation and misfiring in some cycles. The misfiring might be due to failure of the spark plug to provide a spark with enough energy to ignite the charge at higher in-cylinder pressures. This can be avoided by increasing the coil dwell time and re-gaping the spark plug. While ignition timings around 15 °CA aTDC were found to be a proper choice, later timings resulted in a lower IMEP and much higher COV_{IMEP}.

Ignition Timing	IMEP (bar)	COV_{IMEP} (%)
30 bTDC	5.5	2
20 bTDC	5.3	4
10 bTDC	Unstable operation with some misfiring	
TDC		
10 aTDC		
15 aTDC	4.2	5
20 aTDC	3.3	7

Table 6.3 Engine performance of different ignition timings for SI strategy

Having selected the ignition timing of 15 °CA aTDC the PLIF diagnostic was setup for the study of flame thermal stratification. It should be noted that applying the tracer-based PLIF technique to this study had some difficulties. The first issue was low fluorescence signal intensity within the flame region, as most of the seeded tracer either burned or decomposed due to high surrounding temperature. The second issue was that the Excimer lasers can excite the OH radicals in the flame region which generates fluorescence emission in the similar spectral region of the 3-pentonone. However as the 3-pentonone 2-line PLIF temperature measurement is independent of the tracer mole fraction, even small quantities of left over tracer in the flame region can be used for this measurement, albeit this required further improvements to the diagnostic technique.

Considering 139 μs duration of each crank angle at 1200 rpm engine speed, the ICCD burst periods (delay between two images in a DIF) of tens of μs are short enough for precise measurements of average in-cylinder charge temperature in an almost frozen thermodynamic condition. However this study required a much higher temporal resolution, and therefore the DIF burst period had to be further decreased. Burst periods of 100, 34, 30, 15, and 5 μs were tested. For burst periods shorter than 34 μs, it was required to decrease the Shutter Compensation Time as well. This time is the amount of time inserted between the end of exposure time and the beginning of the array readout which allows time for phosphor to decay. Although the PI-MAX camera exploits the P46 phosphor with a very fast decay time of 2 μs, even after 100 μs there is still some residual image (ghosting) from the first image in the second image. Where the residual image is an issue, either the shutter compensation time

should be increased or a fraction of the first image should be subtracted from the second image during image post processing. Using only the XeCl laser, a series of DIFs were captured to find the best combination of burst period and shutter compensation time that resulted in lowest residual intensity on the second image and provided a high temporal resolution for flame thermal stratification measurements. Figure 6.20 shows the residual intensity of the first image (average of 40 frames) on the second image as a function of burst period and shutter compensation time. As it can be seen from the graph the minimum left over intensity at each burst period is achieved when the shutter compensation time is close to the burst period. In this test a burst period of 5 μs and a shutter compensation time of 4 μs were exploited.

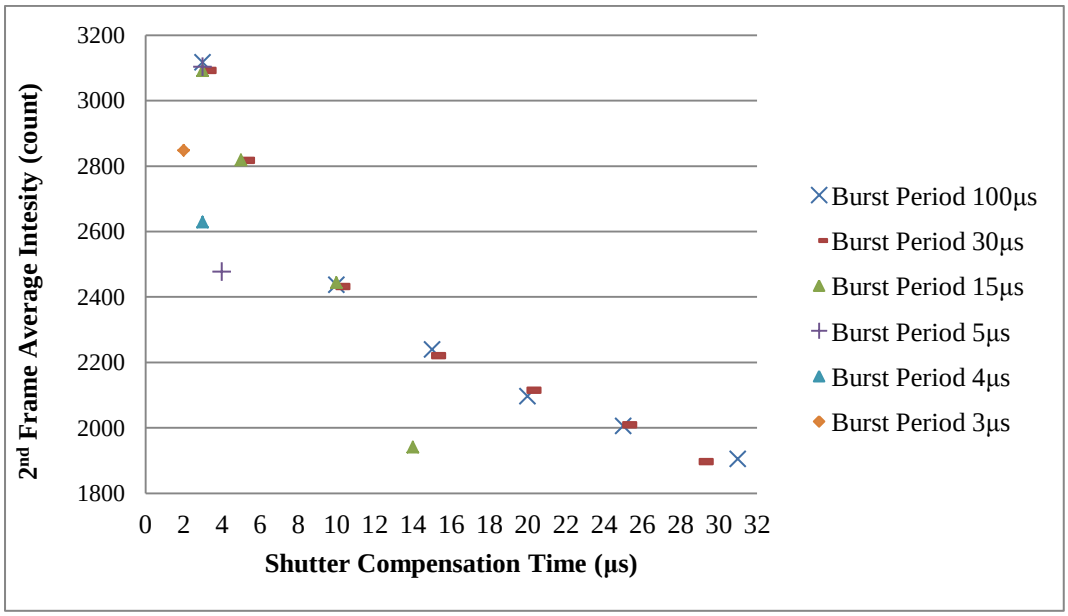

Figure 6.20 Average residual intensity of the first image on the second image in DIF mode as a function of the burst period and shutter compensation time

6.3.4.2 Results and Discussion

For the study of flame thermal stratification, PLIF images were captured with the same method as the measurements of in-cylinder charge temperature, but for image processing a different technique was applied. The images should be divided into two different regions; within and outside the flame area. In the region outside the flame the image post processing was the same as the 2-line PLIF in-cylinder charge temperature measurements. But for the enflamed area, the fluorescence signal

intensity was two orders of magnitude smaller than the fluorescence signal intensity of the areas outside the flame. Consequently the previously mentioned technique for in-cylinder charge temperature measurements could not be used to study the thermal stratification of the flame. Instead an alternative algorithm was utilized for this purpose. First a single background corrected flame image (DI) was normalized by averaged background corrected PI image of the same crank angle. The resultant image (IMG_{Res}) was subtracted from a reference image (IMG_{Ref}) which has the same dimension as the IMG_{Res} but all the pixels have a single value equal to the maximum pixel value on the IMG_{Res}. The technique was applied to both even and odd images (different excitation wavelengths) of the same crank angle and the fluorescence intensity ratio was calculated. This ratio is a function of temperature and represents the thermal stratification of the enflamed region.

$$R_{enflamed} = \frac{IMG(O)_{Ref} - \left[(DI(O)^{SIG}_{X\,°CAD} - BK(O)^{AVG}_{X\,°CAD})/(PI(O)^{AVG}_{X\,°CAD} - BK(O)^{AVG}_{X\,°CAD})\right]}{IMG(E)_{Ref} - \left[(DI(E)^{SIG}_{X\,°CAD} - BK(E)^{AVG}_{X\,°CAD})/(PI(E)^{AVG}_{X\,°CAD} - BK(E)^{AVG}_{X\,°CAD})\right]} \quad (6.0)$$

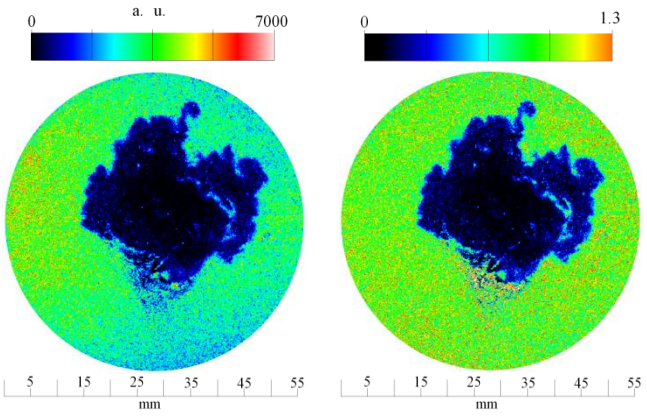

Figure 6.21 Before (left image) and after (right image) removing the effect of laser profile variation and beam attenuation

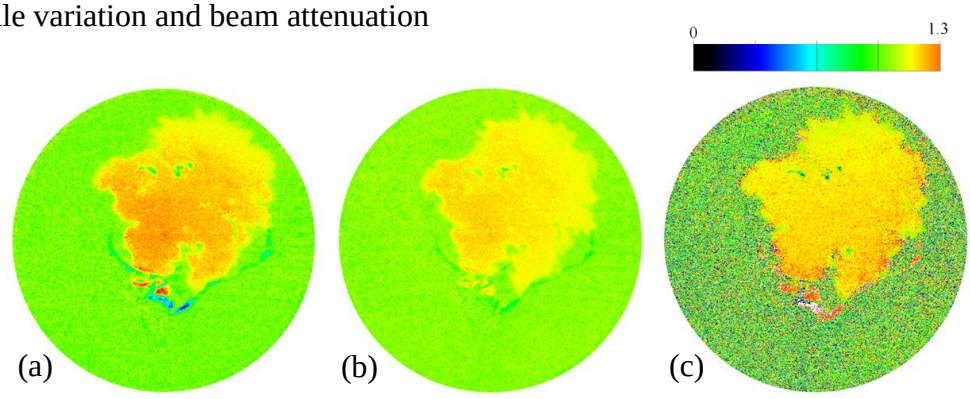

Figure 6.22 Processed single frame images, (a) illumination at 308 nm, (b) illumination at 277 nm, (c) fluorescence intensity ratio of 308 to 277 nm

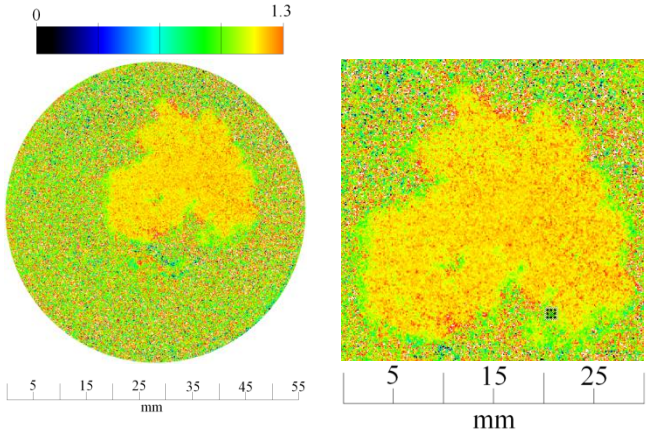

Figure 6.23 Two-line PLIF image of flame thermal stratification

Figure 6.23 represents the thermal image obtained from the Equation 3 showing flame at 35 °CA ATDC for ignition timing of 15 °CA ATDC. Figure 6 (b) shows a magnified enflamed region (400×400 pixels) with spatial resolution of 13.3 pixel/mm. Number of Region of Interest (ROI) with a size of 13×13 pixels (~1 mm^2) were assigned and the fluorescence intensity ratio of the two excitation wavelengths of the pixels within each ROI was calculated and averaged. The difference between the minimum and maximum calculated averaged ratios was more than 30% which can be translated to the temperature gradient using a suitable calibration technique. It should be noted that as the hydroxyl fluorescence spectrum expands from ~300 to 320 nm with peak intensity at 310 nm [171, 172], there was a minimum interference with the 3-pentanone fluorescence captured on the ICCD as the Schott WG360 filter was employed for the PLIF imaging. Also it was realized that the calculated flame mean expansion speed on the imaging plane of this ignition timing was lower than typical ignition timings. This might be due to the fact that as the piston moves down and increases the in-cylinder volume the flame expands evenly on both X and Y axis while for the ignition timing before TDC as the piston moves towards the TDC, flame can only expands on the imaging plane. As it can be seen from the magnified flame image, unlike the direct photography that shows the luminous or post-flame zones, the two-line PLIF thermometry can detect the thermal stratification in the flame front. The relatively narrow green band, with the width varying from of ~0.1 to ~3 mm, enclosing the flame can be associated with the preheat and reaction zones. In this band the flame temperature rises from the unburned charge temperature to the temperature of burned gas in the luminous zone. Although single-line PLIF images can also show the flame structure, but the single-line PLIF images are dependent on the tracer concentration and can only represent the flame structure for a premix

flame in a homogenous charge prior to ignition. On the other hand as the two-line PLIF images are independent of tracer concentration they can be utilized to study premix flame structure in a non-homogenous charge, e.g. at presence of large amount of EGR or possibly diffusion flame of diesel engines.

6.3.5 Two-line PLIF Simultaneous Exhaust Gas Residual and Temperature Measurements

The final series of experiments in this work was based on simultaneous measurements of exhaust gas residuals mole fraction and in-cylinder charge temperature during stable CAI operation.

6.3.5.1 Experimental Setup

To achieve a stable CAI operation, extensive tests were carried out on the engine assembled with all metal components. Four different fuel injection timings at EVC (during NVO), IVO, intake valves fully opened and at IVC were studied. Only with early injection at EVC, a stable CAI could be achieved. The other three injection timings resulted in unstable CAI and very high in-cylinder peak pressures of 60-65 bar. It was found that the most important factor for a stable CAI operation was the in-cylinder peak pressure and at a much lower degree, intake air temperature. For in-cylinder pressures of >25 bar, the spark plug could be switched off after first few cycles (which was necessary to initiate EGR to start a CAI operation) and engine could run stable (CoV_{IMEP} <4%) with an intake air temperature of as low as ~320 K. In-cylinder motoring pressures between 22-25 bar resulted in unstable CAI/SI operation while the spark plug should be kept on all the time. For the pressures below 22 bar engine could only operate on the SI mode unless high intake air temperature of more than ~450 K is utilized.

Although it was fairly easy to achieve an in-cylinder peak pressure of 25 bar for the engine assembled with all metal components, for the engine with optical configuration this was a challenge due to the additional crevices and leakages from optical accesses (at the piston crown and sandwich plate) and different sealing

techniques applied[2]. Therefore to boost the in-cylinder peak pressure, the nominal compression ratio was further increased to 12.4:1. Fuels with different octane rating were tested and ignition timing was investigated for each and varied from 40 °CA bTDC to 10 °CA bTDC, to find the optimum timing that provided the maximum in-cylinder peak pressure and a stable operation. Also to further increase the in-cylinder temperature a 3kW Omega tape heater was installed on the intake port to work in conjunction with an electric air heater mounted on the intake port. With this setup it was possible to reach intake air temperatures of up to 570 K. However it was found that intake air temperature of above ~370 K would result in tracer decomposition (as the tracer is also injected into the intake port), and therefore could not be used.

6.3.5.2 Test Procedure

After the engine was motored and steadied at 1200 rpm, the intake air temperature was set at 318 K. The spark plug was switched on and then the DI injector was turned on having set the fuel injection duration for a normal SI operation (about 15 mg fuel injection per cycle). After a few cycles, the fuel injection duration was reduced to below 10 mg/cycle and both the air and fuel injection duration were adjusted to achieve λ=1. It should be noted that for stable CAI operation, the λ value should be kept at or above 1 as a rich mixture would switch the engine back to the SI operation. The 2-line PLIF simultaneous T/EGR measurements were then performed as it was described earlier in this chapter for the in-cylinder charge temperature measurements.

6.3.5.3 Results and Discussion

The PLIF signal in the linear excitation limit is given by Equation 4.6. Taking the ratio of two fluorescence signals for motoring (subscript '*cal*') and firing (subscript '*dt*') cycles at the same crank angle and solving for the tracer mole fraction ratio, we get:

[2] For cleaning purpose, only temporary gaskets that allow dissembling of components during the tests could be used on the side windows.

$$\frac{\mathrm{X}_{tr-dt}}{\mathrm{X}_{tr-cal}} = \frac{P_{cal}T_{dt}\sigma_{cal}(\lambda, T_{cal})\phi_{cal}(\lambda, T_{cal}, P_{cal}, X_{i,cal})S_{dt}}{P_{dt}T_{cal}\sigma_{dt}(\lambda, T_{dt})\phi_{dt}(\lambda, T_{dt}, P_{dt}, X_{i,dt})S_{cal}} \tag{6.1}$$

For the NVO operation if we take the in-cylinder contents as consisting of three quantities of intake air, fuel and exhaust gas residuals (EGR) and assume that all of the seeded tracer in the air and fuel is consumed during combustion [110, 161], then we have

$$\mathrm{X}_a + \mathrm{X}_f + \mathrm{X}_{EGR} = 1 \tag{6.2}$$

where 'X_a' is the air mole fraction, 'X_f' is the injected fuel mole fraction, and 'X_{EGR}' is the EGR mole fraction. Also the tracer mole fraction can be calculated from

$$\mathrm{X}_{tr} = \mathrm{X}_s(\mathrm{X}_a + \mathrm{X}_f) \tag{6.3}$$

where X_s is the mole fraction of the tracer seeded into the air and the fuel. As there is no fuel injection during the motoring cycles $\mathrm{X}_{tr-cal} = \mathrm{X}_s\mathrm{X}_a$ where $\mathrm{X}_a = 1$. Thus

$$\frac{\mathrm{X}_{tr-dt}}{\mathrm{X}_{tr-cal}} = \frac{\mathrm{X}_s(\mathrm{X}_a + \mathrm{X}_f)}{\mathrm{X}_s(\mathrm{X}_{a,})} = \mathrm{X}_a + \mathrm{X}_f = 1 - \mathrm{X}_{EGR} \tag{6.4}$$

and from the Equation 6.1

$$1 - \mathrm{X}_{EGR} = \frac{P_{cal}T_{dt}\sigma_{cal}(\lambda, T_{cal})\phi_{cal}(\lambda, T_{cal}, P_{cal}, X_{tr-cal})S_{dt}}{P_{dt}T_{cal}\sigma_{dt}(\lambda, T_{dt})\phi_{dt}(\lambda, T_{dt}, P_{dt}, X_{tr-dt})S_{cal}} \tag{6.5}$$

In this equation;

- **a.** P_{cal} and P_{dt} are the in-cylinder pressure data
- **b.** T_{cal} and T_{dt} are calculated from the PLIF images
- **c.** S_{dt}/S_{cal} is calculated from the PLIF images
- **d.** σ_{cal} and σ_{dt} are calculated from [157-159]

$$\sigma(\lambda) = A(T)\exp(-\left(\frac{\lambda - \lambda_c(T)}{\omega(T)}\right)^2) \tag{6.6}$$

where

$$A(T) = 4.67 \times 10^{-23}T + 4.84 \times 10^{-20} \tag{6.7}$$

$$\lambda_c(T) = 0.0184T + 274 \tag{6.8}$$

$$\omega(T) = 1.04 \times 10^{-2} T + 25 \tag{6.9}$$

where 'T' is the calculated temperature from the PLIF images. It is also possible to use the temperature calculated from the in-cylinder pressure data. The latter removes the PLIF temperature errors from the EGR calculation. Figure 6.24 below shows the calculated values of 3-pentanone absorption cross-section as a function of temperature for two excitation wavelengths at 308 and 277 nm.

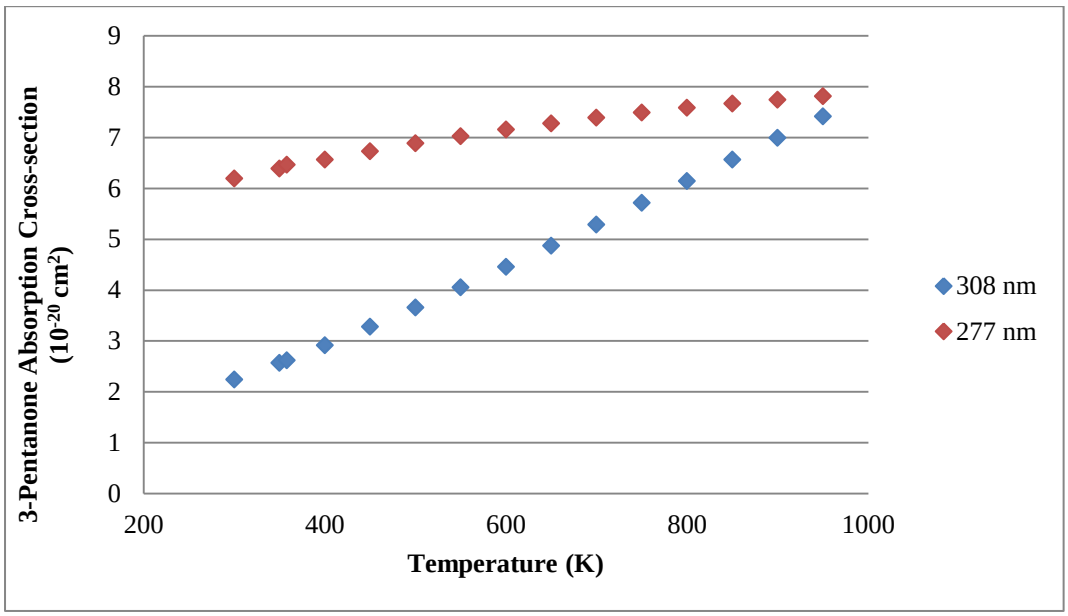

Figure 6.24 3-pentanone absorption cross-section as a function of temperature

e. ϕ_{cal} and ϕ_{dt} are calculated from the frequency quantum yield model [157-159]

In the frequency quantum yield model, the total probability of emission per absorbed photon is expressed by

$$\phi = \phi^1 + \sum_{i=2}^{N-1} (\phi^i \prod_{j=1}^{i-1} P_{Vib}^j) + \phi^N \prod_{j=1}^{N-1} P_{Vib}^j \tag{6.10}$$

where ϕ^i is the probability of emitting a photon and P_{Vib}^j is the probability that the molecule undergoes a vibrational relaxation versus the other possible processes given by

$$\phi^i = \frac{k_f}{k_f + k_{Vib} + k_{NR}^i + k_{O_x}^i} \tag{6.11}$$

$$P_{Vib}^j = \frac{k_{Vib}}{k_f + k_{Vib} + k_{NR}^j + k_{O_x}^j} \tag{6.12}$$

k_f, is the rate of fluorescence emission, k_{vib} is the rate of vibrational relaxation, k_{NR} is the rate of intramolecular non-radiative decay $and\ k_{O_x}$ is the oxygen quenching rate given by

$$k_f = 4.2 \times 10^5 \quad s^{-1} \tag{6.13}$$

$$k_{vib} = \sum_{k=1}^{M} Z_{Coll}^k \, n^k \tag{6.14}$$

$$k_{NR} = \mathrm{A} + B(E - E_1)^3 + C(E - E_2)^{10} + Dexp(-\left(\frac{E - E_3}{W}\right)^2) \tag{6.15}$$

where

Coefficient	Value	Unit
A	3.84×10^8	s^{-1}
B	2.4×10^{-3}	s^{-1}
C	5×10^{-33}	s^{-1}
D	5×10^7	s^{-1}
E_1	2400	cm^{-1}
E_2	1800	cm^{-1}
E_3	1175	cm^{-1}
W	500	cm^{-1}

Table 6.4 Coefficient values for the rate of intramolecular non-radiative decay (k_{NR})

and

$$k_{O_x} = P_{O_x}(E) Z_{Coll}^{O_2} n^{O_2} \tag{6.16}$$

$P_{O_x}(E)$ is the energy dependent probability that a collision will result in deactivation, $Z_{Coll}^{O_2}$ is the collision frequency for collisions of 3-pentanone with oxygen [cm^3s^{-1}], and n^{O_2} is the oxygen number density [cm^{-3}]. In 2011, Cheung [159] corrected the previous $P_{O_x}(E)$ expression developed by Koch [157] as

$$P_{O_x}(E) = P_{O_{x0}} exp(\frac{E}{E_{O_x}}) \tag{6.17}$$

where $P_{O_{x0}} = 0.0023$ and $E_{O_x} = 2000\ cm^{-1}$.

To calculate the FQY from the abovementioned model, a C^{++} code originally developed by Thurber [162] and Koch [157] was adapted and corrected for all the recently modified expressions and parameters' value. The C^{++} code is presented in Appendix J.

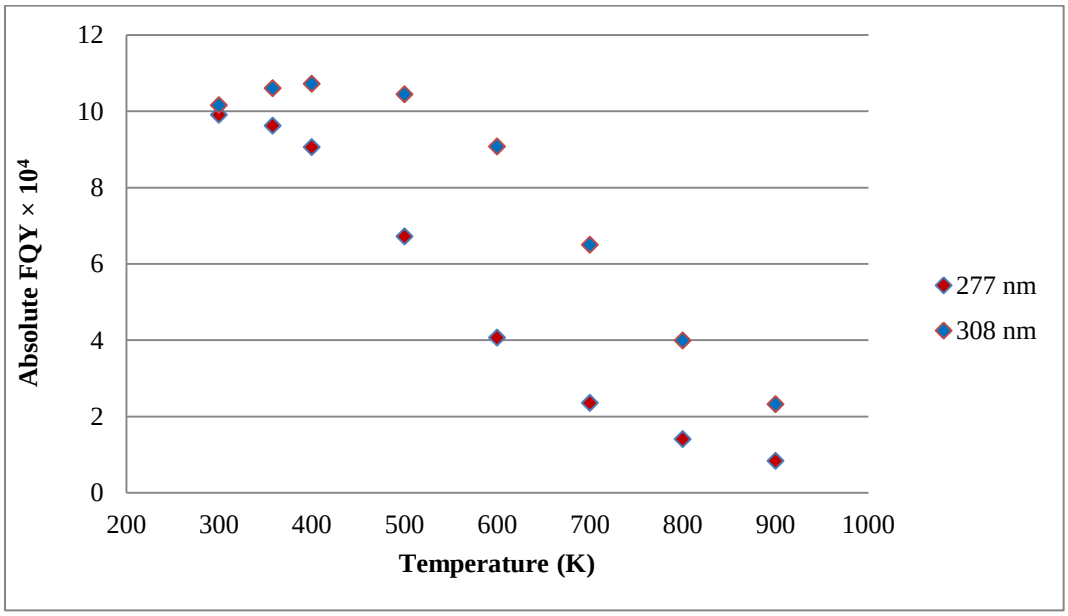

Figure 6.25 Absolute frequency quantum yield as a function of temperature for two excitation wavelengths at 308 and 277 nm. The mixture pressure, oxygen partial pressure and tracer mole fraction were taken as 1 *bar*, 0.213 *bar* and 1% respectively.

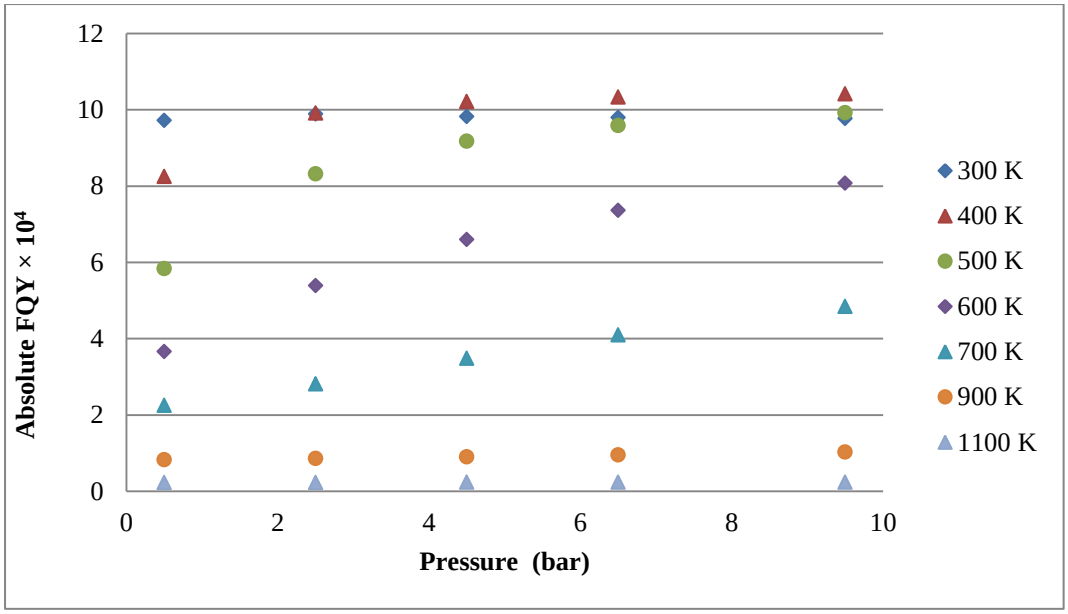

Figure 6.26 Absolute frequency quantum yield of the excitation wavelength at 277 nm as a function of pressure at different mixture temperature. The oxygen partial pressure and tracer mole fraction were taken as 0.213 *bar* and 1% respectively

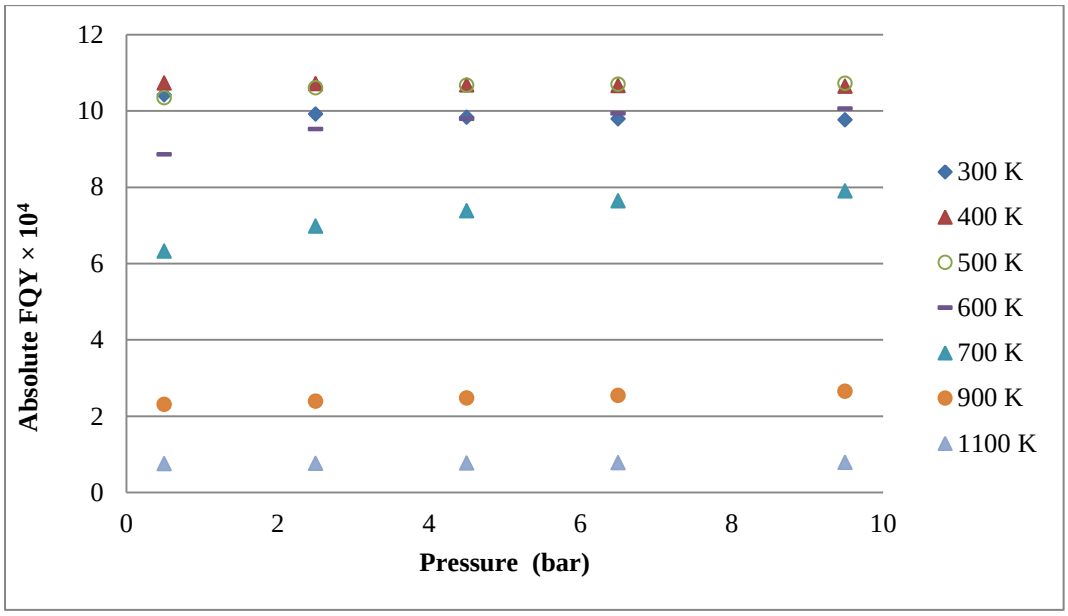

Figure 6.27 Absolute frequency quantum yield of the excitation wavelength at 308 nm as a function of pressure at different mixture temperature. The oxygen partial pressure and tracer mole fraction were taken as 0.213 *bar* and 1% respectively

6.3.5.3.1 Simultaneous T/EGR Measurements Sample Calculation

The 2-line PLIF imaging was performed at nine different crank angles on the compression stroke and the DIFs were captured and post processed to calculate the in-cylinder temperature. The in-cylinder pressure at each imaged crank angle was obtained by averaging 100 cycles of the recorded pressure data. The absorption cross sections and frequency quantum yields were calculated for the excitation wavelength at 308 nm using temperature values from the PLIF measurements. For the FQY calculation the oxygen partial pressure and 3-pentanone mole fraction were taken as 0.213 bar and 1% respectively. Finally the fluorescence signal ratios of S_{dt}/S_{cal} were obtained by first setting a ROI (501×501 pixels) on the DIFs and calculating the average pixel values within the assigned region. Table 6.5 shows the calculated values of the abovementioned parameters for 2-line PLIF simultaneous T/EGR measurements.

		94.5 bTDC	80 bTDC	73 bTDC	65.5 bTDC	58.5 bTDC	51 bTDC	44 bTDC	37 bTDC	34.5 bTDC
P_{cal} ($\times 10^5\ Pa$)		1.75	2.32	2.73	3.27	3.99	5.14	6.55	8.49	9.15
P_{dt} ($\times 10^5\ Pa$)		1.68	2.20	2.57	3.06	3.69	4.70	5.90	7.53	8.08
T_{cal} (K)	PLIF	**353.6**	**381.7**	**400.2**	**429.4**	**446.4**	**480.9**	**526.1**	**585.9**	**608.3**
	P data	371.7	403.8	423.5	446.3	468.8	509.3	546.5	589.4	609.3
T_{dt} (K)	PLIF	**484.8**	**518.9**	**550.3**	**563.1**	**598.7**	**628.3**	**665.0**	**720.3**	**736.6**
	P data	475.0	507.9	528.7	556.9	580.9	618.6	656.2	699.1	718.7
σ_{cal} ($\times 10^{-20}\ cm^2$)		2.589	2.782	2.913	3.124	3.249	3.509	3.859	4.338	4.521
σ_{dt} ($\times 10^{-20}\ cm^2$)		3.539	3.803	4.051	4.153	4.442	4.685	4.991	5.457	5.595
ϕ_{cal} ($\times 10^4$)		10.435	10.620	10.702	10.745	10.751	10.722	10.606	10.195	9.925
ϕ_{dt} ($\times 10^4$)		10.613	10.471	10.240	10.152	9.720	9.281	8.554	7.137	6.684
S_{dt}/S_{cal}		0.492	0.479	0.417	0.402	0.387	0.357	0.348	0.279	0.270
Calculated EGR (%)		**57.20**	**57.48**	**62.83**	**62.88**	**64.07**	**65.73**	**65.26**	**70.95**	**71.45**

Table 6.6 Two-line PLIF simultaneous T/EGR sample calculatoin

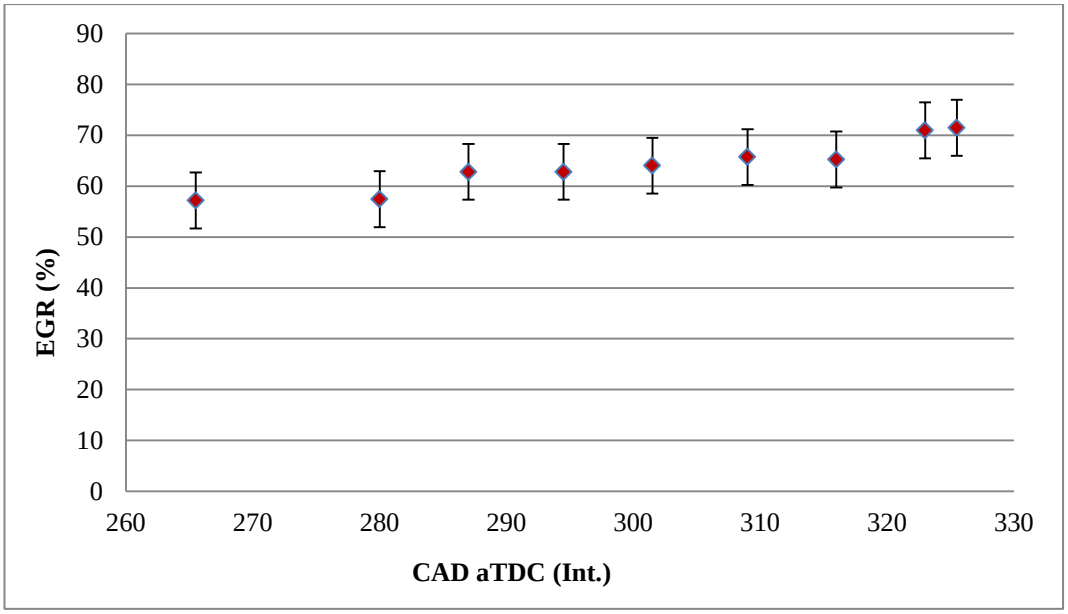

Figure 6.28 Calculated EGR values from the 2-line PLIF measurements

To assess inaccuracy in the PLIF EGR measurements, the calculated EGR values of the same crank angles from different cycles were compared. The PLIF EGR measurement inaccuracy was found to be less than 11%. The main reasons for the higher inaccuracy in EGR measurements compared to the temperature measurements can be summarized as;

i. influence of the PLIF temperature measurements' inaccuracy
ii. inaccuracy of the in-cylinder pressure measurements
iii. inaccuracy in calculation of the absorption cross section and frequency quantum yield from the developed models
iv. engine thermodynamic states variation between different runs

It should be noted that the slight increase in the calculated EGR content with the crank angle through the TDC shown in Figure 6.28 can be associated with possibly a slight EGR vertical stratification due to the lack of in-cylinder tumble motion.

6.3.5.3.2 Two Dimensional T/EGR Maps

Twelve crank angles shown in Figure 6.29 were selected for single frame visualization of in-cylinder T/EGR stratification. The T/EGR calculations were only carried out for the images during the compression stroke.

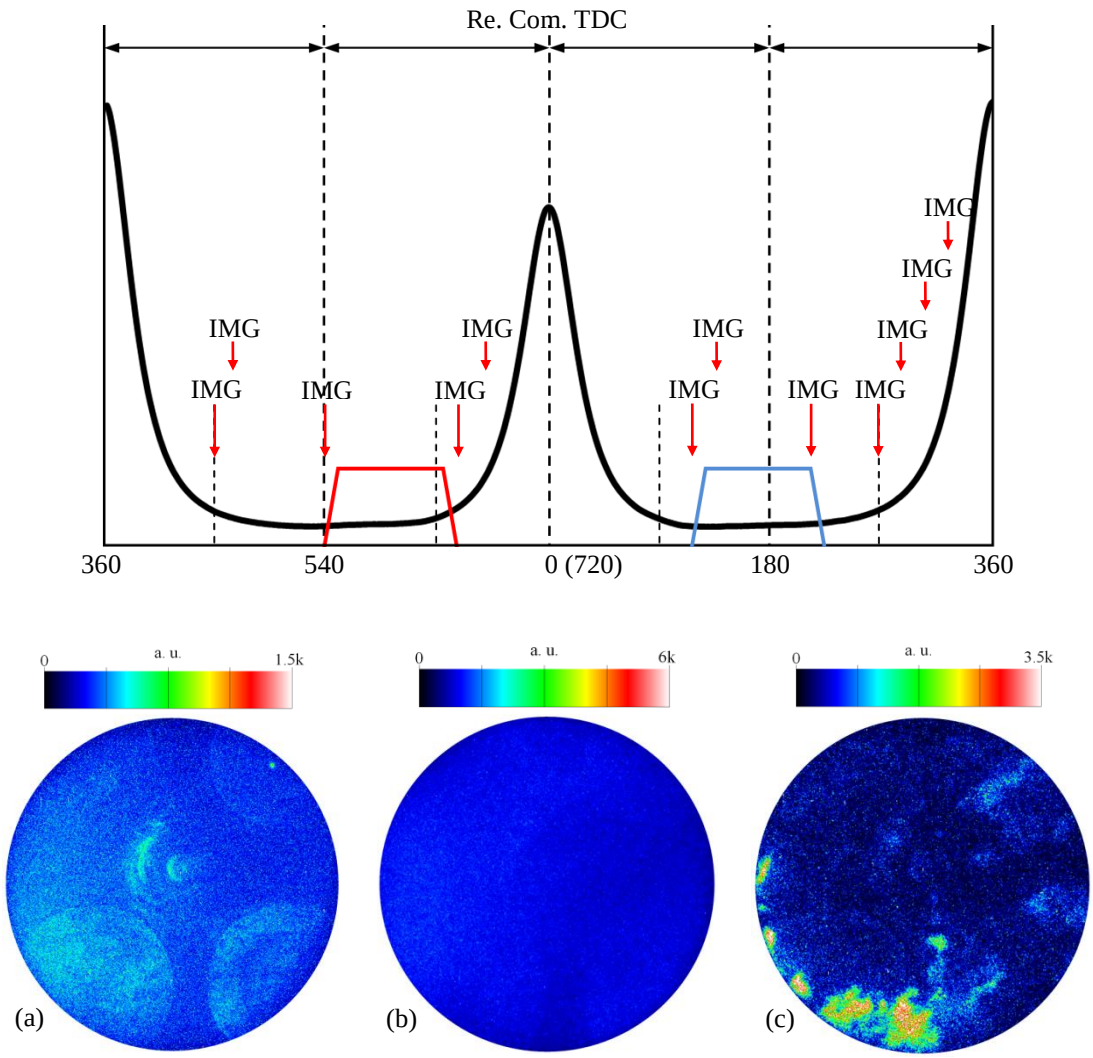

Figure 6.29 Top: Two-line PLIF T/EGR image timing, **Bottom:** Sample images at 90 °CA aTDC (Com.) (a) background, (b) PI (c) DI

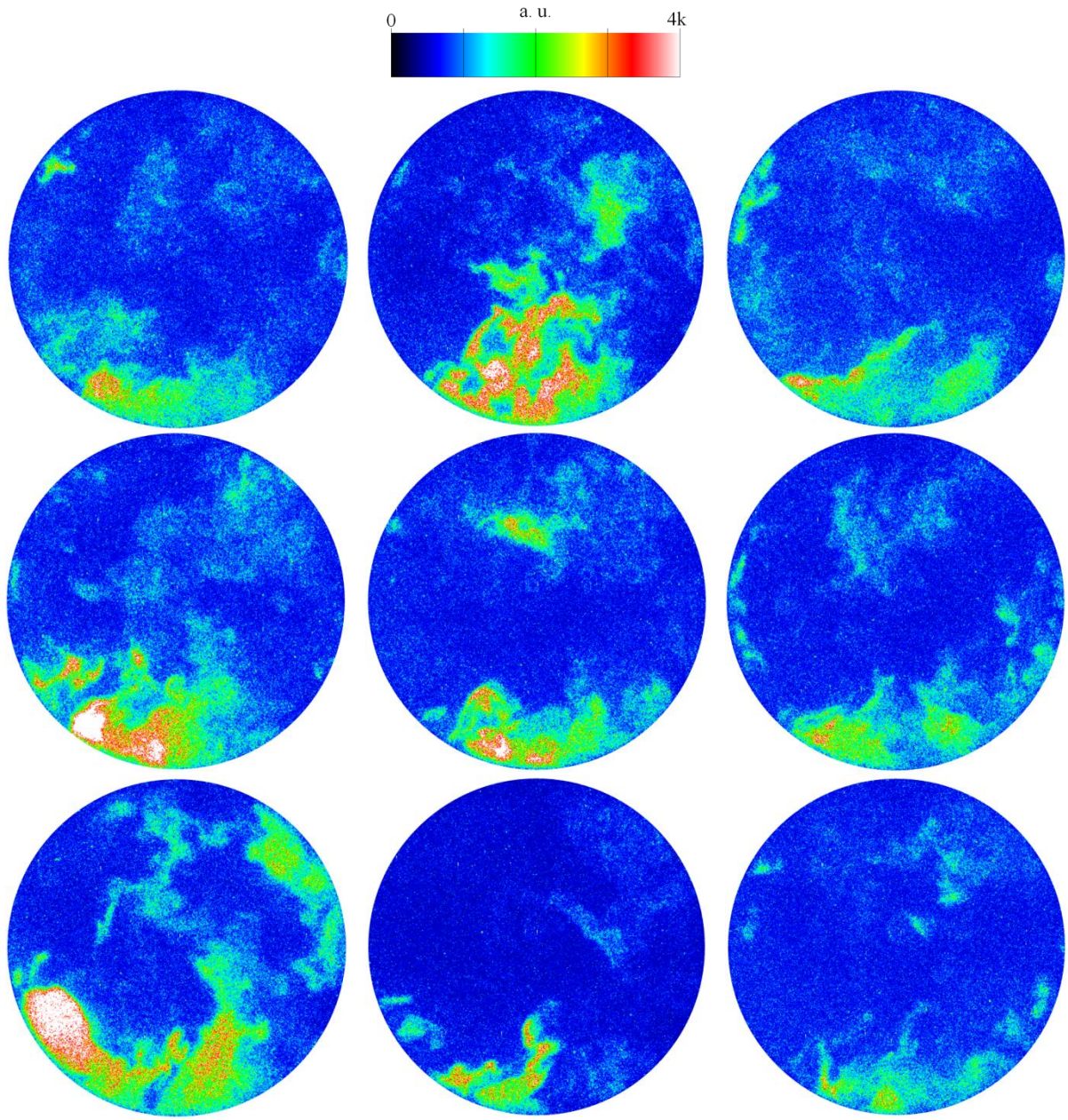

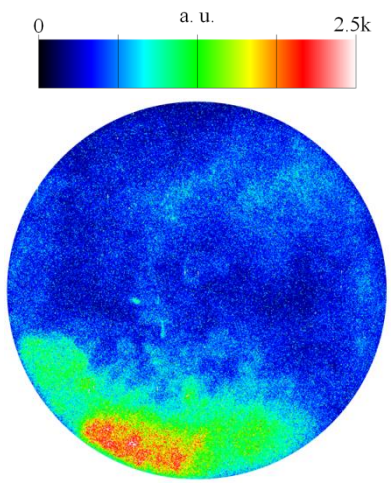

Figure 6.30 Top: Single-shot images at 90 °CA aTDC (Com.) showing fluorescence from unburned tracer during operations with a lower in-cylinder peak temperature or fluorescence from exhaust gases for operations with a higher in-cylinder peak temperature. In the latter case the fluorescence signal could be from aldehyde species, such as formaldehyde and acetaldehyde which have the mole fraction in exhaust gases similar to the tracer mole fraction. Also both absorb and emit radiation in wavelength bands similar to those for 3-pentanone [160]**; Left**: Average of 20 frames

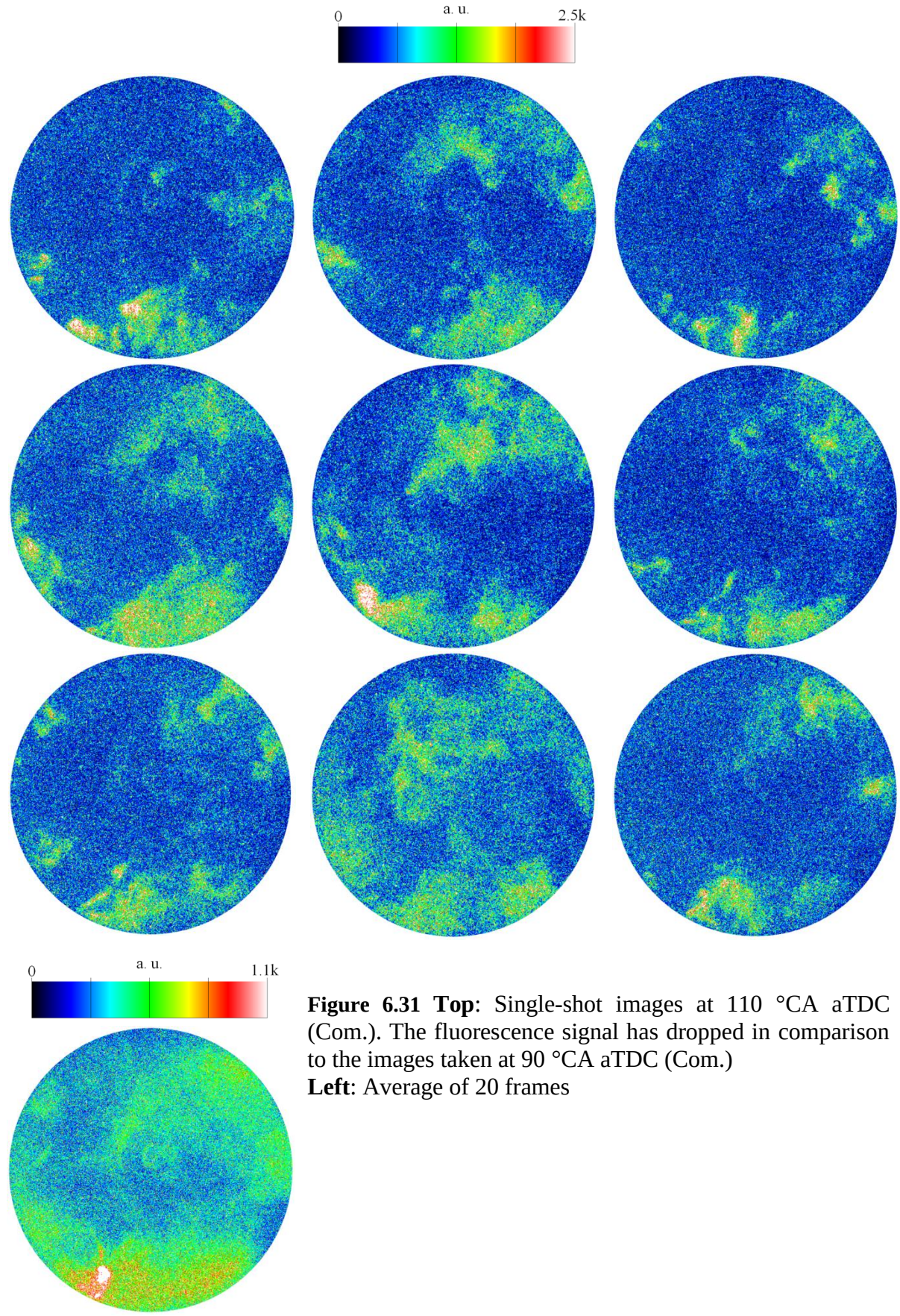

Figure 6.31 Top: Single-shot images at 110 °CA aTDC (Com.). The fluorescence signal has dropped in comparison to the images taken at 90 °CA aTDC (Com.)
Left: Average of 20 frames

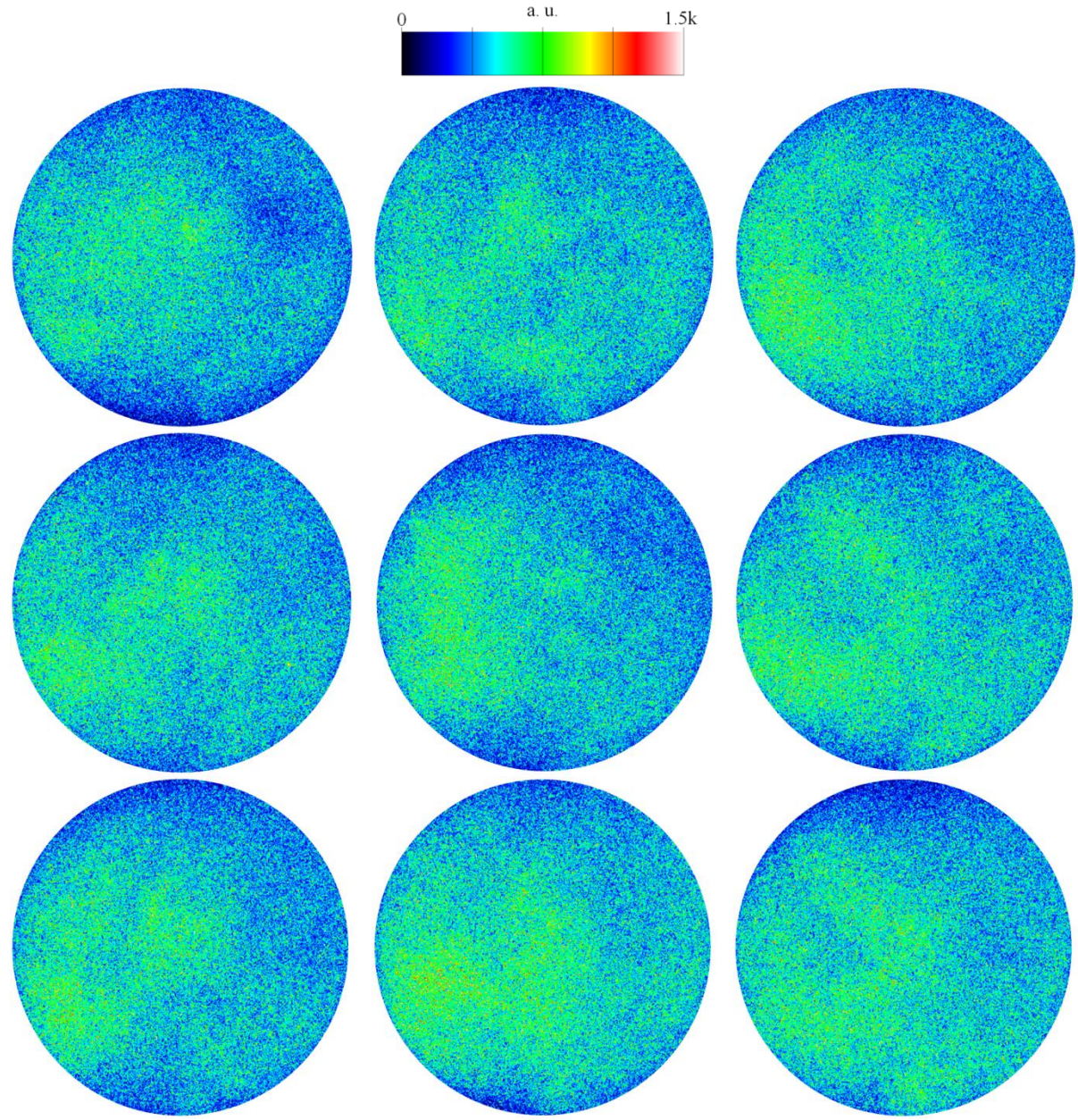

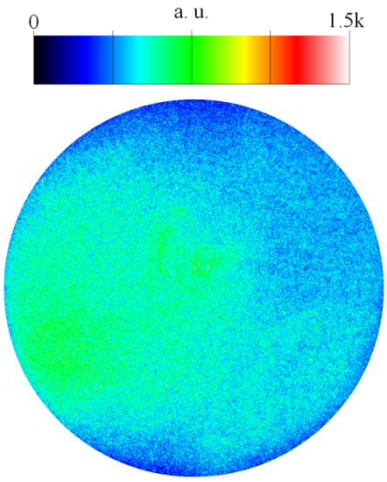

Figure 6.32 Top: Single-shot images at 180 °CA aTDC (Com.) at the exhaust vale opening (EVO). As the piston was at the BDC, these images cannot represent in-cylinder exhaust gas distribution in the sampling area.
Left: Average of 20 frames

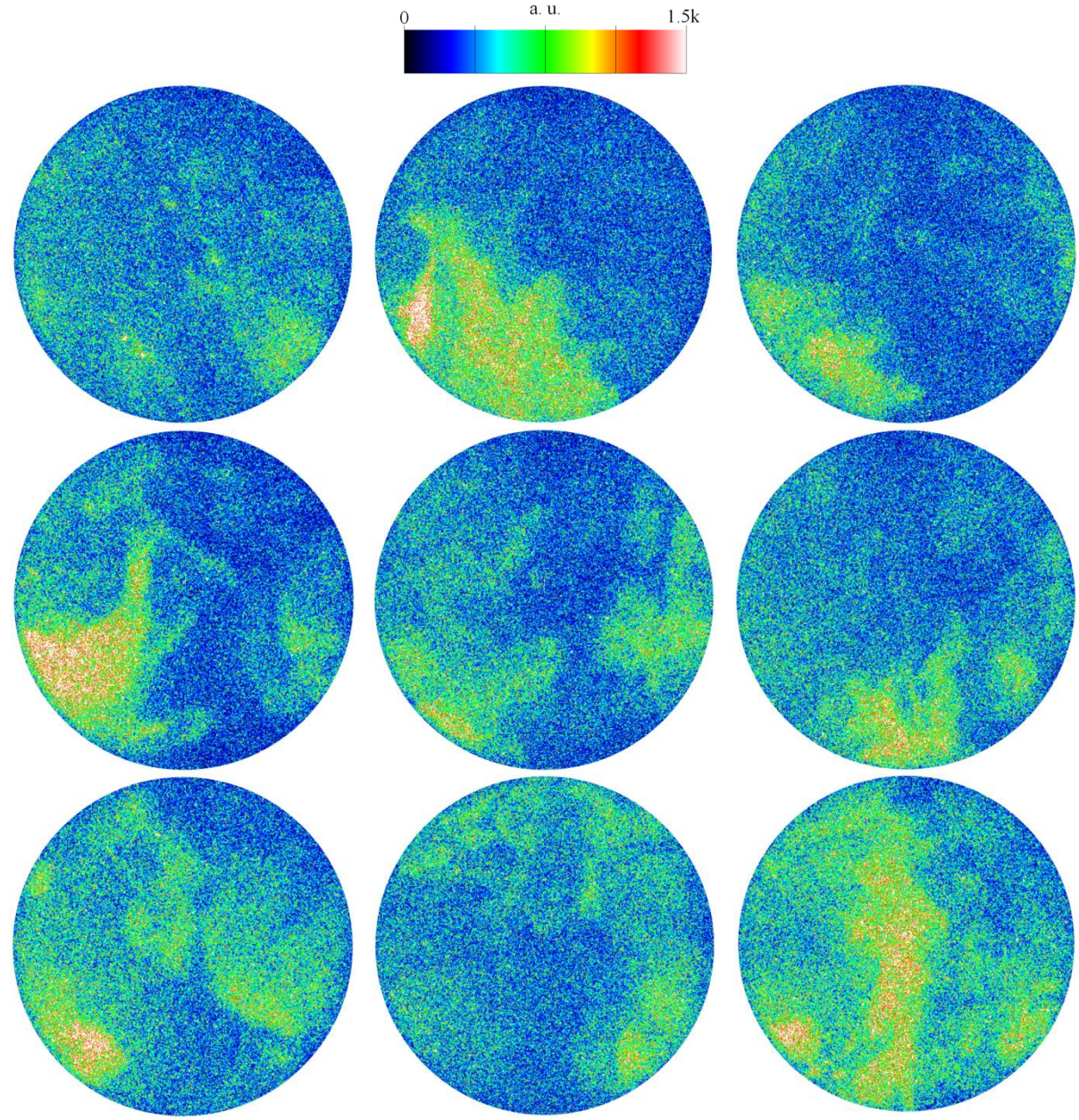

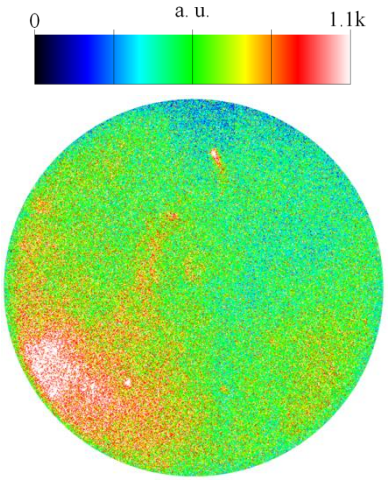

Figure 6.33 Top: Single-shot images at 80 °CA bTDC (R.Com.) at the exhaust vale closing (EVO), showing a stratified distribution of exhaust gases at the imaging plane. **Left**: Average of 20 frames

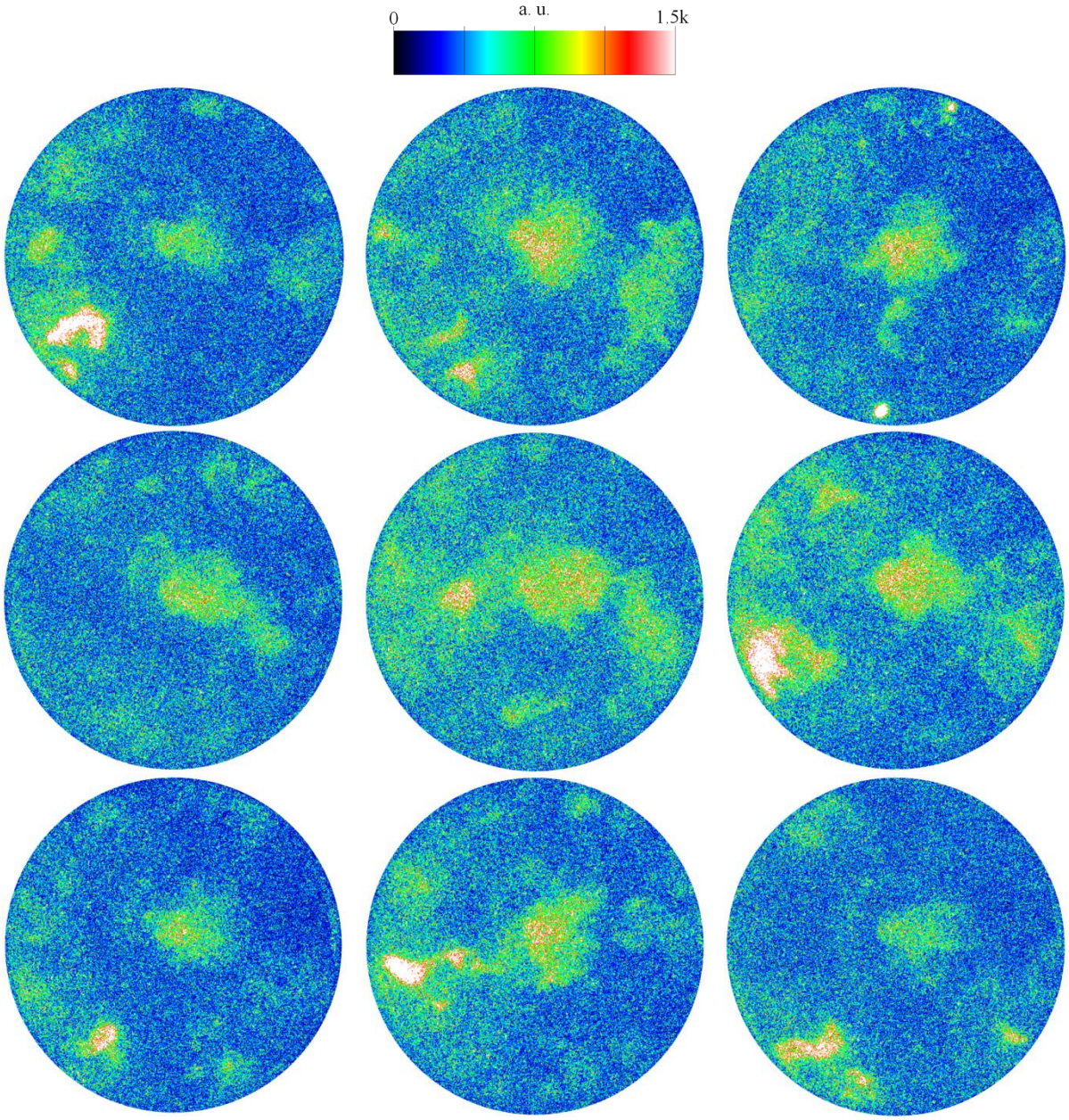

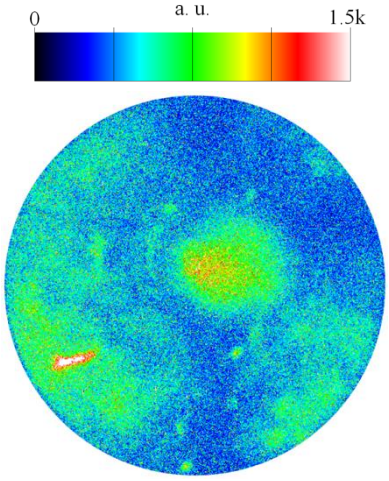

Figure 6.34 Top: Single-shot images at 50 °CA bTDC (R.Com.), showing fuel injection event whit SOI at 80 °CA bTDC (actual ignition event is at 73 °CA bTDC) during the NVO. The most dominate scattering type in these images is the Mie scattering from the injected fuel droplets.
Left: Average of 20 frames

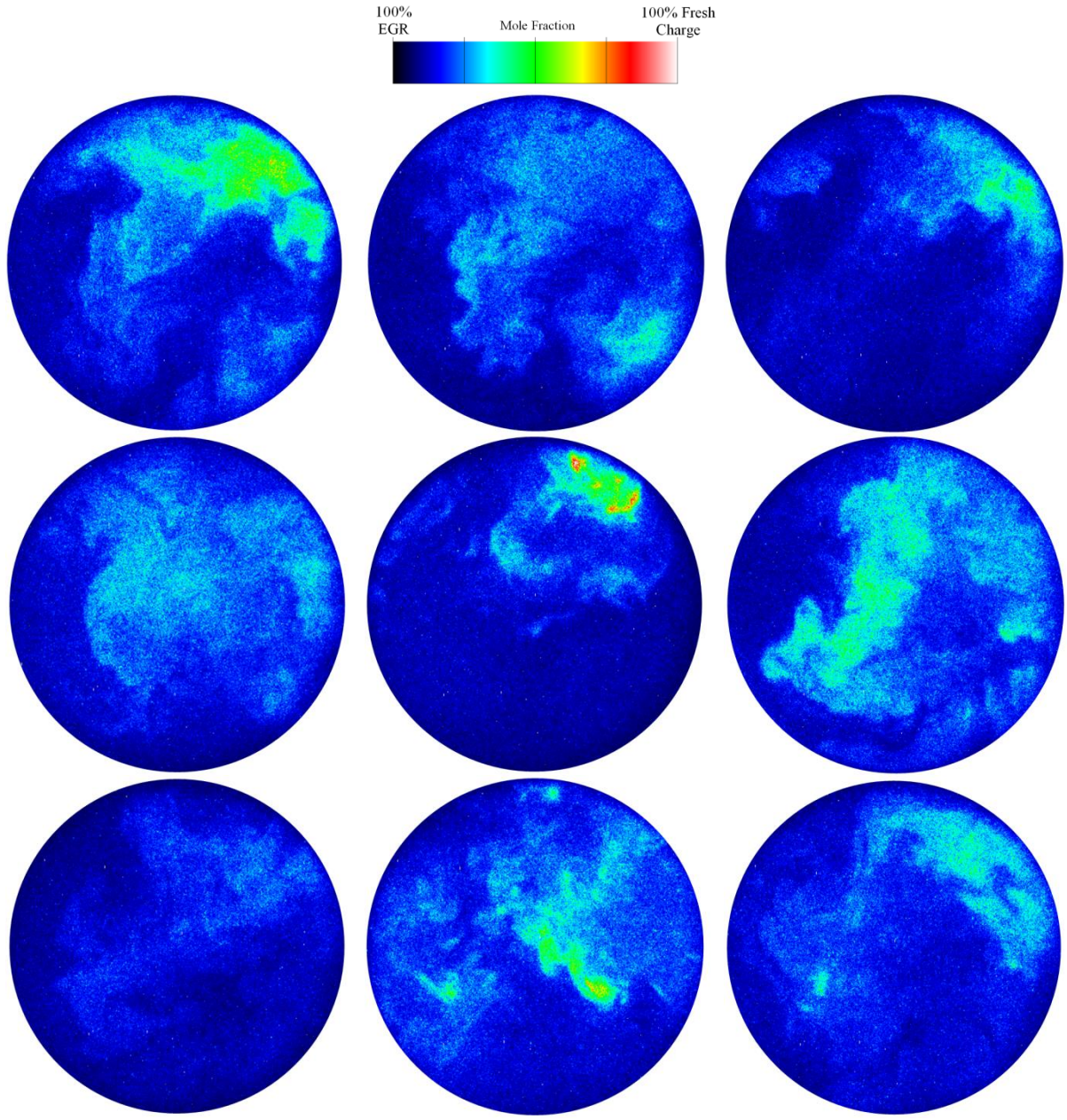

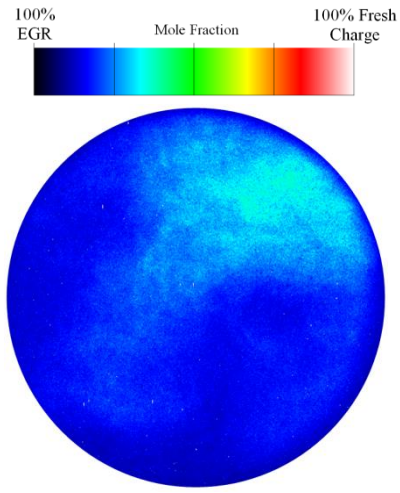

Figure 6.35 Top: Single-shot images at 120 °CA aTDC (R.Com.) at the intake valve opening (IVO), showing the introduction of fresh air-tracer mixture into the cylinder. Considering the position of the intake valves at the bottom of the images, an in-cylinder swirl motion is observed.
Left: Average of 20 frames

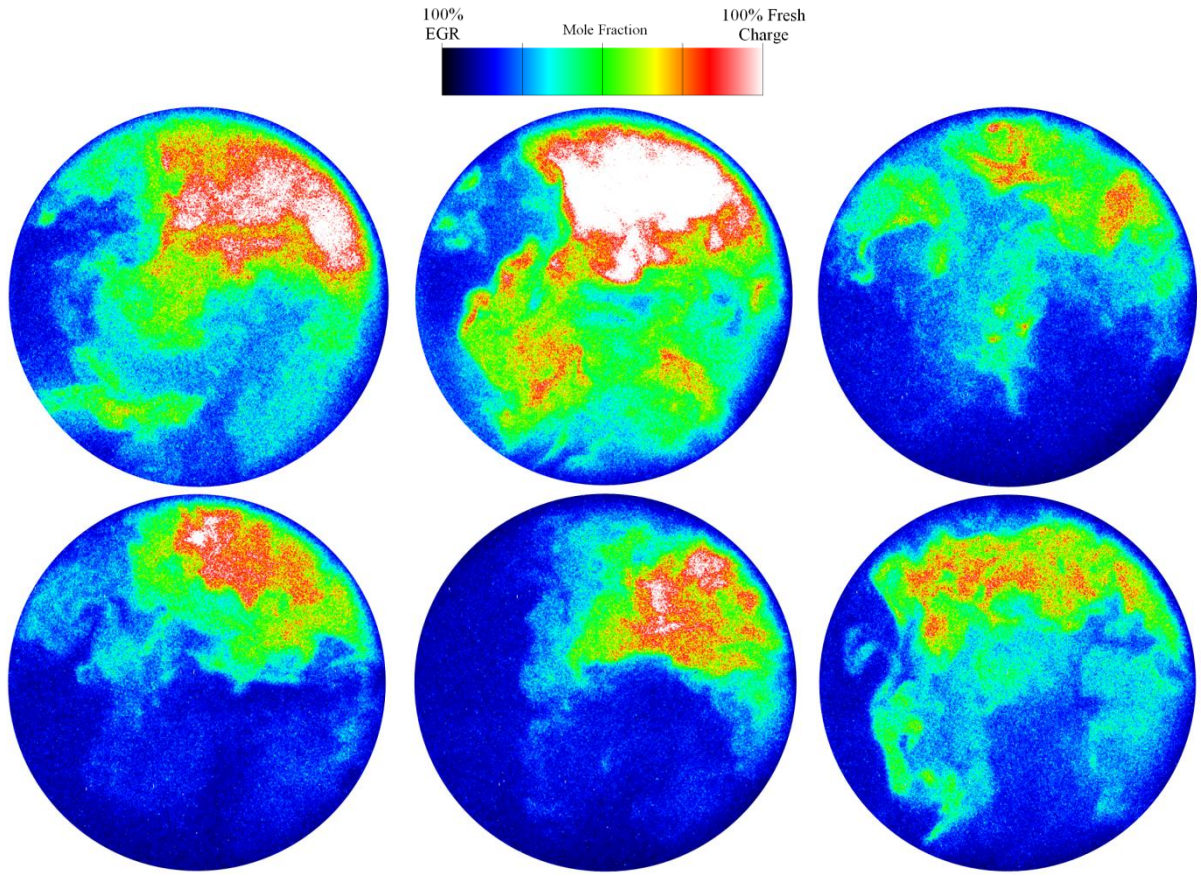

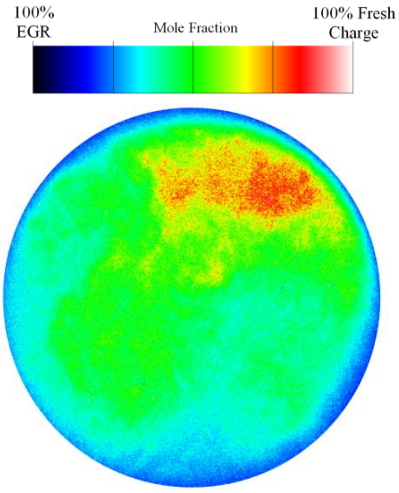

Figure 6.36 Top: Single-shot images at 140 °CA aTDC (R.Com.) **Left**: Average of 20 frames

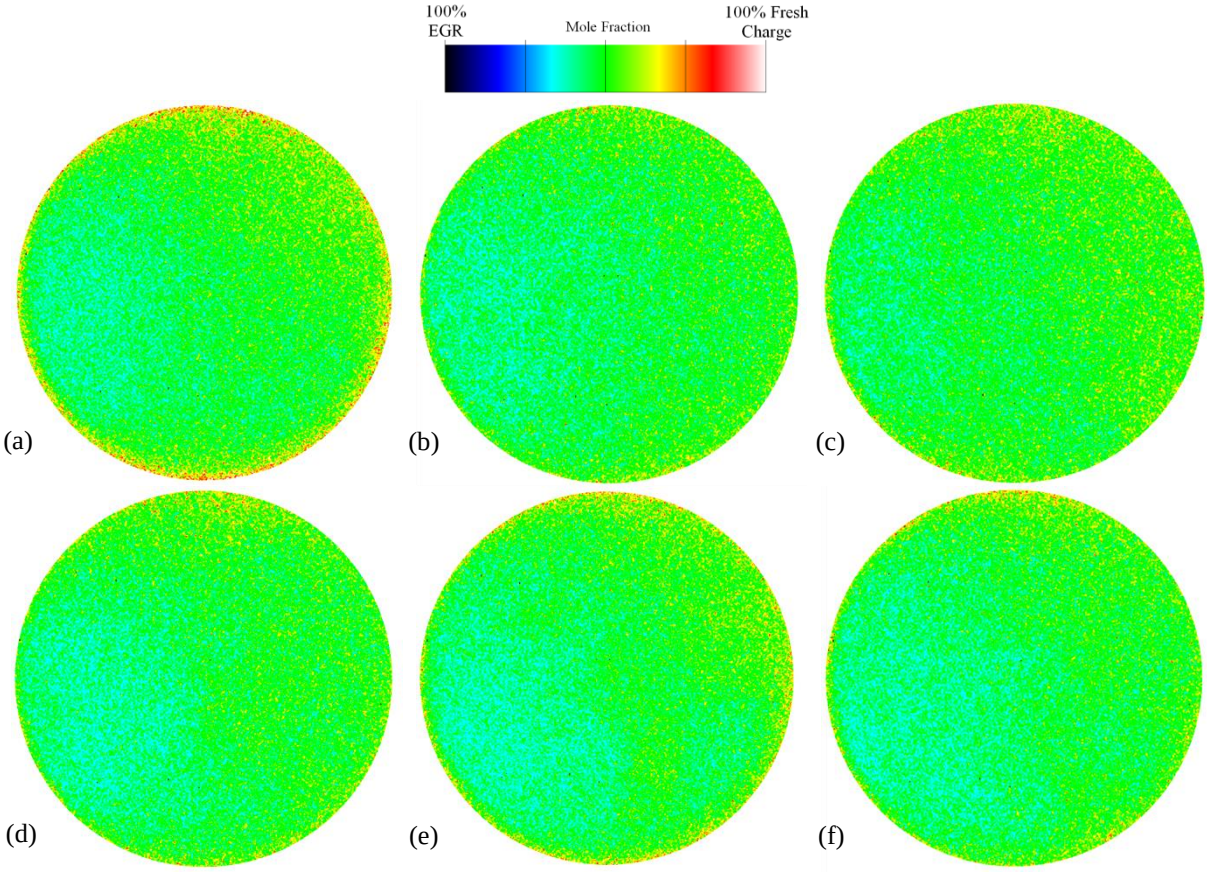

Figure 6.37 Top: Single-shot images of the EGR mixture with the fresh charge taken at 90 °CA bTDC (Com.), showing slight stratification at the compression stroke.

Bottom: Single-shot simultaneous temperature images at 90 °CA bTDC (Com.). The higher intensity ratio seen in the small region shown at the upper left corner of these images is due to the higher 308/277 ratio. Higher temperature is observed at bottom right corner of these images which is due to higher consecration of the EGR in this area.

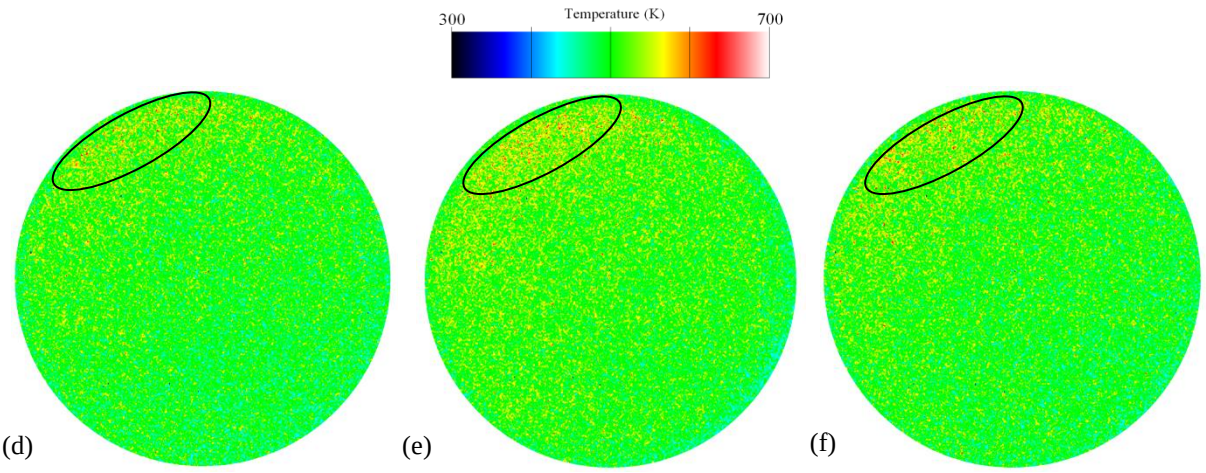

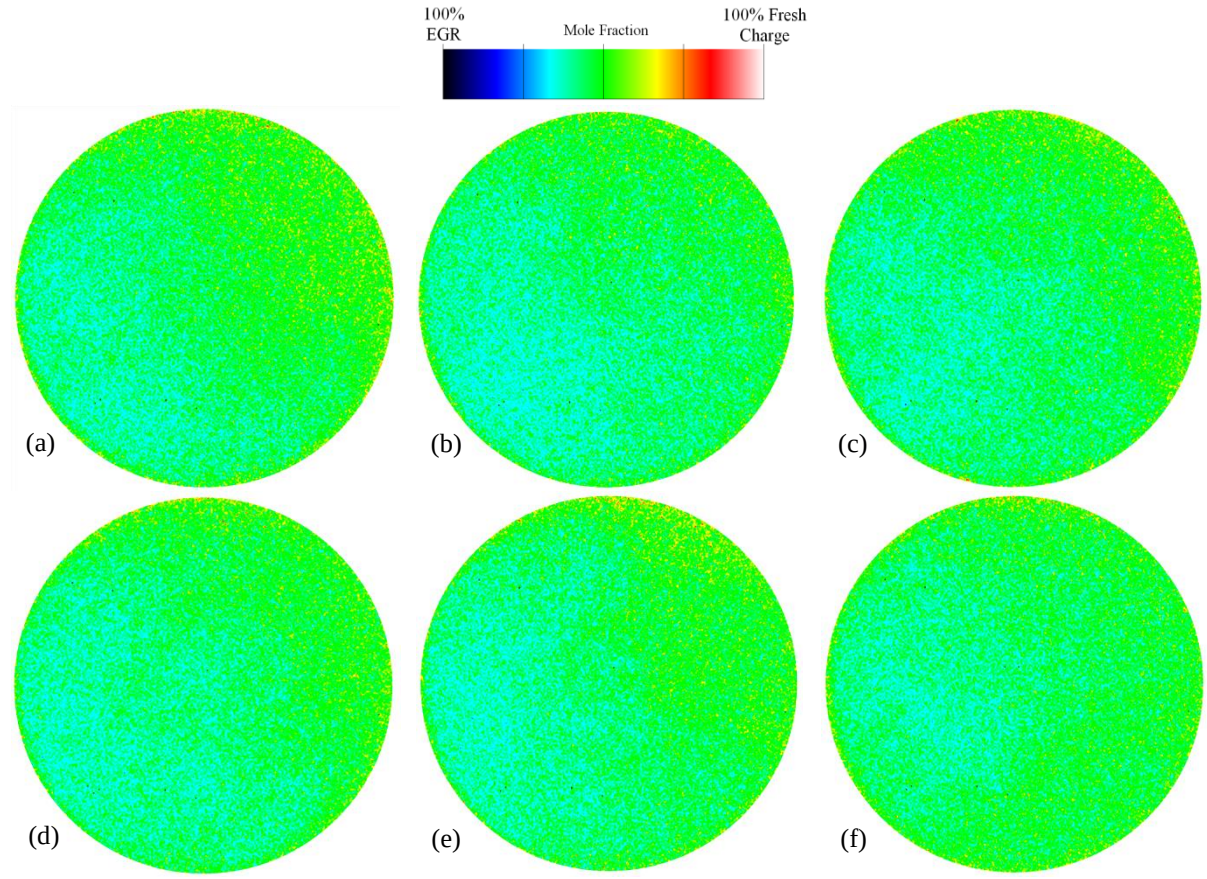

Figure 6.38 Top: Single-shot images of the EGR mixture with the fresh charge taken at 70 °CA bTDC (Com.)
Bottom: Single-shot simultaneous temperature images at 70 °CA bTDC (Com.)

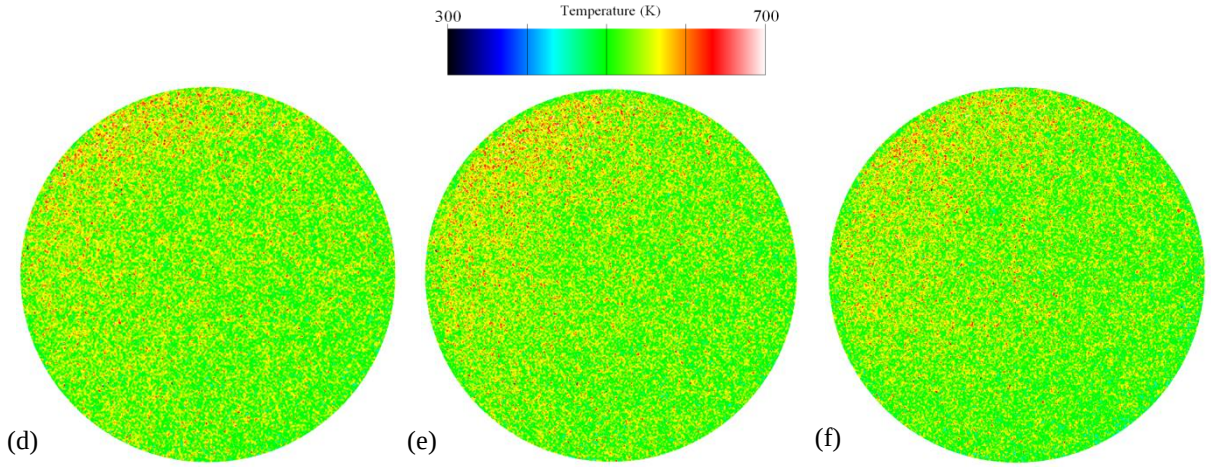

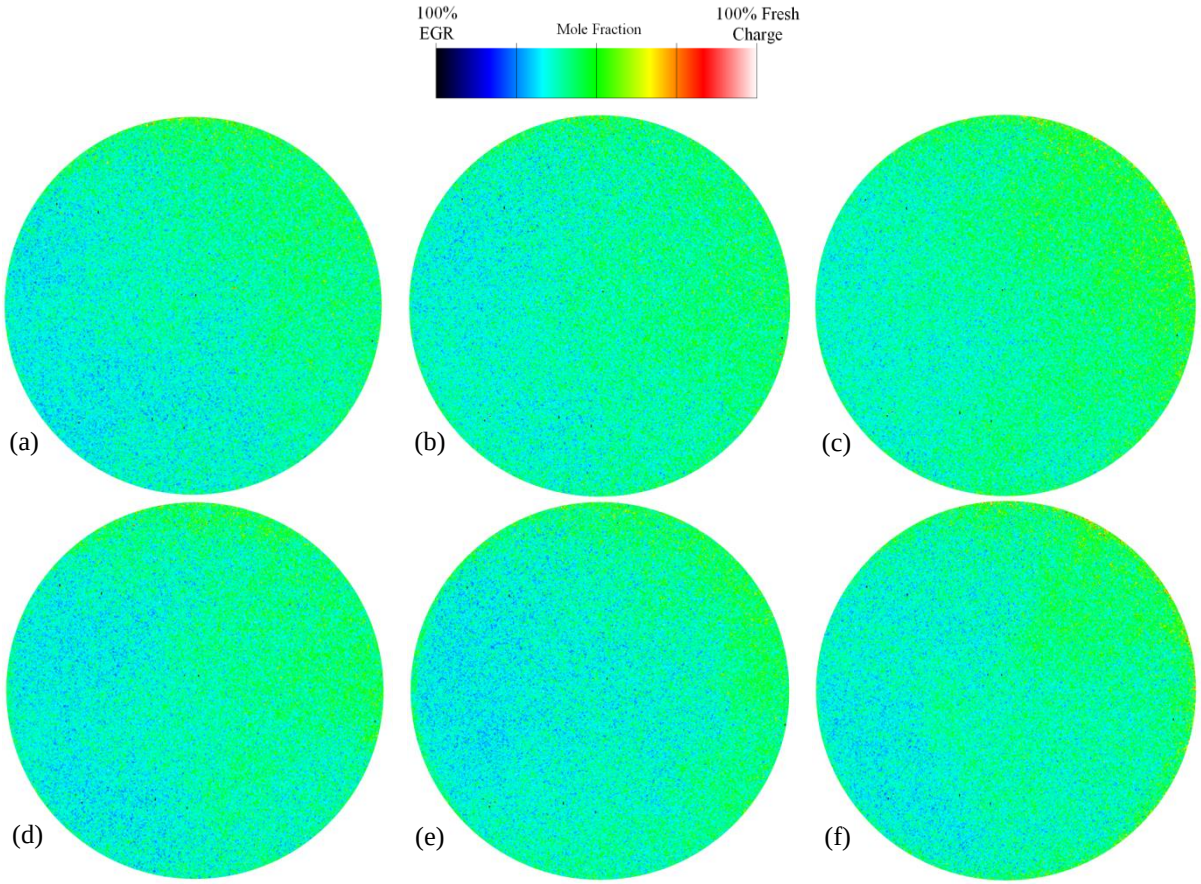

Figure 6.39 Top: Single-shot images of the EGR mixture with the fresh charge taken at 50 °CA bTDC (Com.).
Bottom: Single-shot simultaneous temperature images at 50 °CA bTDC (Com.)

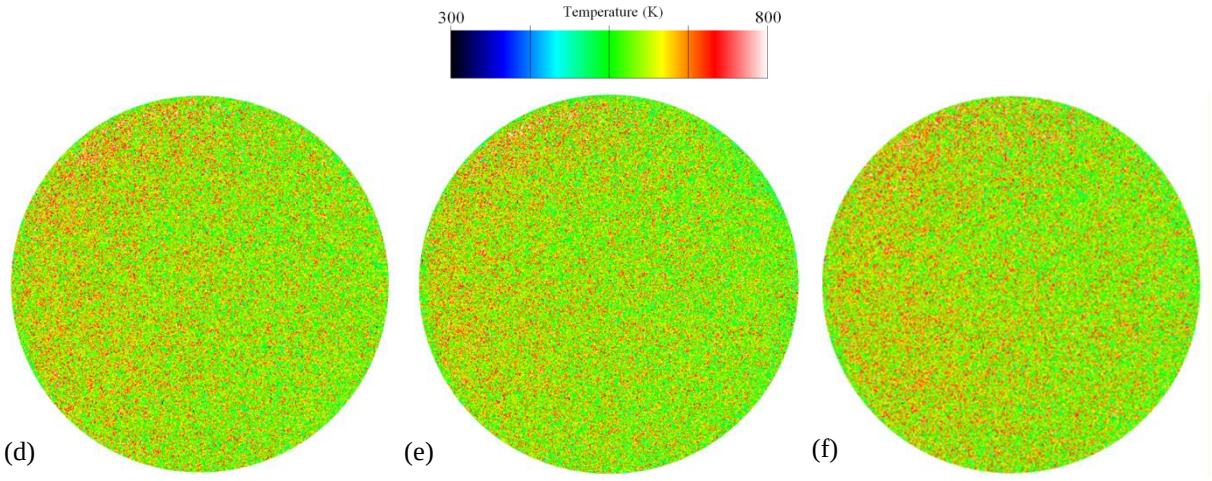

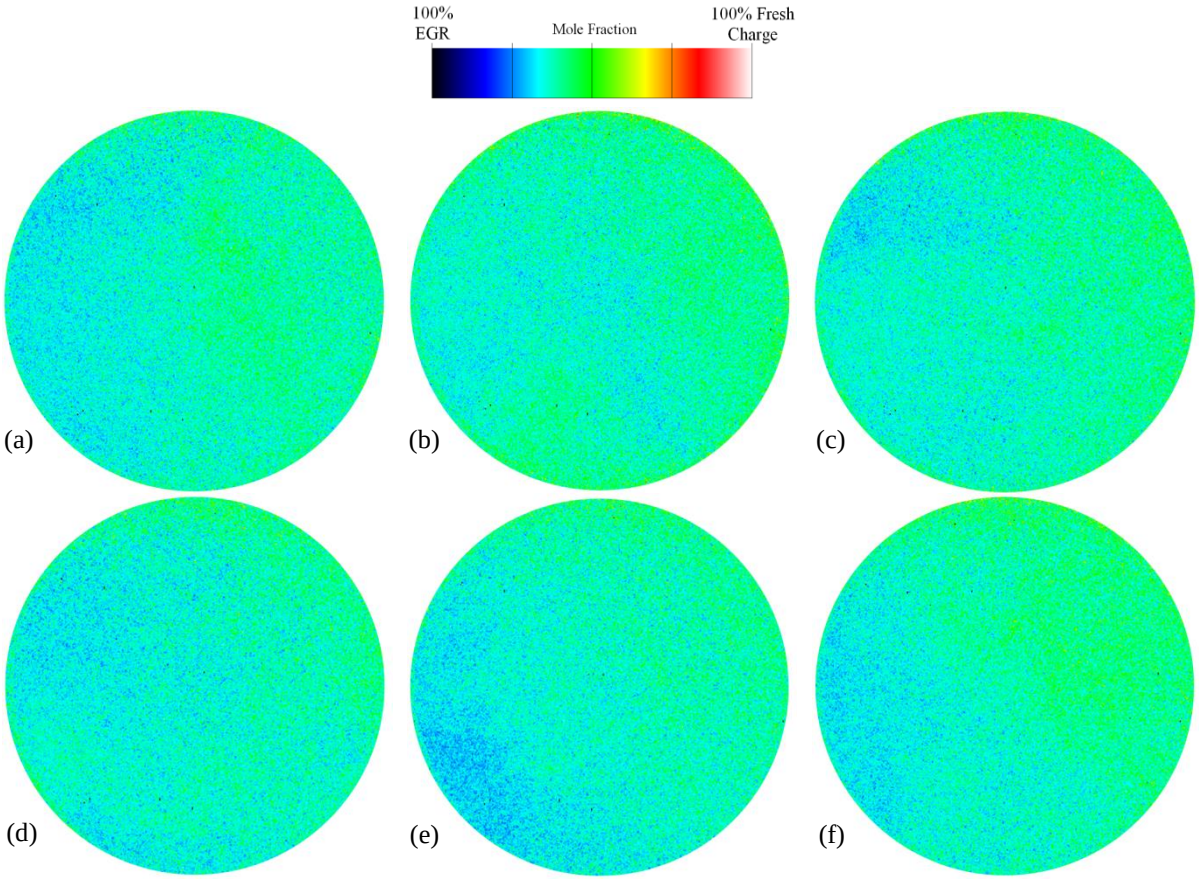

Figure 6.40 Top: Single-shot images of the EGR mixture with the fresh charge taken at 35 °CA bTDC (Com.).
Bottom: Single-shot simultaneous temperature images at 35 °CA bTDC (Com.). The dashed-line square shows the defined region of interest (ROI) of 501×501 pixels size used for calculating the temperature probability density functions (PDFs).

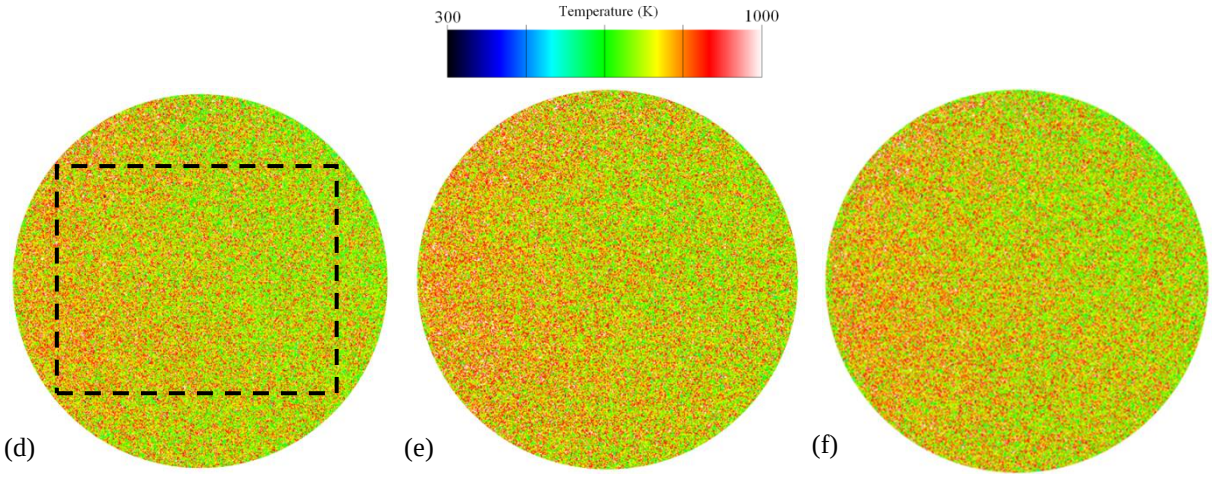

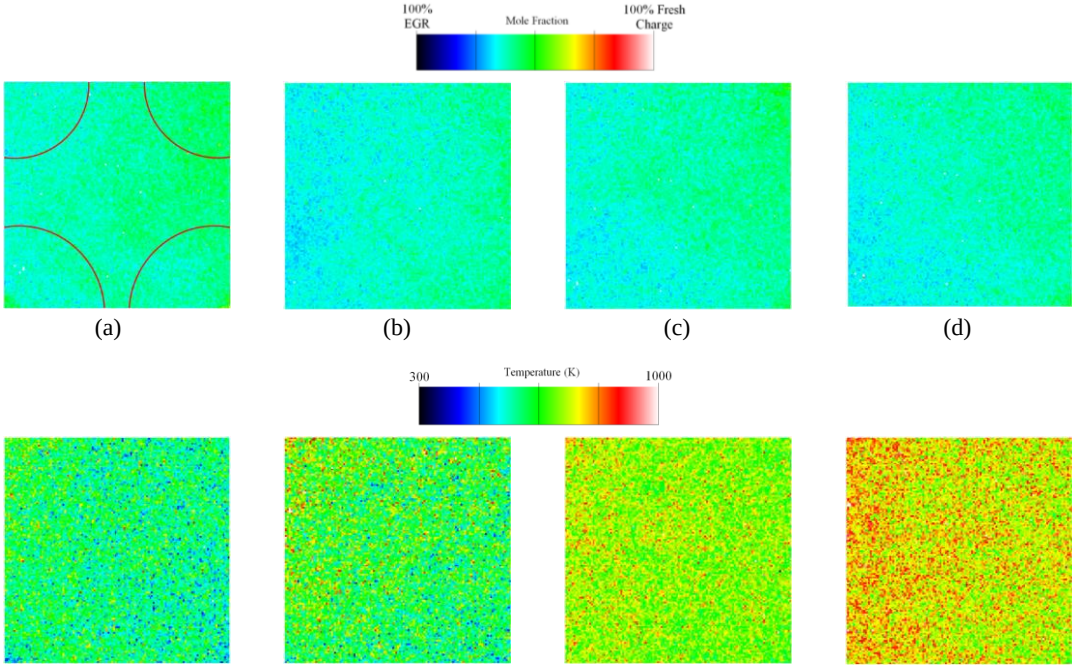

Fig. 6.41 EGR (upper row) and temperature (lower row) maps of the assigned ROI at (a) 90 (b) 70 (c) 50 and (d) 35 °CA bTDC in the compression stroke. For better visualization pixels are grouped 4×4.

6.3.5.3.3 Temperature and EGR Probability Density Functions

Temperature probability density functions (PDFs) were calculated from the single-shot images. For a precise calculation, a region of interest (ROI) 501×501 pixels was defined and the pixels values within this region were processed. The PDFs were calculated at 90, 70, 50 and 35 °CA bTDC during the compression stroke.

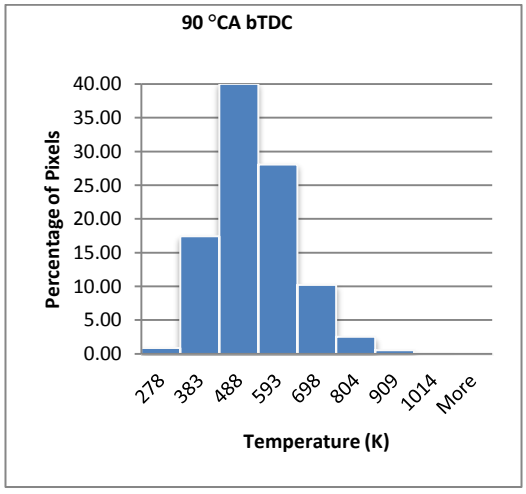

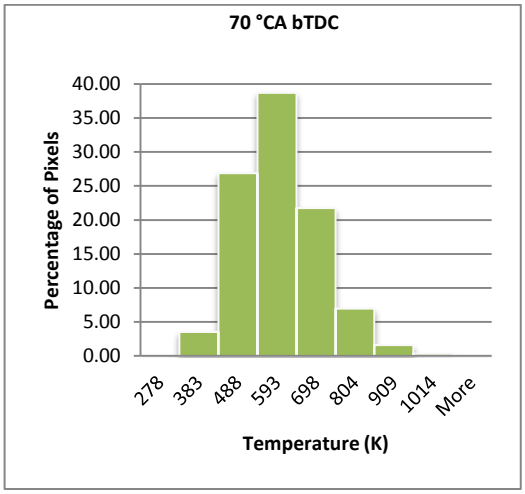

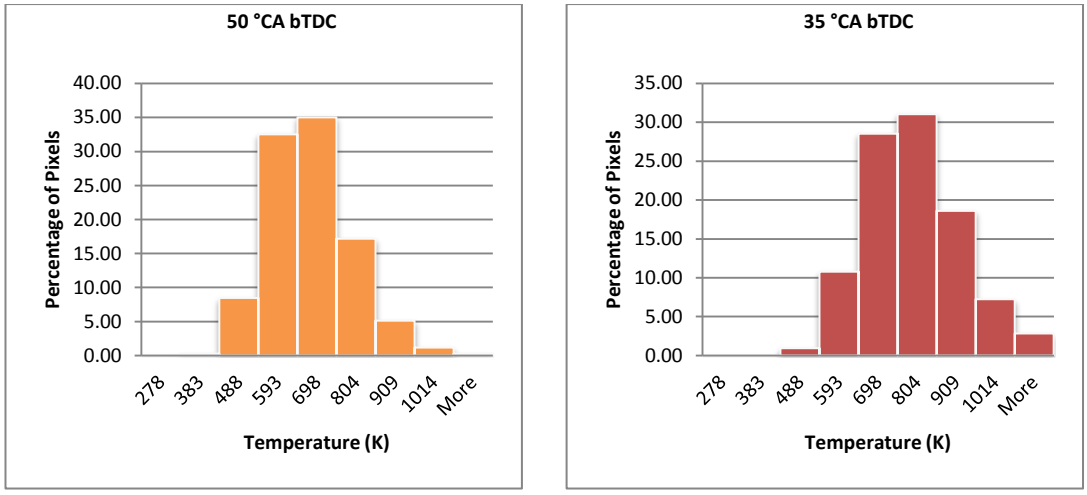

Figure 6.42 Calculated temperature PDFs

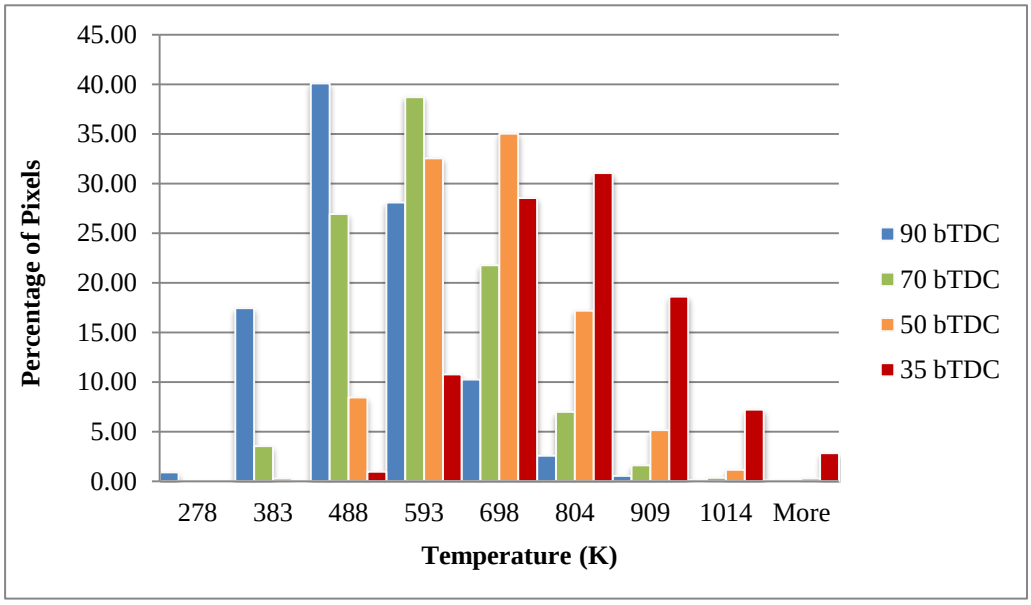

Figure 6.43 Comparison of the temperature PDFs at 90, 70, 50 and 35 °CA bTDC (Com.).

The temperature probability density functions show a Gaussian distribution which can be expressed by [173]

$$f(T;\mu,\sigma^2) = \frac{1}{\sigma\sqrt{2\pi}} e^{-\frac{1}{2}(\frac{T-\mu}{\sigma})^2} \tag{6.18}$$

where T is the temperature, μ is the mean temperature value and σ is the standard deviation. The σ^2 is defined as the variance which is a measure of how far a set of temperature values at each crank angle is spread out. It can be seen that as the

temperature mean value increases as we get closer to the TDC, the temperature variance is almost constant for all the imaged crank angles. In addition, it is noted that the temperature distribution is more skewed to higher temperature at 90°CA bTDC, which corresponds to the presence of inhomogeneous mixed hot residual gas. The skewness reduces as the crank angle decreases. At 35 °CA bTDC, the temperature distribution becomes more symmetrical as the thermal stratification between hot residual gas and fresh cold air is diminished.

The EGR PDFs were calculated for a ROI of 501×501 pixels on a single odd image (illumination at 308 nm) of DIFs at 90, 70, 50 and 35 °CA bTDC during the compression stroke. All the values for pressure, temperature, absorption cross section and frequency quantum yield at the selected crank angles were calculated as described earlier in section 6.3.5.3 for both the MPI and DI data images. The S_{dt}/S_{cal} values were obtained from the fluorescence signal ratio of DI data images to the MPI data images of the same crank angle after subtracting their averaged background image.

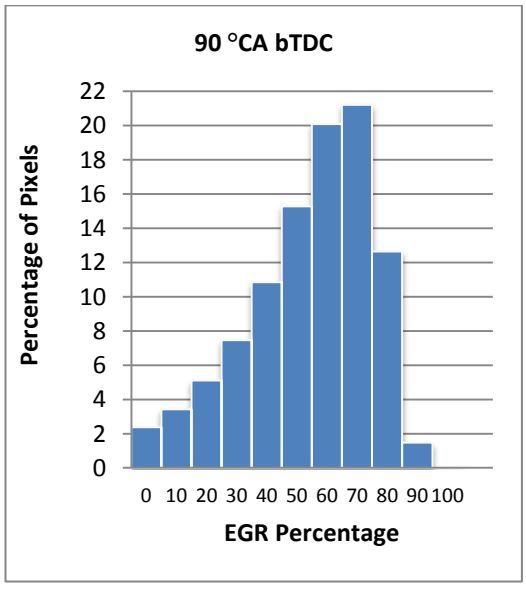

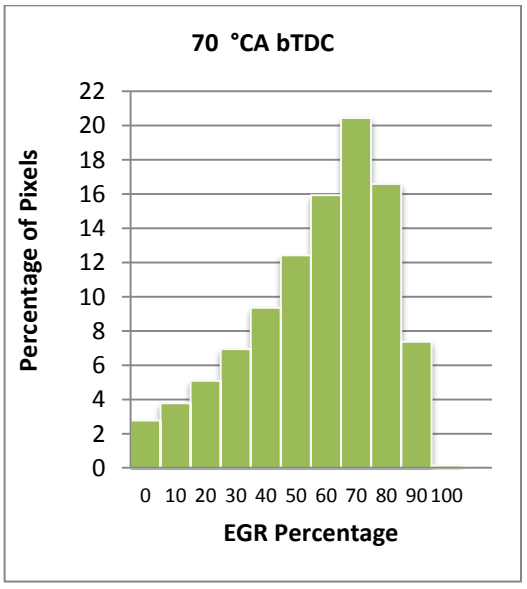

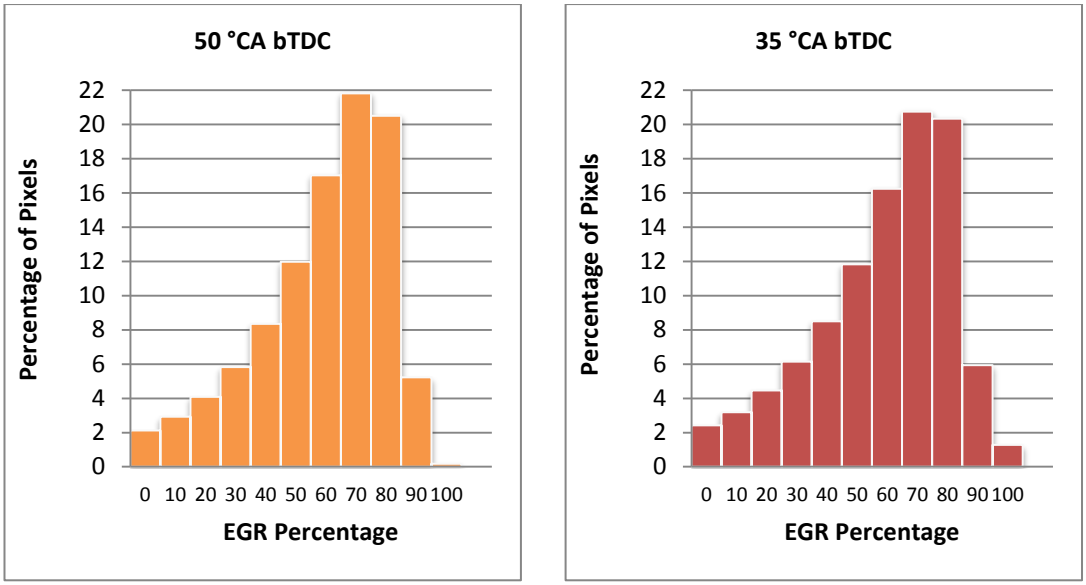

Figure 6.44 Calculated EGR PDFs

The EGR PDFs show a similar pattern for all the selected crank angles during the compression stroke. About 2% of total 501×501 pixels within the ROIs indicate a 0-10% EGR or 90-100% fresh charge. The percentage of the pixels increases exponentially for the EGR bands of 10% to 60% and drops sharply after 70% EGR band. The percentage of pixels at 90, 70, 50 and 35 °CA bTDC that indicate 100% EGR are 0.03, 0.13, 0.17 and 1.3% respectively. Figure 6.43 shows the comparison of the EGR PDFs at the selected crank angles. All the EGR PDFs show a negatively skewed or left-skewed distribution where the left tail is longer than the right tail. This distribution is also featured by the mean being smaller than the mode where 'mean' defines the centre of distribution in probability distribution and 'mode' defines the highest occurrence probability. The mean EGR values at each crank angle calculated from the above PDFs for single images are about 2 to 4% higher than the averaged values calculated in section 6.3.5.3. The result is promising as it shows the optimised 2-line PLIF technique can be utilised for the EGR measurements of not only the averaged frames but also individual single frames.

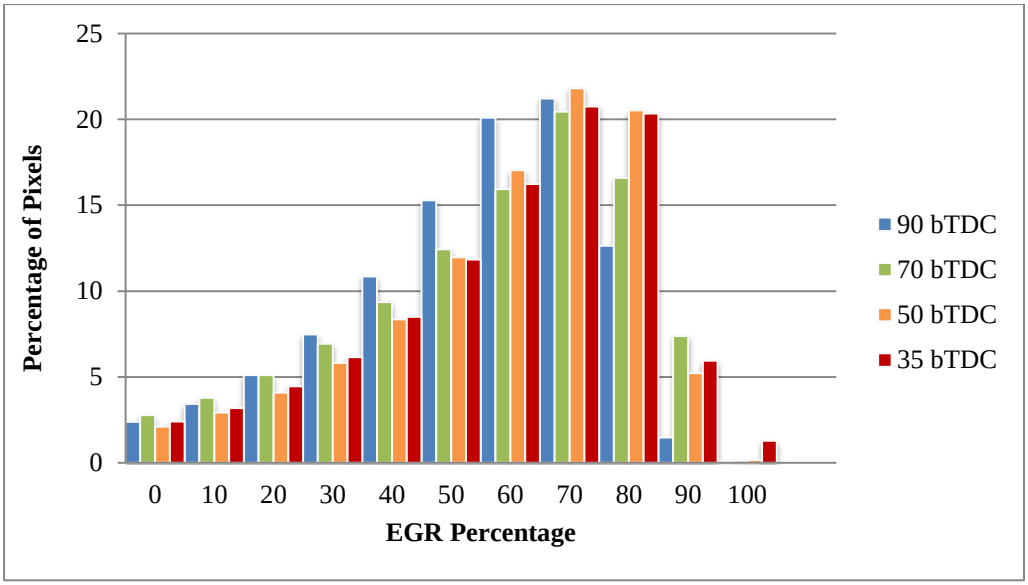

Figure 6.45 Comparison of the EGR PDFs at 90, 70, 50 and 35 °CA bTDC (Com.)

6.4 Summary

Following the calibration and validation measurements of the 2-line PLIF technique presented in Chapter 5, this chapter included the applications of the developed technique in both motoring and firing measurements. The experimental setup and test procedure for each individual test was described and results were discussed. The in-cylinder charge temperature was measured independent of the 3-pentanone models using the calibration curve obtained from the static tests on the constant volume chamber. The 3-pentanone models were corrected by the most recent updated equations and coefficients' value and were exploited to calculate absorption cross-section and frequency quantum yield for different conditions. The values were later used to calculate the exhaust gas residual (EGR) mole fraction in simultaneous T/EGR measurements. Finally the temperature and EGR probability density functions were calculated and discussed.

Chapter 7
Conclusions and Recommendations for Future Work

7.1 Conclusions

This study has focused on design, optimization and implementation of the 2-line planar laser induced fluorescence technique for combustion measurements in a single cylinder optical gasoline direct injection engine.

Following a review of the laser diagnostic techniques applied to combustion measurements, the 2-line planar laser induced fluorescence was selected as combustion diagnostic for this work due to its high signal to noise ratio which allows planar measurements of inhomogeneous temperature and mixture distributions inside the combustion chamber. The survey of the 2-line PLIF works performed previously has shown their limitations and at the same the potential for further improvements of the technique. Some of the main issues include: low fluorescence signal to noise ratio, pixel binning, low spatial resolution and measurements of a relatively small area inside the combustion chamber which can not represent the overall charge state. Also in-cylinder charge temperature values were calculated using theoretical models of the dopant tracer. These models are typically developed using experimental results of studies of the photo-physical properties of specific tracer based on several different assumptions. Obviously both the assumptions and measurements uncertainties affect the accuracy of the models. As a result these models are tuned to give the most accurate temperature readings on particular test conditions and therefore cannot be simply applied to any experiment. The current work was carried

out to provide in-cylinder charge temperature maps independent of the tracer models as well as to further optimize the 2-line PLIF technique by:

- Applying a quasi in situ calibration technique
- Enhancing the fluorescence SNR and improving measurements precision
- Improving temporal and spatial resolutions
- Increasing the sampling/measurement area inside the combustion chamber

This would allow the applications of the 2-line PLIF technique to be further expanded to measurements of other combustion phenomena. Following the design and development of the 2-line PLIF, the technique was calibrated using static measurements on a specially designed constant volume chamber and its accuracy was investigated by measurements of average CVC premix gas temperature. The absolute value of the coefficient of variation of the temperature calibration measurements was less than 3%. The thermometry technique was then validated by measurements of average in-cylinder charge temperature during the compression stroke of both motoring and firing cycles and comparing the PLIF results with the values calculated from in-cylinder pressure data assuming a polytropic compression. The technique was then applied to study of fuel spray characteristics, direct injection charge cooling effects, flame thermal stratification and simultaneous measurements of in-cylinder charge temperature and exhaust gas residuals.

7.1.1 Improving Fluorescence SNR and Imaging Quality

Following a study of Excimer lasers beam characteristics and minimizing the pulse to pulse variations, several image pre- and post-processing techniques were employed to improve the 2-line PLIF imaging quality. Light reflections from the combustion chambers' roof and cylinder walls were eliminated by both covering the cylinder head with candle soot and focusing laser sheets behind the sandwich plate. The PI-MAX camera DIF mode noise was avoided by triggering the camera with even frequencies. Rayleigh and Mie scattering signals were significantly reduced by using an appropriate band pass filter, fine adjustment of the ICCD gate timing, and exploiting extra short gate widths. The fine adjustment of the ICCD gating was achieved by a precise time budgeting through study of all the delays in electronic devices. The CCD accumulated dark charge was minimised by operating the camera

at the lowest CCD array temperature (-20 °C) as well as programming the camera to perform CCD clean cycles. The background subtraction also utilised as an image post-processing technique to further enhance the signal to noise ratio.

7.1.2 Calibration Measurements

Calibration of the 2-line PLIF diagnostic was another area for further optimization of the technique. In this work a constant volume chamber was designed and manufactured so direct calibration measurements can be performed independently. The CVC exploited same optical components as the engine and allowed calibration measurement to be performed with the same 2-line PLIF setup as the engine measurements without any requirements for re-aligning the optics. The temperature calibration curve was obtained by conducting a series of static tests on the CVC and studying the relation between fluorescence signal intensity ratios of excitation wavelengths and temperature. The absolute value of the coefficient of variation of the temperature calibration measurements was less than 3%.

7.1.3 Validation Measurements

To validate the developed 2-line PLIF thermometry, the technique was applied to measurements of the average in-cylinder charge temperature during the compression stroke for both motoring and firing cycles. The average in-cylinder charge temperature from the intake valve closing (IVC) to ignition timing was also calculated from the in-cylinder pressure data assuming polytropic compression. The computed values were then compared to the 2-line PLIF data. For the motoring case average percent difference between the two methods was 3% with standard deviation of 2%, while for the firing test the average percent difference was 2% with standard deviation of 1%. The higher value of the average percent difference for the motoring case is due the fact that all the motoring images were normalized by a single PFI image taken early in the compression stroke while each of the firing images was normalized by a PFI image of the same crank angle.

7.1.4 Application of the Technique

7.1.4.1 Single-line PLIF Fuel Spray Visualization

The single-line PLIF fuel spray visualization was performed to get a better insight into the behaviour of the air-assisted direct injector as well as to provide reference images for comparison with NIRAT measurements. The tests were carried out for both normal and negative valve timings at three different injection timings of 120 ºCA aTDC (Int.), 140 ºCA bTDC (Com.) and 90 ºCA bTDC (Com.). For early injection at 120 ºCA aTDC (Int.) as the injection occurs during the intake, the introduced air rapidly disturbs the injection cone and mixes the fuel droplets providing a homogeneous mixture. For the fuel injection at 140 ºCA bTDC (Com.) due to lower in-cylinder large scale flow, the spray cone was developed. However this injection timing could not provide the homogenous mixture prior to ignition. Although the air-assisted DI injector utilizes a very low injection pressure of 6.5 bar, fuel impingement was observed around 100 °CA bTDC due to a high fuel injection depth of penetration for this injection timing. The injection event at 90 ºCA bTDC (Com.) was also studied for both valve timing strategies. This injection timing can be utilised for stratified charge operation. For both valve timings, injection at 120 ºCA aTDC (Int./Re.Com.) occurs when the intake valves are opened while injection at 140 ºCA bTDC (Com.) occurs when the intake valves are fully closed. As a result no significant change in spray pattern was observed between the two different valve timings.

7.1.4.2 Two-line PLIF Study of Direct Injection Charge Cooling Effects

The 2-line PLIF technique was employed to study direct injection charge cooling effects. Two injection quantities of 10 and 30 mg/cycle were studied for injection timings at 90 ºCA aTDC (Int.) and 110 ºCA bTDC (Com.). In-cylinder charge temperature measurements were carried out during motoring cycles and results were compared with the computed temperature values from in-cylinder pressure data. The PLIF values are slightly higher than the values calculated from the polytropic compression. For the low injection quantity of 10 mg/cycle, both techniques showed a very good agreement with less than 2% variation in calculated temperature. While

for high injection quantity of 30 mg/cycle, 7% deviation in the calculated temperature between the two methods was observed which was mainly due to interference signals from the fuel droplets. The longest fuel droplet life time was approximated from the PLIF data to be more than 90 °CA for 30 mg/cycle injection at 90 °CA aTDC (Int.). The shortest fuel droplet life time was less than 20 °CA for 10 mg/cycle injection at 110 °CA bTDC (Com.) which was mainly due to the injection quantity and higher in-cylinder temperature at the injection timing. It was also observed that the later injection resulted in higher in-cylinder charge temperature drop. This is due to fact that for injection timing after IVC, the in-cylinder mass is constant. As the fuel is injected into the cylinder, fuel droplets absorb heat from the gas mixture and evaporate reducing the in-cylinder charge temperature. For early injection during the intake, the in-cylinder gas temperature drop is compensated by increased air into the cylinder. To the best of the author's knowledge this was the first application of tracer-based 2-line PLIF technique for study of direct injection charge cooling effect. The 2-line PLIF technique not only provides in-cylinder charge temperature maps with extremely high temporal and spatial resolution but also allows fuel spray visualization and study of fuel impingement which results in over-estimating the charge cooling effects in other diagnostics.

7.1.4.3 Two-line PLIF Study of Flame Thermal Stratification

After high-speed imaging of the combustion using the Memrecam fx-6000 camera, and study of start of ignition, combustion duration and EGR formation, the flame formation and propagation was investigated at much higher spatial resolution using the PI-MAX camera. For engine operation with normal valve timing even with early injection that provides a homogeneous mixture prior to the ignition, it was observed that the flame kernel moves faster towards the exhaust side. This could be due to the flame quenching at the cold areas as well as higher temperature at the exhaust side which can provide a better fuel/air mixture. Further investigation showed that the flame moves away from the spark plug ground electrode.

Following some preliminary studies, the 2-line PLIF technique was applied to investigate the flame thermal stratification. As the piston crown blocks the sandwich plate optical access for 25 ºCA either side of TDC, it was not possible to illuminate

the combustion chamber at the start of flame formation and therefore an atypical injection timing of 15 ºCA aTDC was utilised for these tests. The DIF images were captured with a same procedure as the in-cylinder charge temperature measurements but an alternative image post-processing technique was applied. Unlike the direct photography that shows the luminous or post-flame zones, the two-line PLIF thermometry can detect the thermal stratification in the flame front. Although single-line PLIF images can also show the flame structure, but the single-line PLIF images are dependent on the tracer concentration and can only represent the flame structure for a premix flame in a homogenous charge prior to ignition. On the other hand as the two-line PLIF images are independent of tracer concentration they can be utilized to study premix flame structure in a non-homogenous charge, e.g. at presence of large amount of EGR or possibly diffusion flame of diesel engines. This was the first application of the 2-line PLIF technique for study of flame thermal stratification in IC engines. The technique can be used in calculating the flame growth rate and the mean expansion speed based on the flame structure measurements and reduce the disperse data reported on the flame behaviour.

7.1.4.4 Two-line PLIF Simultaneous Exhaust Gas Residual and Temperature Measurements

As for the simultaneous temperature and EGR mole fraction measurements a stable CAI operation was required, extensive tests were carried out on the engine to find the optimum injection and ignition timings as well as the required intake air temperature that provide the lowest cycle to cycle variation. It was found that the most important factor for a stable CAI operation is the in-cylinder peak pressure and at a much lower degree, intake air temperature. For in-cylinder pressures of >25 bar, the spark plug could be switched off after a first few cycles (which was necessary to initiate EGR to start a CAI operation) and engine could run stable (CoV_{IMEP} <4%) with an intake air temperature of as low as 318 K. In-cylinder pressures between 22-25 bar resulted in unstable CAI/SI operation while the spark plug had to be kept on all the time. For the pressures below 22 bar, the engine could only operate on SI mode. The PLIF EGR measurement inaccuracy was found to be less than 11%. The main reasons for the higher inaccuracy in EGR measurements compared to the temperature measurements can be summarized as;

i. influence of the PLIF temperature measurements' inaccuracy
ii. inaccuracy of the in-cylinder pressure measurement
iii. inaccuracy in calculation of the absorption cross section and frequency quantum yield from the developed models
iv. engine thermodynamic states variation between different runs

It should be noted that all the EGR and temperature maps and PDFs were obtained for a relatively large area (501×501 pixels, 13 pixels/mm resolution) inside the combustion chamber. This was to ensure that the results can represent the overall in-cylinder thermodynamic state.

7.2 Recommendations for Future Work

7.2.1 Sandwich Plate with Side Windows

In the current design of this plate, the optical widow is first placed inside the sandwich plate mounted on the engine and then a metal clamp secures the window in its place. During the engine operation it is required to have an access to the combustion chamber to frequently clean the sandwich plate side and piston top windows. With the current design both the side window and metal clamp should be first removed and then resealed and assembled after cleaning the optics. Due to the number of contact surfaces that should be sealed as well as having a combination of glass and metal, gasketing for engine operation above 23 bar was found to be problematic. A better design would be a case where the optical window was placed and sealed permanently inside a metal frame. The metal frame should also have wider contact surfaces with the sandwich plate for better sealing.

7.2.2 Cylinder Block

Although the sandwich plate with side windows provides an easy access to the combustion chamber and it is very easy to assemble and it perfectly protects the optics especially during longer engine runs, it does not allow laser illumination ±25 °CA around the TDC. If PLIF imaging in this time slot is required then the sandwich plate with the optical ring should be used. However with this sandwich plate it is not possible to have access to the combustion chamber during the tests as the cylinder head should be completely dismounted. A cylinder block that sits on hydraulic jacks

can provide an easy access to the combustion chamber and is essential if PLIF imaging at this timing is required.

7.2.3 Calibration Measurements

Another area for further work is extension of the calibration measurements in the constant volume chamber. The calibration measurements can be performed at much higher temperatures and elevated pressures. The current CVC was made out of aluminium for ease of manufacturing. Aluminium puts limit on both the maximum working temperature and pressure. The maximum working temperature is limited to the low melting point of aluminium plus the safety factor considered. The maximum working pressure on the other hand is limited by aluminium softness and the fact that the connecting threads for the fittings on the chamber cannot stand high amount of stress when the chamber is filled to a high pressure. Also sealing of the CVC components is challenging due to the relatively high thermal expansion of aluminium. A CVC with the exact same design made from e.g. 4130 alloy from 41XX steel family would allow extension of the calibration measurements to higher temperatures and pressures.

7.2.4 Flame Thermal Stratification

Further optimisation of the 2-line PLIF technique in this work has provided the opportunity of applying the technique to other combustion measurements such as study of flame thermal stratification. The current calibration method can only provide relative temperature values at different sections of the flame. For measurements of the absolute temperature values alternative calibration techniques should be exploited. Calibration measurements of steady laminar flames such candle flame may provide the required information. The current constant volume chamber can be simply modified to allow such measurements to be performed for further investigation.

Appendix A. Engine Control Units and NIDAQ System Connection Diagram

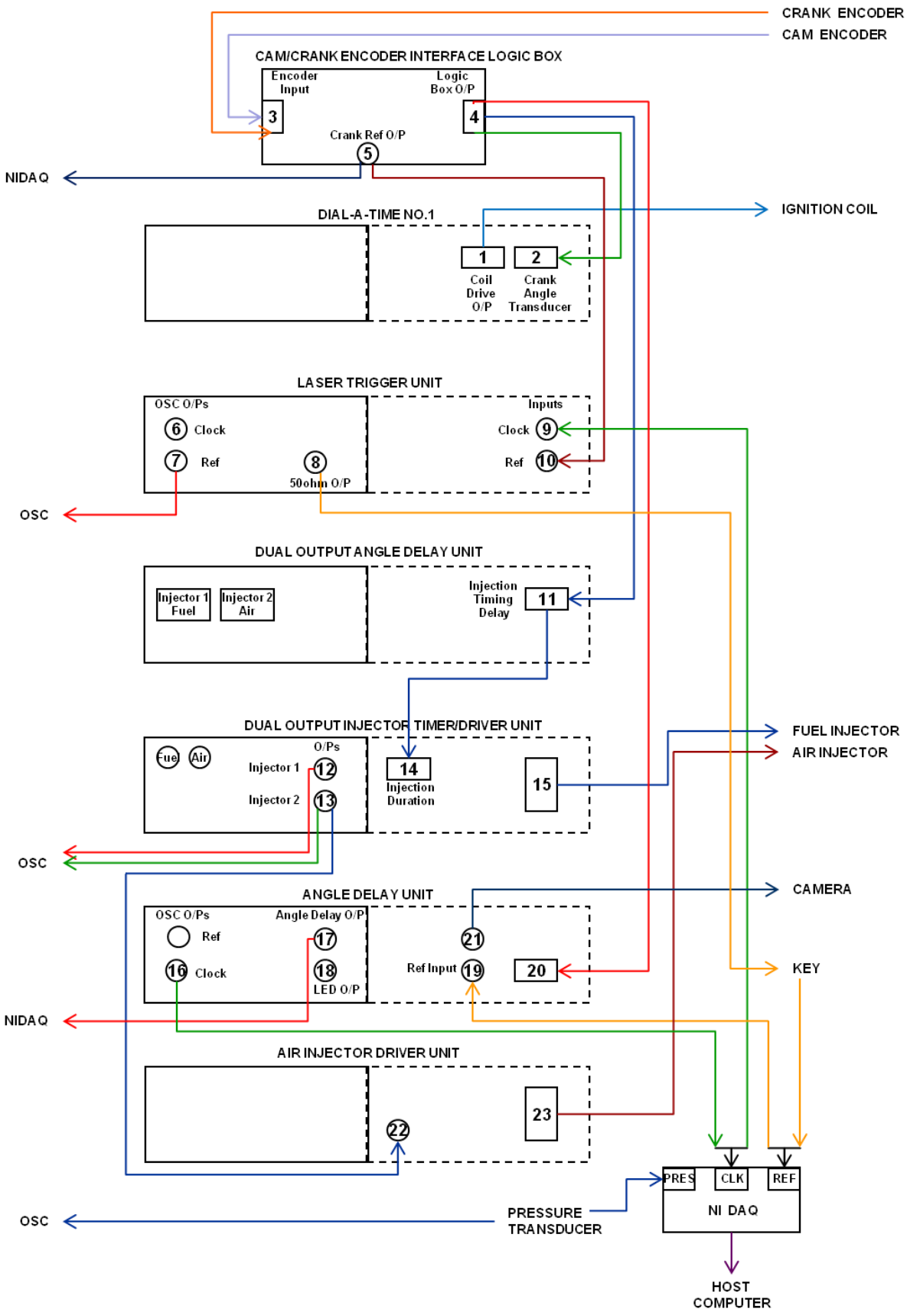

Appendix B. Gasketing

Sealing Section	Gasket/Sealant	Thickness
Camshaft Lobes Covers	Gaskoid Jointing	0.25 mm
Camshaft Covers	Hylomar PL32 Medium Non-sticky Instant Gasket	–
Sandwich plate optical window and metal window dummy	Hermetite SDSHM202 Instant Rubber Silicon Gasket	–
Sandwich plate window clamp	Gaskoid Jointing	0.25 mm
Cylinder head-sandwich plate contact surface	Chieftain Gasket Jointing	1 mm
Sandwich plate-cylinder block contact surface	Chieftain Gasket Jointing	1 mm
Piston quartz window-piston crown	Klingersill C-4400	1.5 mm
Constant volume chamber-sandwich plate contact surface	Klinger TSM-AS graphite gasket	2 mm

Appendix C. Technical Drawings of the Designed Engine Components

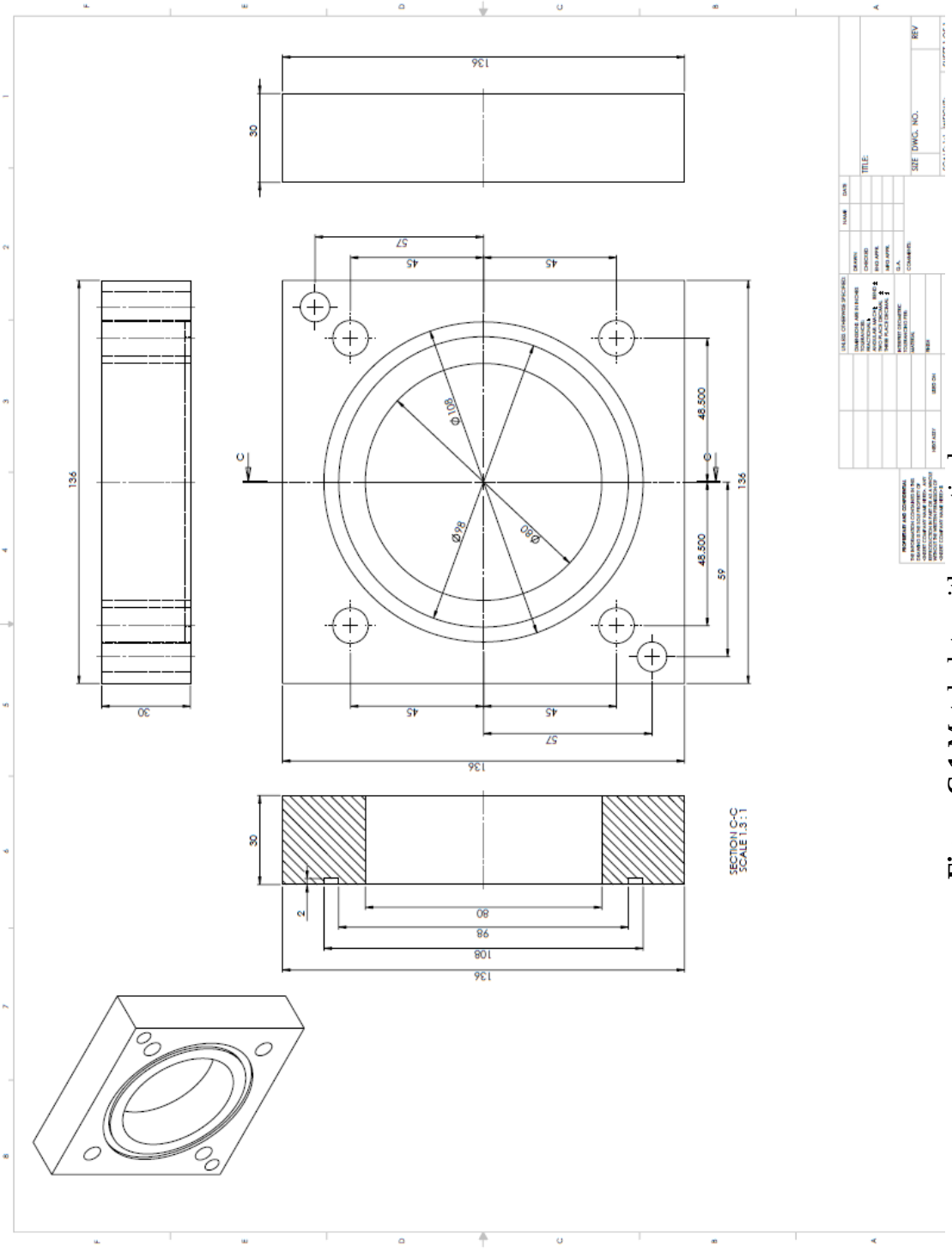

Figure C.1 Metal plate with no optical access

Appendix C.

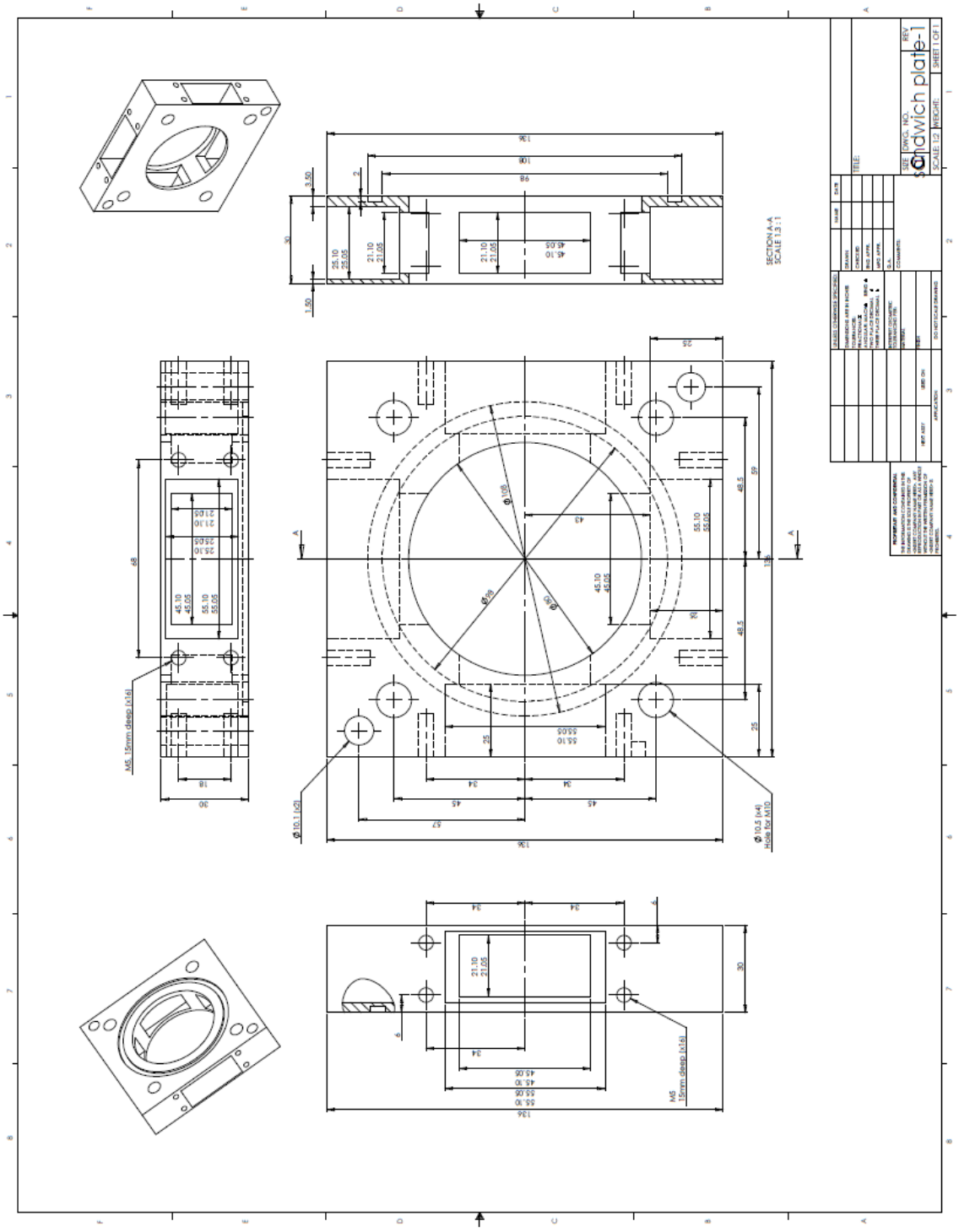

Figure C.2 Window plate

Appendix C.

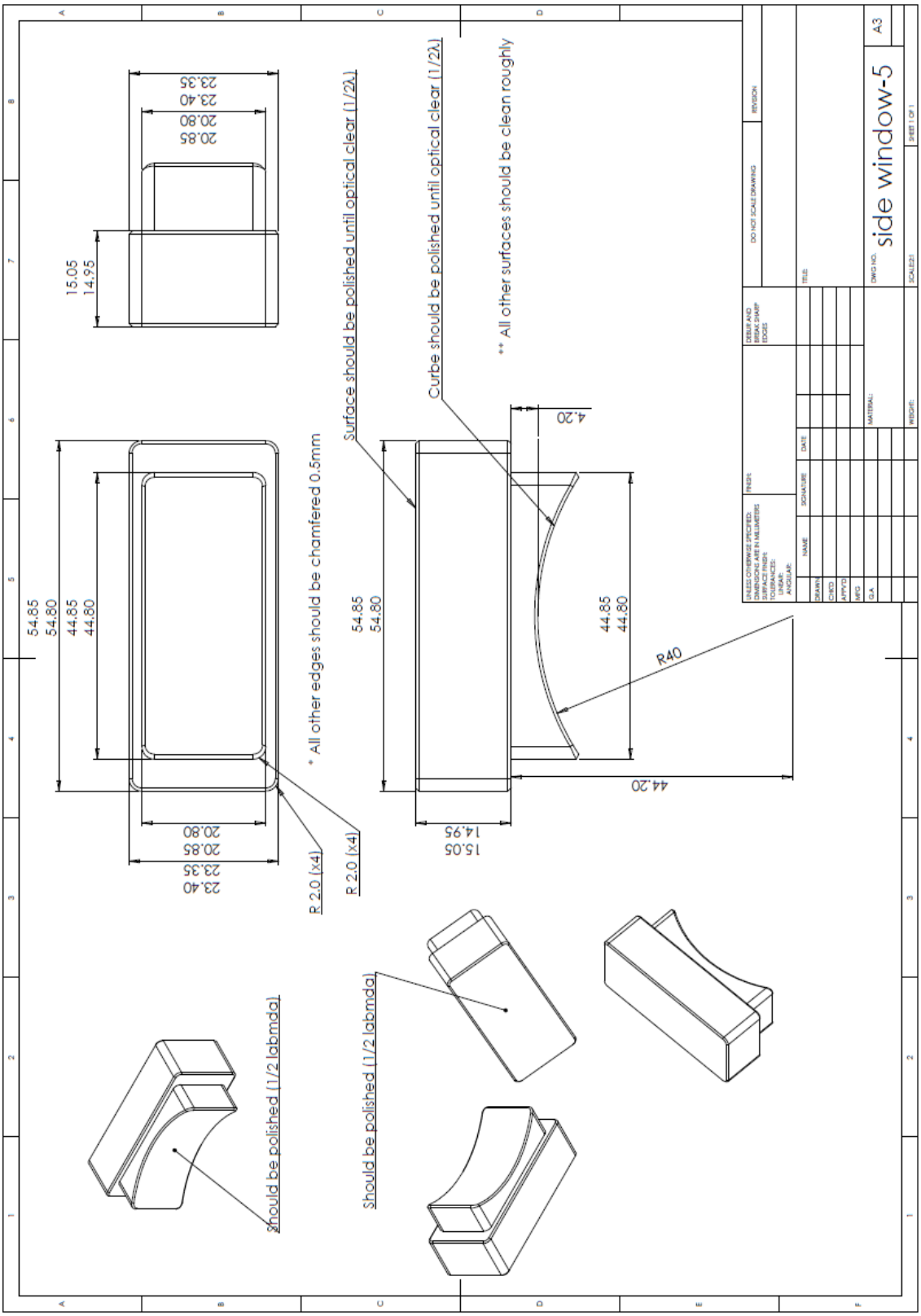

Figure C.3 Side window

Appendix C.

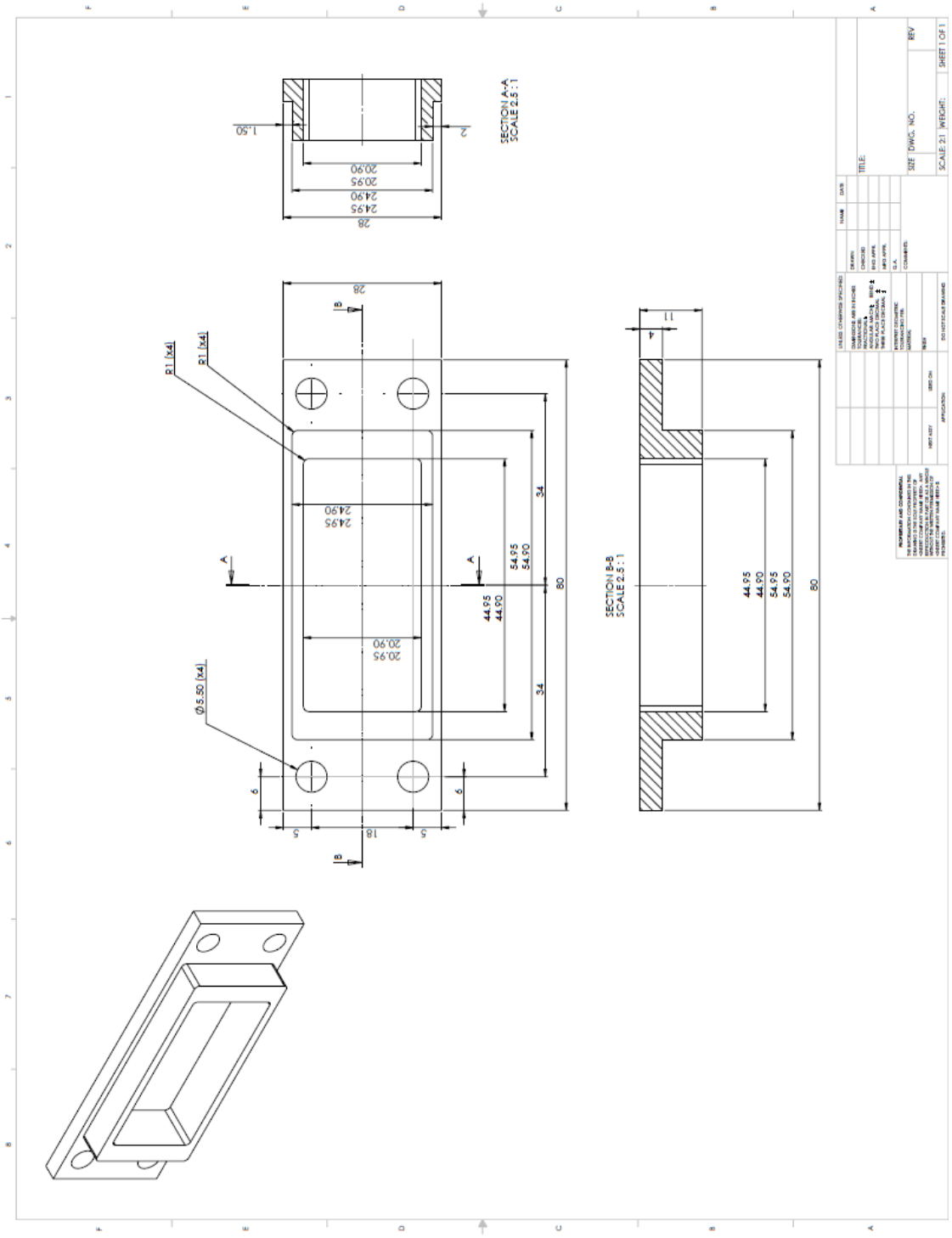

Figure C.4 Window clamp

Appendix C.

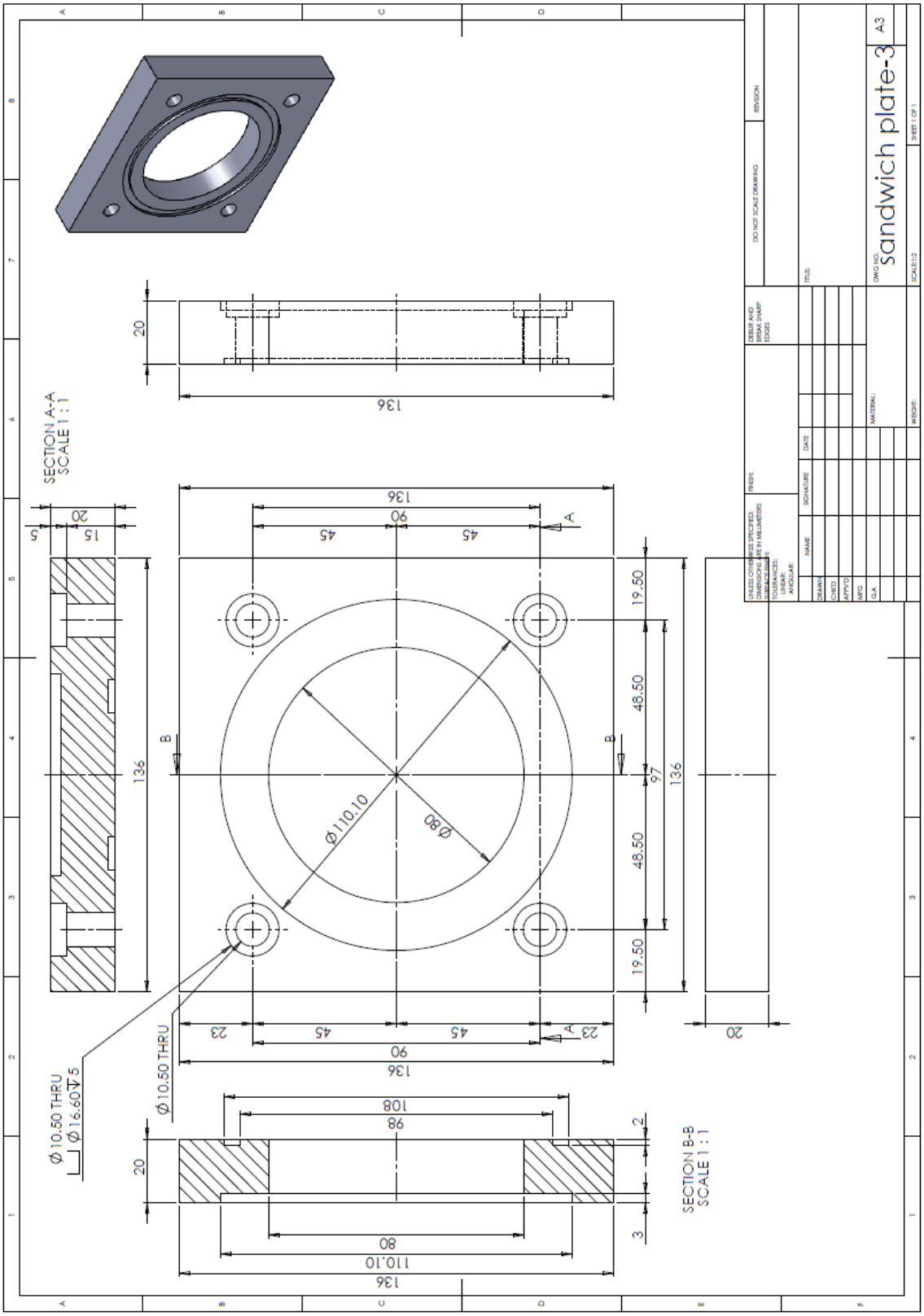

Figure C.5 Original ring plate

Appendix C.

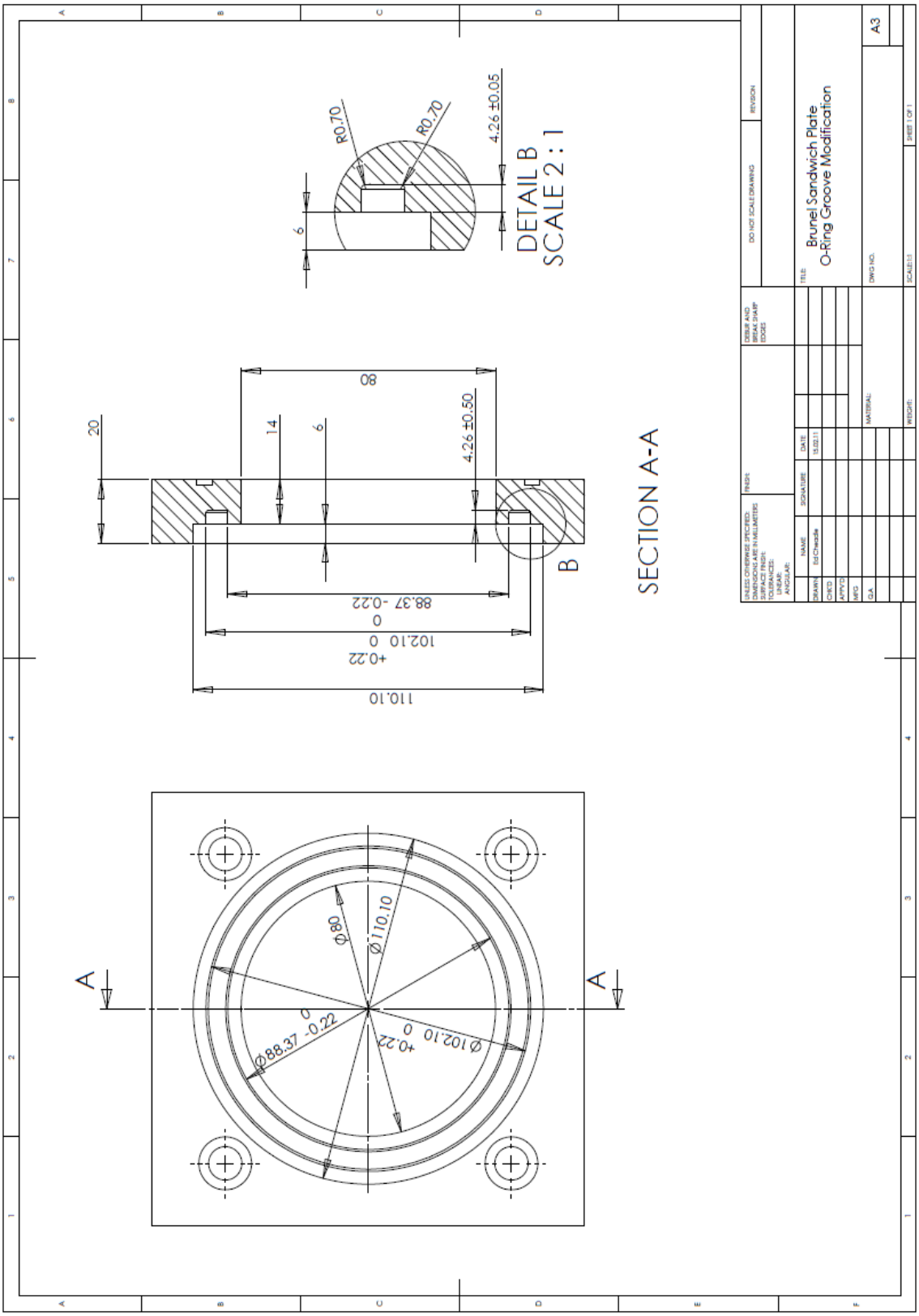

Figure C.6 Modified ring plate

Appendix C.

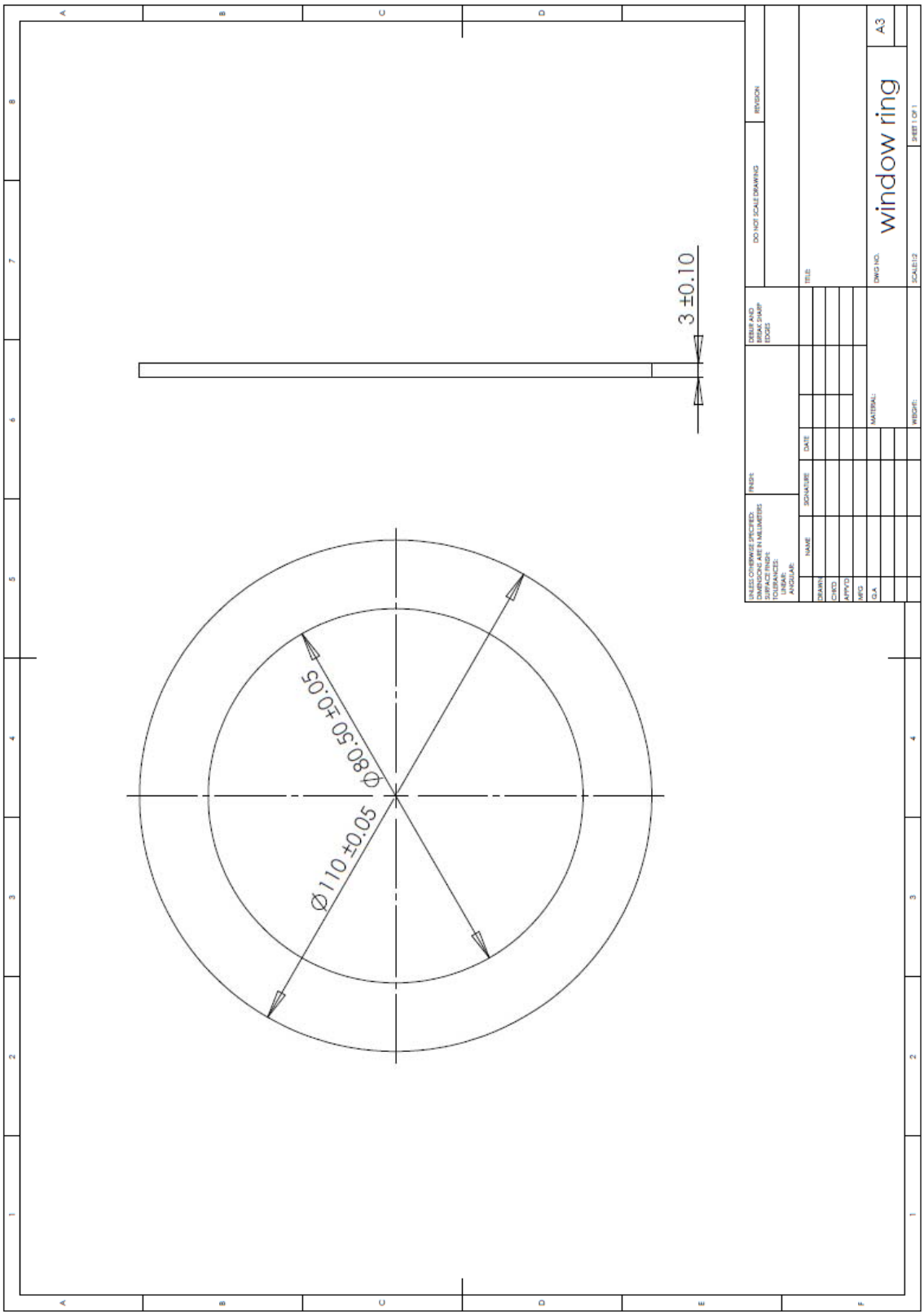

Figure C.7 4130 alloy slip ring

Appendix C.

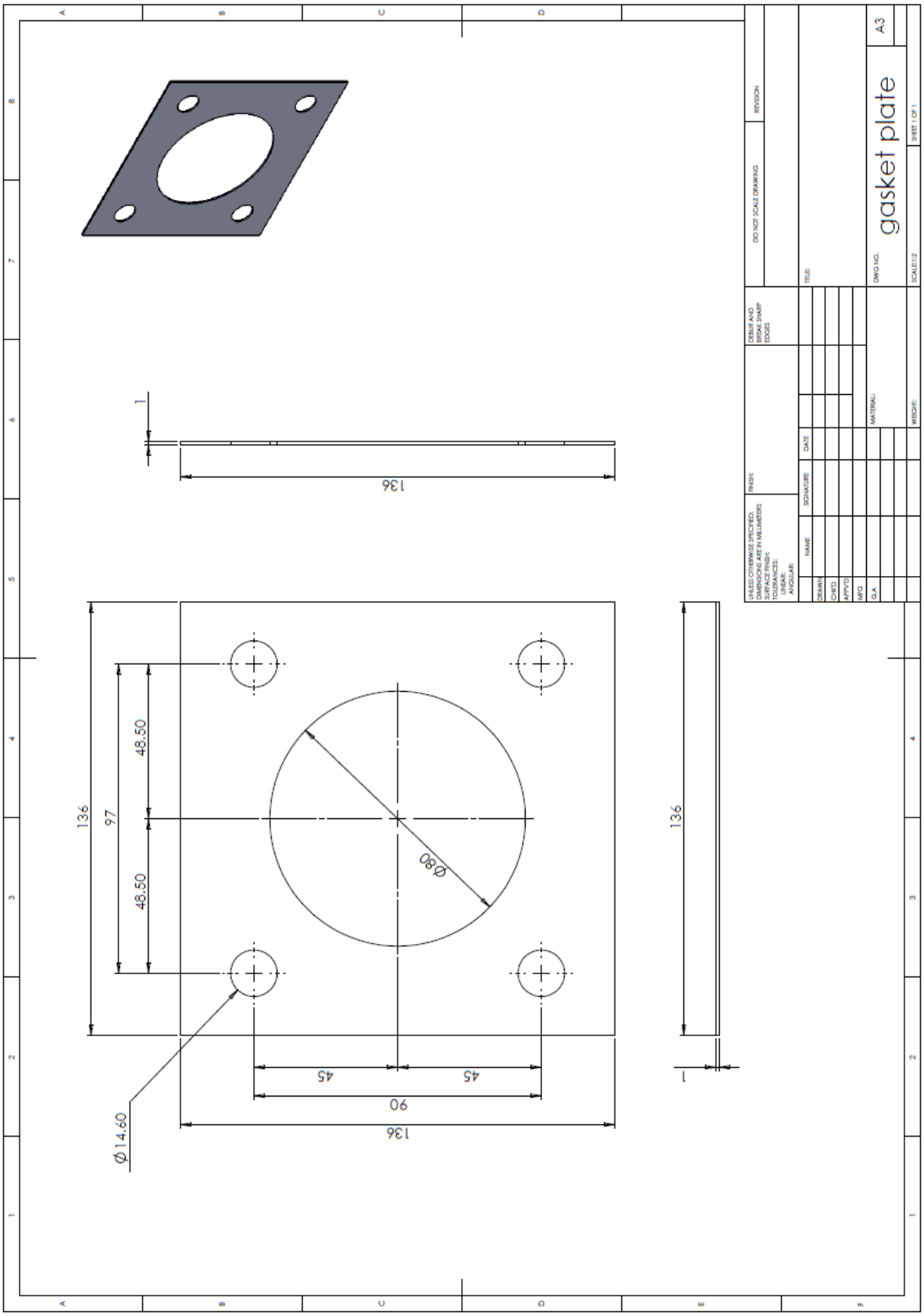

Figure C.8 4130 alloy gasket plate

Appendix C.

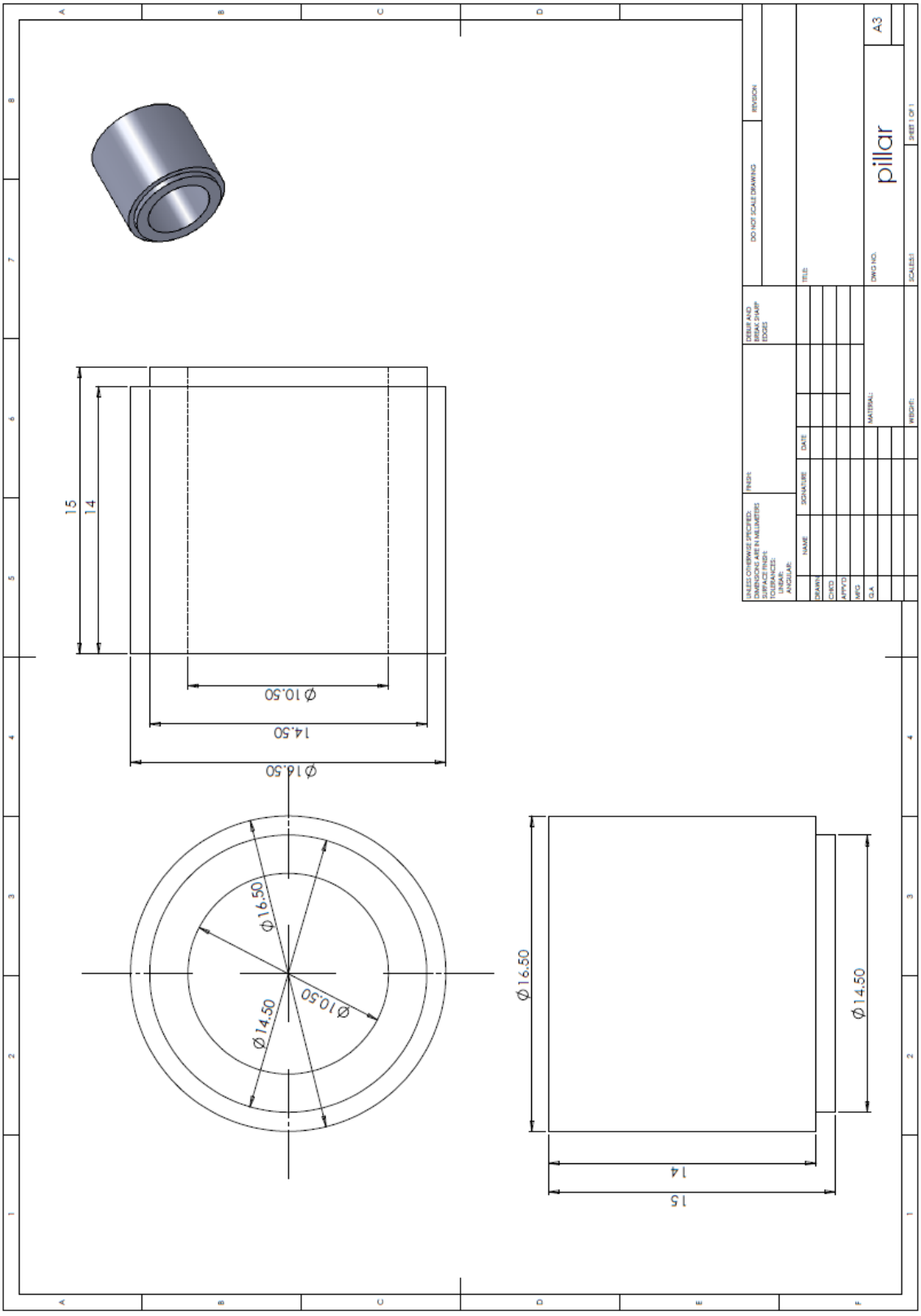

Figure C.9 Pillar

Appendix C.

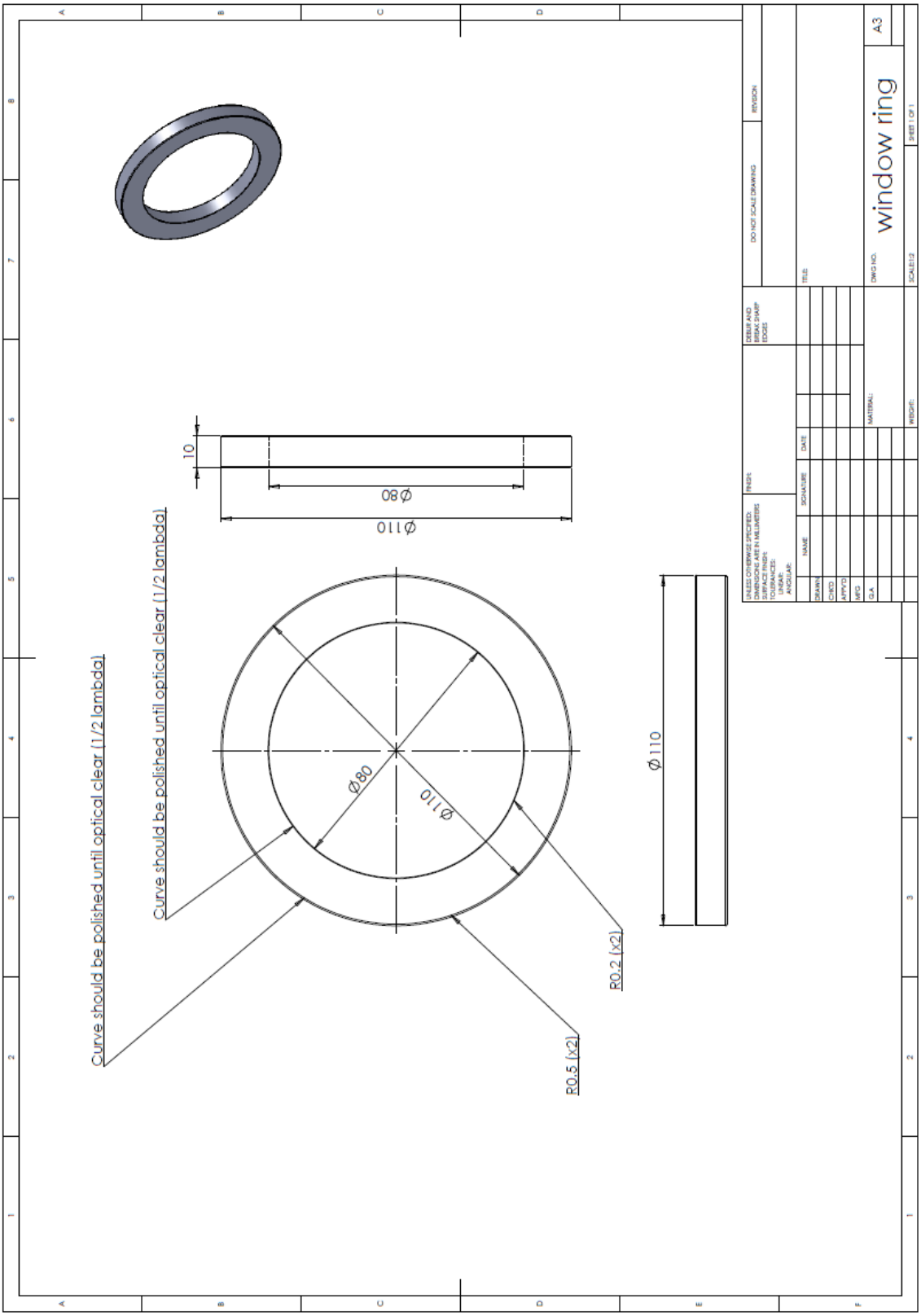

Figure C.10 Optical ring

Appendix C.

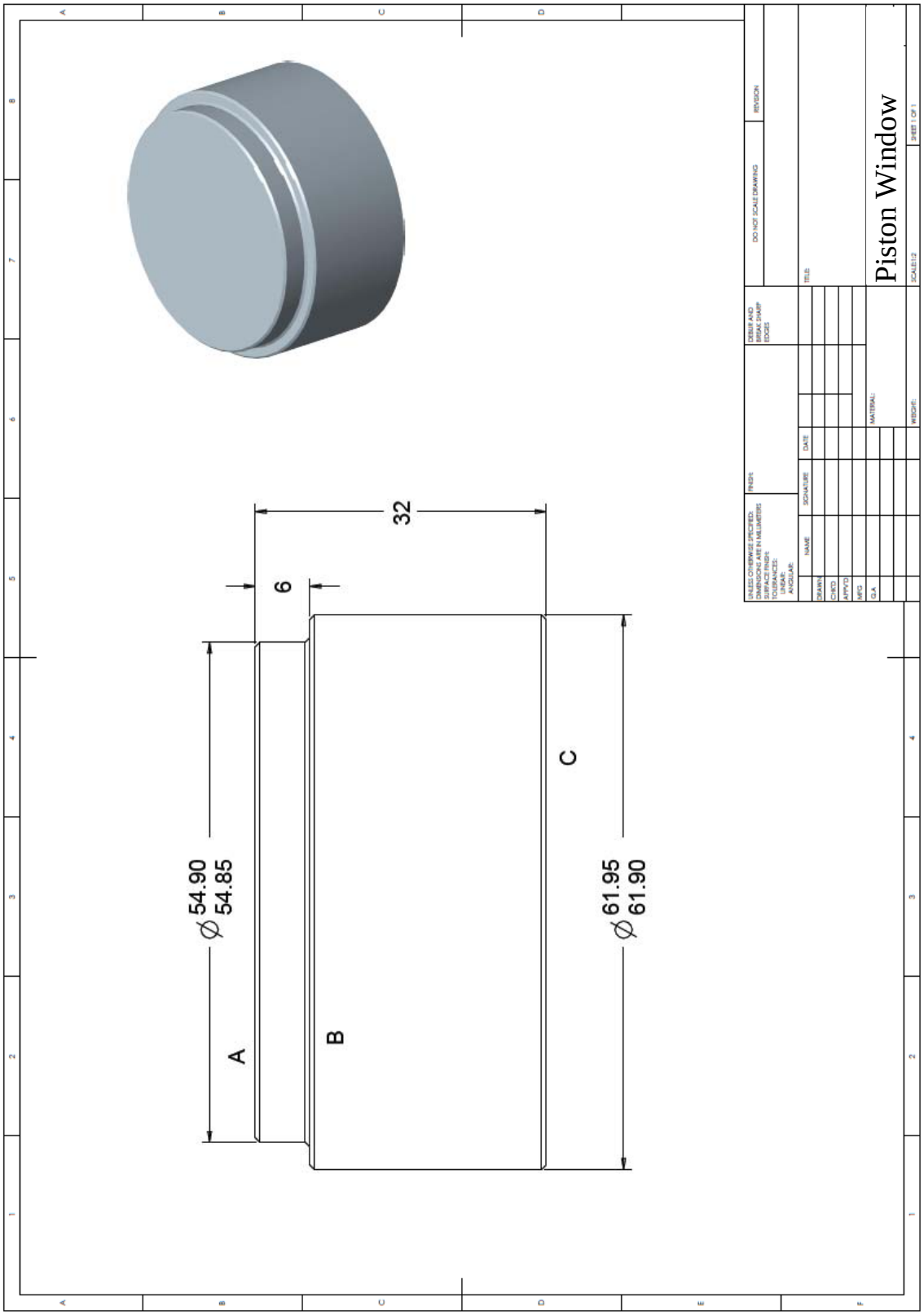

Figure C.11 Piton top window

Appendix D. MPI and DI Injection Calibration Curves

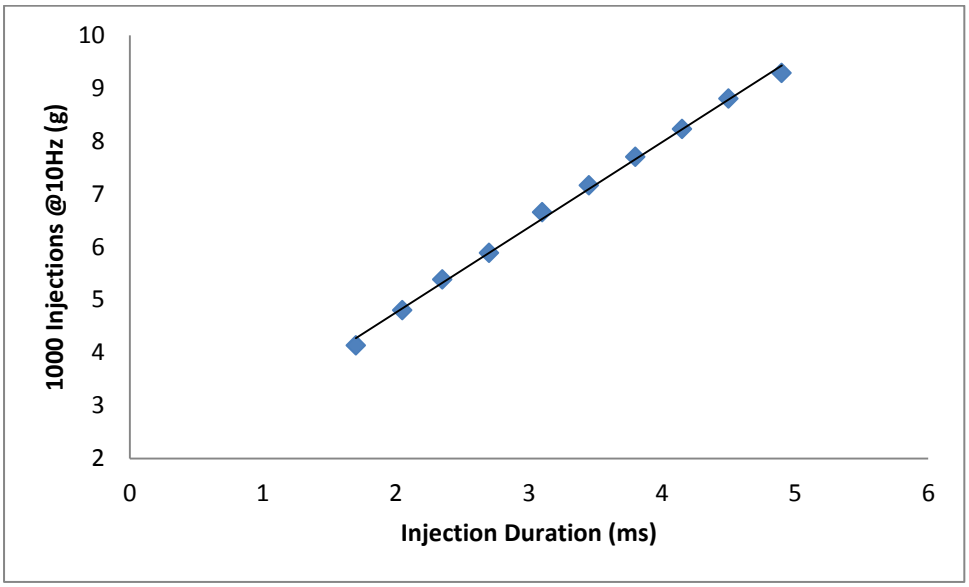

Figure D.1 MPI injection calibration curve

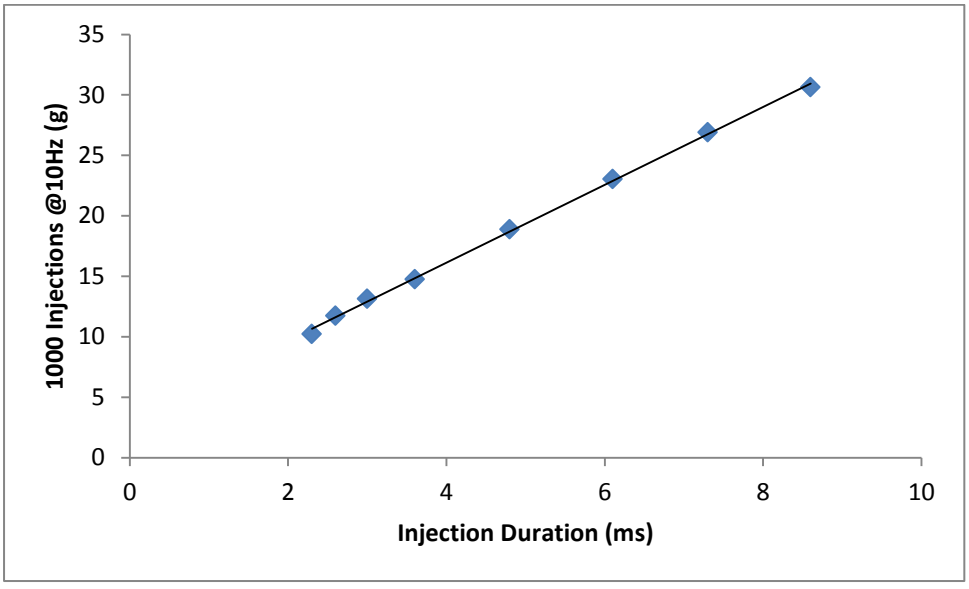

Figure D.2 DI injection calibration curve

Appendix E. Raman Convertor Filling Instruction

1. Wear safety glasses.
2. Decouple the Fill Valve Assembly from the RC.
3. Make sure the VCO O-ring is in place.
4. Attach the VCO connector to the Fill Valve Assembly.
5. Using a screw driver make sure the Fill Valve Assembly is closed.
6. Check all the connections to be tight.
7. Crack open the H_2 tank valve and immediately close it.
8. Adjust the regular pressure control valve to a pressure just a bit higher than the desired RC fill pressure.
9. Check the H_2 tank regulator output gauge and make sure it holds the pressure and that the there is no leakage.
10. Exhaust the trapped gas in the regulator and tubing by bleeding the gas through the Valve Assembly using a screw driver.
11. Connect the Valve Assembly to the RC through the Quick Connector.
12. Open the H_2 tank valve.
13. With one hand supporting the Valve Assembly, use the screwdriver and gently open the valve until the RC pressure gauge shows the pressure rise.
14. Decouple the RC pressure gage and insert the QC stem connected to the exhaust line.
15. Allow the RC to flush for about one minute.
16. Remove the QC stem and insert the RC pressure gage.
17. Continue to fill the RC until the desired fill pressure.
18. Stop the H_2 flow by first closing the regulator output valve and then closing the Valve Assembly.
19. Close the H_2 tank valve.
20. Release the pressure in the regulator and tubing by slightly loosing the pressure release valve.
21. Decouple the VCO and put on a blind nut.
22. It is suggested to use the RC with both the pressure gauge and the Valve Assembly coupled.

Appendix F. Specifications of Optical Components

308/633 nm Dual Band Reflector ×4	
Reflectance at 308nm	≥ 97% @ 45º. AOI
Reflectance at 633nm	≥ 60% @ 45º. AOI
Material	UV Grade Fused Silica
Diameter	76.19 mm ± 0.12 mm
Thickness	12.7 ± 0.25 mm
Surface Figure	S1 λ/10 & S2 λ/4 @ 632.8 nm
Surface Quality	20-10 scratch and dig
Parallelism	≤3 arc minutes
Chamfer	0.5 mm x 45º. nominal
Clear Aperture	90% of central dimension
Laser Damage Threshold (LDT)	4 J/cm^2 , 20 ns, 20 Hz @ 1064 nm
Unit Price	£ 541 (Acton Optics)
Ultra-Stable Kinematic Ø3" Mirror Mount Unit Price	£124 (ThorLabs)

277/633 nm Dual Band Reflector ×4	
Reflectance at 277nm	≥ 97% @ 45º. AOI
Reflectance at 633nm	≥ 60% @ 45º. AOI
Material	UV Grade Fused Silica
Diameter	76.19 mm ± 0.12 mm
Thickness	12.7 ± 0.25 mm
Surface Figure	S1 λ/10 & S2 λ/4 @ 632.8 nm
Surface Quality	20-10 scratch and dig
Parallelism	≤3 arc minutes
Chamfer	0.5 mm x 45º. nominal
Clear Aperture	90% of central dimension
Laser Damage Threshold (LDT)	4 J/cm^2 ,20 ns, 20 Hz @ 1064 nm
Unit Price	£ 541 (Acton Optics)
Ultra-Stable Kinematic Ø3" Mirror Mount Unit Price	£124 (ThorLabs)

Appendix F.

Long Wave Pass Dichroic Beam-splitter ×1	
Material	UV Grade Fused Silica
Diameter	76.20 ± 0.25mm
Thickness	12.70 ± 0.25mm
Surface Figure	λ/10 @ 633 nm before coating
Surface Quality	10-5 scratch and dig
Coating	
Transmission	>85% in long wave pass to 2200 nm
Reflectance	≥99.5% @ 266 nm
AOI (Angle of Incident)	0° Un-polarized
Clear Aperture	≥85% of central dimension
Laser Damage Threshold (LDT)	10 J/cm^2, 20 ns, 20 Hz @ 1064 nm
Unit Price	£ 805 (CVI Melles Griot)
Ultra-Stable Kinematic Ø3" Mirror Mount Unit Price	£124 (ThorLabs)

High-Precision Equilateral Dispersive Prism ×1	
Material	UV Grade Fused Silica
Dimensions	50.8 ± 0.25mm
Angular Deviation	±3 arc min
Surface Figure	λ/10 @ 633 nm before coating
Surface Quality	10-5 scratch and dig
Parallelism	≤3 arc minutes
Coating	2 sides AR coated @ 277nm
Clear Aperture	≥85% of central dimension
Laser Damage Threshold (LDT)	15 J/cm^2, 20 ns, 20 Hz @ 1064 nm
Unit Price	£ 1160 (CVI Melles Griot)
Rotary Assembly with Prism Mount	£ 118 (Edmund Optics)

Appendix F.

Rectangular Cylindrical Plano-Convex Singlet Lens ×2	
Material	UV Grade Fused Silica
Dimensions	x=76.2 ± 0.25mm, y=38.1 ± 0.25mm
Focal Length	1500 mm
Paraxial Focal Length	f ± 0.5%
Surface Figure (before coating)	x direction λ/4 cm rms @ 633 nm
	y direction λ/2 cm rms @ 633 nm
Surface Quality	20-10 scratch and dig
Parallelism	≤3 arc minutes
Coating	Single Side AR coated @ 248 to 355nm
Clear Aperture	≥85% of central dimension
Laser Damage Threshold (LDT)	10 J/cm^2, 20 ns, 20 Hz @ 1064 nm
Unit Price	£ 791 (CVI Melles Griot)
Kinematic Cylindrical Lens Mount	£59 (ThorLabs)

Schott BG7 Band-pass Polished filters ×1	
Size	50.0 x 50.0 mm,
Thickness	3.0 mm
AOI (Angle of Incident)	0°
Unit Price	£ 32
Schott BG39, Band-pass Polished filter ×1	
Size	50.0 x 50.0 mm,
Thickness	1.0 mm
AOI (Angle of Incident)	0°
Unit Price	£ 42
Schott WG320 Long-pass Polished filter ×1	
Size	50.0 x 50.0 mm,
Thickness	3.0 mm
AOI (Angle of Incident)	0°
Unit Price	£ 32

Appendix F.

Schott WG360 Long-pass Polished filter ×1	
Size	50.0 x 50.0 mm,
Thickness	3.0 mm
AOI (Angle of Incident)	0°
Unit Price	£ 32

Piston Window ×4	
Material	UV Fused Silica
Dimensions	Please refer to the technical drawing
Surface Figure	λ/4
Parallelism	≤3 arc minutes
Unit Price	£ 302 (Gooch & Housego)
Window Ring ×2	
Material	UV Fused Silica
Dimensions	Please refer to the technical drawing
Surface Figure	λ/4
Parallelism	≤3 arc minutes
Unit Price	£ 631 (Gooch & Housego)
Side Window ×4	
Material	UV Fused Silica
Dimensions	Please refer to the technical drawing
Surface Figure	λ/4
Parallelism	≤3 arc minutes
Unit Price	£ 355 (Gooch & Housego)

Appendix F.

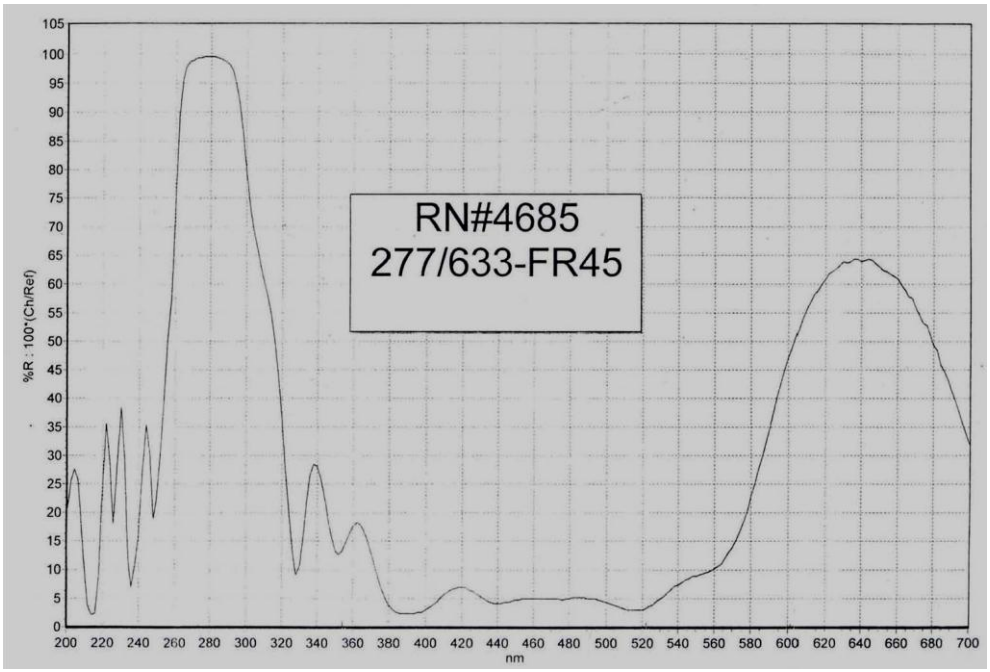

Figure F.1 Reflectivity vs. wavelength of 277/633 nm HR coated mirror (Acton Optics)

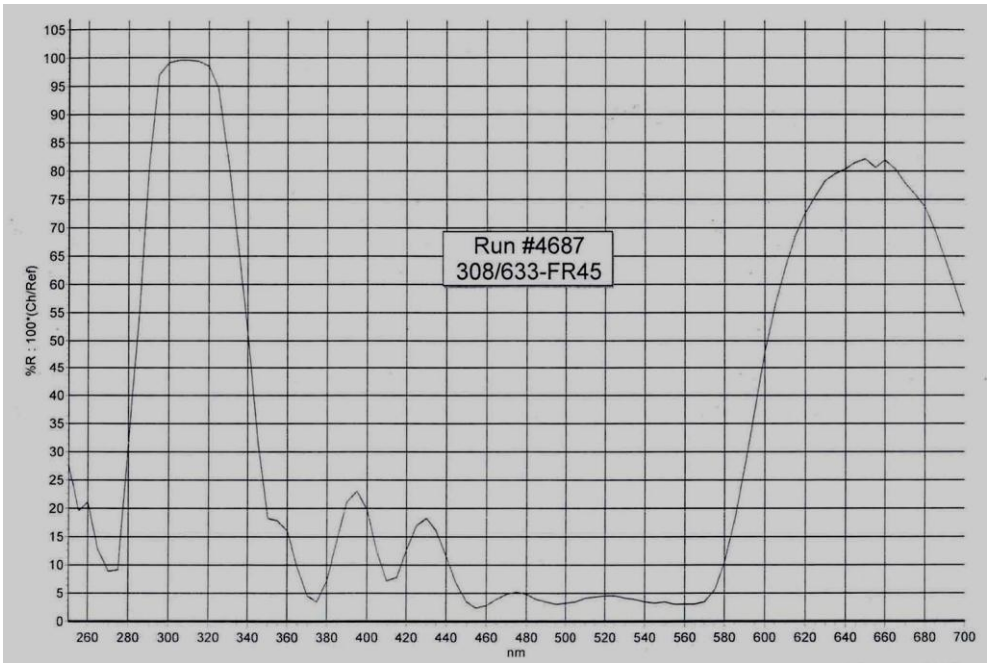

Figure F.2 Reflectivity vs. wavelength of 308/633 nm HR coated mirror (Acton Optics)

Appendix F.

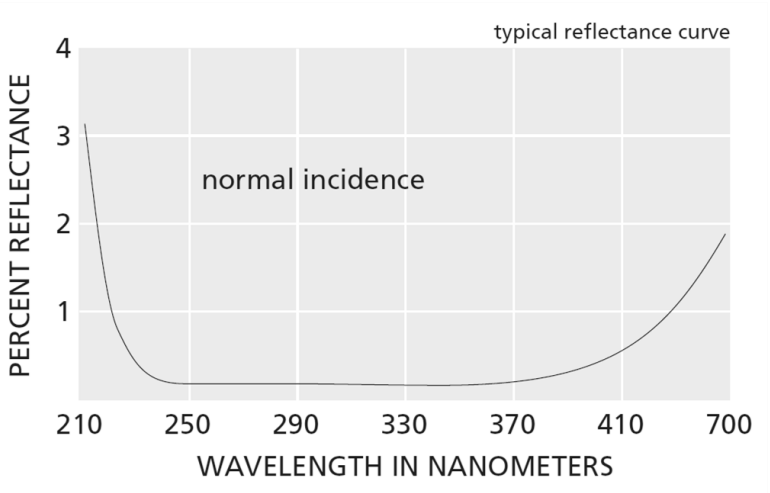

Figure F.3 BBAR 248-355 coating for UV region for 0° incidence (CVI)

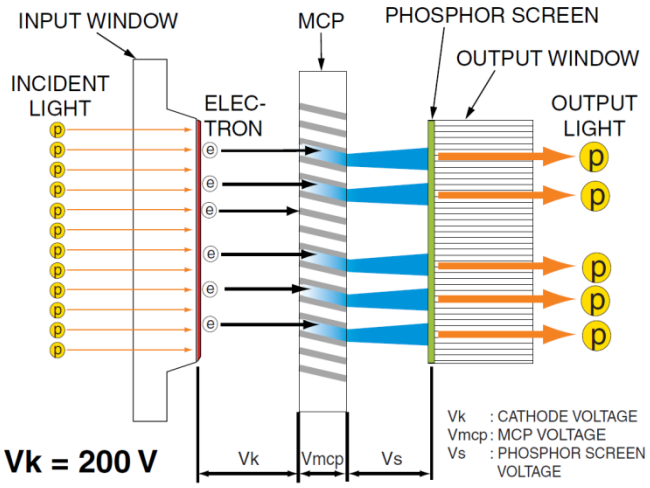

Figure F.4 Structure of the image intensifier [174]

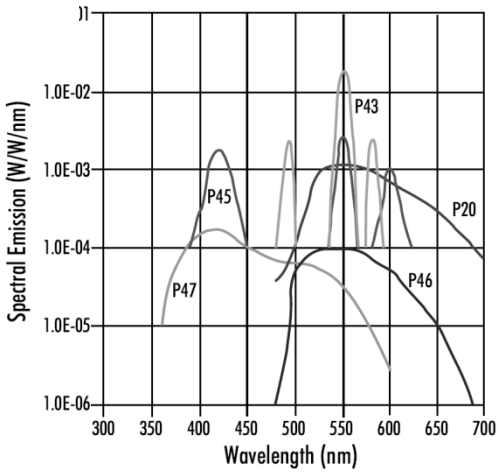

Figure F.4 Emission spectra of intensifier phosphor screen coatings [175]

Appendix G. Imaging Parameters

Detector Temperature	-20ºC
Hardware	
Read Out	Double Image Frame (DIF)
Logic Out	None
Shutter Compensation Time	4 µs
Cleans/Skips	No. of Cleans: 1 No. of Strips/Cleans: 1024 Vertical Skips: Min Block Size: 2 No. of Blocks: 5
Pulsar_PTG	
Trigger	External Slope: Positive Coupling: DC Termination: High Threshold: 1.7 V
Gate Delay	External Trigger-in
Gating Mode	Repetitive
Gate Width	1 µs
Repeat Width/ Delay	1
Gate/Exposure	1
Burst	On
Number of Gain	2
Burst Period	5 µs
Bracket Pulsing	Off
Experiment Setup (Main)	
Number of Images	2
Region of Interest	Full Chip
Number of Accumulations	1
Gain	255
Experiment Setup (Data File)	
Auto Increment	Enable
Overwrite	On
Experiment Setup (Timing)	
Single Trigger Mode	
Fast Mode	
Shutter Control	Disabled Opened
ADC Rate	100 kHz

Table G.1 DIF imaging parameters

Appendix H. Image Post Processing Visual Basic Codes

```
VERSION 5.00
Begin VB.Form frmSumFrames
   Caption         =   "Sum Frames"
   ClientHeight    =   3195
   ClientLeft      =   60
   ClientTop       =   345
   ClientWidth     =   4680
   LinkTopic       =   "Form1"
   ScaleHeight     =   3195
   ScaleWidth      =   4680
   StartUpPosition =   3  'Windows Default
   Begin VB.CheckBox cbAverage
      Caption         =   "Average"
      Height          =   495
      Left            =   1560
      TabIndex        =   1
      Top             =   1080
      Width           =   1215
   End
   Begin VB.CommandButton go
      Caption         =   "Go"
      Height          =   495
      Left            =   120
      TabIndex        =   0
      Top             =   1080
      Width           =   1215
   End
End
Attribute VB_Name = "frmSumFrames"
Attribute VB_GlobalNameSpace = False
Attribute VB_Creatable = False
Attribute VB_PredeclaredId = True
Attribute VB_Exposed = False
Private Sub cbAverage_Click()
    If cbAverage Then
        frmSumFrames.Caption = "Average"
    Else
        frmSumFrames.Caption = "Sum"
    End If
End Sub

Private Sub go_Click()

    'Sum all frames in active window, output new file
    Dim afp As DocFile
    Dim nfp As New DocFile
    Dim dw As DocWindow
    Dim dws As New DocWindows
    Dim pi As New DocInfo

    Dim iFrameCtr As Integer

    ' get active document
    Set dw = dws.GetActive
    If dw Is Nothing Then
      MsgBox "An Active Window must be open", vbExclamation, "Error"
      Exit Sub
    End If
```

Appendix H.

```
    Set afp = dw.GetDocument

    ' populate pi obj with params from active file
    ' to create new file
    pi.Name = "new file.spe"
    ' set correct data type depending on processing
    ' summing frames may result in data values > 2^16 -1
    ' division results in non integer values
    If cbAverage Then
        pi.dataType = X_DOUBLE
    Else
        pi.dataType = X_LONG
    End If
    pi.FileType = dt_SPE
    pi.X = afp.GetParam(DM_XDIM)
    pi.Y = afp.GetParam(DM_YDIM)
    pi.Z = 1

    ' change caption on button to let user know
    ' something is happening
    go.Caption = "working"
    go.Enabled = False
    cbAverage.Enabled = False

    iFrameCtr = 1
    nfp.OpenNew "", pi
    ' get the buffer from the created file
    nfp.GetFrame 1, sumbuff
    '  set  the  buffer  to  the  correct  data  type  depending  on
processing
    Dim ac As New ArrayConverter
    ac.UnsignedInput = True
    If cbAverage Then
        ac.Convert sumbuff, vbDouble
    Else
        ac.Convert sumbuff, vbLong
    End If
    ' clear buffer
    For j = 0 To pi.X - 1
      For k = 0 To pi.Y - 1
        sumbuff(j, k) = 0
      Next k
    Next j

    ' calculate the sum
    For i = 1 To afp.GetParam(DM_FRAMECOUNT)
      afp.GetFrame i, buff
      If cbAverage Then
          ac.Convert buff, vbDouble
      Else
          ac.Convert buff, vbLong
      End If
      For j = 0 To pi.X - 1
        For k = 0 To pi.Y - 1
            sumbuff(j, k) = sumbuff(j, k) + buff(j, k)
        Next k
      Next j
      ac.Convert buff, vbInteger
    Next i

    ' calculate the average
```

Appendix H.

```
    If cbAverage Then
      frameCount = afp.GetParam(DM_FRAMECOUNT)
      For j = 0 To pi.X - 1
        For k = 0 To pi.Y - 1
            sumbuff(j, k) = sumbuff(j, k) / frameCount
        Next k
      Next j
    End If

    ' put new data data into file
    nfp.PutFrame 1, sumbuff
    ' show the data to the user
    nfp.Update

    ' set the button back to default
    go.Caption = "Process"
    go.Enabled = True
    cbAverage.Enabled = True
End Sub
```

Appendices

Appendix I. Sample Calculation of the In-cylinder Charge Temperature

A. In-cylinder Motoring and Firing Charge Temperature at IVC

The in-cylinder charge temperature at the start of compression (T_{IVC}) was calculated by the enthalpy balance equation

$$T_{IVC} = \frac{m_s \times c_{p,a} \times T_{in} + m_r c_{p,r} \times T_{ex}}{m_s \times c_{p,a} + m_r \times c_{p,r}}$$

where T_{in}, is intake gas temperature measured at 50mm above the intake port, T_{ex}, is exhaust gas temperature measured at 50 mm above the exhaust port, m_s is mass of scavenging gas ($m_s = m_{air} + m_{fuel} + m_{tracer}$) calculated by measuring air flow rate and fuel and tracer injection quantities, m_r is mass of residual gas and $c_{p,a}$ (air) and $c_{p,r}$ (residual gas) are specific heat at constant pressure.

- Motoring intake air flow rate =54 *litre/min*
  =0.09 *litre/cycle* at1200 rpm

- Firing intake air flow rate =84 *litre/min*
  =0.14 *litre/cycle* at 1200 rpm

- Tracer port injection = 4.5 *mg/cycle*
- Fuel direct injection = 13 *mg/cycle*

- Air density: $\rho_{air} = \frac{P_{intake\ (average\ from\ IVO\ to\ IVC)}}{R_{specific} \times T_{in}}$

R (specific gas constant) =287.058 $\frac{J}{kg.K}$

$P_{in\text{-}m}$ = 0.98 bar (averaged from IVO to IVC)

$P_{in\text{-}f}$ = 0.91 bar (averaged from IVO to IVC)

T_{in} = 315° K

$$\rho_{air\ (motoring)} = 1.083\ kg/m^3$$

$$\rho_{air\ (firing)} = 1.006\ kg/m^3$$

Appendix I.

- $m_{air} = \rho V$

$$m_{air\,(motoring)} = 97\ mg/cycle$$
$$m_{air+tracer} = 101\ mg/cycle$$

$$m_{air\,(firing)} = 141\ mg/cycle$$
$$m_{air+tracer+fuel} = 158\ mg/cycle$$

- Tracer mole fraction$= \frac{tracer\ mg/min}{air\ mg/min} \times \frac{molar\ mass\ air}{molar\ mass\ tracer} = 0.010 = 1\%$

- Residual mass $(m_r) = \frac{PVM}{\tilde{R}T}$

  P,V, T are at EVO (*T* from exhaust thermocouple)

  $\tilde{R} = 8.3144\ \frac{J}{kg.mol}$,

  Molecular weight of burned isooctane-air mixture for λ=1, M_b = 28.8 *kg* [27]

  Molecular weight of unburned isooctane-air mixture for λ=1, M_u = 30.3 *kg* [27]

  $P_{EVO\text{-}m}$ = 1.77 *bar*

  $P_{EVO\text{-}f}$ = 1.56 *bar*

  $T_{EVO\text{-}m}$ = 324° *K*

  $T_{EVO\text{-}f}$ = 443° *K*

  V_{EVO} = 275 *cc*

$$m_{r-m} = 520\ mg/cycle$$
$$m_{r-f} = 352\ mg/cycle$$

Taking the ratio of specific heats for unburned and burned mixture as $\gamma_u = 1.31$, $\gamma_b = 1.21$ respectively and the specific heats at constant volume for unburned $c_{v-u} = 0.96$ and burned mixture $c_{v-b} = 1.5$ [27]; the specific heats of residual gas at constant pressure for unburned and burned mixture were calculated as $c_{p-r-u} = 1.25$ and $c_{p-r-b} = 1.81$ respectively, resulting in IVC charge temperature of:

$$T_{IVC-m} = 323°K$$
$$T_{IVC-f} = 418°K$$

Appendix I.

B. In-cylinder Motoring and Firing Charge Temperature from IVC to IGN

Having calculated the temperature at IVC, the average in-cylinder charge temperature from start of compression to ignition timing was calculated using averaged in-cylinder pressure of 100 cycles assuming an polytropic compression

$$T_2 = T_{IVC}\left(\frac{P_{IVC}}{P_2}\right)^{\frac{n-1}{n}}$$

where n is the polytropic constant calculated from *log P-log V* diagram between IVC to IGN timing.

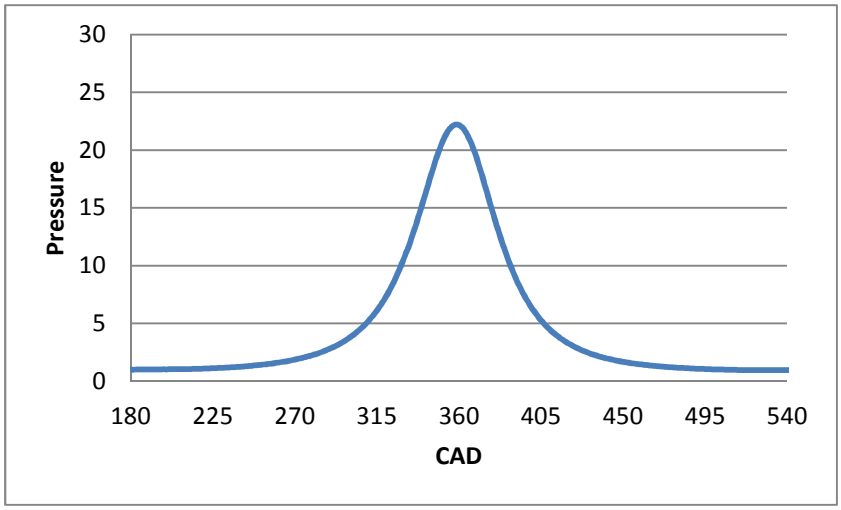

Figure I. 1 Average in-cylinder charge pressure for 100 motored cycles

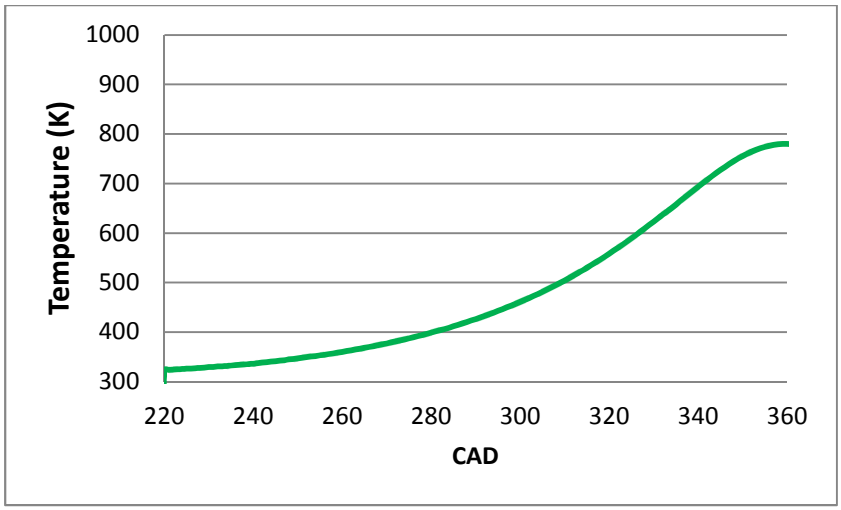

Figure I. 2 Calculated average charge temperature of 100 motored cycles during the compression stroke

Appendix I.

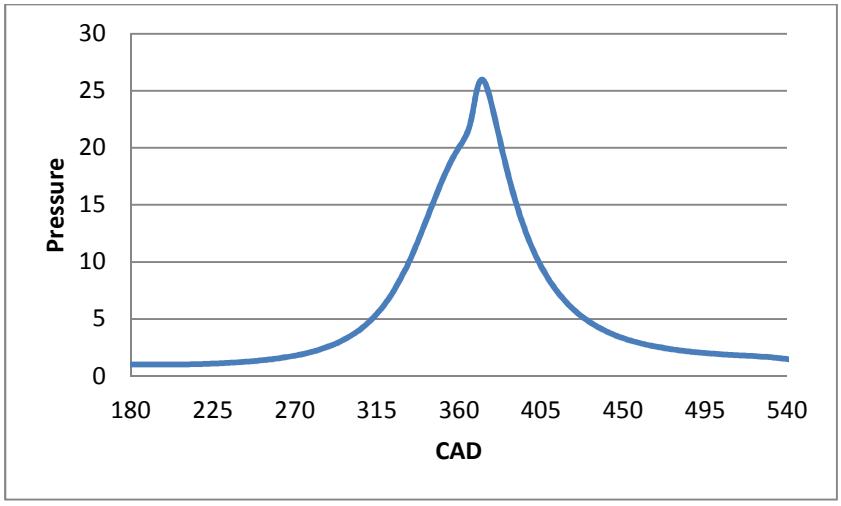

Figure I. 3 Average in-cylinder charge pressure for 100 firing cycles

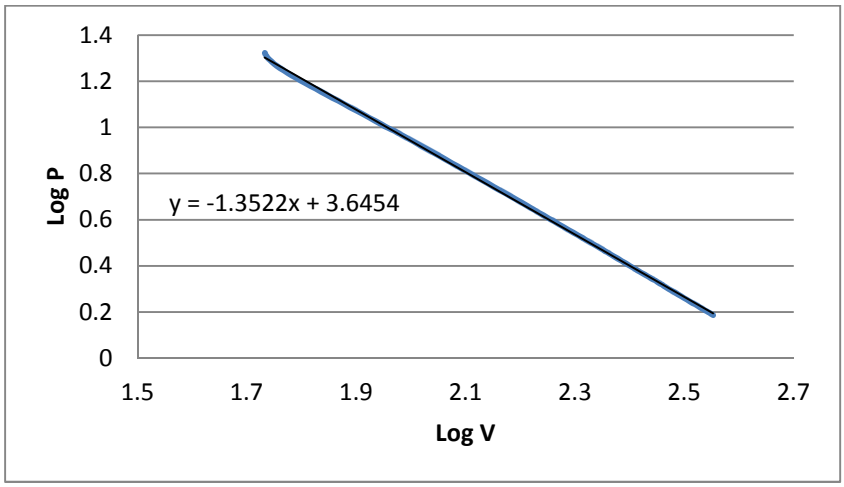

Figure I. 4 Log P- log V diagram

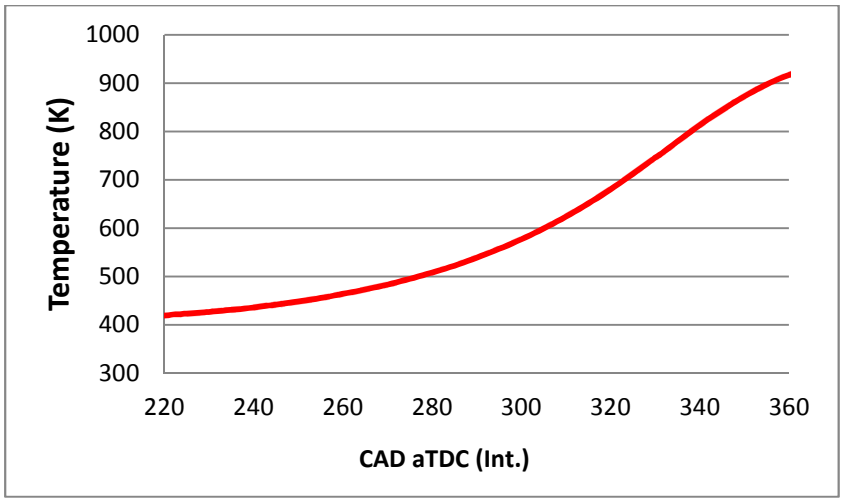

Figure I. 5 Calculated average charge temperature of 100 firing cycles during the compression stroke

Appendix J. 3-Petanonen FQY Calculation Code

```
// TEST4.cpp : Defines the entry point for the console application.
//

#include "stdafx.h"
using namespace std;

	//=============================================================
	//get_energy():  Determines  average  thermal  energy  in  3-
pentanone
	// vibrational modes at the input temperature, T.
	//=============================================================
	double get_energy(double T)
	{
		//3-pentanone vibrational frequencies for 42 vibrational
modes
		double                        freq[42]                    =
{21.53,69.49,203.10,217.84,239.51,324.61,423.84,
		489.00,652.08,739.86,821.13,851.84,1009.17,
		1038.96,1057.23,1066.22,1165.67,1185.07,1196.65,
		1313.31,1357.95,1414.97,1455.98,1471.05,1477.77,
		1500.03,1513.69,1540.67,1540.95,1546.58,1548.44,
		1887.78,3119.43,3128.77,3145.22,3146.12,3159.21,
		3170.53,3230.63,3230.96,3240.69,3241.11};
		double energy=0.0;
		int numFreq = 42;
		for(int i=0; i<numFreq; i++)
		{
			energy = energy+freq[i]/(exp((1.44*freq[i])/T)-1);
		}
		return(energy);
	}//end get_energy
	//=============================================================
	//CalcYield(): Calculates the fluorsecence quantum yield for
	// 3-pentanone as function of temperature, total
	// pressure, O2 partial pressure, and excitation
	// wavelengths. The model used to calculate the
	// data comes from Jon Koch's thesis (Stanford 2005)
	//=============================================================
	double calcYield(double lambda, double P, double PrOx,
	double X3P, double T)
	{
		//array used to store probability of getting to energy E
		double* prob = new double[100000];
		//array used to store FQY information for each energy E
		double* phi=new double[100000];
		double PI = 4.0*atan(1.0);
		double RG = 8.314E+7; //Gas constant [erg/mol-K]
		double KB = 1.38054E-16; //Boltzmann constant [erg/K]
		double E0 = 30770; //Excited singlet orgin for 3P [cm^-
1]
		double  KF  =  4.2e+5;  //Fluorescence  rate  [s^-1]  3-
pentanone
		double SIG3P = 6.05E-8; // Lennard-Jones coll diameter
3P [cm]
		double EDK3P = 432; // Lennard-Jones epsilon/kb 3P [K]
		double M3P = 86.016; // molecular weight 3P
		double SIGN2 = 3.798E-8; // L-J coll diam N2 [cm]
		double EDKN2 = 71.40; // L-J epsilon/kb, N2 [K]
```

Appendix J.

```
            double MN2 = 28.02; // molecular weight, N2 [g/mol]
            double SIGO2 =3.798E-8; // Lennard-Jones coll. diameter
O2 [cm]
            double EDKO2 = 71.4; // L-J epsilon/kb, o2 [K]
            double MO2 = 32.00; // molecular weight, O2 [g/mol]
            //exponent changes to 1.35 from Koch's value of 1.2
            double exponent=1.35; //Exponent for alpha T dependence
            double alphaN2 = 0.050*pow((T/300),(-exponent));
            double alphaO2 = 0.050*pow((T/300),(-exponent));
            double alpha3P = 0.15;
            double P3P = X3P*P;
            double PrO2 = PrOx;
            P = P - PrO2-P3P; //calculate nitrogen partial pressure

      ////////////////////////////////////////////////////////////
            // Solve for Lennard-Jones coll. parameters and coll.
frequency

      ////////////////////////////////////////////////////////////
            // L-J coll diam for 3P collisions with N2 [cm]
            double sig = ((SIG3P + SIGN2)/2.0);
            SIGO2 = ((SIG3P + SIGO2)/2.0); // L-J coll diam [cm] o2-
3p
            double edk = sqrt(EDK3P*EDKN2); // L-J eps/kb [K]
            EDKO2 = sqrt(EDK3P*EDKO2); // L-J eps/kb [K]
            double muN2 = M3P*MN2/(M3P + MN2); // reduced mass,
3P/N2 [g/mol]
            double muO2 = M3P*MO2/(M3P + MO2); // reduced mass,
3P/O2 [g/mol]
            double mu3P = M3P*M3P/(M3P+M3P); // reduced mass, 3P/3P
[g/mol]
            //Calculate collision integrals
            double omegaN2 = 1/(0.636 + 0.567*log10(T/edk)); //Coll
int. 3P/N2
            double omegaO2 = 1/(0.636 + 0.567*log10(T/EDKO2));//coll
int. 3p/O2
            double omega3P = 1/(0.636 + 0.567*log10(T/EDK3P));//coll
int. 3p/3p
            //Calculate collision frequencies [cm^3/s]
            double ZN2= PI*(sig*sig)*sqrt(8*RG*T/(PI*muN2))*omegaN2;
//3P/N2
            double                                                ZO2=
PI*(SIGO2*SIGO2)*sqrt((8*RG*T)/(PI*muO2))*omegaO2;//3P/O2
            double
Z3P=PI*(SIG3P*SIG3P)*sqrt(8*RG*T/(PI*mu3P))*omega3P*0.5;//3P
            //Kcoll per 3p molec [1/s] (collision rate)
            double                          kcoll                 =
ZN2*P*1.00E+6/(KB*T)+ZO2*PrO2*1.0E+6/(KB*T)
            +Z3P*P3P*1.0E+6/(KB*T);
            //Calculate number densities
            double nO2 = PrO2*1.0E+6/(KB*T); //O2 number density
            double nN2 = P*1.0E+6/(KB*T); //N2 number density
            double n3P = P3P*1.0E+6/(KB*T); //3P number density
            double                          alpha                 =
alphaN2*(ZN2*nN2)/kcoll+alphaO2*(ZO2*nO2)/kcoll
                  +alpha3P*(Z3P*n3P)/kcoll;
            double Eex = 1.0e7/lambda; //Excitation energy [cm^-1]
            double Eth = get_energy(T); //Thermal energy [cm^-1]
            double Ehigh = Eex + Eth - E0; //Energy of excited state
[cm^-1]
            //Additional variables for FQY calculations
```

Appendix J.

```
            double E = Ehigh; // start vib energy at initial state
in S1
            double close = 1; // terminate summation if within 1
cm^-1 of Eth
            double dEav;
            double phitot;
            double po2,ko2;
            double knr = 0.0;
            int i=0, j, inum;

      ////////////////////////////////////////////////////////////
            // Find contribution of each energy E to overall
fluorescence yield

      ////////////////////////////////////////////////////////////
            do
            {
            //New expression for knr
            //Old
(Koch):knr=3.78E+8+8.15E+6*exp(E/2466)+216*exp(E/10220);
                  knr     =     3.84E+8+2.4E-3*pow((E-2400),3.0)+5E-
33*pow((E-1800),10.0)
                        +0.5E+8*exp(-(E-1175)*(E-1175)/(500*500));
                  dEav = alpha*(E - Eth);
            //modified expression for probability of O2 quenching
the
            //large step in po2 at 11000 cm^-1 was eliminated from
the
            //original expression used by Koch
                  po2 = 0.0023*exp(E/20000.0);
                  ko2 = po2*ZO2*nO2;
                  prob[i] = kcoll/(kcoll +ko2+ knr + KF);//Prob. of
getting to E
                  if ((E - dEav - Eth) > close)
                  {
                        phi[i] = KF/(kcoll +ko2+ knr + KF);//FQY for
energy E
                  }
                  else phi[i] = KF/(ko2+knr + KF); //FQY for E~Eth
                  for (j = 0; j < i; j=j+1)
                  {
                        phi[i] = phi[i] * prob[j]; //Contribution to
overall FQY
                  }
                  E = E - dEav; // Decrement energy
                  i=i+1; // Increment count
            }
            while(E - Eth > close);
            inum = i;

      ////////////////////////////////////////////////////////////
            // Sum contributions to FQY from each energy level in
the cascade

      ////////////////////////////////////////////////////////////
            phitot = 0;
            for (i = 0; i < inum; i=i+1)
            {
                  phitot = phitot + phi[i]; // add contribution from
step i
            }
```

Appendix J.

```
	//kill dynamic arrays
	delete[] phi;
	delete[] prob;
	//return final value calculated for FQY
	return phitot;
} //End calcYield

int _tmain(int argc, _TCHAR* argv[])
{
	double lambda;
	double theP;
	double Prx;
	double XP;
	double Tem;
	cout << "lambda: ";
	cin >> lambda;
	cout << "P: ";
	cin >> theP;
	cout << "PrOx: ";
	cin >> Prx;
	cout << "X3P: ";
	cin >> XP;
	cout << "T: ";
	cin >> Tem;
	double result =calcYield(lambda,theP,Prx,XP,Tem);
	cout << result;
	cin >> result;
	return 0;
                                                    }
```

References

1 World Crude Oil Reserves, Organization of the Petroleum Exporting Countries (OPEC), Available at: http://www.opec.org/opec_web/en/data_graphs/330.htm/ (Accessed: 10 August 2012)

2 International Energy Statistics, U.S. Energy Information Administration (EIA), Available at: http://www.eia.gov/cfapps/ipdbproject/IEDIndex3.cfm?tid=5&pid=57&aid=6 (Accessed: 10 August 2012)

3 Weiss, M., Heywood, J. (2000) '*On the Road in 2020: A life Cycle Analysis of New Automobile Technologies*', MIT Energy Laboratory Report EL00-003, MIT, Cambridge, MA.

4 UK Fuel Duty, '*How much Fuel Duty do we pay?*' (2012), Available at: http://whatgas.com/car-finance/fuel-duty.html/ (Accessed: 10 August 2012)

5 Laws and Regulations, California Air Resource Board (CARB), Available at: http://www.arb.ca.gov/html/lawsregs.htm (Accessed: 10 August 2012)

6 Laws & Regulations, Environmental Protection Agency (EPA), Available at: http://www.epa.gov/lawsregs/ (Accessed: 10 August 2012)

References

7 Regulations and Environmental Law, Ministry of Environment Government of Japan, Available at: http://www.env.go.jp/en (Accessed: 10 August 2012)

8 Air Quality Legislation, European Union, Available at: http://europa.eu/legislation_summaries/environment/air_pollution/index_en.htm (Accessed: 10 August 2012)

9 Emission Standards, Cars and Light Trucks, Available at: http://www.dieselnet.com/standards/eu/ld.php (Accessed: 10 August 2012)

10 Road transport: Reducing CO2 emissions from vehicles, Available at: http://ec.europa.eu/clima/policies/transport/vehicles/index_en.htm (Accessed: 10 August 2012)

11 Iwamoto, Y., Noma, K., Nakayama, O., Yamauchi, T. et al. (1997) 'Development *of Gasoline Direct Injection Engine*', SAE Technical Paper 970541.

12 Harada, J., Tomita, T., Mizuno, H., Mashiki, Z. et al. (1997) '*Development of Direct Injection Gasoline Engine*', SAE Technical Paper 970540.

13 Zhao H. (ed.) (2010) *Advanced Direct Injection Combustion Engine Technologies and Development: Volume 1: Gasoline and Gas Engines*. Science and Technology, Woodhead Publishing, Cambridge.

14 Cohn, D.R., Bromberg, L., Heywood, J.B. (2005) '*Direct Injection Ethanol Boosted Gasoline Engines: Biofuel Leveraging For Cost Effective Reduction of Oil Dependence and CO2 Emissions*', MIT Laboratory for Energy and the Environment Report LFEE.

15 Bromberg, L., Cohn, D., R., Heywood, J., B. (2006) '*Calculations of Knock Suppression in Highly Turbocharged Gasoline/Ethanol Engines Using Direct Ethanol Injection*', MIT Laboratory for Energy and the Environment Report LFEE.

References

16 Bromberg, L., Cohn, D., R. (2007) '*Effect of Compression Ratio and Manifold Pressure on Ethanol Utilization in Gasoline/Ethanol Engines*', MIT Plasma Science and Fusion Centre, PSFC-JA-07-03.

17 Bromberg, L., Cohn, D., R. (2008) '*Effective Octane and Efficiency Advantages Of Direct Injection Alcohol Engines*', MIT Laboratory for Energy and the Environment Report LFEE.

18 Tongroon, M., Zhao, H. (2010) '*Combustion Characteristics of CAI Combustion with Alcohol Fuels*', SAE Technical Paper 2010-01-0843.

19 Tongroon, M. (2010) '*Combustion Characteristics and In-cylinder Process of CAI Combustion with Alcohol Fuels*', PhD Thesis, Brunel University.

20 Gomes, P., Ecker, R., Kulzer, A., Kufferath, A. et al. (2011) '*Study on Boosted Direct Injection SI Combustion with Ethanol Blends and the Influence on the Ignition System*', SAE Technical Paper 2011-36-0196.

21 Christie, M., Fortino, N., Yilmaz, H. (2009) '*Parameter Optimization of a Turbo Charged Direct Injection Flex Fuel SI Engine*', SAE Int. J. Engines 2(1):123-133.

22 Blumberg, P., Bromberg, L., Kang, H., Tai, C. (2009) '*Simulation of High Efficiency Heavy Duty SI Engines Using Direct Injection of Alcohol for Knock Avoidance*', SAE Int. J. Engines 1(1):1186-1195.

23 Ikoma, T., Abe, S., Sonoda, Y., Suzuki, H. et al. (2006) '*Development of V-6 3.5-liter Engine Adopting New Direct Injection System*', SAE Technical Paper 2006-01-1259.

24 Stein, R., House, C., Leone, T. (2009) '*Optimal Use of E85 in a Turbocharged Direct Injection Engine*', SAE Int. J. Fuels Lubr. 2(1):670-682.

References

25 Atkinson, J. (1887) '*Gas-Engine*', U.S. Patent 367,496, Filed Apr. 13, 1880, Issued Aug. 2, 1887.

26 Miller, R. (1957) '*Supercharged Engine*', U.S. Patent 2,817,322, Filled Apr. 30, 1956, Issued Dec. 24, 1957.

27 Heywood, J.B. (1988) *Internal Combustion Engine Fundamentals* McGraw-Hill Science Engineering.

28 Product History, Toyota Prius, Available at: http://www.toyota.com/about/our_business/our_history/product_history/pdf/prius.pdf (Accessed: 10 August 2012)

29 Official announcement data of Yamaha Motor (1999) '*Environment-Friendly SD (Super Diesel) Engine Developed*', Available at: http://www.yamaha-motor.co.jp/global/news/1999/03/23/super-diesel.html (Accessed: 10 August 2012)

30 Drangel, H., Olofsson, E., Reinmann, R. (2002) '*The Variable Compression (SVC) and the Combustion Control (SCC) - Two Ways to Improve Fuel Economy and Still Comply with World-Wide Emission Requirements*', SAE Technical Paper 2002-01-0996.

31 Turner, J., Blundell, D., Pearson, R., Patel, R. et al. (2010) '*Project Omnivore: A Variable Compression Ratio ATAC 2-Stroke Engine for Ultra-Wide-Range HCCI Operation on a Variety of Fuels*', SAE Int. J. Engines 3(1):938-955.

32 Rabhi, V., Beroff, J., Dionnet, F. (2004) '*Study of a Gear-Based Variable Compression Ratio Engine*', SAE Technical Paper 2004-01-2931.

33 MCE-5 VCRi: Pushing back the fuel consumption reduction limits, Available at: http://www.mce-5.com/english/pop_up/atouts_technologiques/pdf

/Piston_kinematics_US.pdf (Accessed: 10 August 2012)

34 Volkswagen News (2005) '*Volkswagen Golf GT TSI - Supercharged and Turbocharged 1.4l'*, Volkswagen AG, Available at: http://www.vwvortex.com/cgi-bin/artman/exec/view.cgi?archive=7&num=1496&printer=1 (Accessed: 10 August 2012)

35 Birch, S. (2012) '*Ford's new 1.0-L EcoBoost I-3 is big on low-friction technology*', SAE Automotive Engineering International Magazine, Feb. 2012, Available at: http://www.sae.org/mags/aei/10714/ (Accessed: 10 August 2012)

36 Introducing the CVCC, Available at: http://world.honda.com/history/challenge/1972introducingthecvcc/text05/index.html (Accessed: 10 August 2012)

37 Schwarz, C., Schünemann, E., Durst, B., Fischer, J., Witt. A. (2006) '*Potentials of the Spray-Guided BMW DI Combustion System*', SAE Technical Paper 2006-01-1265.

38 Benson J. (1972) '*The Influence of Engine and Fuel Factors on After-run*', SAE paper 720085.

39 Ingamells J. (1979) '*Effect of Gasoline Octene Quality and Hydrocarbon Composition on after-run*', SAE paper 790939.

40 Lavy, J., Dabadie, J., Angelberger, C., Duret, P. et al. (2000) '*Innovative Ultra-low NOx Controlled Auto-Ignition Combustion Process for Gasoline Engines: the 4-SPACE Project*', SAE Technical Paper 2000-01-1837.

41 Law, D., Kemp, D., Allen, J., Kirkpatrick, G. et al. (2001) '*Controlled Combustion in an IC-Engine with a Fully Variable Valve Train*', SAE Technical Paper 2001-01-0251.

References

42 Koopmans, L., Denbratt, I. (2001) '*A Four Stroke Camless Engine, Operated in Homogeneous Charge Compression Ignition Mode with Commercial Gasoline'*, SAE Technical Paper 2001-01-3610.

43 Li, J., Zhao, H., Ladommatos, N., Ma, T. (2001) '*Research and Development of Controlled Auto-Ignition (CAI) Combustion in a 4-Stroke Multi-Cylinder Gasoline Engine*', SAE Technical Paper 2001-01-3608.

44 Zhao, H., Li, J., Ma, T., Ladommatos, N. (2002) '*Performance and Analysis of a 4-Stroke Multi-Cylinder Gasoline Engine with CAI Combustion*', SAE Technical Paper 2002-01-0420.

45 Cao, L., Zhao, H., Jiang, X., Kalian, N. (2005) '*Mixture formation and controlled auto-ignition combustion in four-stroke gasoline engines with port and direct fuel injections*' International Journal of Engine Research 6: 311-330.

46 Standing, R., Kalian, N., Ma, T., Zhao, H. et al. (2005) '*Effects of Injection Timing and Valve Timings on CAI Operation in a Multi-Cylinder DI Gasoline Engine*', SAE Technical Paper 2005-01-0132.

47 Cao, L., Zhao, H., Jiang, X., Kalian, N. (2006) '*Investigation into the Effect of Injection Timing on Stoichiometric and Lean CAI Operations in a 4-Stroke GDI Engine'*, SAE Technical Paper 2006-01-0417.

48 Li, Y., Zhao, H., Brouzos, N., Ma, T. (2007) '*Parametric Study on CAI Combustion in a GDI Engine with an Air-Assisted Injector*', SAE Technical Paper 2007-01-0196.

49 Cao, L., Zhao, H., Jiang, X. (2008) '*Analysis of controlled auto-ignition/HCCI combustion in a direct injection gasoline engine with single and split fuel injections'*, Combustion Science and Technology 180: 176-205.

References

50 Williams, M. (2008) '*HCCI: GM making advances with its "newest" fuel-economy improving engine tech*', Motor Trend, June 2008, Available at: http://www.motortrend.com/features/auto_news/2008/112_0806_gm_hcci_fuel_efficient_system/viewall.html/ (Accessed: 10 August 2012)

51 Joseph, N. (2007) '*Diesel, without the diesel: Mercedes-Benz debuts DiesOtto*', Available at: http://www.autoblog.com/2007/07/25/diesel-without-the-diesel-mercedes-benz-debuts-diesotto/ (Accessed: 10 August 2012)

52 Vijayenthiran, V. (2007) '*Volkswagen's future technology*', June 2007, Available at: http://www.motorauthority.com/news/1027127_volkswagens-future-technology (Accessed: 10 August 2012)

53 Dunham, B. (1974) '*Automatic On/Off Switch Gives 10-Percent Gas Saving*', Popular Science, p. 170, October 1974, Available at: http://books.google.com/books?id=RkeRDMj1r2kC&pg=PA170/ (Accessed: 10 August 2012)

54 Mazda i-Stop, Idling Stop Technology, Available at: http://www.mazda.com/mazdaspirit/env/engine/siss.html/ (Accessed: 10 August 2012)

55 Laurendeau, N. M. (1991) *Temperature Measurements by Light Scattering Methods*, in Chigier, N. (ed.) *Combustion Measurements.* Washington, DC.: Hemisphere Pub. Corp.

56 Eckbreth, A. C. (1996) *Laser Diagnostics for Combustion Temperature and Species*. 2nd edn. Amsterdam: Gordon and Breach Publishers.

57 Zhao, H., Ladammatos, N. (2001) *Engine Combustion Instrumentation and Diagnostics.* Warrendale, Pa.: SAE Inc.

References

58 Kohse-Hoinghaus, K. (ed.), Jeffries, J. B. (Ed.) (2002) *Applied Combustion Diagnostics*, London: Taylor Francis.

59 Zhao, H. (2012) '*Laser Diagnostics and Optical Measurements Techniques*' in *Internal Combustion Engines*, Warrendale, Pa.: SAE Inc.

60 Goulard, R. (1974) *Combustion Measurements: Modern Techniques and Instrumentation*. Washington, DC.: Hemisphere.

61 Heitor, M. V., Moreira, A. L. N. (1992) '*Probe Measurements of Scalar Properties in Reacting Flows'* in Durao, D., F., G., et al. *Combusting Flow Diagnostics*. Dordrecht: Kluwer Academic Press, pp. 79-136.

62 Taylor, A., M., K., P. (ed.) (1993) *Instrumentation for Flows with Combustion*. London: Academic Press.

63 Gaydon, A., G. (1974) *The Spectroscopy of Flames*. London: Chapman and Hall.

64 Measures, R., M. (1984) *Laser Remote Sensing*. New York: John Wiley.

65 Long, D., A. (1977) *Raman Spectroscopy*. New York: McGraw-Hill.

66 Drake, M., C., Hastie, J., W. (1981) '*Temperature Profiles of Inhibited Flames Using Raman Spectroscopy*', Combustion and Flame 40:201.

67 Lapp, M., Penney, C., M., Goldman, L., M. (1972) '*Raman Scattering from Flames*' Science Vol. 175 no. 4026 pp. 1112-1115.

68 Drake, M., C., Lapp, M., Penney, C., M. (1982) '*Use of the Raman Effect for Gas Temperature Measurements*' in Schooley, J., F. (ed.) *Temperature: Its Measurement and Control in Science and Industry* Vol. 5, pp. 631-638, New York: American Institute of Physics.

References

69 Smith, J. (1980) '*Temperature and Density Measurements in an Engine by Pulsed Raman Spectroscopy*', SAE Technical Paper 800137.

70 Lapp, M., Penney, C., M. (1974) *Laser Raman Gas Diagnostics*. New York: Plenum.

71 Smith, J., R., Green, R., M. (1984) '*An experimental and modeling study of engine knock*', Symposium (International) on Combustion, Vol. 20, Issue 1, pp. 91–100.

72 Drake, M., C., Rosenblatt, G., M. (1978) '*Rotational Raman Scattering from Premixed and Diffusion Flames*', Combustion and Flame 33: 179.

73 Eckbreth, A., C. (1981) '*Recent Advances in Laser Diagnostics for Temperature and Species Concentration in Combustion*', Eighteenth Symposium on Combustion, pp. 1472- 1488, Petersburg, PA.: The Combustion Institute.

74 Penney, C., M. (1969) '*Light Scattering in Terms of Oscillator Strengths and Refractive Indices*', Journal of the Optical Society of America, 59:34.

75 Namer, I., Schefer, R., W. (1985) '*Error Estimates for Rayleigh Scattering Density and Temperature Measurements in Premixed* Flames', Exp. Fluids 3:1.

76 Orth, A., Sick, V., Wolfrum, J., Maly, R. R., Zahn, M. (1994) '*Simultaneous 2D-Single Shot Imaging of OH Concentrations and Temperature Fields in a SI Engine Simulator*', Symposium (International) on Combustion 25(1): pp. 143-150.

77 Bräumer, A., Sick, V., Wolfrum, J., Drewes, V. et al. (1995) '*Quantitative Two-Dimensional Measurements of Nitric Oxide and Temperature Distributions in a Transparent Square Piston SI Engine*', SAE Technical

Paper 952462.

78 Schulz, C., Sick, V., Wolfrum, J., Drewes, V., Zahn, M., Maly, R., (1996) '*Quantitative 2D Single-Shot Imaging of no Concentrations and Temperatures in a Transparent SI Engine*', Symposium (International) on Combustion 26 (2): pp. 2597-2604.

79 Bechtel, J., H. (1979) '*Temperature Measurements of the Hydroxyl Radical and Molecular Nitrogen in Premixed, Laminar Flames by Laser Techniques*' Applied Optics 18:2100.

80 Anderson, W., R., Decker, L., J., Kotlar, A., J. (1982) '*Temperature profile of a Stoichiometric CH4/N2O Flame from Laser Excited Fluorescence Measurements on OH*', Combustion and Flame 48: 179.

81 Chan, C., Daily, J., W. (1980) '*Measurement of Temperature in Flames Using Laser Induced Fluorescence Spectroscopy of OH*', Applied Optics 19:1963.

82 Zizak, G., Horvath, J., J., Winefordner, J., D. (1981) '*Flame Temperature Measurement by Redistribution of Rotational Population in Laser-excited Fluorescence: An Application to the OH Radical in a Methane-Air Flame*', Applied Spectroscopy 35:488.

83 Furuya, Y., Yamamoto, M., Takubo, Y. (1985) '*Rotational Energy Transfer in A2Σv'=0 State of OH in Flame: On the Use of Laser-Induced Fluorescence Spectrum for Flame Temperature Measurement*', Japanese Journal of Applied Physics 24:455.

84 McKenzie, R., L, Gross, K., P. (1981) '*Two-Photon Excitation of Nitric Oxide Fluorescence as a Temperature Indicator in Unsteady Gasdynamic Processes*', Applied Optics 20:2153.

References

85 Roller, A., Paul, A., Decker, M., Sick, V. et al. (1995) '*Non-intrusive Temperature Measurements during the Compression Phase of a DI Diesel Engine*', SAE Technical Paper 952461.

86 Laurendeau, N., M. (1988) '*Temperature Measurements by Light-scattering Methods*', Progress in Energy and Combustion Science, Vol. 14, Issue 2, pp. 147-170.

87 Kaminski, C., F., Engström, J., Aldén, M. (1998) '*Quasi-instantaneous Two-Dimensional Temperature Measurements in a Spark Ignition Engine Using 2-line Atomic Fluorescence*', Proc. Comb Inst., 27:85-93.

88 Engström, J., Kaminski, C., Aldén, M., Josefsson, G. et al. (1999) '*Experimental Investigations of Flow and Temperature Fields in an SI Engine and Comparison with Numerical Analysis*', SAE Technical Paper 1999-01-3541.

89 Hanson, R., K. (1988) '*Combustion Diagnostics: Planar Imaging Techniques*', Twenty-First Symposium (International) on Combustion, p. 1677.

90 Felton, P., G., Mantzaras, J., Bomse, D., S., Woodin, R., L. (1988) '*Initial Two-Dimensional Laser Induced Fluorescence Measurements of OH Radicals in an Internal Combustion Engine*', SAE paper 881633.

91 Schipperijn, F., W., Nagasaka, R., Sawyer, R., F., Green, R., M. (1988) '*Imaging of Engine Flow and Combustion Processes*', SAE paper 881631.

92 Fansler, T., D., French, D., T., Drake, M., C. (1995) '*Fuel Distributions in a Firing Direct-Injection Spark-Ignition Engine Using Laser-Induced Fluorescence Imaging*', SAE Paper 950110.

References

93 Winklhofer, E., Philipp, H., Fraidl, G., Fuchs, H. (1993) '*Fuel and Flame Imaging in SI Engines*', SAE Paper 930871.

94 Reboux, J., Puechberty, D. (1994) '*A New Approach of PLIF Applied to Fuel/Air Ratio Measurement in the Compressive Stroke of an Optical SI Engine*' SAE technical paper series No. 941988.

95 Lozano, A. (1992) '*Laser-Excited Luminescent Tracers for Planar Concentration Measurements in Gaseous Jets*', Ph.D. dissertation, Stanford University.

96 Lozano, A., Yip, B., Hanson, R., K. (1992) '*Acetone - a Tracer For Concentration Measurements in Gaseous Flows by Planar Laser-induced Fluorescence'*, Experiments In Fluids, 13(6):369-376.

97 Bazile, R., Stepowski, D. (1995) '*Measurements of Vaporized and Liquid Fuel Concentration Fields in a Burning Spray Jet of Acetone Using Planar Laser-induced Fluorescence*', Experiments in Fluids, 20(1):1-9.

98 King, G., F., Lucht, R., P., Dutton, J., C. (1997) '*Quantitative Dual-tracer Planar Laser-induced Fluorescence Measurements of Molecular Mixing*', Optics Letters, 22(9):633-5.

99 Marro, M., A., T., Miller, J., H. (1998) '*Acetone Fluorescence as a Conserved Scalar Marker in a Laminar Methane Air Diffusion Flame*', Combustion Science and Technology, 140(1-6):13.

100 Su, L., K., Clemens, N., T., (1999) '*Planar Measurements of the Full Three-Dimensional Scalar Dissipation Rate in Gas-phase Turbulent Flows*', Experiments in Fluids, 27(6):507-21.

101 Barreras, F., Lozano, A., Yates, A., J., Dopazo, C. (1999) '*The Structure of Subsonic Air Wakes Behind a Flat Plate*', Experiments in Fluids, 26(5):478-

80.

102 Bryant, R., Driscoll, J., F. (2000) '*Acetone Laser Induced Fluorescence for Low Pressure, Low Temperature Flow Visualization*', Experiments in Fluids, 28:417-476.

103 Lide D., R. (ed.) (1999) *CRC Handbook of Chemistry and Physics*, 80th ed., CRC Press.

104 Glassman, I. (1996) *Combustion*, 3rd ed., Academic Press, San Diego.

105 Bartok, W., Sarofim, A., F. (Eds.), (1991) *Fossil Fuel Combustion-A Source Book*, John Wiley, New York.

106 *Merck Product Catalogue*, (1999) Merck, Darmstadt.

107 Yaws C., L. (1995) *Handbook of transport property data-viscosity, thermal conductivity, and diffusion coefficients of liquids and gases*, Gulf Publishing Company, Houston.

108 Neij H. (1998) '*Development of laser-induced fluorescence for precombustion iagnostics in spark-ignition engines*', PhD thesis, Lund Institute of Technology.

109 Grossmann, F., Monkhouse, P., Ridder, M., Sick, V., Wolfrum, J. (1996) '*Temperature and Pressure Dependences of the Laser-Induced Fluorescence of Gas-Phase Acetone and 3-Pentanone*', Applied Physics B 62, 249-253.

110 Einecke S., Sick., V. (1998) '*Two-Dimensional Temperature Measurements in an SI Engine Using Two-line Tracer LIF*', SAE Technical Paper, 982468.

111 Einecke, S., Schulz, C, Sick, V. (2000) '*Measurement of Temperature, Fuel Concentration and Equivalence Ratio Fields Using Tracer LIF in IC Engine*

Combustion', Applied Physics B-Lasers and Optics, 71(5):717-723.

112 Strand, T., E., Rothamer, D., A., Ghandhi, J., B. (2001) '*Flame Structure Visualization of Stratified Combustion in a DISI Engine via PLIF*', SAE Paper 2001-01-3649.

113 Kakuho, A., Nagamine, M., Amenomori, Y., Urushihara, T., Itoh, T. (2006) '*In-cylinder Temperature Distribution Measurement and its Application to HCCI Combustion*', SAE Paper 2006-01-1202.

114 Rothamer, D., A., Snyder, J., A., Hanson R., K., Steeper, R., R. (2008) '*Two-Wavelength PLIF Diagnostic for Temperature and Composition*', SAE Technical Paper 2008-01-1067.

115 Rothamer, D., A., Snyder, J., A., Hanson, R., K., Steeper, R., R. (2010) '*Optimization of a tracer-based PLIF diagnostic for simultaneous imaging of EGR and temperature in IC engines*', Applied Physics B 99: 371-384.

116 Snyder, J., A., Hanson, R., K., Fitzgerald, R., P., Steeper, R., R. (2009) '*Dual-Wavelength PLIF Measurements of Temperature and Composition in an Optical HCCI Engine with Negative Valve Overlap*', SAE Int. J. Engines, 2009-01-0661.

117 Rothamer, D., A., Snyder, J., A., Hanson, R., K., Steeper, R., R., Fitzgerald, R., P. (2009) '*Simultaneous Imaging of Exhaust Gas Residuals and Temperature During HCCI Combustion*', Proceedings of Combustion Institute 32 2869-2876.

118 Snyder, J., Dronniou, N., Dec J., Hanson, R., K. (2011) '*PLIF Measurements of Thermal Stratification in an HCCI Engine under Fired Operation*', SAE Int. J. Engines, 2011-01-1291.

References

119 Dronniou, N., Dec, J. (2012) '*Investigating the Development of Thermal Stratification from the Near-Wall Regions to the Bulk-Gas in an HCCI Engine with Planar Imaging Thermometry*', SAE Int. J. Engines 5(3):1046-1074.

120 The Ricardo/Cussons Standard Hydra Engine and Test Bed Manual, Issue 8, October 1986.

121 Houston, R., Cathcart, G. (1998) '*Combustion and Emissions Characteristics of Orbital's Combustion Process Applied to Multi-Cylinder Automotive Direct Injected 4-Stroke Engines*', SAE Paper 980153.

122 Cathcart, G., Zavier, C. (2000) '*Fundamental Characteristics of an Air-Assisted Direct Injection Combustion Systems as Applied to 4-Stroke Automotive Gasoline Engines*', SAE Paper 2000-01-0256.

123 Boretti, A., Jin, S-H., Brear, M., Zakis, G., Attard, W., Watson, H., Brewster, S., Bryce, W. (2008) '*Experimental and numerical study of a spark ignition engine with air-assisted direct injection*', Processing of IMechE Vol. 222 Part D: J. Automobile Engineering, pp. 1103-1119.

124 Piepmeier, E., H. (1972) '*Theory of Laser-saturated Atomic Resonance Fluorescence*', Spectrochimica Acta, Vol. 27B, pp. 431-443.

125 McKenzie, R., L., Gross, K., P. (1981) '*Two-photon Excitation of Nitric Oxide Fluorescence as a Temperature Indicator in Unsteady Gasdynamic Processes*', Applied Optics, Vol. 20, Issue 12, pp. 2153-2165.

126 Anderson, W., R., Decker, L., J., Kotlar, A., J. (1982) '*Temperature Profile of a Stoichiometric CH4/N2O Flame from Laser Excited Fluorescence Measurements on OH*', Combustion and Flame, Vol. 48, pp. 163–177.

References

127 Hansen, D., A., Lee, E., K., C. (1975) '*Radiative and Nonradiative-transitions in First Excited Singlet-state of Symmetrical Methyl-substituted Acetones*', Journal Of Chemical Physics, Vol. 62(1), pp. 183-189.

128 Heicklen, J., Noyes, Jr., W., A., (1959) '*The Photolysis and Fluorescence of Acetone and Acetone Biacetyl Mixtures*', Journal of the American Chemical Society, Vol. 81, Issue 15, pp. 3858–3863.

129 Koch, J., D., Hanson, R., K. (2003) '*Temperature and Excitation Wavelength Dependencies of 3-pentanone Absorption and Fluorescence for PLIF Applications*', Applied Physics B Vol. 76, No.3, pp. 19–24.

130 Koch, J., Gronki, J., Hanson, R., K. (2008) '*Measurements of near-UV absorption spectra of acetone and 3-pentanone at high temperatures*', Journal of Quantitative Spectroscopy and Radiative Transfer, 109, pp. 2037-2044.

131 Equilateral Dispersing prisms (2009), CVI Melles Griot Technical Guide, Vol. 2, Issue 2.

132 Optical Coatings (2009), CVI Melles Griot Technical Guide, Vol. 2, Issue 2.

133 Operator's Manual for the Intensified Lens Systems Type ILS-3-11 (2004), DRS Data & Imaging Systems Inc.

134 PI-MAX System Manual (2009), Princeton Instrument, Roper Scientific Inc.

135 Macro Photography, Available at: http://www.photography.com/articles/types-of-photography/macro-photography/ (Accessed: 10 August 2012)

136 Special application lenses, UV-Nikkor 105mm f/4.5, Available at: http://www.mir.com.my/rb/photography/companies/nikon/nikkoresources/special/105UVmm.htm (Accessed: 10 August 2012)

137 Micro-Nikkor 60 mm f/2.8D, Available at: http://www.kenrockwell.com/nikon/60mm-afd.htm (Accessed: 10 August 2012)

138 Micro-Nikkor 60mm f/2.8D, Available at: http://www.nikonusa.com/en/Nikon-Products/Product/Camera-Lenses/1987/AF-Micro-NIKKOR-60mm-f%252F2.8D.html (Accessed: 10 August 2012)

139 Calibration data, Coherent J-50MUV-248 Energy Sensor (Certificate Number: 100901085323) and FieldMaxII-TOP Power/Energy Meter (Certificate Number: 100916093918)

140 Paetzel, P., '*Comparison Excimer Laser-Solid State Laser*', Lambda Physik AG, Available at: http://www.coherent.com/Downloads/ComparisonExcimerLaserSolidStateLaserRev2.pdf (Accessed: 10 August 2012)

141 Wagner, F., X., Scaggs, M., Koch, A., Endert, H., Christen, H., M., Knauss, L., A., Harshavardhan, K., S., Green, S., M. (1998) '*Epitaxial HTS Thin Films Grown by PLD with a Beam Homogenizer*', Applied Surface Science Vol. 127 Issue. 129 p. 477.

142 Nikolajeff, F., Hard, S., Curtis, B. (1997) '*Diffractive Microlenses Replicated in Fused Silica for Excimer Laser Beam Homogenizing*', Applied Optics, Vol. 36, pp. 8481-8489.

143 Bollanti, S., Di Lazzaro, P., Murra, D., Tefouet Kana, E., Felici, G. (2004) '*Edge Steepness and Plateau Uniformity of a Nearly Flat-top-shaped Laser Beam*', Applied Physics B vol. 78, Issue 2, pp. 195-198.

144 Lewis, C., L., S., Weaver, I., Doyle, L., A., Martin, G., W., Morrow, T., Pepler, D., A., Danson, C., N., Ross, I., N. (1999) '*Use of a random phase*

plate as a KrF laser beam homogenizer for thin film deposition applications', Review of Scientific Instruments Vol. 70 Issue. 4, p. 2116.

145 Kopp, C., Ravel, L., Meyrueis, P. (1999) '*Efficient Beamshaper Homogenizer Design Microlens Array and Random Phase Plate*', Journal of Optics. A Vol. 1, pp. 398-403.

146 Cable Design Equations-Coaxial Cable, General Cable, Carol Brand Technical Information (2009), P. 195.

147 Scattering, Michigan Tech. Dept. of Geological and Mining Engineering and Sciences, Available at: www.geo.mtu.edu/~scarn/teaching/GE4250/scattering_lecture.ppt, (Accessed: 10 August 2012)

148 Loree, T., R., Sze, R., C., Barker, D., L., Scott. P., B. (1979) '*New Lines in the UV: SRS of Excimer Laser Wavelengths*', IEEE Journal of Quantum Electronics, Vol. QE-15, No. 5, pp. 337-342.

149 Grant, W., B., Browell, E., V., Higdon, N., S. Ismail, S. (1991) '*Raman Shifting of KrF Laser Radiation for Tropospheric Ozone Measurements*', Applied Optics, Vol. 30, No. 18, pp. 2628-2633.

150 Lay, T., T., Wada, S., Tashiro, H., Toyoda, K. (1996) 'Relation of Pump-beam Quality and Conversion Efficiency in the Raman Downward Conversion', Applied Physics, B. 62, pp. 59-64.

151 Telescope Aberrations: Effects on image quality, Available at: http://www.telescope-optics.net/effects1.htm (Accessed: 10 August 2012)

152 A Better Method of Measuring Optical Performance, Available at: http://www.rfroyce.com/standards.htm (Accessed: 10 August 2012)

References

153 Strehl Ratio, Available at: http://www.telescope-optics.net/Strehl.htm (Accessed: 10 August 2012)

154 Iida, N., Yamasaki, Y., Sato, S., Kumano, K., Kojima, Y. (2004) '*Study on Auto-Ignition and Combustion Mechanism of HCCI Engine*', SAE Paper 2004-32-095.

155 Febler, M., Wetzel, M., Schenk, M., Rottengruber, H., Huhn, W. (2008) '*Determination of Thermodynamic Potentials for Alternative Ignition Systems in Spray-Guided Combustion'*, Proceedings of the 8th International Symposium on Internal Combustion Engine Diagnostics.

156 Orlandini, I., Gartung, K., Schlerfer, J. (2009) '*Application of 3D-CFD Simulations in the Development of Spark Plugs*', SAE Technical Paper 2009-01-0706.

157 Koch, J., D. (2005) '*Fuel Tracer Photophysics for Quantitative Planar Laser-induced Fluorescence*', PhD thesis, Stanford University.

158 Rothamer, D., A. (2007) '*Development and Application of Infrared and Tracer-Based Planar Laser-induced Fluorescence Imaging Diagnostics*', PhD thesis, Stanford University.

159 Cheung, B., H. (2011) '*Tracer-based Planaer Laser-induced Fluorescence Diagnostics: Quantitative Photophysics and Time-resolved Imaging*', PhD thesis, Stanford University.

160 Schulz, C., Sick, V. (2005) '*Tracer-LIF Diagnostics: Quantitative Measurement of Fuel Concentration, Temperature and Fuel/air Ratio in Practical Combustion Systems*', Progress in Energy and Combustion Science, 31(1):75,121.

References

161 Rothamer, D., A., Ghandhi, J., B. (2003) '*Determination of flame-front equivalence ratio during stratified combustion*', *SAE Technical Paper*, 2003-01-0069.

162 Thurber, M., C. (1999) '*Acetone Laser-Induced Fluorescence for Temperature and Multiparameter Imaging in Gaseous Flows*', PhD thesis, Stanford University.

163 Stockinger, V., Schapertons, H., Kuhlmann, U. (1992), '*Investigation on Gasoline Engine Working with Self-ignition by Compression*', MTZ, Vol. 53, pp. 80-85.

164 Yang, J., Culp, T., Kenney, T. (2002) '*Development of a Gasoline Engine System Using HCCI Technology - The Concept and the Test Results*', SAE Technical Paper 2002-01-2832.

165 Hyvönen, J., Haraldsson, G., Johansson, B. (2003) '*Operating range in a Multi Cylinder HCCI engine using Variable Compression Ratio*', SAE Technical Paper 2003-01-1829.

166 Yang, J. Kenney, T. (2006) '*Robustness and Performance Near the Boundary of HCCI Operating Regime of a Single-Cylinder OKP Engine*', SAE Technical Paper 2006-01-1082.

167 Fuerhapter, A., Piock, W., Fraidl, G. (2003) '*CSI - Controlled Autoignition - the Best Solution for the Fuel Consumption - Versus Emission Trade-Off?*' SAE Technical Paper 2003-01-0754.

168 Fuerhapter, A., Unger, E., Piock, W., Fraidl, G. (2004) '*The new AVL CSI Engine - HCCI Operation on a Multi Cylinder Gasoline Engine*', SAE Technical Paper 2004-01-0551.

References

169 Koopmans, L., Backlund, O., Denbratt, I. (2002) '*Cycle to Cycle Variations: Their Influence on Cycle Resolved Gas Temperature and Unburned Hydrocarbons from a Camless Gasoline Compression Ignition Engine*', SAE Technical Paper 2002-01-0110.

170 Koopmans, L., Ström, H., Lundgren, S., Backlund, O. et al. (2003) '*Demonstrating a SI-HCCI-SI Mode Change on a Volvo 5-Cylinder Electronic Valve Control Engine*', SAE Technical Paper 2003-01-0753.

171 Serpengüzel, A., Hahn, R., Acker, W. (1993) '*Single Pulse Planar Laser Induced Fluorescence Imaging of Hydroxyl Radicals in a Spark Ignition Engine*', SAE Technical Paper 932701.

172 Arnold, A., Buschmann, A., Cousyn, B., Decker, M., et al. (1993) '*Simultaneous Imaging of Fuel and Hydroxyl Radicals in an In-Line Four Cylinder SI Engine',* SAE Technical Paper 932696.

173 Bernardo, J., Smith, A., F., M., (2000) *Bayesian Theory*. New York: John Wiley

174 Image Intensifiers Catalogue, Hamamatsu Photonics, 2009.

175 Introduction to Image Intensifiers for Scientific Imaging, Princeton Instruments, 2012.


MECH. ENG.
Main Workshop
'AN OASIS OF PROMISE IN A DESERT OF DESPAIR'